SYNTHESIS & CHARACTERISATION OF NANOZSM-5 & MOR ZEOLITES, CHARACTERIZATION OF ZNS IN THE PORE NETWORK OF MOR

Pirzada Afridi

Wolfson College
University of Oxford

Thesis submitted for the degree of Doctor of Philosophy
Inorganic Chemistry Laboratory 2017

Supervisor

Professor Peter P Edwards FRS
Inorganic Chemistry Laboratory
Department of Chemistry
University of Oxford

Department of Chemistry, University of Oxford

Syntheses & Characterization of NanoZSM-5 & MOR Zeolites, Characterization of ZnS in The Pore Network of MOR

Pirzada (Wolfson College)

A thesis submitted in partial fulfilment of the requirements for the degree of Doctor of Philosophy in Inorganic Chemistry, Trinity Term 2017

Abstract

This study was carried out on the synthesis of mordenite zeolite and ZSM-5 zeolite. In Chapter 3 reports the growth of ZnS nanoclusters in the pore channels of mordenite zeolite. ZnS as an important wide-band-gap (3.6 eV) semiconductor nanoclusters and have various technological applications such as photocatalysis, nonlinear optics, sensors, solar cells, injection lasers, flat panel displays, ultraviolet light emitting diodes (LED).

Zeolites have several different applications in industries, such as in catalysis, ion exchange adsorption and gas separation. Zeolites are mostly used as a catalyst in the petrochemical industry. ZSM-5 zeolite is widely used a heterogeneous catalyst in the petrochemical industry due to its unique porous structure. Special attention has been made to synthesize nano-ZSM-5 in order to improve its catalytic activity. Catalysis depends on the characteristics length scale of the active sites, while the rate depends on the accessible active sites. In order to improve the performance of ZSM-5 zeolite used as a catalyst in the petrochemical industry, the researchers amid to produce nanocrystalline of the ZSM-5 zeolite. That will help to reduce the path length for the reaction and hence will increase the rate of a reaction. Comparative synthesis nano-particles of ZSM-5 zeolite using two different methods of treatment i.e. pre-treatment and interrupted treatment with ultrasound and without ultrasound was studied, its effect on aging and crystal growth during the hydrothermal treatment.

In Chapter 4 the pre-treatment with ultrasound and without ultrasound (static) with an increasing time intervals have been reported. The resulting product the particle size is clearly decreased by using ultrasound pre-treatment. While in Chapter 5 using a different method of treatment called interrupted of the hydrothermal process. As in this method, we stopped the hydrothermal process for 20 minutes and treated the gel with ultrasound for 15 minutes. This treatment was repeated after every 2 hours of hydrothermal treatment. Similarly, the same method was applied to the experiment but without the use of ultrasound called a static method of aging.

A 3rd method was also applied to investigate the effect of ultrasound on the particle size distribution of the synthesized crystalline powder. All the results showed that the ultrasound not only effects on the particle size but it also affects the crystallinity too i.e. increased the crystallinity and the reduced in the particle size.

Syntheses & Characterization of NanoZSM-5 & MOR Zeolites, Characterization of ZnS in The Pore Network of MOR

Pirzada (Wolfson College)

A thesis submitted in partial fulfilment of the requirements for the degree of Doctor of Philosophy in Inorganic Chemistry, Trinity Term 2017

Extended Abstract

The zeolites are broadly used for three main applications: catalysts, adsorption, and ion exchange due to its unique porous structure.

Highly siliceous crystalline mordenite zeolite was synthesized without an organic template (OSDA). Ludox HS30 was used as a silicon precursor, while sodium aluminate was utilized as the Al source. The ion exchange method was performed in two steps in order to create zinc sulfide (ZnS) nanoclusters in the MOR framework pores. Zinc nitrate Zn(NO3)2 · 6H2O was used as a source of Zn2+ ion and sodium sulfide was utilized as a source of S2- ion in the ion exchange steps for the syntheses of the guest ZnS nanoclusters. The as-synthesized mordenite (NaMOR) zeolite and exchanged samples (first ZnMOR, and then ZnSMOR) were characterised by using powder X-ray diffraction (XRD), solid state nuclear magnetic resonance (SS MAS NMR), scanning electronic microscopy (SEM), transmission electron microscopy (TEM), N2 adsorption and desorption BET surface analysis, energy-dispersive X-ray spectroscopy (EDXS). Decreases in the unit cell parameters are observed from NaMOR > ZnMOR > ZnSMOR. N2 adsorption and BET surface analysis show a significant drop in micropore surface areas in the ZnSMOR. There is a remarkable change in the adsorption isotherm of ZnSMOR sample as compare to ZnMOR. These can be explained by the presence of zinc ions (Zn2+) after ion exchange and hint at the

presence of zinc sulfide nanoclusters. EDXS confirm the presence of Zn and S in the final exchanged mordenite samples. TEM provides evidence of ZnS accumulated on the surface and adhered to the inner surface of the pore channels.

The chemistry of nano-zeolites has also received significant attention, because of their most important textural properties, such as high surface area, well-defined porosity and the number of active acidic sites plays an effective role in the rate of reaction, product selectivity, and low coke formation. ZSM-5 is one of the most important zeolites used in the petrochemical industries for catalysis in various petrochemical processes because of its unique geometrical structure.

In this work, it is aimed to develop a novel method for the synthesis of nanoZSM-5 on the basis of pre-treatment/aging before the conventional hydrothermal process and interrupting hydrothermal treatment using ultrasound. The whole syntheses processes were investigated by means of ultrasound treatment. About 10-30 nm particle size has been obtained by using the interrupted ultrasound method as compared with the other methods of syntheses reported in this study. The effect of pre-treatment/aging on the crystallite size of the synthesized product was examined. The nanoZSM-5 zeolite aggregates were synthesized from alkaline aluminosilicate gel mixture applied two different aging/pre-treatments methods i.e. static/stand-by (without stirring and ultrasound) and ultrasonication (using ultrasound bath) before the hydrothermal process. Ultrasound bath is functioning at 35 kHz at a controlled temperature. It was then compared with the static pre-treatment/aging method. Each method has the same experimental conditions such as pre-treatment time, crystallization period and temperature at autogenous pressure. The interruption was performed for 15 minutes after every 2 hours during the course of hydrothermal treatment. The

synthesis was performed at 170 ºC for 24 hours and the final product was investigated. The nano-particles synthesized in the interrupted and uninterrupted conventional hydrothermal route was compared. Micro and nanoZSM-5 were characterized by X-ray powder diffraction (XRD) for geometrical phase confirmation, scanning electron microscopy (SEM) particles morphology and dynamic light scattering (DLS) were used to investigate the particle size distribution, transmission electron microscopy (TEM) was used for identification of crystallite size, N2 adsorption/desorption BET surface analysis was used to examine the surface area and porosity, solid state magic angle spinning nuclear magnetic resonance spectroscopy (SS MAS NMR) was used for the determination of Si and Al ratio (SAR) and also gives structural information.

The work described in this thesis was carried out in the Inorganic Chemistry Laboratory, University of Oxford, from October 2012 until June 2016, under the supervision of Professor Peter P Edwards and Dr. Asel Sartbaeva. All of the work is mine own unless otherwise stated and has not been submitted previously for any other degree at this or any other university.

Pirzada Afridi

July, 2017

To my parents, my wife, my brothers and sisters for their continued prayers, love, caring and compassion, and for being close to me all the time

…and to every teacher who has helped and made me able to do this work.

Acknowledgments

My DPhil would not have been successful without the strength, elegance, and courage that come from Allah.

I would like to express my deepest and heartfelt gratitude to my research advisor, Professor Peter P. Edwards for giving me an opportunity to work in KACT and Oxford Petroleum Research Centre (KOPRC) of his research group. With all his guidance and advice, a large amount of time that he has devoted to discussions of my research, I have been able that complete my DPhil. I am very grateful towards my supervisor for his patience and for his care for all things. I have learned from him over the past three years, and I ma grateful for the intellectual freedom granted me during the research and fruitful discussions during our group meetings. I am also extremely grateful to my co-supervisor Dr. Asel Sartbaeva, who provided me with the opportunity to work in the Zeolite Research Group. She introduced me to the field of zeolite chemistry and trained me on the various techniques of characterization, for helping me both with useful comments and as well as assistance with the analytical data acquisition. I would also like to thanks, Dr. Vladimir Kuznetsov, Dr. Xiao Tiancun, Dr. Liam France, Dr. Michael Jones, Dr. Sergio Gonzalez-Cortes for their support and advice throughout my project. I am very much thankful to Ms. Linda Webb the Inorganic Chemistry Laboratory Secretary for her kind help and support during my research work. Special thanks to Ka Leung (Thomas), Alex Vai and Bonan Liu of PPE group for their support and help in the lab. I would like to also thank all the PPE group members for working together and the help and support that they gave me and for the very friendly working environment. I would like to say to everyone, I

would not have been able to pull this through without your help, patience, and understanding.

Likewise, I am deeply grateful to Dr. Kerstin Jurkschat to introduce and trained me on different techniques of characterization at Oxford Materials. I am thankful to Dr. David C. Apperley of the Department of Chemistry University of Durham for the acquisition of Solid-state Nuclear Magnetic Resonance data and their interpretation. I am also very thankful to Paul Pattinson for having trained me on the SEM, which was very useful to complete the zeolite particles characterization at the Department of Physics, University of Oxford.

I really appreciate and thanks to all the administrative staff of the Inorganic Chemistry Laboratory University of Oxford for all their help and support.

I would like to say thanks and appreciate the help of all the administrative staff of the Wolfson College University of Oxford for giving me a place to do DPhil.

Furthermore, I want to express my sincere thanks to my friends Mohammad Zaman Marofkhail (Ali), Ijaz Khan Durrani, Amir Ali, Yasir Khan, and Zahid Khan for their support, help, and hospitality during my stay at Oxford. I am very much grateful to Mr. Hidayat Ullah Khan and Hazrat Ali for their help and support from the beginning to end.

I would like to say deepest thanks to Mr. Farid Sherzad (Birmingham, UK) and his family for their all the time caring, love and support.

Pirzada Afridi

July 2017, Oxford, UK

Table of Contents

Abstract……..…..…iii

Acknowledgment……..viii

List of Figures.……...……....xv

List of Tables.……...…….……..xxvii

1. WHAT IS A ZEOLITE? 1

1.1 THE STRUCTURE AND COMPOSITION OF ZEOLITES 3

1.2 TYPES OF ZEOLITES 8

1.2.1 Natural Zeolites 8

1.2.2 Synthetic Zeolites 9

1.3 PROPERTIES AND APPLICATIONS OF ZEOLITES 9

1.3.1 Catalysis 11

1.3.2 Acidity and Basicity of Zeolites 13

1.3.3 Adsorption and Separation 15

1.3.4 Ion Exchange 16

1.4 MORDENITE ZEOLITE 17

1.4.1 ZnS Semiconductor Nano-particles 20

1.5 ZEOLITE SOCONY MOBIL-5 (ZSM-5) ZEOLITE 21

1.5.1 Why Nano-crystalline ZSM-5 Zeolite? 24

1.6 AIMS OF THE STUDY 25

1.6.1 ZnS Nano-clusters Within The Mordenite Pore Network 25

1.6.2 Solid Acid Catalyst NanoZSM-5 Particles/Crystals 26

1.7 LITERATURE REVIEW 27

1.7.1 The Synthesis of MOR Zeolite 27

1.7.2 The Synthesis of ZnS Nano-clusters Within The MOR Pore Network 28

1.7.3 The Synthesis of NanoZSM-5 Zeolite 30

1.8 REFERENCES 34

2. SYNTHESIS, INSTRUMENTAL & ANALYTICAL TECHNIQUES 43

2.1 SOURCES AND MATERIALS 43

2.1.1 Sources of Water 43

2.1.2 Aluminium Precursors 44

2.1.3 Silicon Precursors 44

2.1.4 Sources of Cations 45

2.2 SYNTHESIS OF ZEOLITES 45

2.2.1 Zeolite Crystallization 47

2.2.2 Aging or Pre-treatment of a Solution/Mixture 47

2.2.3 Nucleation 48

2.2.4 Crystal Growth 49

2.3 X-RAY DIFFRACTION 51

2.4 TRANSMISSION ELECTRON MICROSCOPY (TEM) 54

2.5 SCANNING ELECTRON MICROSCOPY (SEM) 57

2.6 ENERGY DISPERSIVE X-RAY SPECTROSCOPY (EDXS) 60

2.7 N_2 ADSORPTION/DESORPTION 62

2.8 SOLID-STATE MAGIC ANGLE SPINNING NUCLEAR MAGNETIC RASONANCE (MAS NMR) 66

2.9 DYNAMIC LIGHT SCATTERING (DLS) 72

2.10 REFERENCES 74

3. SYNTHESIS OF MOR ZEOLITE & ZNS NANO-CLUSTERS 79

3.1 EXPERIMENTAL 80

3.1.1 Chemicals, Reagents Used and Synthesis Procedure 80

3.1.2 Synthesis of Mordenite Zeolite 80

3.1.3 Ion Exchange Method 82

3.2 RESULTS AND DISCUSSION 83

3.2.1 Powder X-ray Diffraction Patterns of Mordenite Zeolite 83

3.2.2 Scanning Electron Microscopy (SEM) 88

3.2.3 Transmission Electron Microscopy (TEM) 92

3.2.4 Energy-Dispersive X-Ray Spectroscopy 95

3.2.5 BET Surface Analysis 99

3.2.6 Solid State Magic Angle Spinning Nuclear Magnetic Resonance (MAS NMR) 104

3.3 DISCUSSION 111

3.4 CONCLUSION 113

3.5 REFERENCES 113

4. SYNTHESIS OF NANOZSM-5 WITH & WITHOUT ULTRASOUND PRE-TREATMENT 116

4.1 EXPERIMENTAL 117

4.1.1 Chemicals, Reagents Used and Syntheses 117

4.2 SYNTHESIS OF ZSM-5 ZEOLITE 117

4.2.1 Nucleation and Crystal Growth Mechanism 119

4.2.2 Calcination and Activation of The Catalysts (nanoZSM-5) 122

4.3 RESULTS AND DISCUSSION 122

4.3.1 Powder X-ray Diffraction (XRD) of ZSM-5 Zeolite 122

4.3.2 Transmission Electron Microscopy (TEM) 129

4.3.3 Scanning Electron Microscopy (SEM) 133

4.3.4 Dynamic Light Scattering (DLS) 137

4.3.5 Energy-Dispersive Spectroscopy (EDS) 140

4.3.6 N_2 Adsorption/Desorption 143

4.3.7 Solid State Magic Angle Spinning Nuclear Magnetic Resonance (MAS NMR) 149

4.4 DISCUSSION 156

4.5 CONCLUSION 159

4.6 REFERENCES 159

5. SYNTHESIS OF NANOZSM-5 163

5.1. CHEMICALS, REAGENTS USED AND SYNTHESIS PROCEDURE 163

5.2. SYNTHESIS OF ZSM-5 ZEOLITE 163

5.2.1. Zeolite Synthesis Mechanism 164

5.2.2. Interrupted Ultrasound treatment 166

5.2.3. Calcination and Activation of the Catalysts (NanoZSM-5) 166

5.3. RESULTS AND DISCUSSION 167

5.3.1. Powder X-ray Diffraction (XRD) 167

5.3.2. Transmission Electron Microscopy (TEM) 172

5.3.3. Scanning Electron Microscopy (SEM) 174

5.3.4. Dynamic Light Scattering (DLS) 176

5.3.5. Energy-Dispersive Spectroscopy (EDS) 179

5.3.6. N_2 Adsorption/Desorption 181

5.3.7. Solid State Magic Angle Spinning Nuclear Magnetic Resonance (MAS NMR) 186

5.4. DISCUSSION 193

5.5. CONCLUSION 198

5.6. REFERENCES 199

CONCLUSION 202

FUTURE WORK 203

List of Figures

1.1 Primary sub unit of Si tetrahedra with 4 oxygen. 4

1.2 A proposed mechanism for the combination of PBUs converted to SBUs and ultimately to a zeolite b-cage consisting of 24 silica units tetrahedra. Taken from BZA website.[10] 4

1.3 Secondary building units of zeolites structure, Silicate/aluminate single ring, double rings and other extended single ring block units without the oxygen atom.[13] 5

1.4 Cations and water molecules residing in the pores of zeolites.[17] ... 7

1.5 8-T, 10-T and 12-T membered rings along 001 viewed formed zeolite pore aperture. 7

1.6 A schematic representation of shape selectivity for reactions in zeolite channels. Taken and modified.[41] 13

1.7 Adsorption and separation of gases and purification of zeolites in different stages.[48] 16

1.8 Ion exchange efficiently occurred in the zeolite channels without the affecting its framework.[54] 17

1.9 8-member rings and 12 member rings channels along [001].[61] 18

1.10 Framework strucutre for MOR viewed along c axis the 12 ring one dimensional channel, cations (Na^+) (green) withing the 8 ring. 19

1.11 Zigzag (horizontal) and straight (perpendicular) channels of ZSM-5 pore network. 22

1.12 Systematic Structure mechanism of pentasil units connectivity of ZSM-5 frameworks. 22

1.13 Isomerisation from m-xylene to p-xylene. Hence p-xylene is a favourable product for the ZSM-5 pore channels 24

1.14 Conversion of ethanol to ethanal and H2 gas over Cu-ZSM-5. 24

2.1 Schematic presentation of different steps involved in the zeolite synthesis. Taken and modified from various sources. 47

2.2 Proposed mechanism of nucleation and crystal growth in supersaturation solution. I) Single nucleation and uniform crystal; II) Nucleation, growth and aggregation of smaller subunits; III) Multiple nucleation events and crystals growth.[25] 49

2.3 Proposed schematic representation of crystal growth stepwise transitions. I & II) Growth unit transport of solute to a position near the crystal surface, III) Adsorption onto crystal surface, IV) Growth unit attached to Vacancies (Kinks, Surface or Edge). Taken and Modiefied from.[27] 51

2.4 Presenting Bragg's Law, the incident ray reflected on the particle surface. X-rays interfere constructively when the additional path length 2DSINΘ is equal to integral multiple of the wavelength Λ... 52

2.5 A) Schematic cross section of TEM system presenting basic parts. B) Similarities of the lens environments between TEM diffraction and TEM photos forms.[39] 55

2.6 A beam electrons interaction with material. Red text indicates the backscattered and secondary electrons detected by an SEM in image generation. 58

2.7 A schematic diagram of a scanning electron microscope. 59

2.8 Simplified and systematic sketch of EDS.[44] 61

2.9 IUPAC RECOMMENDED THE SIX MAIN CLASSIFICATION OF ADSORPTION ISOTHERM. TAKEN AND MODIFIED FROM.[50] 64

2.10 SUB-TYPES N_2 ADSORPTION DESORPTION ISOTHERMS, DEMONSTRATE THE PORE SHAPE/STRUCTURE AND DISTRIBUTION. H STANDS FOR HYSTERESIS. [50] 65

2.11 SCHEMATIC OF THE GAS ADSORPTION PROCESS SHOWING PORE FILLING AND EMPTYING AT VARIOUS STAGES OF THE ISOTHERM. PROVIDED BY MICROMERITICS ANALYTICAL SERVICES 66

2.12 DIFFERENT NUCLEAR INTERACTIONS OCCURS IN NMR ANALYSIS 68

2.13 SOLID STATE MAS NMR SPECTRUM OF ZEOLITE A. THE FIVE TYPICAL ^{29}SI CHEMICAL SHIFTS: SI4(AL), SI(3AL), SI2(AL), SI(1AL), AND SI(0AL).TAKEN FROM.[55] 70

2.14 A SIMPLIFIED SKETCH OF DYNAMIC LIGHT SCATTERING INSTRUMENT 73

3.1 THE X-RAY DIFFRACTION PATTERNS OF THE AS SYNTHESIZED MOR USING A FUMED SILICA SOURCE AS A FUNCTION OF INCREASING CRYSTALLIZATION TIME. 85

3.2 THE X-RAY DIFFRACTION PATTERNS OF THE AS-SYNTHESIZED MOR USING LUDOX HS30 AS THE SILICA SOURCE AS A FUNCTION OF INCREASING CRYSTALLIZATION TIME. 86

3.3 CRYSTALLINITY OF MOR ZEOLITE AS A FUNCTION OF CRYSTALLIZATION TIME CALCULATED FROM THE PEAKS INTEGRALS. 86

3.4 X-RAY POWDER DIFFRACTION OF THE NAMOR AND MORDENITE EXCHANGED WITH ZN^{2+} AND ZNS NANO-CLUSTERS REPRESENTED AS ZNMOR AND ZNSMOR RESPECTIVELY, THE BOTTOM CURVE IS THE REFERENCE PATTERN OF MORDENITE. 87

3.5 Different PTFE liner produce different morphologies of mordenite zeolite using otherwise the same experimental conditions. a) 250 ml, b) 100 ml, and c) 50 ml PTFE liner were used in the Parr reactor. ... 89

3.6 SEM micrographs of *as synthesized* mordenite zeolite illustrated different morphologies and particle sizes in samples, using similar reaction conditions. a-d) unidentified morphologies, e-g) Different morphologies and particle size in the range 10-40 mm, h) uniform particle shapes having size 40-45 mm. Note: Size is length wise for all the samples relative to bar scales. 91

3.7 SEM micrograph of the ZnMOR and ZnSMOR after the Zn^{2+} ion exchanged and ZnSMOR after the formation of ZnS in the as-synthesized mordenite pores network..... 92

3.8 TEM images of two different crystals (Left) and their respective elemental composition spectra (Right) of the *as-synthesized* NaMOR 93

3.9 High resolution TEM images of two different crystals (Left) and their respective elemental composition spectra (Right) of the *as-synthesized* ZnSMOR sample..... 94

3.10 TEM images shows the diffused rings of ZnS in the ZnSMOR sample. 95

3.11 EDX micrographs of elemental distribution of a) the ZnSMOR sample, (b) is the supported carbon for sample, (c) and (d) view of the Si and Al atoms respectively, (e) and (f) are oxygen and sodium atom respectively, while (g) and (h) view of the S and Zn atoms

RESPECTIVELY, WHERE THE LOW CONTRAST OF IMAGES (G) AND (H) IS DUE TO THEIR LOW CONCENTRATION. 97

3.12 EDXS SPECTRA NAMOR (NO S AND ZN DETECTED), ZNMOR SPECTRA (ZN DETECTED), ZNSMOR ZN AND S DETECTED, NA, ZN PEAK CAN BE SEEN NEAR 8 KEV. 98

3.13 N_2 ADSORPTION (RED SPHERES) AND DESORPTION (WHITE SPHERES) ISOTHERM OF ZNSMOR. 102

3.14 N_2 ADSORPTION (WHITE SPHERES) AND DESORPTION (RED SPHERES) ISOTHERM OF NAMOR. 103

3.15 N_2 ADSORPTION (WHITE SPHERES) AND DESORPTION (RED SPHERES) ISOTHERM OF ZNMOR. 103

3.16 BJH PORE SIZE DISTRIBUTION FROM THE NITROGEN DESORPTION CURVE FOR NAMOR WHITE CIRCLE, ZNMOR HALF RED CIRCLES AND ZNSMOR RED CIRCLES. NOTE: THE DATA IS NORMALISED. 104

3.17 ^{27}AL SOLID STATE MAS NMR SPECTRA OF NAMOR (BLACK), ZNMOR (RED), AND ZNSMOR (BLUE) SAMPLES. 106

3.18 ^{29}SI SOLID STATE MAS NMR SPECTRA OF THE AS-SYNTHESIZED SAMPLE NAMOR (BLACK), ZNMOR (RED) AND ZNSMOR (BLUE) AFTER THE ION EXCHANGE. 107

3.19 DECONVOLUTED SPECTRA OF ^{29}SI NMR OF A) NAMOR, B) ZNMOR AND C) ZNSMOR. NAMOR AND ZNMOR SHOW THREE (3) SAME NUMBER OF SI COORDINATION ENVIRONMENTS, WHILE IN ZNSMOR 4 ENVIRONMENTS CAN BE DISCERNED. 108

3.20 ^{23}Na solid state MAS NMR spectra of the parent sample NaMOR (black), ZnMOR (red) and ZnSMOR (blue) before and after ZnS nanocluster growth 109

3.21 A proposed two step schematic mechanism of the formation ZnS nano-clusters in the MOR framework. 110

4.1 Simplified synthesis mechanism ZSM-5 zeolite using with and without ultrasound pre-treatment. 118

4.2 Schematic representation of the crystallization mechanism of FAU-type zeolite synthesized under the ambient condition, taken from[2] 120

4.3 XRD pattern of test experiments of *as synthesized* ZSM-5 at different crystallization time and same temperature 123

4.4 XRD pattern of as synthesized ZSM-5 zeolite transition from orthorhombic to monoclinic after calcination at 550 °C 124

4.5 X-ray diffraction of *as synthesized* samples of ZSM-5 zeolite using static aging a) 15 min, b) 30 min, c) 60 min, d) 90 min, and e) 120 minutes at 170 °C 125

4.6 X-ray diffraction of as synthesized samples of ZSM-5 zeolite using ultrasound pre-treatment a) 15 min, b) 30 min, c) 60 min, d) 90 min, and e) 120 minutes. 127

4.7 *As synthesized* nanoZSM-5 zeolite using ultrasound pre-treatment (Red) and static/stand by aging (BLACK) showing Relative Crystallinity increases with the time. 129

4.8 TEM images of the as synthesized micro and nanoZSM-5 using static aging method. Samples were pre-treated a) for 30 minutes, b) for 60

MINUTES, C) FOR 90 MINUTES AND D) FOR 120 MINUTES, AT 170 °C SYNTHESIS TEMPERATURE 130

4.9 TEM IMAGES OF THE AS SYNTHESIZED NANOZSM-5 USING ULTRASOUND PRE-TREATMENT. A) FOR 30 MINUTES, B) FOR 60 MINUTES, C) FOR 90 MINUTES AND D) FOR 120 MINUTES, AT 170 °C SYNTHESIS TEMPERATURE 132

4.10 SEM IMAGES OF THE *AS SYNTHESIZED* MICRO AND NANOZSM-5 PRE-TREATMENT STATIC AGING, A) FOR 15 MINUTES, B) 30 MINUTES, C) FOR 60 MINUTES, D) FOR 90 MINUTES AND E) FOR 120 MINUTES, AT 170 °C SYNTHESIS TEMPERATURE 135

4.11 SEM IMAGES OF THE AS SYNTHESIZED MICRO AND NANOZSM-5 USING ULTRASOUND PRE-TREATMENT, A) FOR 15 MINUTES, B) 30 MINUTES, C) FOR 60 MINUTES, D) FOR 90 MINUTES AND E) FOR 120 MINUTES, AT 170 °C SYNTHESIS TEMPERATURE 136

4.12 DLS DATA OF THE *AS SYNTHESIZED* ZSM-5 SAMPLES USING STATIC AGING AT 30 MINUTES, 60 MINUTES, 90 MINUTES AND 120MIN AT 170 °C CRYSTALLIZATION 138

4.13 DLS DATA OF THE AS SYNTHESIZED ZSM-5 SAMPLES USING ULTRASOUND AGING AT 30 MIN, 60 MIN, 90 MIN AND 120MIN AT 170 ^{O}C CRYSTALLIZATION 139

4.14 N_2 ADSORPTION/DESORPTION ISOTHERMS OF MICRO AND NANOZSM-5 USING STATIC AGING FOR (A) 15 MIN, (B) 30 MIN, (C) 60 MIN, (D) 90 MIN AND (E) 120 MIN AT 170 °C CRYSTALLIZATION 144

4.15 N_2 ADSORPTION/DESORPTION ISOTHERMS OF MICRO AND NANOZSM-5USING ULTRASOUND PRE-TREATMENT (A) 15 MIN, (B) 30 MIN, (C) 60 MIN, (D) 90 MIN AND (E) 120 MIN AT 170 °C CRYSTALLIZATION 147

4.16 BJH PORE SIZE DISTRIBUTION OF THE SAMPLES TREATED WITH STATIC AGING AT (A) 15 MIN, (B) 30 MIN, (C) 60 MIN, (D) 90 MIN AND (E) 120 MIN. 148

4.17 BJH PORE SIZE DISTRIBUTION OF THE SAMPLES TREATED USING ULTRASOUND TREATMENT AT (A) 15 MIN, (B) 30 MIN, (C) 60 MIN, (D) 90 MIN AND (E) 120 MIN..... 148

4.18 ^{27}AL MAS NMR OF AS SYNTHESIZED SAMPLES USING STATIC METHOD OF AGING AT 15 MIN, 30 MIN, 60 MIN, 90 MIN AND 120 MIN..... 150

4.19 ^{27}AL MAS NMR OF AS SYNTHESIZED SAMPLES USING ULTRASONIC METHOD OF AGING AT 15 MIN, 30 MIN, 60 MIN, 90 MIN AND 120 MIN..... 151

4.20 ^{29}SI MAS NMR OF AS SYNTHESIZED ZSM-5 ZEOLITE USING STATIC METHOD OF AGING AT 15 MIN, 30 MIN, 60 MIN, 90 MIN AND 120 MIN..... 152

4.21 ^{29}SI MAS NMR DECONVOLUTED SPECTRA OF *AS SYNTHESIZED* ZSM-5 ZEOLITE USING STATIC METHOD OF AGING AT 15 MIN, 60 MIN AND 120 MIN. 153

4.22 ^{29}SI MAS NMR SPECTRA OF *AS SYNTHESIZED* ZSM-5 ZEOLITE USING ULTRASOUND PRE-TREATMENT METHOD AT 15 MIN, 30 MIN, 60 MIN, 90 MIN AND 120 MIN. 155

4.23 ^{29}SI MAS NMR DECONVOLUTED SPECTRA OF *AS SYNTHESIZED* ZSM-5 ZEOLITE USING ULTRASOUND PRE-TREATMENT METHOD AT 15 MIN, 60 MIN AND 120 MIN..... 156

5.1 THREE DIFFERENT MECHANISMS REPRESENTING THE ZEOLITE CRYSTAL GROWTH. PATH I) CONSIDERED MONOMER PRECURSOR AND THE AMORPHOUS GEL PARTICLES MAINTAINED AVERAGE SIZE. PATH II) FOLLOWS BY THE ADDITION OF PRIMARY PARTICLES AND GROW THE CRYSTALS. PATH III) LARGE PARTICLES WERE GROWN FROM THE AGGREGATION OF THE SMALL PARTICLES.[2] 165

5.2 X-RAY DIFFRACTION OF TEST EXPERIMENTS OF *AS SYNTHESIZED* ZSM-5 ZEOLITE AT DIFFERENT CRYALLIZATION TEMPERATURE..... 168

5.3 X-RAY DIFFRACTION OF THE *AS SYNTHESIZED* NANOZSM-5 BY DIFFERENT METHODS OF INTERRUPTION USING ULTRASOUND AND WITHOUT ULTRASOUND 169

5.4 TEM MICROGRAPHS OF THE *AS SYNTHESIZED* SAMPLES A) INTERRUPTED SYNTHESIS WITHOUT ULTRASOUND WITH INCREASING TEMPERATURE FROM 25-170 °C B) INTERRUPTED SYNTHESIS WITH ULTRASOUND WITH INCREASING TEMPERATURE FROM 25-170 °C C) INTERRUPTED SYNTHESIS WITHOUT ULTRASOUND AT CONTACT TEMPERATURE 170 °C D) INTERRUPTED SYNTHESIS WITH ULTRASOUND AT CONTACT TEMPERATURE 170 °C..... 173

5.5 SEM IMAGES OF THE *AS SYNTHESIZED* SAMPLES A) INTERRUPTED SYNTHESIS WITHOUT ULTRASOUND WITH INCREASING TEMPERATURE FROM 20-170 °C B) INTERRUPTED SYNTHESIS WITH ULTRASOUND WITH INCREASING TEMPERATURE FROM 20-170 °C..... 175

5.6 SEM IMAGES OF THE AS SYNTHESIZED SAMPLES C) INTERRUPTED SYNTHESIS WITHOUT ULTRASOUND AT FIXED TEMPERATURE 170 °C D) INTERRUPTED SYNTHESIS WITH ULTRASOUND AT FIXED TEMPERATURE 170 °C..... 176

5.7 DLS DATA OF THE *AS SYNTHESIZED* MICRO AND NANOZSM-5 SAMPLES A) INTERRUPTED SYNTHESIS WITHOUT ULTRASOUND WITH INCREASING TEMPERATURE FROM 20-170 °C B) INTERRUPTED SYNTHESIS WITH ULTRASOUND WITH INCREASING TEMPERATURE FROM 20-170 °C 177

5.8 DLS DATA OF THE AS SYNTHESIZED MICRO AND NANOZSM-5 SAMPLES C) INTERRUPTED SYNTHESIS WITHOUT ULTRASOUND AT 170 °C D) INTERRUPTED SYNTHESIS WITH ULTRASOUND AT 170 °C 178

5.9 EDS HISTOGRAM ILLUSTRATED THE ELEMENTAL COMPOSITION OF THE AS SYNTHESIZED SAMPLES (A), (B), (C) AND (D) 180

5.10 N_2 ADSORPTION/DESORPTION ISOTHERMS OF MICRO AND NANOZSM-5 OF THE SAMPLES A) INTERRUPTED SYNTHESIS WITHOUT ULTRASOUND WITH INCREASING TEMPERATURE 25-170 °C B) INTERRUPTED SYNTHESIS WITH ULTRASOUND WITH INCREASING TEMPERATURE 25-170 °C. 182

5.11 N_2 ADSORPTION/DESORPTION ISOTHERMS OF MICRO AND NANOZSM-5 OF THE SAMPLES C) INTERRUPTED SYNTHESIS WITHOUT ULTRASOUND AT 170 °C D) INTERRUPTED SYNTHESIS WITH ULTRASOUND AT 170 °C. 183

5.12 N_2 ADSORPTION/DESORPTION OF MICRO AND NANOZSM-5 A) INTERRUPTED SYNTHESIS WITHOUT ULTRASOUND WITH INCREASING TEMPERATURE 25-170 °C B) INTERRUPTED SYNTHESIS WITH ULTRASOUND WITH INCREASING TEMPERATURE 25-170 °C 184

5.13 N_2 ADSORPTION/DESORPTION OF MICRO AND NANOZSM-5 C) INTERRUPTED SYNTHESIS WITHOUT ULTRASOUND AT 170 °C D) INTERRUPTED SYNTHESIS WITH ULTRASOUND AT 170 °C. 185

5.14 ^{27}AL SPECTRA OF THE SAMPLES OBTAINED BY DIFFERENT SYNTHESES METHODS A) INTERRUPTED SYNTHESIS WITHOUT ULTRASOUND WITH INCREASING TEMPERATURE FROM 25-170 °C B) INTERRUPTED SYNTHESIS WITH ULTRASOUND WITH INCREASING TEMPERATURE FROM 25-170 °C C) INTERRUPTED SYNTHESIS WITHOUT ULTRASOUND AT CONTACT TEMPERATURE AT 170 °C D) INTERRUPTED SYNTHESIS WITH ULTRASOUND AT 170 °C..... 188

5.15 ^{29}SI SPECTRA OF THE SAMPLES OBTAINED BY DIFFERENT SYNTHESES METHODS A) INTERRUPTED SYNTHESIS WITHOUT ULTRASOUND WITH INCREASING TEMPERATURE FROM 25-170 °C B) INTERRUPTED SYNTHESIS WITH

ULTRASOUND WITH INCREASING TEMPERATURE FROM 25-170 °C C) INTERRUPTED SYNTHESIS WITHOUT ULTRASOUND AT CONTACT TEMPERATURE AT 170 °C D) INTERRUPTED SYNTHESIS WITH ULTRASOUND AT 170 °C..... 189

5.16 $^{1}H \rightarrow ^{29}Si$ CROSS POLARIZATION (CP) SPECTRA OF THE SAMPLES OBTAINED BY DIFFERENT SYNTHESES METHODS A) INTERRUPTED SYNTHESIS WITHOUT ULTRASOUND WITH INCREASING TEMPERATURE FROM 25-170 °C B) INTERRUPTED SYNTHESIS WITH ULTRASOUND WITH INCREASING TEMPERATURE FROM 25-170 °C C) INTERRUPTED SYNTHESIS WITHOUT ULTRASOUND AT CONTACT TEMPERATURE AT 170 °C D) INTERRUPTED SYNTHESIS WITH ULTRASOUND AT CONTACT TEMPERATURE AT 170 °C..... 190

5.17 DECONVOLUTED ^{29}Si SPECTRA OF ALL THE SAMPLES OBTAINED BY DIFFERENT SYNTHESES METHODS A) INTERRUPTED SYNTHESIS WITHOUT ULTRASOUND WITH INCREASING TEMPERATURE FROM 25-170 °C B) INTERRUPTED SYNTHESIS WITH ULTRASOUND WITH INCREASING TEMPERATURE FROM 25-170 °C C) INTERRUPTED SYNTHESIS WITHOUT ULTRASOUND AT CONTACT TEMPERATURE AT 170 °C D) INTERRUPTED SYNTHESIS WITH ULTRASOUND AT CONTACT TEMPERATURE AT 170 °C..... 192

5.18 FREE ENERGY DIAGRAM FOR NUCLEATION. TAKEN FROM[33]..... 194

5.19 1) ONE PATHWAY OF ZEOLITE NUCLEATION INVOLVES THE AGGREGATION OF PRIMARY PARTICLES FOLLOWED BY THEIR STRUCTURAL REARRANGEMENT. THE PRIMARY PARTICLES ARE COMPOSED OF ALUMINOSILICATE POLYMERS WITH ENTRAINED SOLVENT. 2) CONVERSION INTO THE CRYSTALLINE PRODUCT. DURING THIS PROCESS THE AMORPHOUS AGGREGATE INVOLVE STRUCTURAL REARRANGEMENT. THE CRYSTALS MAY CONTAIN VOIDS OR DEFECTS (E.G MISALIGNED DOMAINS). TAKEN FROM[34]..... 195

5.20 FLOW SHEET OF SYNTHESIS MECHANISM OF NANOZSM-5 USING ULTRASOUND AND WITHOUT ULTRASOUND INTERRUPTED HYDROTHERMAL TREATMENT AT 170 °C..... 197

List of Tables

1.1 SOME OF THE NATURAL AND SYNTHETIC ZEOLITES HISTORY. TAKEN FROM VARIOUS SOURCES. 2

1.2 CLASSIFICATION OF ZEOLTIES FRAMEWORKS ACCORDING TO SECONDARY BUILDING UNITS (SBUS) 6

1.3 CLASSIFICATION OF ZEOLITES ACCORDING TO THE TETRAHEDRAL ATOMS DISTRIBUTION IN RINGS. 8

1.4 ZEOLITES CHARACTERISTICS ACCORDING TO THE OXYGEN ATOM IN THE RING AND PORE SIZES. 11

1.5 ACIDIC AND BASIC ZEOLITES CLASSIFICATION ACCORDING TO SI/AL RATIO.[45] 14

1.6 NATURE OF THE ACIDIC (LEWIS AND BRÖNSTED) AND CATIONIC SITES IN ZEOLITES.[44] 15

2.1 RANGES OF ^{29}SI FIVE DIFFERENT CHEMICAL SHIFTS 71

3.1 MOLAR RATIO OF MORDENITE ZEOLITE 80

3.2 THE *AS SYNTHESES* MORDENITE ZEOLITE AND EXPERIMENTAL CONDITIONS USED. 82

3.3 UNIT CELL PARAMETER AND VOLUME OF AS-SYNTHESIZED MOR ZEOLITE, ZNS AND Na^+ ION EXCHANGED MOR. 88

3.4 DIFFERENT SIZES PRODUCED BY USING DIFFERENT PTFE LINER VOLUME IN THE PARR REACTOR (AUTOCLAVE). 90

3.5 OBSERVED RELATIVE CRYSTALLINITY AND CRYSTAL SIZES OF THE AS-SYNTHESIZED MORDENITE ZEOLITE POWDER. 90

3.6 WEIGHT PERCENT (%) CHEMICAL COMPOSITION OBTAINED BY EDX 99

3.7 RATIOS OF SI, NA, ZN AND S WITH RESPECT TO AL IN NAMOR, ZNMOR AND ZNSMOR..... 99

3.8 N_2 ADSORPTION ON MORDENITE ZEOLITE BEFORE AND AFTER SYNTHESIS ZNS NANO-CLUSTERS BET SURFACE ANALYSIS AND PORE DISTRIBUTION..... 100

3.9 ^{27}AL, ^{29}SI, ^{23}NA SOLID STATE MAS NMR DATA TAKEN FROM THE SAMPLES NAMOR, ZNMOR AND ZNSMOR 110

4.1 MOLAR COMPOSITION OF REACTING MATERIALS..... 118

4.2 AS SYNTHESISED NANOZSM-5 WITH AND WITHOUT ULTRASOUND, UNIT CELL PARAMETERS CALCULATED WITH HELP OF UNITCELL PROGRAM 125

4.3 REPRESENTING THE OBSERVED AVERAGE FWHM VALUES CORRESPOND TO STATIC AGING TIME AND RELATIVE CRYSTALLINITY OF *AS SYNTHESIZED* ZSM-5 ZEOLITE..... 126

4.4 REPRESENTING THE OBSERVED AVERAGE FWHM VALUES CORRESPOND TO ULTRASOUND PRE-TREATMENT TIME AND RELATIVE CRYSTALLINITY OF *AS SYNTHESIZED* ZSM-5 ZEOLITE..... 127

4.5 AVERAGE PARTICLES SIZE OF *AS SYNTHESIZED* ZSM-5 OBSERVED ON TEM MICROGRAPHS USING STATIC AND ULTRASOUND PRE-TREATMENTS 133

4.6 AVERAGE PARTICLE SIZE OF *AS SYNTHESIZED* ZSM-5 OBTAINED ON SEM MICROGRAPHS USING STATIC AND ULTRASOUND PRE-TREATMENTS..... 136

4.7 PARTICLE SIZE OF *AS SYNTHESIZED* ZSM-5 OBTAINED ON DLS USING STATIC AND ULTRASOUND PRE-TREATMENT..... 140

4.8 WEIGHT PERCENT (%) CHEMICAL COMPOSITION OF AS SYNTHESIZED ZSM-5 ZEOLITE USING STATIC AGING OBTAINED BY EDS..... 141

4.9 WEIGHT PERCENT (%) CHEMICAL COMPOSITION OF AS SYNTHESIZED ZSM-5 USING ULTRASOUND PRE-TREATED OBTAINED BY EDS..... 141

4.10 PARTICLES SIZE DISTRIBUTION OF AS SYNTHESIZED ZSM-5 ZEOLITE OBSERVED ON DIFFERENT SPECTROSCOPIC TECHNIQUES WITH RESPECT TO SAR USING STATIC AGING PRE-TREATMENT..... 142

4.11 PARTICLES SIZE DISTRIBUTION OF *AS SYNTHESIZED* ZSM-5 ZEOLITE OBSERVED ON DIFFERENT SPECTROSCOPIC TECHNIQUES WITH RESPECT TO SAR USING ULTRASOUND PRE-TREATMENT. 143

4.12 BET SURFACE AREA, EXTERNAL SURFACE AREA AND PORE VOLUME OBSERVED OF AS SYNTHESIZED SAMPLES TREATED WITH STATIC METHOD OF AGING 145

4.13 BET SURFACE AREA, EXTERNAL SURFACE AREA AND PORE VOLUME OBSERVED OF AS SYNTHESIZED SAMPLES TREATED WITH STATIC METHOD OF AGING 146

5.1 MOLAR COMPOSITION OF REACTING MATERIALS 164

5.2 THE AS SYNTHESIZED NANOZSM-5 SAMPLES INTERRUPTED SYNTHESIS WITH AND WITHOUT ULTRASOUND, CRYSTALLITE SIZE AND THE CALCULATED RELATIVE CRYSTALLANITY (%). 171

5.3 UNIT CELL PARAMETERS CALCULATED WITH HELP OF UNITCELL PROGRAM OF THE SAMPLES SYNTHESIZED WITH INTERRUPTED ULTRASOUND AT CONSTANT TEMPERATURE (170 ºC) AND WITH INTERRUPTED ULTRASOUND AT INCREASING TEMPERATURE (25 ºC TO 170 ºC) 171

5.4 COMPARING THE PARTICLE SIZE DISTRIBUTION OBTAINED FROM XRD, TEM, SEM AND DLS ANALYSIS OF THE SYNTHESIZED WITH AND WITHOUT INTERRUPTED ULTRASOUND TREATMENT 179

5.5 AVERAGE WEIGHT PERCENT (%) CHEMICAL COMPOSITION OBTAINED ON EDS STATIC WITH AND WITHOUT INTERRUPTED ULTRASOUND SYNTHESIS. 180

5.6 PARTICLE SIZE DISTRIBUTION INVESTIGATED ON DIFFERENT SPECTROSCOPIC AND MICROSCOPIC TECHNIQUES WITH RESPECT TO SAR USING ULTRASOUND PRE-TREATMENT. 181

5.7 BET SURFACE AREA, EXTERNAL SURFACE AREA AND PORE VOLUME OF THE NANOZSM-5 PREPARED WITH AND WITHOUT ULTRASOUND INTERRUPTED SYNTHESIS. 183

Chapter 1

1. What Is a Zeolite?

Zeolites are naturally occurring minerals created from the reaction between volcanic rock ash and alkaline water (sea, lake). The favourable temperature for this reaction ranges from 27 °C to 55 °C with a pH of 9 to 10. These reactions require 50 to 50,000 years to complete.[1,2] A Swedish mineralogist, Axel Frederik Cronstedt, in 1756 discovered zeolite for the first time, by producing steam after heating a kind of stone.[3] Zeolites were found in the relatively small cavities in rocks of volcanic origin.[3–5] They are crystalline, microporous, hydrated aluminosilicates that are formed from an infinite three-dimensional network of silica $[SiO_4]^{4-}$ and alumina $[AlO_4]^{5-}$ tetrahedra connected to each other via oxygen atom–formed cavities, where cations and water molecules may be accommodates.[6,7] There are 200 unique zeolite frameworks that have been artificially created, whilst 40 naturally occurring zeolite frameworks have been identified.[2,8] The advancement in zeolite studies developed new synthetic methods and characterisation. A broad general discussion has been adopted to focus on acid zeolite catalysis for industrial applications. The history of some of the natural and synthetic zeolites and their applications are shown in Table 1.1

Table 1.1 History of some of the natural and synthetic zeolites. Taken from various sources.

Year	Name of zeolite and their function
1756	The first ever natural zeolite discovered named stilbite
1825	Natural zeolite lecynite
1842	Natural faujasite discovered
1862	First synthetic zeolite discovered, levynite
1864	Natural mordenite discovered
1890	Discovery of natural erionite
1929	Potential as strong acid has been studied
1932	Zeolites explored as molecular sieves
1930–34	Investigated the zeolite structure
1942–45	Zeolites were used as molecular sieves for quantitative separations
1948	Synthetic mordenite produced
1949	Acid zeolites prepared
1960	Introduction of zeolite-based cracking catalysts
1956–64	Preparation of zeolite A, X and Y (union carbide)
1975	Ethyl benzene produced on ZSM-5 catalyst
1948–1978	ZSM-5 and ZSM-11 structure identified
1980	Zeolite chemistry studied on high-resolution microscopy and solid-state MAS NMR
1985	ZSM-5 zeolite used as a catalyst for methanol to gasoline conversion
1986	Highly siliceous and aluminophosphate zeolites UN-1 and FU-1 produced

1.1 The Structure and Composition of Zeolites

In 2001, IUPAC recommended the terms *framework-* and *structure-type zeolites*. The framework type is 'the corner-sharing network of tetrahedrally coordinated atoms' (Si, Al, P, Ga, B, Be etc.) whilst the structure type is 'composed of the framework and extra-framework'.[4,7,8] The zeolite unit cell chemical formula is typically composed as given in equation (1).

$$M_{x/n}\left((AlO_2)_x\,(SiO_2)_y\right)\cdot\ mH_2O \qquad (1)$$

where n is the valency of metal ion M which neutralises the negative charge of the framework. The numbers x and y depend on the framework, e.g., the sodium form of zeolite A has x = y = 12 in a 1:1 ratio.[7,9]

Zeolites possess crystallographically well-defined channels and pore structures. They have three-dimensional framework structures formed from corner-sharing $[SiO_4]^{4-}$ and $[AlO_4]^{5-}$ tetrahedral units. In Figure 1.1, Si is surrounded by four oxygen atoms in a tetrahedral unit, which is called the primary building unit (PBU).[7,9] The PBUs interlink to build polyhedral units called secondary building units (SBUs), which then convert to a concerted framework as shown in Figure 1.2.

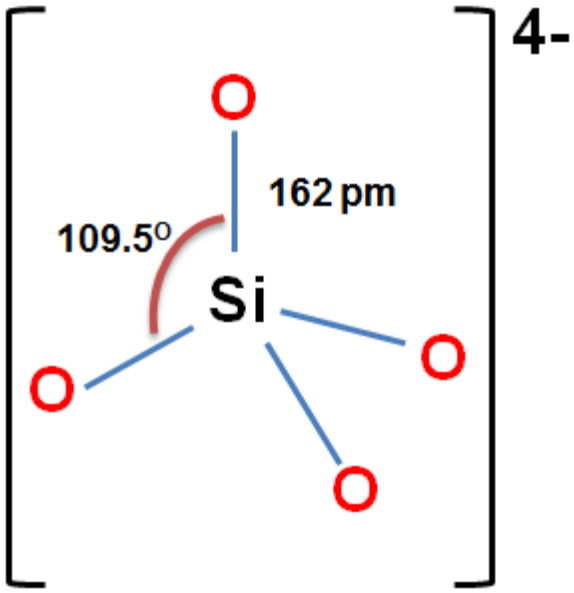

Figure 1.1 Primary subunit of Si tetrahedra with 4 oxygen.

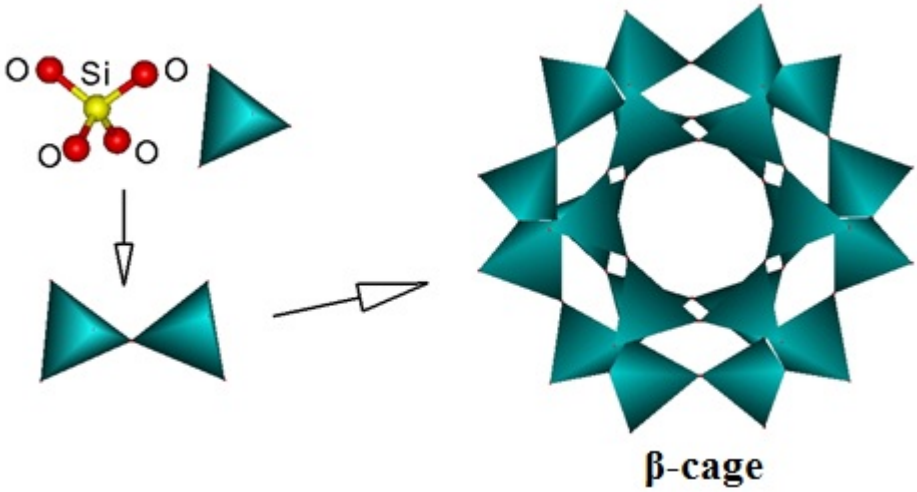

Figure 1.2 A proposed mechanism for the combination of PBUs converted to SBUs and ultimately to a zeolite β-cage consisting of 24 silica units tetrahedra. Taken from the BZA website.[10]

Many different SBUs are found in a zeolite framework, and the framework density of the zeolite frameworks can be defined as the number of T-atoms per 1000 Å^3 as given in equation (2).[11]

$$\mathrm{FD} = \frac{\text{Number of T} - \text{Atoms}}{1000\ \text{Å}^3} \qquad (2)$$

For zeolites with a fully cross-linked framework, FD = 20.6 – 21.1, whilst for a nonzeolitic, denser framework structure, FD > 21. The zeolite framework density is helpful for differentiating zeolites and zeolite-like materials from denser materials. A framework density value less than 12 has only been encountered for the interrupted framework of cloverite zeolite (-CLO). [11] Some of the different zeolite framework densities are listed in Table 1.2. There are 16 or more different SBUs which help describe the structure of each zeolite in Figure 1.3.[4,9,12] A zeolite framework unit cell consists of multiple SBUs.[7,9]

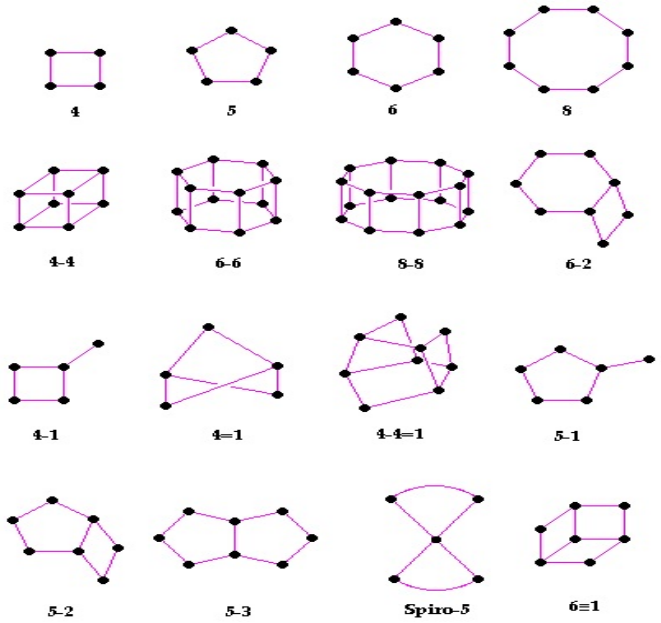

Figure 1.3 Secondary building units of zeolite structure: silicate/aluminate single ring, double rings and other extended single-ring block units without the oxygen atom.[13]

Table 1.2 Classification of zeolite frameworks according to secondary building units (SBUs).

Structure type designation		Secondary building units				Cage units	Framework density; no. of T-atom (nm^3)
Cage	Full name						
FAU	**Faujasite**	4	6		6-6	B	12.7
LTA	**Linde type A**	4	6	8	4-4	A, B	12.9
RHO	**Rho**	4	6	8	8-8	A	14.3
CHA	**Chabazite**	4	6				14.6
KFI	**ZK-5**	4	6	8		A	14.7
OFF	**Offretite**		6			D	15.5
PHI	**Phillipsite**	4		8			15.8
ERI	**Erionite**	4	6			D	15.6
LTL	**Linde type L**		6			D	16.4
MOR	**Mordenite**		5-1				17.2
MEL	**ZSM-11**		5-1				17.7
MFI	**ZSM-5**		5-1				17.9

The IZA Structure Commission designates a three-letter code (three capital letters) to be adopted for a known system topology regardless of components. The codes are typically obtained from the zeolite name, e.g., LTA for Linde type zeolite A; FAU for faujasite topology, e.g., zeolites X and Y; MOR for mordenite topology and MFI for the ZSM-5 and silicalite topologies[14,15] as shown in Table 1.2. The zeolite aluminosilicate frameworks carry a negative charge, which is balanced by a cation located in the cage-like cavities. The cations and water molecules can be accommodated with a complex framework structure[8,12] shown in Figure 1.4. Zeolites with 14-, 16-, 18- and 30-membered rings have been synthesised.[16]

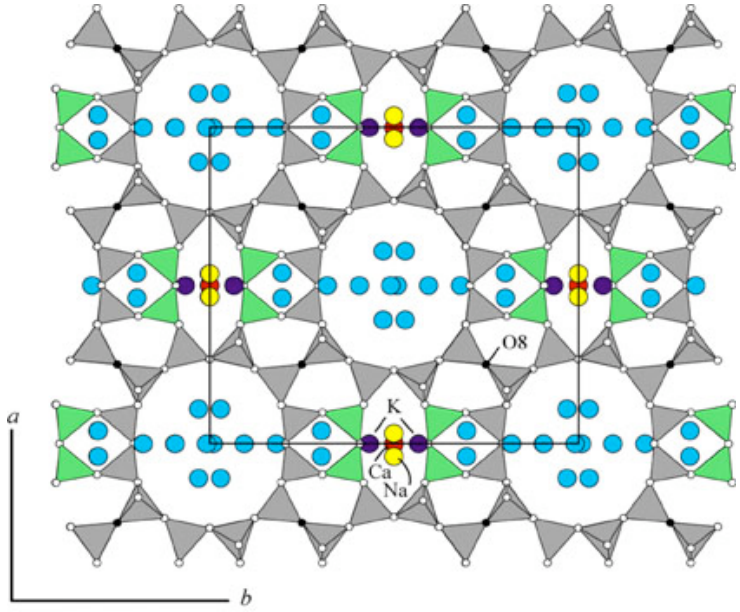

Figure 1.4 Cations and water molecules residing in the pores of zeolites.[17]

The silicon and aluminium ions are connected to each other through oxygen bridges. The group of tetrahedra builds polyhedral units, which further link to form the entire framework[7,9,18] as shown in Figure 1.2. Rings may be formed from the polyhedral tetrahedra. However, 4-T, 6-T, 8-T, 10-T and 12-T are the most common rings. Some of them are shown in Figure 1.5.[6,8,19]

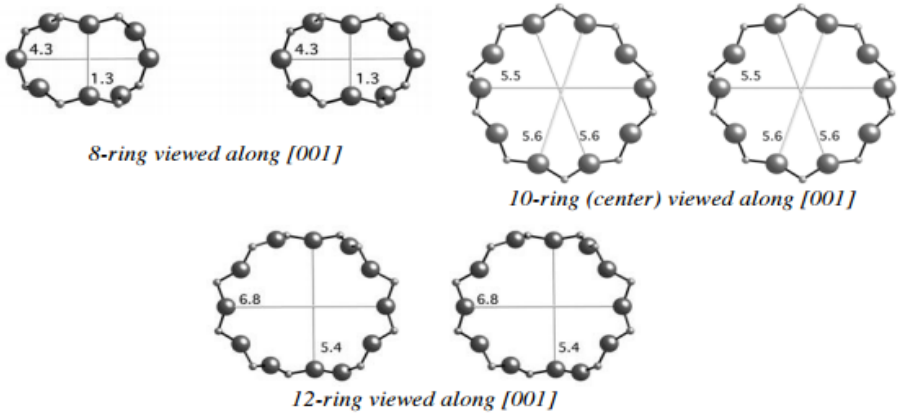

Figure 1.5 8-T, 10-T and 12-T membered rings along [001] viewed formed zeolite pore aperture.

The zeolite frameworks with component units found in tetrahedral frameworks are called secondary building units (SBUs).[12,20] Some basic zeolite

SBUs and their simple descriptions are given in Table 1.2 and Table 1.3. The ways to combine these tetrahedrons are numerous.

Table 1.3 Classification of zeolites according to the tetrahedral atom distribution in rings.

Number of linked tetrahedra	SBUs created	Pore size description
4	4 oxygen rings	S4R
5	5 oxygen rings	S5R
6	6 oxygen rings	S6R
8	8 oxygen rings	S8R
8	4-4 oxygen rings	D4R
12	6-6 oxygen rings	D6R
16	8-8 oxygen rings	D8R
KEY: D = Double, S = Single, R = Ring		

1.2 Types of Zeolites

There are two types of zeolites: naturally occurring zeolites and synthetic zeolites.

1.2.1 Natural Zeolites

Around 40 naturally occurring zeolites have been reported forming in both volcanic and sedimentary rocks.[8,21] They are produced at a relatively low-temperature geological environment. Volcanic rocks and basalt may consist of different climatic crystal groups of zeolites. Zeolites also occur in alkaline desert lake sediments, in alkaline soils in deserts and in marine sediments.[21] Clinoptilolite (Na, K) ($AlSi_5 O_{12} 3H_2O$) is one of the economically most important zeolites built by the transformation of smooth volcanic deposits by the underground water.[22] Natural zeolites are environmental and economically

tolerable hydrated aluminosilicate materials with extraordinary ion-exchange and sorption character. Their adequacy in distinctive industrial methods depends on their physicochemical properties. Naturally occurring zeolites have many applications because of their three-dimensional porous structure.[23]

1.2.2 Synthetic Zeolites

Today synthetic zeolites have more applications than natural zeolites because of their uniform particle size distribution and purity. They can also be produced in large varieties with different chemical properties, greater thermal stability and tailored pore sizes.[20,24] Synthetic zeolites were first synthesised in the late 1940s whilst nearly 200 different zeolites structures have now been synthesised. Different methods have been applied to a synthesised range of zeolites.[8] One remarkable and significant procedure is the aluminosilicate alkaline gel hydrothermally treated in a closed system from room temperature to 180^{o}C and at autogenous pressure.[25,26] In another method, kaolin clay is heated until it begins to melt, cooled and crushed to fine powder, mixed with salt and water, aged and heated.[27,28] In all the synthetic methods, the pure crystalline zeolites depend on the compositions of the reacting materials and the reaction conditions, including acidity, water and pressure.[25,29]

1.3 Properties and Applications of Zeolites

Zeolites are used as molecular sieves because of their intrinsic high porosity. The internal surface area of the zeolite is extremely large compared to its external surface area because of its microporous structure.[7,21] The micropores are open allowing molecules, ions or clusters of molecules to move within the

intracrystalline space of the zeolite. The microporous three-dimensional networks act as highly effective reaction channels. These may be mono-, bi- or three-dimensional channel systems.[30] Because of the presence of these channels, the zeolite acts as a catalyst with enhanced selectivity and high reactivity. Some of the particularly interesting properties of the zeolite are given below:[21,31]

1. Surface area.
2. Pore diameters < 10 Å, having molecular dimension.
3. High adsorption capacity.
4. Partitioning ability of reactants/products.
5. Possibility of preactivating molecules in the pores by strong electric fields and molecular confinement.
6. Cations present have the ability to exchange, with different resulting properties.
7. Availability of strong acid sites for catalysis.

Zeolites can be classified into three classes on the basis of their pore size: small, medium and large. The pores lead to channels, and there are also cages in some zeolites.[32] The pore sizes vary according to the number of oxygen atoms in the ring[32,33] as shown in the Table 1.4.

Table 1.4 Zeolite characteristics according to the oxygen atom in the ring and pore size.

Zeolites	No. of oxygen atoms in the ring	Dimensions of pore structure	Size of channels Å
Zeolite A	8	3	4.1
ZSM-5	10, 10	3, 3	5.4 × 5.6, 5.1 × 5.5
Mordenite	12, 8	2, 2	6.7 × 7.0, 2.9 × 5.7
Faujasite	12	3	7.6

By modifying the structure of the zeolite with cations, resizing the pore size and standardising the acid site, zeolite applications are found in diverse areas of chemistry. Therefore, the composition and structural understanding of zeolites are significantly important for adsorptive and catalytic applications in industries.[34,35] There are three main commercial applications of zeolites in industries. The most prominent is catalysis, but zeolites are also used for adsorption, separation and ion exchange.[31]

1.3.1 Catalysis

Zeolites are highly applicable in various important industrial petrochemical processes. The most remarkable reactions are cracking, isomerisation and hydrocarbon production in the petrochemical industries. Zeolites can boast a huge number of catalytic reactions along with acid-base and metal modified reactions.[36] Shape selectivity is one of the most important properties of zeolites used in catalytic processes. This property of zeolites can be modified by carefully optimising the composition of the precursor materials.[37] Different types of shape-selective catalysis occur within the zeolite pores, critically dependent on whether

pore size restrains access to the reactant molecule, or leaves product, or forms various transition states.[10,38] Shape selectivity was first reported by Weisz et al. in 1960;[37] they described its various properties and uses. The author studied the shape selectivity of hydrogenation of n-olefins over Ca-A and Pt-ZSM-5 catalysts.[37,39,40] There are three basic types of shape selectivity in zeolite catalysts.

1.3.1.1 Reactant Shape Selectivity

The reactant molecules have dimensions small enough to enter into the catalyst pores and react there.[41] The schematic representation of reactant shape selectivity is shown in Figure 1.6 A.

1.3.1.2 Product Selectivity

The product molecules are bulky enough to diffuse out from the catalyst pores as the observed products. For example, in the conversion of xylene isomers in cavities, only para-xylene can depart from the active site, and the other isomers may block the pores and deactivate the catalyst[41] as shown in Figure 1.6 B.

1.3.1.3 Restricted Transition State Shape Selectivity

This form of shape selectivity limited the long transition state step because of limited space availability in the catalyst pore channels and cavities. Therefore, the reactants and products are barred from departing the catalyst pores, which block the pores and deactivate the catalyst. The reaction needs a small transition state to occur readily[41][42] as shown in Figure 1.6 C.

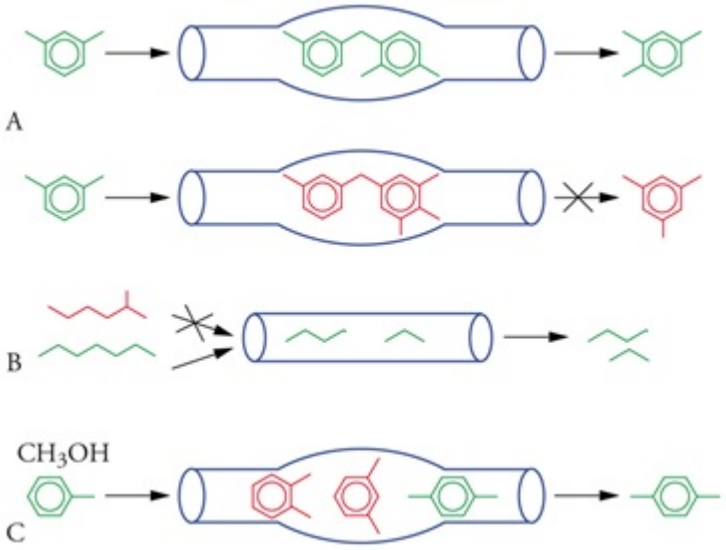

Figure 1.6 A schematic representation of shape selectivity for reactions in zeolite channels. Taken and modified.[41]

1.3.2 Acidity and Basicity of Zeolites

Zeolites have unique catalytic properties based on their acidic character. It is very difficult to characterise the presence of both Lewis acid and Brønsted acid sites in a zeolite structure especially the availability of heterogeneous dissemination of acid site strengths.[43] Lewis acidity is linked to Al or cationic elements, alkaline earth or other cations. The number of replaceable cations in the framework depends on the number of Al^{3+} ions in the zeolite structure; therefore, the catalyst properties are closely dependent on the Si/Al ratio[44]. The zeolites with a higher number of protons are highly hydrophilic having greater affinity for polar small molecules to enter the pores. Similarly, highly siliceous zeolites are hydrophobic and can take up organic molecules from water-organic mixtures, and such phenomena were reported the Si/Al ratio is about 10.[45] Acidic zeolites can be classified with different Si/Al ratios as shown in the Table 1.5. Microporous solids are interesting materials for heterogeneous catalysis because the Brønsted acid sites occur on the surface of the zeolites.[46] Brønsted acid sites are the hydroxyl

protons, as located on the oxygen bridges linked between tetrahedrally coordinated silicon and aluminium cations.

Table 1.5 Acidic and basic zeolite classification according to Si/Al ratio.[45]

Si/Al Ratio	Zeolites	Acid/Base Properties
Low (1–1.5)	A, X	Relatively low stability of lattice Low stability in acids High stability in bases High concentration of acid groups of medium strength
Medium (2–5)	Erionite, Chabazite, Clinoptilolite, Mordenite, Y	
High (About 10–60)	ZSM-5, Dealuminated, Erionite, Mordenite, Y	Relatively high stability of lattice High stability in bases Low concentration of acid groups of strength

The possible acidic (Lewis and Brönsted) sites are the hydroxyl (OH) group, specifically the oxygen bridging between Si and Al, Si to Si or Al to Al configurations as shown in Table 1.6. Al – Al via oxygen bridging occurs very rarely. Kasge et al. explored different methods for the identification of various acid (Lewis and Brönsted), basic and cationic sites in the zeolite structure, i.e., titration method, temperature desorption programme (TPD), microcalorimetry, infrared (IR) spectroscopy, UV-VIS spectroscopy, ^{1}H MAS NMR, test reactions, solid-state MAS NMR of ^{27}Aland ^{29}Si, and ESR spectroscopy.[44] Inductively coupled plasma-mass spectrometry (ICP-MS) can be used for measuring the cation exchange.[47]

Table 1.6 Nature of the acidic (Lewis and Brönsted) and cationic sites in zeolites.[44]

Types of Site	Site Examples	Analysis Technique
Brönsted	Bridging OH, Al-OH, P-OH	IR, IR + Probes, ^{1}H MAS NMR, ^{15}N NMR
Lewis	≡Al(Framework), AlO^{+}, $[Al_xO_y]^{(3x-2y)+}$, Al-Oxides	IR + Probes, ^{27}Al MAS NMR, ^{15}N NMR, ESR + Probes
Cations	Other Oxides, Cations, Me^{n+}	IR + Probes

1.3.3 Adsorption and Separation

Zeolites are used extensively for gas separation. Because of their porous structure, molecules have a certain size dimension that can pass through the pore channels given in Figure 1.7. Cation-associated zeolites are widely used as desiccants because of their high affinity for water, and they are also sources for gas isolation, where molecules are preferably absorbed because of isolation of their electrostatic interactions with the cations. Hydrophobic silica zeolites especially absorb organic solvents. Therefore, zeolites can isolate molecules on the preference of size, shape and polarity.[13,38]

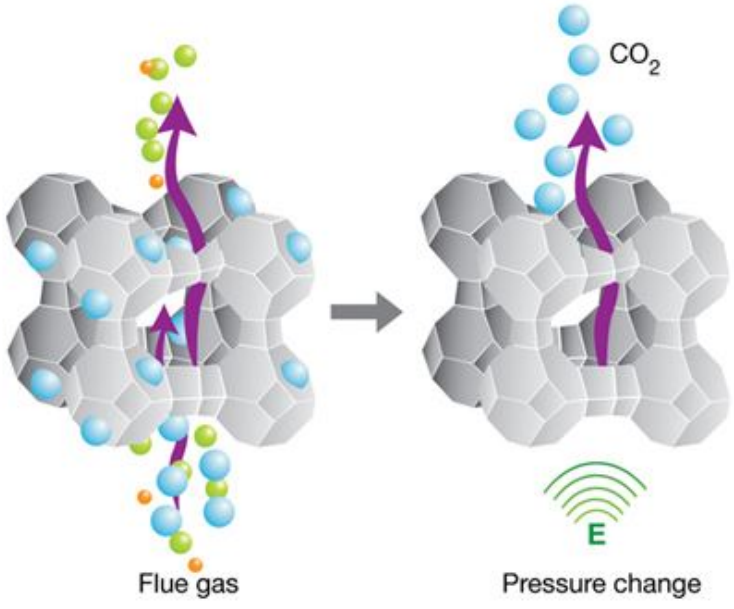

Figure 1.7 Adsorption and separation of gases and purification of zeolites in different stages.[48]

1.3.4 Ion Exchange

The hydrated metal ions in the zeolite frameworks are loosely bound in the frameworks channels as shown in Figure 1.8. They are used as detergents (as a water softener), which can be readily exchanged with the other cations in the aqueous solution. Because of this property, zeolites are used in water softening instruments, detergents and soaps.[49] It is also used for water cleaning, i.e., removal of radioactive ions. Zeolites are also used in a noteworthy manner in water softening, where soluble base metals like sodium Na^+ and potassium K^+ are exchanged in the zeolite frameworks, being supplanted by the 'hard' calcium Ca^{2+} and magnesium Mg^{2+} ions from water. Zeolites being used in ion exchange to balance out clusters and nanoparticles of outside materials on their surface and inside their channels has also taken a unique significance.[50,51] This assistance to embed nano-objects permits one to synthesise composites with several new applications, for example, materials for solar cells, photodetectors, light-radiating diodes, switches, and photocatalysis.[52,53] In equation (3) at the *as-synthesised* product, cation A, in the zeolite phase (Z), has been replaced by the uptake of cation B from the aqueous phase (aq):

$$AZ_{(s)} + B_{(aq)} \rightarrow BZ_{(s)} + A_{aq} \quad (3)$$

where A and B are the cations and Z represents the zeolite.

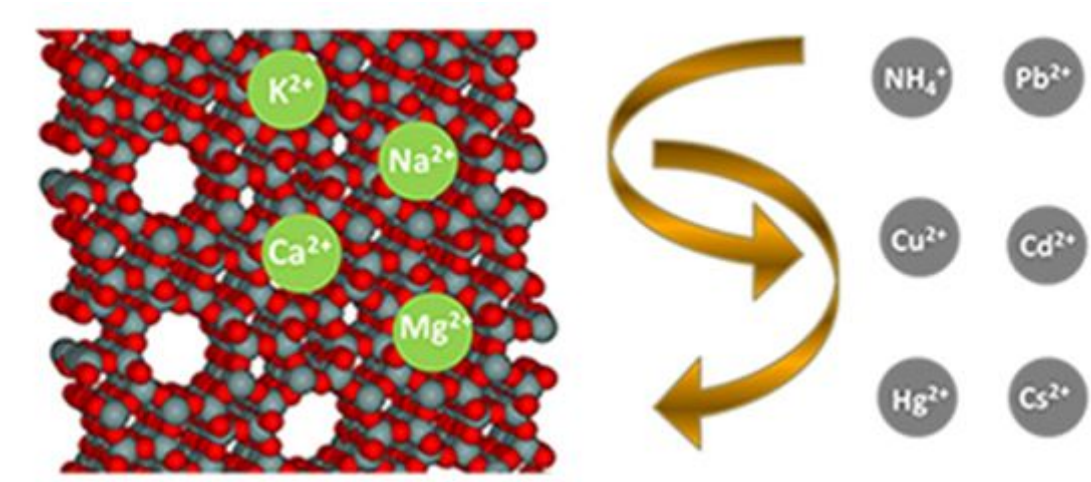

Figure 1.8 Ion exchange efficiently occurring in the zeolite channels without affecting the framework.[54]

1.4 Mordenite Zeolite

Mordenite was first found in the Bay of Fundy, Nova Scotia, Canada. This mineral has an ideal composition of $(Na_2,K_2,Ca,)_4[Al_8Si_{40}O_{96}]28H_2O$.[55] It is one of the six most abundant zeolites available in the world and is used commercially.[56,57] Optically it may be colourless, white, yellow or pink depending on what materials are present. The symmetry of mordenite zeolite is orthorhombic.[56,57] Meier in 1961 reported the mordenite crystal structure, and it was further investigated by Gramlich in 1971. It has two types of pore channels: an elliptical pore channel (6.7 Å × 7.0 Å) which is parallel to the c-axis and another pore channel which runs parallel to the b-axis (2.9 Å × 5.7 Å).[56,58] The reported unit cell parameters are a=18.121 Å, b=20.517 Å and c=7.544 Å.[9] The framework structure is characterised by five-member rings formed from tetrahedral units of silicate and aluminate. The silicate and aluminate tetrahedral units link together via four oxygen atoms at each corner of the tetrahedra forming polytetrahedra along c, which is in turn connected by four rings to build a rough perforated sheet with eight-member ring holes, which are oriented parallel to

[001] as shown in Figure 1.9. These sheets linking together with 4 rings and 12 rings build channels parallel to [010][59,60] as shown in Figure 1.10.

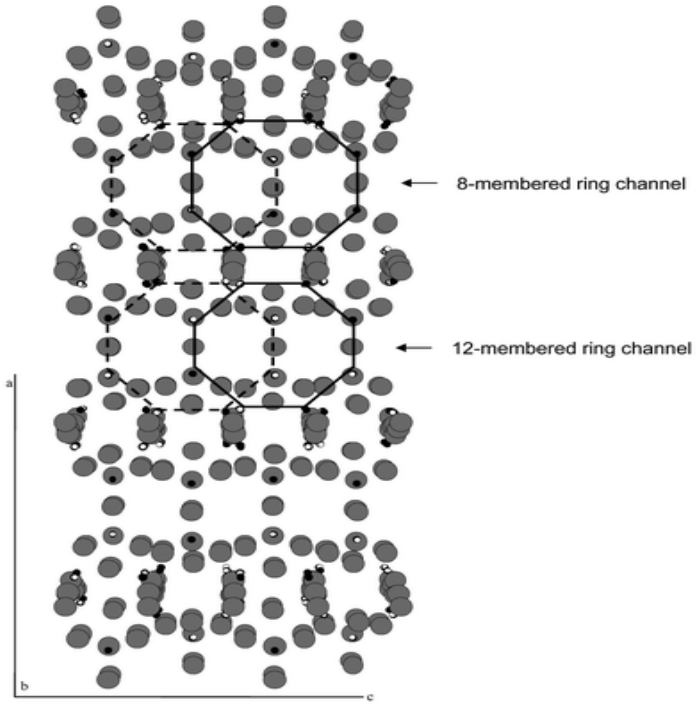

Figure 1.9 8- and 12-member ring channels along [001].[61]

Raatz in 1983[62] reported that synthetic mordenite zeolite can accommodate cations and molecules with diameters larger than 4.5 Å, whilst natural mordenite cannot.[62] Mordenite is a highly siliceous zeolite; the Si, Al and the metal ion composition of the framework are slightly variable. The nonframework is commonly sodium (Na^+) as shown in Figure 1.10.

Aside from nonspecific applications in the fields of farming and building industry (as measurement stone), also used are known as sorbent and the atomac strainer. Gas partition procedures accounted for the creation of high-review O_2 from the air by weight-swing working generators. Full-scale plants in light of mordenite-rich tuffs have been working in Japan subsequent to the end of 1960.[63] In New Zealand, a mordenite-bearing zeolitic solid material is dried and pulverised to deliver a mixture of items including adsorbents for cleaning up

oil/synthetic spills, animal food supplements, water analysis, and moderate-discharge compost.[56]

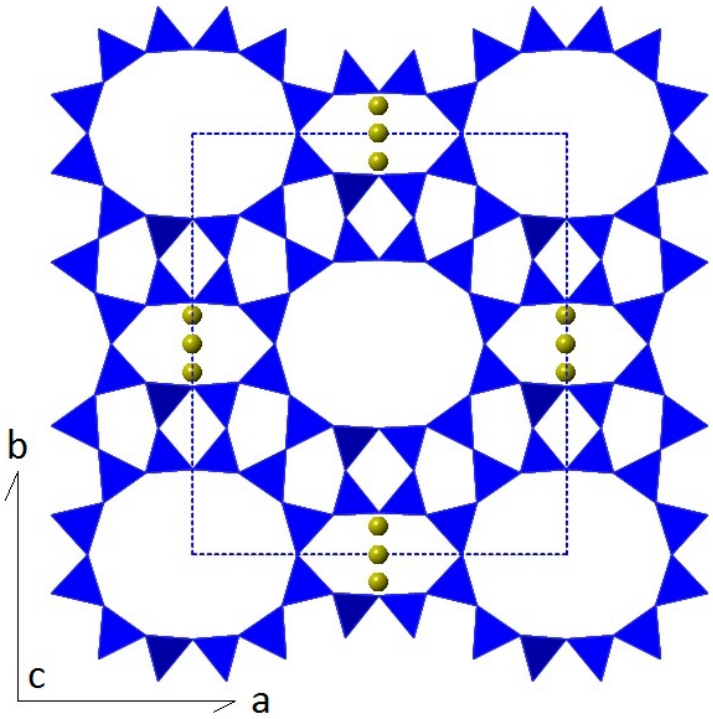

Figure 1.10 Framework structure for MOR viewed along the c-axis, the 12-ring one-dimensional channel and cations (Na^+) (green) within the 8-ring.

Scientifically and technologically, semiconductor clusters in the zeolite hosts are one of the most interesting advance materials. Mordenite zeolite can carry semiconductor nanoclusters of foreign materials on their surface and inside their pore channels; this property has taken a unique importance among researchers. This assistance to embed nanoparticles allows one to produce composites with several new applications, for example, materials for solar cells, flat-panel displays, sensors, switches, and photocatalysis.[64–66] In optoelectronics, aviation, vehicles, and atomic vitality commercial ventures, this sort of composite material is additionally being utilised for specific applications.[64]

1.4.1 ZnS Semiconductor Nanoparticles

ZnS semiconductor nanomaterials have been under intense study for the last several decades because of their size-dependent physical and chemical properties.[67,68] Optical absorption spectrum, size-dependent luminescence, oscillator strength and nonlinear optical effects are some interesting properties exhibited by these nanocrystals. All these properties are the perceptible indications of the quantisation effect, which increases because of the increasing quantum confinement of the electrons and holes and the reducing size of the crystallites and the follow-up changes in the electronic structures.[68] Many researchers take a very deep interest in semiconductor nanostructure materials consisting of porous silicon, carbon nanotubes, nanocomposites etc. For scientific and technological consideration, the semiconductor nanoclusters are valuable advanced materials because of their structures. ZnS has important wide-band gap (3.6 eV) semiconductor nanoclusters and has various technological applications such as photocatalysis, nonlinear optics, sensors, solar cells, injection lasers, flat-panel displays, ultraviolet light–emitting diodes (LED) etc.[66,69] Most semiconductor nanoclusters belong to group II–IV materials, as they are relatively easy to synthesise. Among all the nanoclusters of group II–IV compounds, CdS and ZnS are the most studied semiconductors. Zeolites are ideal as a host for such nanoclusters. They have three-dimensional super lattice in which nanoclusters can be grown.

In this thesis, we studied and characterised the formation of ZnS clusters within the pore network of mordenite zeolite, which was crystallised without organic structure-directing agents.

1.5 Zeolite Socony Mobil-5 (ZSM-5) Zeolite

Argauer and Landolt[70] first introduced ZSM-5 using organic amines as a structure-directing agent (i.e., template) tetrapropylammonium compounds (TPA^+). The first catalytic cracking test was carried out in the laboratory by the refiner Neste Oy at Naantali, Finland.[71] In the middle of the 1960s, ZSM-5 was synthesised in a very limited amount, but after the evaluation of waxy gas oil processing, ZSM-5 observed a shape-selective material that can break the isoparaffins or slightly branched paraffins.[72] Wu et al.[73] in 1979 reported for the first time the structure of ZSM-5. ZSM-5 is a type of zeolite belonging to the pentasil family of zeolites and having the zeolite Mobil five (MFI) framework.[72] ZSM-5 has an interesting orthorhombic framework structure with an organic template, which then changes into monoclinic after calcination. This behaviour is not only concerned with calcination, but it also depends on other factors.[74,75] The framework has the space group Pnma and has the unit cell parameters a = 20.090 Å, b = 19.738 Å and c = 13.142 Å. The ZSM-5 framework is built from several five-membered rings called pentasil units. In each of the five-membered rings, Al and Si are linked together through oxygen atoms. These pentasil units are connected to each other via corner-sharing oxygen atoms to form pentasil chains as shown in Figure 1.12. The two different types of pore channels in the ZSM-5 framework, straight and zigzag channels, are shown in Figure 1.11[8,76]. The reported pore sizes of the channels are 5.3–5.6 Å (straight channels) and 5.1–5.5 Å (zigzag channels).[76]

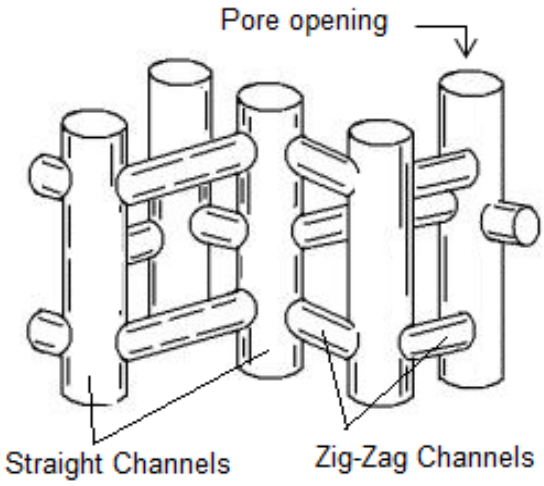

Figure 1.11 Zigzag (horizontal) and straight (perpendicular) channels of the ZSM-5 pore network.

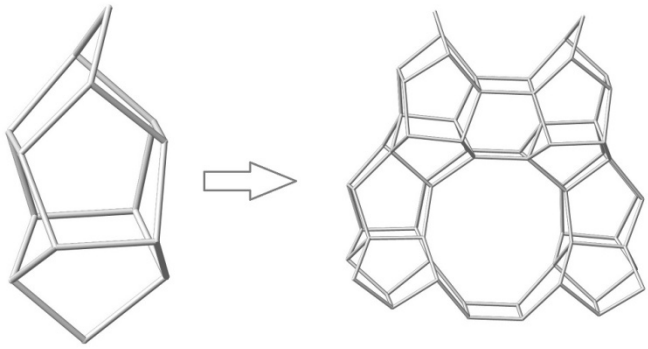

Figure 1.12 Systematic structure mechanism of pentasil unit connectivity of ZSM-5 frameworks.

The unit cell of ZSM-5 is composed of 96 (Si or Al) T sites and 192 oxygen atom sites. The number of extra framework cations in the unit cell depends on the Si/Al ratio, which ranges from 12 to infinity.[77]

ZSM-5 is a synthetic zeolite, and there are many ways to synthesise it; a common method is the alkaline solution of aluminosilicate mixed with an organic template (TPA^+), which is then treated at high temperature and autogenous pressure in a stainless-steel autoclave for a specific time. The product in its pure form will be ZSM-5, and analcime + alpha quartz are impurities[78] as shown below in a simplified chemical reaction.

$SiO_2 + NaAlO_2 + NaOH + N(CH_2CH_2CH_3)_4Br + H_2O \rightarrow$ ZSM-5 + Analcime + alpha - quartz

ZSM-5 can be produced by using varying ratios of SiO_2- and AlO_2-containing compounds.[79]

ZSM-5 has a high silicon-to-aluminium ratio. At whatever point an Al^{3+} cation replaces a Si^{4+} cation, an extra positive charge is introduced to keep the framework charge-neutral. A proton (H^+), as the cation, gives an acidic site to the framework. Consequently, the acidity depends on the Al content in the framework.[20,80] The unique pore network (zigzag) and the acidity of ZSM-5 are used as solid acid catalysts, for example, in hydrocarbon isomerisation and the alkylation of hydrocarbons.[20]

One such catalyst-based reaction is the isomerisation of meta-xylene to para-xylene. In the ZSM-5 zeolite pore network, the rate-of-diffusion coefficient of para-xylene is much higher than that of meta-xylene. At the point when the isomerisation response is permitted to happen inside of the pores of ZSM-5, para-xylene has the capacity to navigate along the zeolite's pores, rapidly diffusing out of the catalyst as shown in the reaction equation in Figure 1.13. This size selectivity permits m-xylene isomerisation reaction over ZSM-5 rapidly in high production.[81]

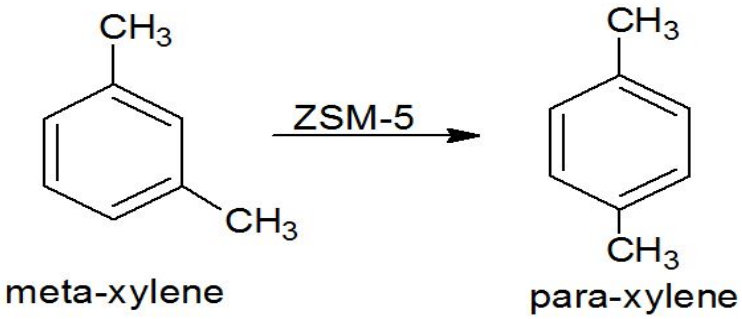

Figure 1.13 Isomerisation from m-xylene to p-xylene. Hence, p-xylene is a favourable product for the ZSM-5 pore channels.

ZSM-5 has been used for hydrogen production by modifying it with metal deposited on the zeolite surface. For example, copper is deposited on the ZSM-5 zeolite surface, and a stream of ethanol is passed through at a temperature of 240–320^{o}C. The ethanol is oxidised to acetaldehyde and releases 2 hydrogen atoms as hydrogen gas H_2 as shown in the chemical reaction in Figure 1.14.[20]

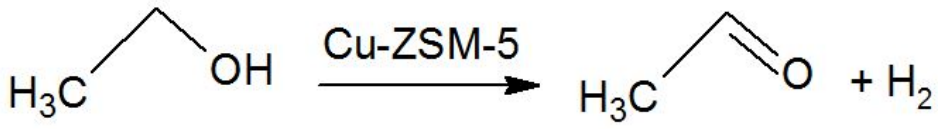

Figure 1.14 Conversion of ethanol to ethanal and H2 gas over Cu-ZSM-5.

H-ZSM-5 is also used for methanol-to-gasoline (MTG) conversion by doping the zeolite with different metals to enhance catalytic performance.[82,83] Recently, researchers are taking an interest to reduce the particle/crystallite size of the ZSM-5 zeolite for enhancing performance. There is also an investigation to create mesopores in the framework to increase the efficiency of the zeolite.

1.5.1 Why Nanocrystalline ZSM-5 Zeolite?

Zeolites are normally produced from an aluminosilicate gel framework, which is formed by aqueous crystallisation from an alkaline solution, giving micron-sized particles. It is generally understood that the selectivity of a catalyst depends on the characteristic length scale of the active sites, whilst the rate depends on the number of accessible active sites. In any case, huge mass transport restrictions to and from the dynamic sites in the micropores limit the reaction rate. To overcome these limits, different approaches have been proposed, such as the use of nanosized zeolites, ultrasubstantial pore zeolites, zeolite analogues and

mesoporous materials.[80,84] Moreover, decreasing the particle size causes a large increase in the surface-to-volume ratio, which is very important for catalytic reactions. We are intrigued to present novel systems for investigating nanocrystalline zeolites forming catalyst bodies to explore the small-size effect in specialised reactors.

1.6 Aims of the Study

The purpose of this work is the synthesis and characterisation of ultrasound-assisted nanoZSM-5 and MOR zeolites with ZnS nanoclusters in the MOR pore networks in the view of both existing and novel procedures, improving their potential application to petrochemical industries and advanced electronic engineering, respectively. Zeolite synthesis is a complex process, and numerous experiments have been performed in light of variations in fundamental parameters and postsynthesis.

This thesis reports (1) the preparation of ZnS nanoclusters within the pore network of MOR zeolite and (2) the synthesis of nanoZSM-5 zeolite using ultrasound treatment, which is a new method devoted to all aspects of synthesis and properties of this new thriving domain.

The thesis is committed to novel architectures at the nano level with an emphasis on new combinations of synthesis and characterisation techniques.

1.6.1 ZnS Nanoclusters within the Mordenite Pore Network

1. To study the synthesis condition of mordenite zeolite, specifically the impact of reaction time on the ensuing zeolite.

2. To study MOR zeolite with 'medium' pore size and strike a balance between a desired large number of exchangeable sodium cations and a desired small number of catalytic sites, with the interaction between the catalytic sites and clusters in the pores.
3. To grow the ZnS nanoclusters within the pores of mordenite zeolite by using ion-exchange methods.
4. To study ZnS nanostructure, in which great efforts have been focused on synthesis and physicochemical properties.
5. To characterise ZnS nanoclusters in the framework of MOR zeolite using various experimental techniques including solid-state NMR, X-ray diffraction (XRD), scanning electron microscopy (SEM) and N_2 adsorption and desorption (BET) surface analysis and transmission electron microscopy (TEM).

1.6.2 Solid Acid Catalyst NanoZSM-5 Particles/Crystals

1. To develop reproducible synthetic routes for nanoZSM-5 zeolite.
2. Ultrasound treatment synthesising nanoscale ZSM-5 as a route to scaling up adequately gives a large amount of nanoZSM-5 product. This could lead to a genuine, novel 'green chemistry' course to industrial preparation.
3. To probe the nature of particles down to the subnanometre scale whilst avoiding, if possible, the process of aggregation, and to fully characterise these materials from a structural point of view.
4. To produce solid acid nanoZSM-5 (catalysts and nanoadsorbent) for application in the energy- and environment-amicable processes not only

hydrocarbon catalytic reactions but also CO_2 adsorption, CO oxidation, etc.

5. To investigate the separation of nucleation and crystal growth by using aging time and treatment with ultrasound (pretreated and interrupted treatment of crystallisation).
6. To study the effect of ultrasound on crystal growth and crystallinity of ZSM-5 zeolite.
7. To investigate the particles with a variety of advanced physical techniques.

1.7 Literature Review

1.7.1 The Synthesis of MOR Zeolite

Lu et al.[85] synthesised the high-silica MOR zeolite using tetraethylammonium hydroxide by mixing several seed crystals. These authors did not employ NaF and grew the seed crystals with a Si/Al ratio of 15. A Si/Al ratio of approximately 30 and a crystal length of ≈8 μm XRD were used to identify the MOR crystals. Yu et al.[86] characterised different aluminosilicate zeolites by Raman spectroscopy. They described that UV Raman spectra of these zeolites with bands at 470–530, 370–430, 290–410 and 220–280 cm^{-1} could be assigned to bending modes of 4-, 5-, 6- and 8-membered rings of aluminosilicate zeolites, respectively. They also suggested that the band intensities depend on the Si/Al ratio of zeolites. Jin et al.[87] investigated the hydrothermal synthesis of MOR zeolite under perturbation by changing the temperature of crystallisation and using different organic templates. During the process, three different types of mesoporous materials were received from the gel containing the ternary organic templates. At low temperature, two of the three crystalline materials partially crystallised whilst

mesoporous MOR fully crystallised at high temperature. The morphology was studied with TEM of the MOR mesoporous intracrystalline material. Lv et al.[88] reported the utilisation of two different templates for the synthesis of highly siliceous mordenite zeolite, i.e., TEAOH hemamethylene imine (HMI). MOR zeolite crystallised quickly when NH_4NO_3 was added to the mixture and kept the Si/Al ratio at 60. As-synthesised MOR was characterised by MAS NMR of ^{27}Al and ^{29}Si to determine the coordination of the aluminium ion in the framework. The ^{13}C NMR was used for the identification of both the amines of the templates used for the crystallisation. Both templates play a very important role in the crystallisation of mordenite zeolite. Lu et al.[89] synthesised large crystals (60–85 μm) of mordenite (MOR) zeolite from a concentrated solution without using any additives. They observed small-pore-volume mordenite (Na-MOR) zeolites were synthesised by using $Al(NO_3)_3$, $Al_2(SO_4)_3$ and $AlCl_3$ as Al source, and by using $Al(OH)_3$ (Al source), a larger-pore-volume mordenite zeolite was synthesised. Shiokawa et al.[90] synthesised sodium mordenite zeolite with different Si/Al ratios and characterised the crystal structure with the help of X-ray diffraction (XRD). The natural and synthetic mordenite zeolites have the same framework structure. The extra framework cation, water molecule and atomic position of all prepared mordenite zeolites with different Si/Al ratios have been characterised.

1.7.2 The Synthesis of ZnS Nanocluster within the MOR Pore Network

Martines et al.[91] reported the synthesis of ternary semiconductor ZnxCd1-XS in MOR zeolite matrices. They used Zn and Cd for the synthesis of the semiconductor nanocluster. Thiourea is used as a source of sulphur element. This study explained the determination of Zn diluted with ZnCd ternary alloy in the

final product during the synthesis. Raman and photoluminescence spectroscopy were used for the characterisation. Raymond et al.[92] investigated the different mixtures of ZnS and ZnCdS systems grown in the synthetic MOR zeolite by ion exchange. The sulfidation process was done with the hydrogen sulfide flow. The characterisation was carried out with XRD, SEM, TEM and EDS. The relative wt% of Zn, Cd and sulphur was studied with help of EDS. Garcia et al.[67] determined the synthesis of CdS and ZnS nanocluster in mordenite zeolite matrices by hydrothermal process using $CdCl_2$ and $ZnCl_2$ as Cd and Zn sources. The sulfidation process was carried out by hydrogen sulfide flow. The authors noticed that when the Zn and Cd concentration increases, it affects the MOR framework. The MOR and the MOR with nanoclusters were characterised by XRD and Raman spectroscopy. Dimos et al.[93] synthesised ZnS semiconductor nanocluster inside the pores of MCM-41 zeolite by melt exchange reaction. The sulfidation reaction was carried out with the H_2S flow. XRD, EDS and BET were used for the characterisation. The EDS analysis was used to find the final composite product, which came out at 9.3 wt% ZnS. There was no deformation of the framework of the MCM-41. Jeong et al.[94] proposed the synthesis of MX (M = Cd, Zn and Mn, X = S or Se) semiconductors in zeolite Y. They reported that quantum dots are readily expelled out from the zeolite host upon exposure to ambient temperature because of moisture adsorption. But the quantum dots remained within the zeolite host upon exposure to moist atmosphere for several weeks, whilst the surface of the zeolite hosts silylated with a silylating agent. This method is helpful for the determination of quantum dots inside the zeolite host and will be helpful in finding many useful applications. Iacomi in 2003[68] reported the growth of CdS and ZnS particles within the framework of natural and

synthetic zeolites. The Cd^{2+} or Zn^{2+} particle traded structures with 1 molar fluid arrangement of Na_2S. The clusters are linked to each other in the form of aggregates from the absorption and photoluminescence emission spectra. The interface and host affect dynamics and optical retention. Garcia et al.[67] studied and examined the CdS nanoparticles synthesised in the zeolite pore network channels. MOR zeolite was hydrothermally synthesised and used as a host for the CdS nanoparticles to be created in the pore networks. The as-synthesised material was characterised by Raman spectroscopy, optical absorption and N_2 physical adsorption. Garcia et al reported the partial collapse of the framework with grown CdS nanoclusters. Lee et al.[95] investigated the ZnO clusters within the pores of zeolite Y and zeolite A by oxidation of Zn-loaded zeolites, synthesised by Zn vapor deposition. All the samples were characterised by XRD, which demonstrates a small shift to higher 2θ, and changes of relatively higher intensities in XRD spectra of the example from those zeolites preceding the Zn vapor statement may demonstrate the ZnO group development in the zeolite pore network. MacDougall et al.[96] demonstrated that the GaP small clusters were successfully synthesised inside the pores of a zeolite, and that can change the optical properties by optimising the experimental conditions. The NMR results affirm the hypothesised science and the suitability of this analysis to screen the change of micro disperse GaP during the preparation. In agreement with the UV-vis results and by a relationship with the ^{77}Se NMR investigating the colloidal CdSe, they recommend that, with legitimate alignment, a solid-state NMR chemical shift can be helpful to determine the average cluster sizes of such bodies.

1.7.3 The Synthesis of NanoZSM-5 Zeolite

Triantafyllidiset et al.[97] worked on ZSM-5 with different reaction conditions such as temperature and time. Water glass was used as a silicon source, and sodium aluminate solution was used as an aluminium source resulting in a product that was partially crystalline. The Si/Al ratio used was ~28, whilst the crystal size ranged 20–30 nm. The crystallisation occurred at $180^{O}C$ over 24–72 hours. Reding et al.[98] also used their own method to produce crystals with a dimension of ~100 nm. This was achieved using a Si/Al ratio of ~60 and the treatment of a solution with colloidal silicate-1 seed crystals under autogenous pressure. They also reported the ability to control the crystal size distribution and Si/Al ratio of the products. Schmidt et al.[99] reported confined space synthesis, which is a new procedure for nanosized zeolites. In this process, crystallisation of the zeolite occurs in the pore networks of the mesoporous cages. With the help of this method, they synthesised nanosize ZSM-5 and zeolite beta-controlled size distribution. All the samples were characterised by XRD, transmission electron microscopy and nitrogen adsorption/desorption, and the crystallite size reported was 20–75 nm. The carbon materials were then removed by a combustion method, which results in highly crystalline and pure nanozeolite. The authors claimed the confined space synthesis of nanozeolite is an attractive method to control size distribution. Pan et al.[100] synthesised nanosized ZSM-5 aggregates by solid-state conversion using leached metakaolin by solid-state transformation. The synthesis was based on the conditions of molar ratios of TPA^{+} /SiO_2, $NaOH/SiO_2$ and SiO_2/Al_2O_3, and the final product was examined. The aggregates of nanosized ZSM-5 were then characterised by XRD, SEM, HRTEM, MAS NMR, NH_3—TPD, TG and N_2 adsorption and desorption and particle size analysis. The reports showed that the nanosized ZSM-5 was produced within two hours by solid-state

conversion. TEM revealed that the ZSM-5 powder aggregates were irregular spheres consisting of nanosized crystallites about 30–50 nm. Grieken et al.[101] described the synthesis of nanocrystalline ZSM-5 by a hydrothermal method for 24 hours using a clear supersaturated homogeneous solution. The uses of aluminium source, aging time, pH, water content and presence of alkaline cations have been investigated to produce nanocrystalline ZSM-5. The product was then characterised by XRD, solid-state MAS-NMR, TEM and nitrogen adsorption (BET) to examine the crystallisation mechanism. The procedure includes the arrangement of an undefined amorphous solid powder before the zeolite crystallisation, which is slowly changed into nanocrystalline ZSM-5 through solid-solid conversion. Tang et al.[102] introduced MFI-type (ZSM-5) and FAU-type (NaY) zeolite nanocrystals of 20~30 nm dimension built inside the mesopores of carbon nanotubes (CNTS). X-ray diffraction (XRD), Fourier change infrared (FTIR), transmission electron magnifying lens (TEM) and scanning electron magnifying lens (SEM) are used to demonstrate that the nanocrystals of the as-synthesised zeolites' morphology is not quite the same as that of micro-sized zeolites. Askari et al.[103] studied the impacts of ultrasound on the preparation of various types of zeolites. Ultrasound has been connected to crystallisation because of its critical impacts on impelling periods and nucleation. There is a comparative study of ultrasound-assisted aging, static aging and microwave aging. Utilisation of ultrasound can impact the size and morphology of the crystals, crystallisation time and the crystallinity of the zeolites. They reported in this study that the utilisation of ultrasound can enhance crystallisation time; it also enhances the crystallinity of the as-synthesised zeolites. Overall, utilisation of ultrasound-assisted aging prompts changed morphologies and size of particles.

Andac et al.[104] reported the comparative study of ultrasound-assisted synthesis and ordinary static-method-synthesised zeolite A from a clear sodium aluminosilicate solution under the same condition of reaction temperatures and times. It was conceivable to get highly crystalline zeolite A in the vicinity of ultrasound, which affected the sorts and stability of the stages that were framed amid metastable stage changes. Nucleation and crystallisation rates and the yield of zeolite A increase after the effect of ultrasound. DLS was used for particle size distribution. Thermogravimetric investigations and water adsorption analysis show that the advancement of micropore adsorption limit, which began ahead of schedule in the X-ray amorphous samples received from the 'clear' solution, was likewise sped up with the use of ultrasound. Xue et al.[105] synthesised high-crystalline nanosized NH_4—ZSM-5 zeolites with a high SiO_2/Al_2O_3 ratio directly through seed-incited methodology. The items were described utilising X-ray powder diffraction (XRPD), scanning electron microscopy (SEM), Fourier transform infrared (FT-IR), N_2-sorption test, thermogravimetric (TG) analysis, ammonium temperature programmed desorption (NH_3-TPD), inductively coupled plasma atomic emission spectroscopy (ICP-AES) and ^{27}Al and ^{29}Si MAS NMR. Only confirming the measure of seeding suspension could control the crystal sizes. The as-synthesised NH_4-ZSM-5 can be changed over the acidic H- forming H-ZSM-5 by calcination. Aly et al.[106] utilised aluminium sources, claiming that Al sources have an extraordinary impact on ZSM-5 crystallisation, which shows a difference in the properties of the derived product. The crystallinity of nanosized ZSM-5 zeolite from the antecedent's mixture containing distinctive aluminium sources as sodium aluminate, aluminium chloride and aluminium nitrate has been examined. XRD, SEM, FT-IR, EDS and BET surface area were used to examine

the derived products. The normal crystal size increased in the following order: sodium aluminate < aluminium nitrate < aluminium chloride. Meanwhile, surface area was enhanced as follows: aluminium chloride < aluminium nitrate < sodium aluminate. Musyoka et al.[107] studied the uses of South African coal fly ash mine water as an alternative medium for synthesis of zeolite A. The ultrasound aging was also examined prior to hydrothermal treatment. In this method, first, the experimental conditions were developed by utilising ultra-immaculate water, and thereafter, ultra-deionised water was substituted with raw, untreated mine water (acid mine seepage and circumneutral mine waters) for synthesising zeolite A. They reported that sonication decreased the crystallisation time of pure zeolite A to 60 minutes. Mostafa et al.[108] reported the synthesis of nanosized ZSM-5 without the utilisation of an organic template in a two-step process; the resultant product was partially crystalline with a high surface area (678 m^2/g). The first-time aluminium nitrate was utilised as an aluminium precursor to make ZSM-5 materials. The as-synthesised powder product of the MFI structure was examined through XRD, FTIR, Raman and TEM spectroscopy. Industrially synthesised HZSM-5 was added to the reactants as a seeding agent, which increases the crystallinity of the ZSM-5 yield and consequently reduces the surface area too. They observed that the practically crystalline ZSM-5 have low microporosity and a surprisingly high meso/macropore volume with a pore dimension of around 30 nm.

1.8 References

[1] A. Tiwari, S. Titinchi, *Advanced Catalytic Materials - Wiley Online Library*, Scrivener Publishing LLC, **2015**.

[2] R. Singh, K. Kulkarni, A. D. Kulkarni, *Chem. Mater. Res.* **2011**, *1*, 16–21.

[3] A. F. Cronstedt, *Akad Handl* **1756**, *18*, 120.

[4] J. M. Newsam, *Sci. Artic.* **1986**, *231*, 1093–1099.

[5] A. F. Masters, T. Maschmeyer, *Microporous Mesoporous Mater.* **2011**, *142*, 423–438.

[6] S. M. Auerbach, K. A. Carrado, P. K. Dutta, *Handbook of Zeolite Science and Technology*, CRC Press, **2003**.

[7] A. Dyer, *An Introduction to Zeolite Molecular Sieves*, John Wiley & Sons Australia, Limited, **1988**.

[8] C. Baerlocher, L. McCusker, D. Olson, *Atlas of Zeolite Framework Types*, Online IZA, Elsevier For Printed Version, **2001**.

[9] S. Bhatia, *Zeolite Catalysts: Principles and Application*, CRC Press Inc, Florida, **1989**.

[10] R. G. Bell, "British Zeolite Association http://www.bza.org/zeolites/," **2001**.

[11] W. M. Meier, D. Olson, D. H. Olson, I. Z. A. S. Commission, *Atlas of Zeolite Structure Types*, International Zeolite Association, **1978**.

[12] C. Klein, *Manual of Mineral Science*, Wiley, **2001**.

[13] A. V. McCormick, A. T. Bell, *Catal. Rev.* **1989**, *31*, 97–127.

[14] M. OKeeffe, M. A. Peskov, S. J. Ramsden, O. M. Yaghi, *Acc. Chem. Res.* **2008**, *41*, 1782–1789.

[15] J. Bernholc, W. Lu, S. M. Nakhmanson, P. H. Hahn, V. Meunier, M. Buongiorno, N., W. G. Schmidt, *Mol. Phys.* **2007**, *105*, 147–156.

[16] C. C. Freyhardt, M. Tsapatsis, R. F. Lobo, K. J. Balkus, M. E. Davis, *Nature* **1996**, *381*, 295–298.

[17] "IZA:http://www.iza-online.org/natural/Datasheets/Mordenite/mordenite.htm,"**2005**.

[18] M. F. M. Post, *Introduction to Zeolite Science and Practice*, Elsevier B.V., Amsterdam, **1991**.

[19] B. Bogdanov, D. Georgiev, K. Angelova, K. Yaneva, *Nat. Mathememical Sci.* **2009**, *IV*, 1–5.

[20] A. Chica, M. J. Politi, I. Poulios, R. Sedev, *Chem. Eng.* **2013**, 1–19.

[21] C. Jiri, C. Avelino, Zeolites and Catalaysis Synthesis, Reaction and Application, Wiley-VCH, Weinheim, **2010**.

[22] L. L. Y. Chang, Industrial Mineralogy: Materials, Processes, and Uses, Prentice Hall, Dallas, **2002**.

[23] K. Margeta, N. Zabukovec Logar, M. Siljeg, A. Farkas, *Chapter-5 Natural Zeolites in Water Treatment How Effective Is Their Use*, Intech, **2013**.

[24] C. Martinez, A. Corma, *Coord. Chem. Rev.* **2011**, *255*, 1558–1580.

[25] D. J. Sherman, *Colloqium Pap.* **1999**, *96*, 3471–3478.

[26] A. Petushkov, S. Yoon, S. C. Larsen, *Microporous Mesoporous Mater.* **2011**, *137*, 92–100.

[27] M. Khatamian, M. Irani, *J. Iran. Chem. Soc.* **2009**, *6*, 187–194.

[28] S. Zheng, W. Ding, Y. Zhang, Z. Tan, X. Xu, *Kem. Ind.* **2006**, *55*, 373–379.

[29] M. Flanigen, R. W. Broach, S. T. Wilson, *Zeolites in Industrial Separation and Catalysis*, Wiley-VCH, Weinheim, **2010**.

[30] J. P. L. Martins, Characterization by Model Reactions of Modified EUO and MWW Zeolites, University de Poitiers, France, **2012**.

[31] T. W. Wong, Handbook of Zeolites: Structure, Properties and Applications, Nova Science Publishers, **2009**.

[32] S. Kulprathipanja, *Zeolites in Industrial Separation and Catalysis*, John Wiley & Sons, **2010**.

[33] Q. A. Acton, Advances in Hydrofluoric Acid Research and Application: 2013 Edition, ScholarlyEditions, Atlanta, Georgia, **2013**.

[34] S. M. Grant, M. Jaroniec, *J. Mater. Chem.* **2012**, *22*, 86–92.

[35] J. Weitkamp, P. Luthar, *Catalysis and Zeolite Fundamentals and Applications*, Springer-verlag, NY, **1999**.

[36] M. Wallau, U. Schuchardt, *J. Braz. Chem. Soc.* **1995**, *6*, 393–403.

[37] P. B. Weisz, V. J. Frilette, *J. Phys. Chem* **1960**, *64*, 382.

[38] D. L. Bish, D. W. Ming, Mineralogical Society of America - Natural Zeolites: Occurrence, Properties, Applications, Mineralogy And Geochemistry, USA, **2001**.

[39] W. F. Hoelderich, D. Heinz, *Res. Chem. Intermed.* **1998**, *24*, 337–348.

[40] P. Ratnasamy, *Catal. Today* **1988**, *3*, 531–535.

[41] J. Bellussi, R. Millini, "Zeolites in 'Encyclopedia of Science and Technology' - Treccani," can be found under http://www.treccani.it/enciclopedia/zeoliti_(Enciclopedia_della_Scienza_e_della_Tecnica)/, **2007**.

[42] C. Y. Hsu, A. S. T. Chiang, R. Selvin, R. W. Thompson, *J. Phys. Chem. B* **2005**, *109*, 18804–18814.

[43] W. E. Farneth, R. J. Gorte, *Chem. Rev.* **1995**, *95*, 615–635.

[44] G. Ohlmann, H. Pfeifer, R. Fricke, *Catalysis and Adsorption by Zeolites*, Elsevier, **1991**.

[45] J. Hagen, Industrial Catalysis: A Practical Approach, Wiley, **2015**.

[46] H. V. Bekkum, E. M. Flanigen, P. A. Jacobs, J. A. Jansen, *Introduction to Zeolite Science and Practice*, Elsevier Science B. V., Amesterdam, **2001**.

[47] K. P. Kitsopoulos, *Clays Clay Miner.* **1999**, *47*, 688–696.

[48] Website, "CO2CRC - Leaders in research into Carbon Capture and Storage," can be found under http://www.co2crc.com.au/aboutccs/co2_capture_separation.html, **2004**.

[49] S. Lower, "Hard water and water softening," can be found under http://www.chem1.com/CQ/hardwater.html, **2013**.

[50] D. Inamuddin, *Ion Exchange Technology II Applications*, Springer Science, New York, **2012**.

[51] A. Dyer, T. Las, M. Zubair, *J. Radioanal. Nucl. Chem.* **2000**, *243*, 839–841.

[52] M. S. Oskoui, M. Khatamian, M. Haghighi, A. Yavari, *RSC Adv.* **2014**, *4*, 19569.

[53] Y. V. Meteleva, F. Roessner, G. F. Novikov, *J. Photochem. Photobiol. A Chem.* **2008**, *196*, 154–158.

[54] "Zeolite," can be found under http://www.gordeszeolite.com/zeolite--clinoptilolite-, **2014**.

[55] E. Passaglia, *Am. Mineral.* **1975**, *50*, 65–77.

[56] IZA, "International Zeolites Association," can be found under http://www.iza-online.org/natural/Datasheets/Mordenite/mordenite.htm, **1973**.

[57] Website, "Mordenite zeoltie," can be found under http://www.britannica.com/science/mordenite, **2009**.

[58] E. L. First, C. E. Gounaris, J. Wei, C. A. Floudas, *Phys. Chem. Chem. Phys.* **2011**, *13*, 17339.

[59] M. Bevilacqua, A. G. Alejandre, C. Resini, M. Casagrande, G. Busca, *Phys. Chem. Chem. Phys.* **2002**, *4*, 4575–4583.

[60] P. Simoncic, T. Armbruster, *Am. Mineral.* **2004**, *89*, 421–431.

[61] M. Bevilacqua, A. G. Alejandre, C. Resini, M. Casagrande, J. Ramirez, G. Busca, *Phys. Chem. Chem. Phys.* **2002**, *4*, 4575–4583.

[62] F. Raatz, E. Freund, C. Marcilly, J. Chem. Soc. Faraday Trans. 1 Phys. Chem. Condens. Phases **1983**, 79, 2299.

[63] C. Colella, Zeolites and Ordered Mesoporous Materials: Progress and Prospects, Elsevier, **2005**.

[64] H. V. Garcia, M. H. Velez, O. S. Garrido, J. M. M. Duart, J. Jimenez, *Solid. State. Electron.* **1999**, *43*, 1171–1175.

[65] E. J.-A. Oscar, H. Villavicencio, J. A. Diaz-Hernandez, V. Petranovskii, M. Herrera, O. Raymond-Herrera, *Chem. Mater.* **2014**, *26*, 6152–6159.

[66] M. M. Garcia, H. Villavicencio, M. Hernandez-Velez, O. Senchez, J. M. Martinez-Duart, *Mater. Sci. Eng. C* **2001**, *15*, 101–104.

[67] M. M. Garcia, H. Villavicencio, M. Hernandez-Velez, O. Senchez, J. M. Martinez-Duart, *Mater. Sci. Eng. C* **2001**, *15*, 101–104.

[68] F. Iacomi, *Surf. Sci.* **2003**, *532–535*, 816–821.

[69] A. Pourahmad, *Int. J. Nano Dimens.* **2015**, *6*, 83–88.

[70] R. J. Argauer, G. R. Landolt, M. Oil, *U.S.Patent 3702886* **1972**.

[71] T. F. Degnan, G. K. Chitnis, P. H. Schipper, *Microporous Mesoporous Mater.* **2000**, *35–36*, 245–252.

[72] G. Dwyer, N. Y. Chen, W. E. Garwood, *Shape Selective Catalysis Industrial Applications*, Marcel Dekker Inc, New York, **1996**.

[73] E. L. Wu, S. L. Lawton, D. H. Olson, A. C. Rohrman, G. T. Kokotailo, *J. Phys. Chem.* **1979**, *83*, 2777–2781.

[74] D. G. Hay, H. Jaeger, G. W. West, *J. Phys. Chem.* **1985**, *89*, 1070–1072.

[75] M. Ardit, A. Martucci, G. Cruciani, *J. Phys. Chem.* **2015**, *119*, 7351–7359.

[76] K. B. Yoon, S. Kim, P. Cao, T. Tung, F. Application, P. Data, Uniformly B-Oriented MFI Zeolite Membrane with Variable Thickness Supported on Substrate and Preparation Method, **2012**, Patent No. US 8,153,099 B2.

[77] R. Grau-Crespo, E. Acuay, R. Ruiz-Salvador, *Chem. Commun.* **2002**, 2544–2545.

[78] "IZA Commission on Natural Zeolites structure data base," can be found under http://www.iza-structure.org/databases/, **2005**.

[79] H. V. B. J. Cejka, *Zeolites and Order Mesoporous Materials: Progress and Prospects.*, Elsevier Science B. V., Amsterdam, **2005**.

[80] J. Zhou, Z. Hua, Z. Liu, W. Wu, Y. Zhu, J. Shi, *ACS Catal.* **2011**, *1*, 287–291.

[81] Y. Liu, X. Zhou, X. Pang, Y. Jin, X. Meng, X. Zheng, X. Gao, F.-S. Xiao, *Chem Cat Chem* **2013**, *5*, 1517–1523.

[82] H. A. Zaidi, K. K. Pant, *Catal. Today* **2004**, *96*, 155–160.

[83] M. Bjørgen, F. Joensen, M. Spangsberg Holm, U. Olsbye, K.-P. Lillerud, S. Svelle, *Appl. Catal. A Gen.* **2008**, *345*, 43–50.

[84] H. X. Vu, R. Eckelt, U. Armbruster, A. Martin, *Nanomaterials* **2014**, *4*, 712–725.

[85] B. Lu, T. Tsuda, Y. Oumi, K. Itabashi, T. Sano, *Microporous Mesoporous Mater.* **2004**, *76*, 1–7.

[86] Y. Yu, G. Xiong, C. Li, F. S. Xiao, *Microporous Mesoporous Mater.* **2001**, *46*, 23–34.

[87] Y. Jin, Y. Li, S. Zhao, Z. Lv, Q. Wang, X. Liu, L. Wang, *Microporous Mesoporous Mater.* **2012**, *147*, 259–266.

[88] A. Lv, H. Xu, H. Wu, Y. Liu, P. Wu, *Microporous Mesoporous Mater.* **2011**, *145*, 80–86.

[89] B. Lu, Y. Oumi, T. Sano, *J. Cryst. Growth* **2006**, *291*, 521–526.

[90] K. Shiokawa, M. Ito, K. Itabashi, *Zeolites* **1989**, *9*, 170–176.

[91] O. Martines, *Eur. Phys. J. Appl. Phys.* **2004**, *28*, 265–291.

[92] O. Raymond, H. Villavicencio, V. Petranovskii, J. M. Siqueiros, *Mater. Sci. Eng. A* **2003**, *360*, 202–206.

[93] K. Dimos, I. B. Koutselas, M. A. Karakassides, *J. Phys. Chem. B* **2006**, *110*, 22339–22345.

[94] N. C. Jeong, H. S. Kim, K. B. Yoon, *Langmuir* **2005**, *21*, 6038–6047.

[95] H. B. Lee, H. M. Lim, S. C. Han, *Bull. Korean Chem. Soc* **1998**, *19*, 1002–1005.

[96] J. E. Mac Dougall, H. Eckert, G. D. Stucky, N. Herron, Y. Wang, K. Moller, T. Bein, D. Cox, *J. Am. Chem. Soc.* **1989**, *111*, 8006–8007.

[97] K. S. Triantafyllidis, L. Nalbandian, P. N. Trikalitis, A. K. Ladavos, T. Mavromoustakos, C. P. Nicolaides, *Microporous Mesoporous Mater.* **2004**, *75*, 89–100.

[98] G. Reding, T. Maurer, B. Kraushaar-Czarnetzki, *Microporous Mesoporous Mater.* **2003**, *57*, 83–92.

[99] I. Schmidt, C. Madsen, C. J. H. Jacobsen, *Inorg. Chem.* **2000**, *39*, 2279–2283.

[100] F. Pan, X. Lu, Q. Zhu, Z. Zhang, Y. Yan, T. Wang, S. Chen, *J. Mater. Chem. A* **2014**, *2*, 20667–20675.

[101] R. V. Grieken, J. M. Sotelo, J. A. Melero, *Microporous Mesoporous Mater.* **2000**, *39*, 135–147.

[102] K. Tang, Y. G. Wang, L. J. Song, L. H. Duan, X. T. Zhang, Z. L. Sun, *Mater. Lett.* **2006**, *60*, 2158–2160.

[103] S. Askari, S. Miar Alipour, R. Halladj, M. H. Davood Abadi Farahani, *J. Porous Mater.* **2013**, *20*, 285–302.

[104] O. Andac, M. Tatlıer, A. Sirkecioglu, I. Ece, A. Erdem-Senatalar, *Microporous Mesoporous Mater.* **2005**, *79*, 225–233.

[105] T. Xue, Y. M. Wang, M.-Y. He, *Microporous Mesoporous Mater.* **2012**, *156*, 29–35.

[106] H. M. Aly, M. E. Moustafa, E. A. Abdelrahman, *Der Chem. Sin.* **2011**, *4*, 166–173.

[107] N. M. Musyoka, L. F. Petrik, E. Hums, *IMWA* **2011**, 423–428.

[108] M. M. M. Mostafa, K. N. Rao, H. S. Harun, S. N. Basahel, I. H. A. El-Maksod, *Ceram. Int.* **2013**, *39*, 683–689.

Chapter 2

2. Synthesis, Instrumental and Analytical Techniques

2.1 Sources and Materials

The systematic synthesis of zeolites presented in this thesis derives from the experimental methods reported in the literature.[1,2]

The presence of impurities can significantly disrupt the zeolite framework because of the use of impure starting materials for synthesis. The impurities are unable to dissolve during the crystallisation process or may dissolve to form different silicate precursors.[3] To synthesise pure product, pure chemicals should be used as source materials. Some of the chemicals used as source materials for zeolite synthesis are discussed below.

2.1.1 Sources of Water

Water is the basic component of the synthesis of zeolite. Water has a great effect on the crystallisation of zeolites. The amount of water content may vary; it may be present in bulky hydrated molecules or may come from hygroscopic materials of synthesis sources,[4] e.g., NaOH, H_2F_2 or colloidal silica available commercially. Fumed silica may contain about 3 wt% of water. Similarly, some Al precursors also contain some specific amount of water. Aluminium nitrate ($Al(NO_3)_3 \cdot 9H_2O$) contains up to 43 wt% of water after being exposed to air (moist), whilst aluminium sulfate ($Al_2(SO_4)_3 \cdot 18H_2O$) dehydrates upon exposure to air.[5]

2.1.2 Aluminium Precursors

The most common precursors of Al used in the synthesis of zeolite are, e.g., sodium aluminate, pseudo-boehmite, aluminium hydroxide, aluminium isopropoxide, aluminium nitrate and aluminium sulfate, which influence the crystallisation of the product.[4,6] The use of $[Al(OH)_4]^-$ species as a component material illustrates two factors of the synthesis:[6,7]

I. It increases the zeolite production.

II. It is used as a source of a base in the solution (pH > 10 for a successful zeolite synthesis).

2.1.3 Silicon Precursors

The choice of silicon precursors used has different effects on the synthesis of zeolites. Liquid silicates are widely used as a source for zeolite synthesis.[4,6] The silica source not only influences the crystallisation process but also reduces the crystallite size upon proper dissolution of the silica precursor.[4,8,9] Silicon precursors also have significant effects on the formation of different types of zeolites, which influence some particular features of the zeolites.[10] Some different types of silicates used in the synthesis of zeolites are named here.

- Sodium metasilicate pentahydrate
- Ludox HS-30, Ludox HS-40 (colloidal silica)
- Fumed silica
- TEOS, TMOS and silicon esters
- Silica gel, glasses, clays (kaolinite), volcanic tuffs, sand and quartz

2.1.4 Sources of Cations

Alkali- and alkaline-earth-metal hydroxides are important cation source materials which affect the synthesis of zeolites by providing high concentrations of solution.[6] The presence of inorganic cation may also vary the crystallinity, yield, morphology and the rate of crystallisation of zeolite synthesis.[11,12]

2.2 Synthesis of Zeolites

Conventional synthesis of zeolites is done by the hydrothermal treatment of an alkaline aqueous solution containing Si and Al sources (aluminosilicate gel). Organic structure-directing agents (OSDA) also play an important role in the crystallisation of various types of zeolite. The crystallisation usually occurs in a closed system, a stainless-steel autoclave at different temperatures usually from 50^{o}C to 180^{o}C at autogenous pressure between an hour and extended timescales (days). A simplified schematic flow sheet diagram shown in Figure 2.1 details the experimental conditions for synthesis of zeolites. The effects of these conditions on the synthesised zeolite characteristics are briefly discussed below.[12,13]

- *Reaction composition*: Composition of the reaction materials (silica and alumina sources, alkalinity, presence of inorganic cations as discussed in previous sections). There is a significant effect of the Si/Al ratio on the physical properties of the zeolite. Inorganic cations and OSDA balance the framework charge, but they have a significant effect on crystal purity and product quantity.
- *Temperature effect:* The rate of nucleation is inversely proportional to temperature, and the rate of crystallisation is directly proportional to silicate concentration.

- *pH of the gel/solution*: The synthesis of zeolites is carried out in an alkaline solution with high pH, i.e., pH > 10.
- *Nature of the reactant precursors:* Organic and inorganic materials are used for zeolite synthesis. Organic precursors are quickly interlinked with the network, whilst inorganic precursors produce more hydroxylated surfaces.
- *Reaction time*: Crystallisation time should be optimised to minimise the yield of impurities and to achieve the desired crystalline product.

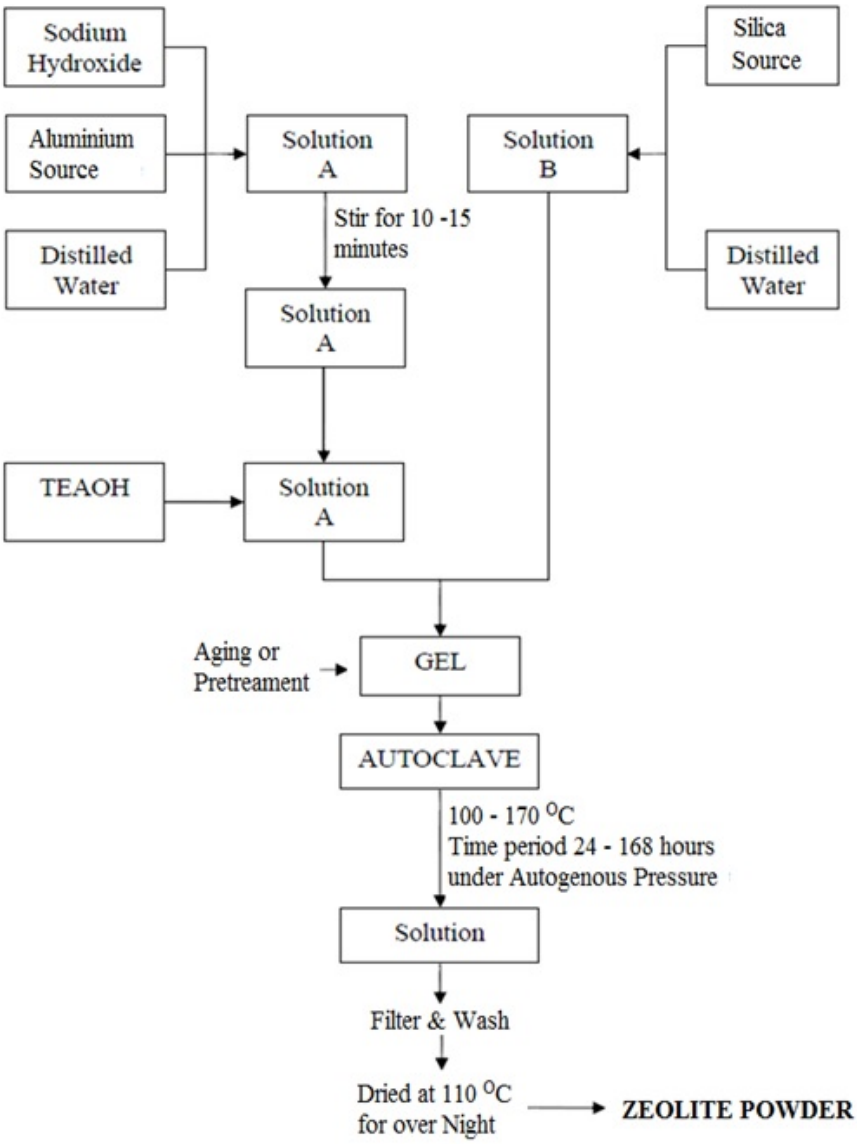

Figure 2.1 Schematic presentation of different steps involved in the zeolite synthesis. Taken and modified from various sources.

2.2.1 Zeolite Crystallisation

Zeolite crystallisation commonly occurs during the hydrothermal treatment initiated by an amorphous gel phase. This process is completed in three different phases, i.e., alkaline solution, amorphous gel and crystalline product.[14] The zeolite synthesis and processing conditions are linked to various physicochemical mechanisms and often competing kinetic processes that govern the nucleation and crystal growth of the product phase.[15]

2.2.2 Aging or Pretreatment of a Solution/Mixture

Aging may be defined as the maximum time between mixing of the chemical materials prior to the hydrothermal treatment for crystallisation. It is reported that the pretreatment/aging of the solution mixture before any hydrothermal process is necessary to produce a crystalline product.[16] It is therefore important to understand nucleation and crystal growth to introduce new and useful zeolitic materials.[16–18] A significant amount of research has been done to investigate the influence of aging on the nucleation and crystal growth kinetics of zeolites.[16,19,20] Aging reduces the process duration of crystallisation at any temperature and also affects the crystal size.[20] It is difficult to understand the precise mechanism of aging, and it has been proposed that during the aging process, the reacting materials rearrange to initiate the nuclei species. Those species remain nonreactive until they are energised via heating during aging periods.[16,18,19]

Ultrasound is an important phenomenon used not only for medical purposes but also to affect the distribution of crystallite size and crystal growth in

the crystallisation process.[21] Initially, in the syntheses of zeolites, the alkaline aluminosilicate gel is normally aged to obtain the smallest crystallite size and to improve the product.[15] Therefore, to enhance the nucleation and to get the required crystallite size, different modes of aging are used. Aging with ultrasound has been a powerful tool for the enhanced nucleation process in liquid- or gel-based solutions.[22,23] In this work, ultrasound was used at different stages in aging/pretreatment and interrupted crystallisation to enhance the nucleation process and achieve the nanoscale particles/crystals of the ZSM-5 zeolite.

2.2.3 Nucleation

Nucleation is a phenomenon in which the 'nucleus', typically a small seed crystal or dust particle in the amorphous phase of a solution, initiates crystallisation. Nucleation is the first step of the crystallisation process.

A significant energy barrier can be overcome at a higher level of supersaturation. If supersaturation is very high, the higher number of nuclei will be formed[24] as shown in Figure 2.2, where step III is a supersaturation leading to a higher number of nuclei. The rate of nucleation is directly related to concentration and is inversely proportional to temperature.

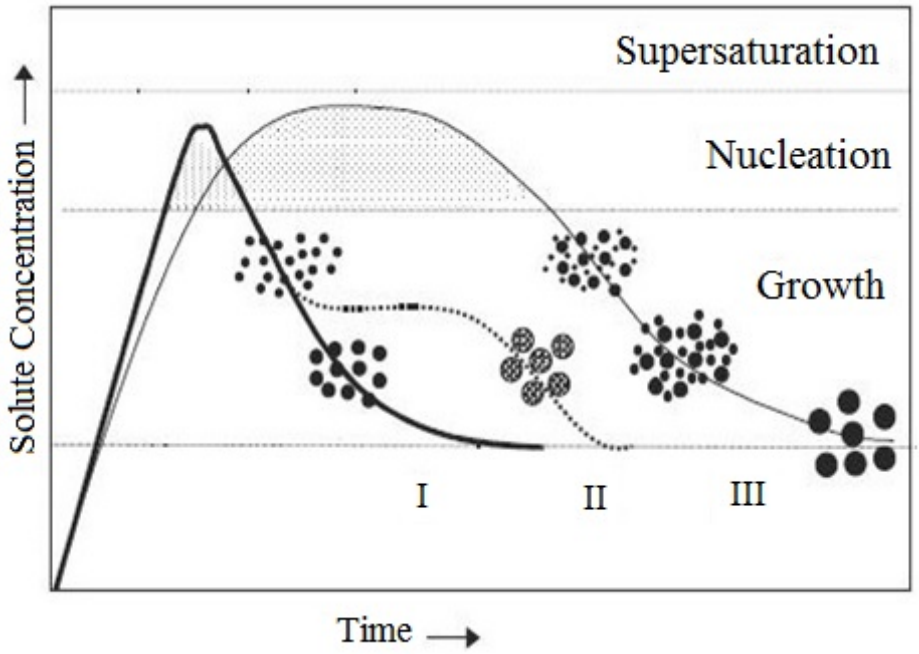

Figure 2.2 Proposed mechanism of nucleation and crystal growth in supersaturation solution: (I) single nucleation and uniform crystal; (II) nucleation, growth and aggregation of smaller subunits; (III) multiple nucleation events and crystal growth.[25]

2.2.4 Crystal Growth

The process in which the materials are arranged from the solution through a growth process is called crystallisation. In the crystallisation process, the crystals grow through a particular mechanism, which is described by equation (4):[2,14,26]

$$\frac{dL}{dt} = G = ks^{a} \quad (4)$$

where a is an exponent, whose value is unity for a plane surface and 1–2 for various surface-reaction-limited growth processes; t is the time; s is the concentration; G is the linear crystal growth rate; k is a temperature-dependent rate constant and L is the characteristic particle size in μm. This particular mechanism can be illustrated in the following four steps and shown in Figure 2.3.[14,26–28]

I. Transport of growth unit through solution

II. Attachment of crystal growth unit to the surface

III. Movement of growth unit on the surface

IV. Attachment of growth unit to edges and kinks

The very first step is the transportation process of crystallisation. All the other steps are considered as surface processes, which may involve many other substeps. Generally, crystal growth theories are developed upon the crystal surface structure. The crystal surfaces are made of many monoatomic heights such as steps or edges. Each surface has an empty space in the form of kinks, edge vacancy or surface vacancy. The area above the step is a terrace; it easily adsorbs a growth unit. These units are attached to the surface by means of bonds depending on the type of vacancy. Different vacancies have a different number of bonds. When the growth units attach to any vacancy, it will trigger crystal growth. So the growth units will fill each type of vacancy by completing the edge or step, and hence, a movement of the face edge will occur. It will thus create a new layer of step via nucleation of the growth units. Generally, this kind of crystal growth mechanism is referred to as layer growth or nucleation growth.

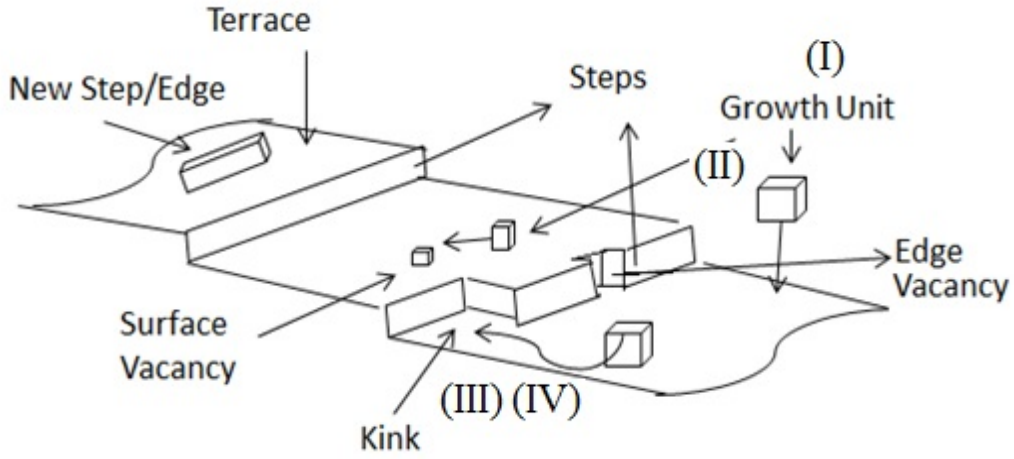

Figure 2.3 Proposed schematic representation of crystal growth stepwise transitions: (I and II) growth unit transport of solute to a position near the crystal surface, (III) adsorption onto the crystal surface, (IV) growth unit attached to vacancies (kinks, surface or edge). Taken and modified from.[27]

This chapter briefly explains the experimental procedures and introduces the major analytical techniques used for synthesised material characterisation, and further explanation will be given where appropriate in subsequent chapters. Specifically, insights concerning particular instrument types, operational parameters, hypothetical standards and the information received from such techniques are briefly discussed.

2.3 X-ray Diffraction

X-ray diffraction (XRD) is one of the most widely used analytical techniques for structure elucidation in biological and materials science. This technique allows the elucidation of the positions of atoms and ions in a crystal lattice and hence gives a description of structure in terms of bond lengths, bond angles and the corresponding positions of ions and molecules in the unit cell of a framework.[6,29,30] This technique also helps identify the phase composition and crystallite size of the crystalline materials.[29,31,32]

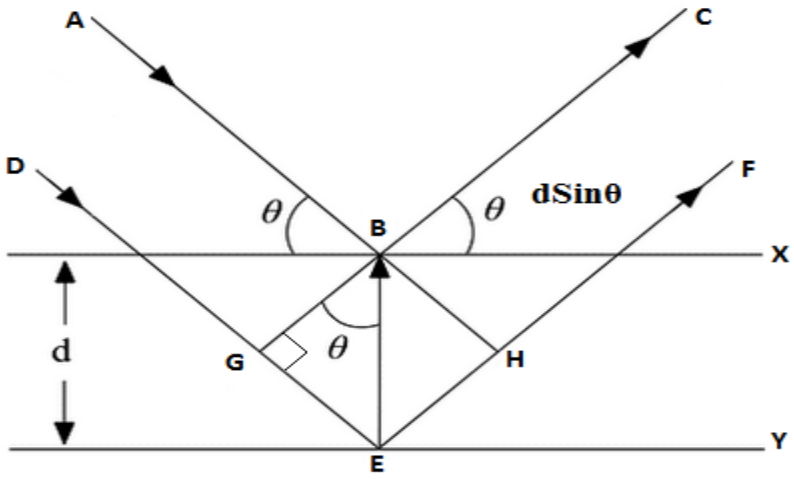

Figure 2.4 Presenting Bragg's law, the incident ray reflected on the particle surface. X-rays interfere constructively when the additional path length 2dsinθ is equal to the integral multiple of the wavelength λ.

A simplified picture of the phenomenon of diffraction is presented in Figure 2.4 where the X-rays impinge on the surface of the crystallite. Some of the X-rays will be scattered from the electron cloud of an atom in the upper layers that are only surface sensitive, whilst the others pass through and scatter from the second layer. XRD worked on the basis of constructive interference of X-rays scattered from atom planes separated by a distance similar to the wavelength of radiation (100 pm). The relationship between the lattice points separated by *d,* the scattering angle θ and the X-ray wavelength λ in which constructive interference will be observed is given by Bragg's equation (5):[6,29]

$$\lambda = 2d \sin \theta \quad (5)$$

The intensity of diffraction X-rays is recorded as a function of scattering angle to produce the diffraction pattern. From the diffraction pattern, not only the crystal lattice but also the crystallite size can determine the peak positions and full width half maximum (FWHM) of a particular peak; parameters and crystallite size, respectively, are used to calculate the lattice.[33] Bragg's equation (5) can also help

measure the lattice spacing of a typical system,[6] e.g., equation (6) presenting a simple cubic system of a crystal lattice:

$$d_{hkl} = \frac{a}{\sqrt{h^2 + k^2 + l^2}} \quad (6)$$

Equation (7) is used for the orthogonal system of a crystal lattice:

$$\frac{1}{d_{hkl}^2} = \frac{h^2}{a^2} + \frac{k^2}{b^2} + \frac{l^2}{c^2} \quad (7)$$

By connecting equation (6) to Bragg's law (5),

$$\left(\frac{\lambda}{2a}\right)^2 = \frac{sin^2\theta}{h^2 + k^2 + l^2} \quad (8)$$

where *a* is the lattice space and *h, k, l* are Miller indices of the Bragg plane.

The peaks' broadening occurs in nanoscale crystallites in XRD powder patterns. Scherrer introduced an equation in 1918, with some subsequent modifications for peaks modelled with Lorentzian and Gaussian functions shown in equations (9) and (10), respectively. This broadening can thus be related to the average size of the crystallite.[34,35]

$$T = \frac{K\lambda}{(\beta_m - \beta_s) \cdot Cos\theta} \quad (9)$$

$$T = \frac{K\lambda}{\sqrt{(\beta_m^2 - \beta_s^2)} \cdot Cos\theta} \quad (10)$$

K is the constant of near unity (0.9) of a crystallite shape, *T* is the average dimension of the crystal in a direction normal to the diffracting plane *hkl*, λ is the X-ray wavelength, B_m is the observed sample peak width, B_S is the peak width of a crystalline standard material, and θ is the angle of diffraction.

The peak shape functions used to model X-ray diffraction peaks generally use a combination of Lorentzian and Gaussian components (a pseudo-Voigt function). Hence, it is important to note that the observer should calculate properly the contributions of Gaussian and Lorentzian components with suitable peak shape functions. According to equations (9) and (10), as the crystallite size increases, the observed peak width decreases.

In this work, X-ray powder diffraction measurements were performed on a PANalytical X'pert high-resolution diffractometer operated at 45 kV and 40 mA, using CuK_{α_1} radiation, in 2θ range from 3° to 50° in steps of 0.02°, with a sampling time of 1 sec/step. These data were used to identify the structure, phase composition and crystallite size MOR and ZSM-5 *as-synthesised* zeolites.

2.4 Transmission Electron Microscopy (TEM)

TEM is a remarkable modern analytical technique developed by Max Knoll and Ernst Ruska in 1931. After some modifications it was used for the characterisation of materials at a nanometre scale across both physical and biological sciences. It reveals information about the internal structure, composition and size and morphology of nanomaterials.[36]

In TEM, the electron beam is in a vertical position, and the recording system is placed horizontally at the bottom. The electron source must have three main requirements: long lifetime, high brightness and a small spread of kinetic electron energy. There are many different electron sources which function on different physical principles.[37] To achieve a significantly high resolution, the electron gun can be replaced with a light source and the voltage maintained (100–

400 kV). Lanthanum hexaboride (LaB_6) particles can produce electron rays with a current density in the order of 1×10^6 Am^{-2}, or a field emission source can produce *ca* 1×10^{10} Am^{-2}. The samples can be prepared in such a way that a thin layer of nanoparticles is mounted on the sample grid when it is exposed to these high-energy electron rays that interact with the sample particles. It gives a high-resolution image of the sample fluorescent screen.[38] A simplified diagram of the TEM instrument is shown in Figure 2.5.

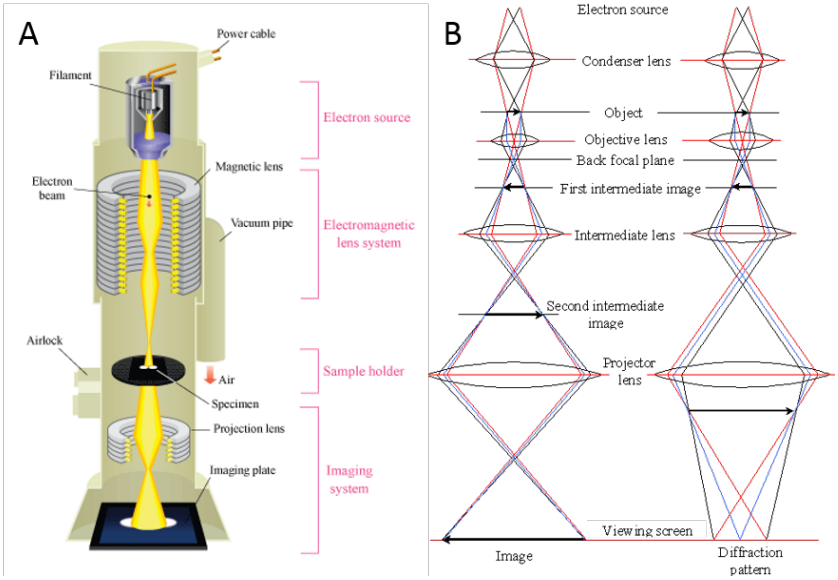

Figure 2.5 (A) Schematic cross section of the TEM system presenting basic parts. (B) Similarities of the lens environments between TEM diffraction and TEM photo forms.[39]

It is important for an electron to hit the specimen to produce a TEM image. This is usually obtained by using different dispersion methods of the nanocrystallite powder such as mechanical thinning, electrochemical thinning, ion milling or drop-dry methods. A typical schematic TEM image is shown in Figure 2.5 (a) and (b). The thickness of the layer of the specimen on the sample grid can be less than 100 nm. The electromagnetic condenser is used to focus the high-energy electrons from the electron gun, whose focus, in turn, is controlled by

varying the lens' current. To target the first image when the beam of electron passes through the sample, elastically scattered electrons transmitted through the sample are refocused by a projection lens by controlling their current. The last image also employs electromagnetic lenses to detect the image on a phosphor screen. Some common screen current densities are in the series of 10^{-10} to 10^{-12} Am^{-10} for large magnifications. Additionally, as the high-frequency electron beam has a very short penetration length in the charged coupled camera used during the operation and where photographs are stored, the microscope column is set up in the vacuum of ~ 10^{-7} torr.[38]

If the maximum ray divergence in the electron microscope is < 1^{O}, then the Rayleigh criterion for the detected image of a specific source can be decreased according to the following Abbe's equation (11),[40]

$$d = \frac{0.61\ \lambda_o}{n \sin \propto} \tag{11}$$

where d is the minimum resoluble distance, α is the aperture angle subtended at the subject by the lens, λ_0 is the wavelength of radiation, and n is the refractive index. So for a given n and α, the minimum dispersible length in the microscope system is in the order of the wavelength. According to equation (11), wavelengths of $\lambda_0 < 0.1$ nm are important to the firmness of crystal lattices of atomic size, and thus, electrons are most favourable to produce such resolution (200 kV has $\lambda_0 =$ 2.5 pm).

The microscope resolution can be improved by enhancing the accelerating voltage, but many species may decompose from the radiation after a long period of exposure. Because of the nonspherical nature of the lens in TEM processing, the resolution is of poorer quality than that of the theoretical Rayleigh limits. This

can be enhanced by decreasing the aberration coefficients for the electromagnetic lenses.

In TEM diffraction mode, functioning similar to XRD, selected area electron diffraction (SAED) can be used to perform elemental identification and examine the structure of the surface and adsorbate layers, depending upon the long-range systems (diffraction pattern composed of an array of spots) or overlap of crystallographic locations (coordinated-ring pattern). By using the space proportions and as well as lattice parameter measurements, crystal lattices can be identified.

High-resolution transmission electron microscopy experiments were carried out on a JEOL 3000F field emission gun instrument. This instrument is equipped with an Oxford Instruments energy-dispersive X-ray spectrometer (EDS) with a super atmospheric thin window (SATW) detector that allows chemical analysis of elements down to boron under suitable conditions. In addition, a Gatan imaging filter (GIF) equipped with a 2k 794IF/20 MegaScan CCD camera allows chemical analysis using electron energy loss spectroscopy (EELS).

2.5 Scanning Electron Microscopy (SEM)

Scanning electron microscopy generates surface images of solid particles using electrons as the source. SEM requires an ultra-high vacuum to reduce the collision of electrons and air molecules because electrons are easily scattered. There are many different interactions between the electron and the target surface as soon as the electron reaches the surface. Figure 2.6 illustrates a few possible results of an electron striking the sample surface, which is important in scanning electron

microscopy. It is very important to understand the arrangement of the parts of the SEM system. Figure 2.7 gives a schematic sketch of its parts and its functions during the operation. The electron beam is generated from the electron gun. There are various distinct electron emission sources, but thermionic emission is one of the most common. The kinetic energy of electrons increases as soon as the filament is heated; as a result, the electrons are emitted from the surface. The filament can be built from a variety of different elements, but normally tungsten is most favourable. Lanthanum and cerium hexaboride are also useful, as they produce electron beams with higher brightness than tungsten. Field emission is another alternative for electron emission source used in SEM, which applies a very high electric field to the surface of the tungsten filament. The electrons generated by this method are brighter than the thermionic design.[41]

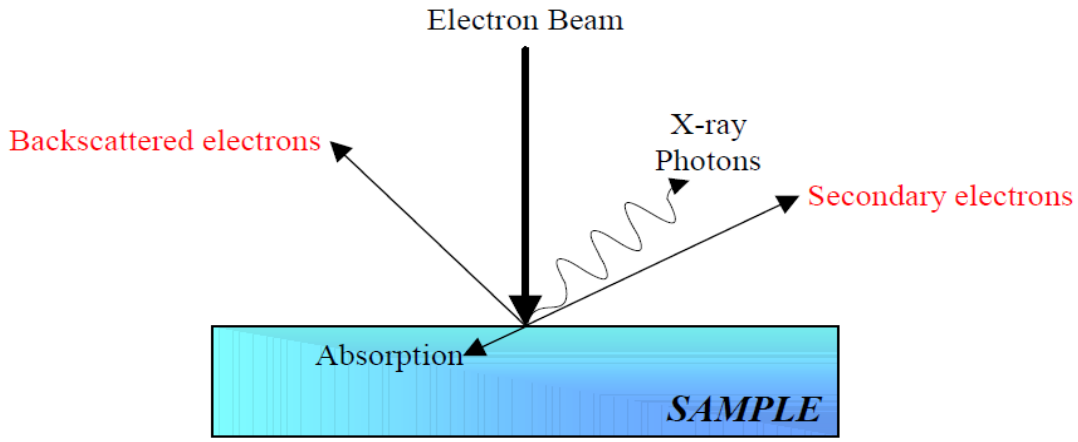

Figure 2.6 A beam electron's interaction with the material. Red text indicates the backscattered and secondary electrons detected by SEM in image generation.

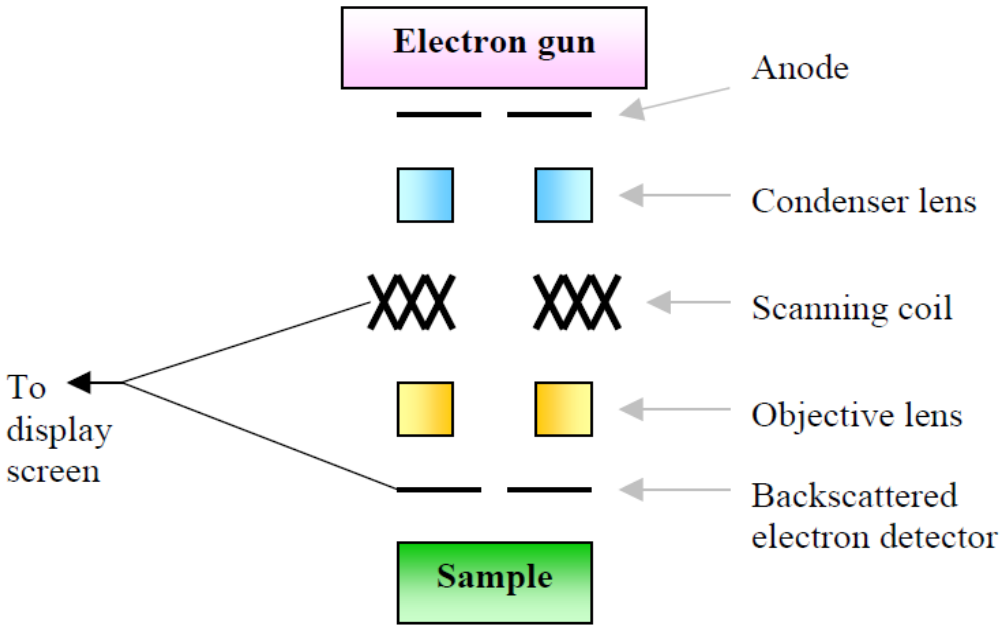

Figure 2.7 A schematic diagram of a scanning electron microscope.

The electrons in the beam leaving the gun are accelerated towards the anode. When the electrons travel, their direction can be altered by an electric or magnetic field with the exception of any parallel field. By altering the current in the coil, the magnetic field strength is affected, and solenoid calibrates the focal length of the lens.[41] Both the condenser and objective lenses are electromagnetic lenses which focus the electron beam. The resulting beam diameter is generally in the range of 20 and 100 Å, much larger than the few Å diameters of an atom, and so the atomic resolution cannot be achieved.[41,42] The scanning coils are responsible for scanning the beam across the sample surface at a constant rate.

The electrons which are deflected by surface collisions are called *'backscattered electrons'* (BSE). The SEM image is produced by collecting BSE, which are then collected by a detector close to the sample, in order to amass a high number of electrons.[43] The electrons are forced onto a phosphor, which emits a flash of light per electron. A photomultiplier tube is used, which enhances

the light signal to produce a better image. A photograph can be seen on the cathode ray tube.

When electrons strike a surface, various processes may occur. As a result of inelastic collisions, a small amount of relatively low-energy secondary electrons is produced, which are emitted from the target surface of the collision. These electrons are representative of a small area and are therefore utilised to create higher-resolution images.

All the probe samples are mounted on a metal stub in the sample chamber of the electron microscope. The *as-synthesised* zeolites (investigated in this work) are nonconducting materials and therefore were coated with platinum to avoid the surface charge. If the surface charge is not conducted to earth, the sample will charge up in a similar manner to a capacitor, and this can affect the scanning beam and therefore the resulting image. The coating process was carried out using a sputter. The ions bombard a platinum foil, which is then deposited on the sample surface. The platinum layer was ≤ 5 nm on all parts of the sample.[42]

The SEM instrument used was a JEOL JSM-840 functioning with an accelerating voltage of 5 kV. This instrument uses field emission for electron beam generation.

2.6 Energy-Dispersive X-ray Spectroscopy (EDXS)

The X-rays produced after the collision of electrons with the probe sample can be utilised in energy-dispersive X-ray spectroscopy, as summarised in Figure 2.8 (abbreviated to EDXS or EDS). The SEM is connected with EDXS to identify the elemental composition of the probe materials. This is carried out by analysing the

X-ray spectrum of the sample and categorising these X-rays with respect to their energy. These X-ray energies are characteristic of each element of the probe material because of the difference in energy levels in the atom which emits particular X-rays of the concerned element or atom.[38]

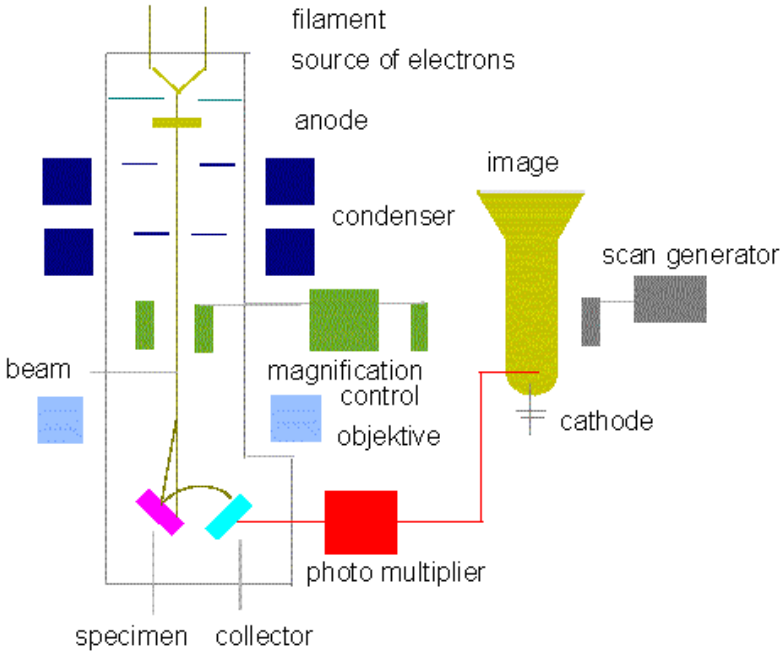

Figure 2.8 A simplified and systematic sketch of EDS.[44]

In EDXS, a solid-state detector is used, which is composed of 'lithium-drifted silicon', written as Si(Li).[41] A preamplifier with liquid nitrogen is used to cool the detector to give a high-low signal-to-noise ratio. The EDXS detector transformed the X-ray energy into a current, corresponding in size to the X-ray energy in the form of photons emitted from the sample where the electron impinges. The pulse, in turn, is converted into a voltage before being enhanced and isolated from the other pulses. Each pulse is plotted according to its energy, and this forms the spectrum of energy versus counts.[38]

2.7 N_2 Adsorption/Desorption

The specific surface area of the solid and porous materials was by adsorbate multilayer adsorption as a function of the relative pressure. BET analysis determined the precise specific surface area of porous materials by nitrogen multilayer adsorption measured as a function of relative pressure using a fully automated analyser. The technique emphasises external area and pore area evaluations to determine the total specific surface area in m^2/g yielding important information in studying the effects of surface porosity and particle size in many applications.

BJH analysis can also be employed to determine pore area and specific pore volume, using adsorption and desorption techniques. This technique characterises pore size distribution independent of the external area because of the particle size of the sample.

This technique was developed from Langmuir's broad and comprehensive analysis on the mechanism of adsorption (1916–1918), with the first measurements made by Stephen Brunauer and Paul Hugh Emmett (1935, 1937) and later improved by the Brunauer Emmett Teller (BET) theory in 1938.[45] BET analysis is used to calculate pore volume and total surface area (internal + external).

BET surface analysis has become a suitable method for determining the surface area of adsorbents, catalysts, nanoparticles and many other finely divided and porous solids.

Equation (12) is used in the linear form to apply to multilayer, physical adsorption,[46,47]

$$\frac{p}{n_a \cdot (p^o - p)} = \frac{1}{n_m \cdot C} + \frac{(C-1)p}{n_m \cdot C\ p^o} \quad (12)$$

where n_a is the quantity adsorbed at the relative pressure p/p^o, n_m is the monolayer capacity and C is the BET constant.

This technique consists of two phases for the evaluation of the surface area from the physisorption isotherm measurement. In the first phase, a BET plot is drawn to evaluate the value of monolayer quantity, n_m, with next phase being the measurement of specific surface area, a (BET), from n_m by accurate examination of average area, σ, engaged by each single molecule in monolayer (i.e., the molecular cross-sectional area). The BET adsorption isotherm is a plot of the volume of the gas adsorbed, n_a, *vs* the relative pressure, p/p^0. The six different stages of the adsorption isotherms exhibited by real surface are presented in Figure 2.9. A type I isotherm is a characteristic of only monolayer adsorption, and there is no interaction between adsorbed molecules. It needs a sharp relative pressure limit to attain the plateau, which is indicative of limited pore size, whilst its horizontal shape is representative of the low surface area. An example of this type of adsorption is water on zeolites.[48] A type II isotherm is a common monolayer-multilayer adsorption on a heterogeneous substrate. The low slope region in the middle of the isotherm indicates the adsorption of the first few multilayers. An example is N_2 adsorption on silica gel. A type III isotherm is relatively rare and corresponds to the situation where adsorbate-adsorbent interaction is weak. The absence of hysteresis indicates adsorption and desorption from a nonporous surface. An example is krypton on polyethylmethacrylate. A type IV isotherm, with a hysteresis loop, indicates the presence of meso- and macropores. The low slope region in the middle of the isotherm is again indicative

of the formation of the first few multilayers. An example is benzene adsorption on the MCM-41 zeolite. A type V isotherm exhibits a hysteresis loop which reflects the mechanism of meso- and macropore filling and also indicates a weak adsorbate-adsorbent interaction similar to that in the type III isotherm at low pressure. A type VI stepped isotherm is associated with layer-by-layer adsorption on a highly uniform surface. Each step of the isotherm shows an adsorbed monolayer. Generally, N_2 adsorption is used for surface area analysis. Additionally, the mechanism of the adsorption and desorption isotherms can provide information on the nature of the material studied.[48,49] There are also four subtypes of isotherms introduced by the IUPAC system as shown in Figure 2.10. The hysteresis loop between the adsorption and desorption strands as shown here on the type H1, H2, H3 and H4 isotherms gives information about pore structure.

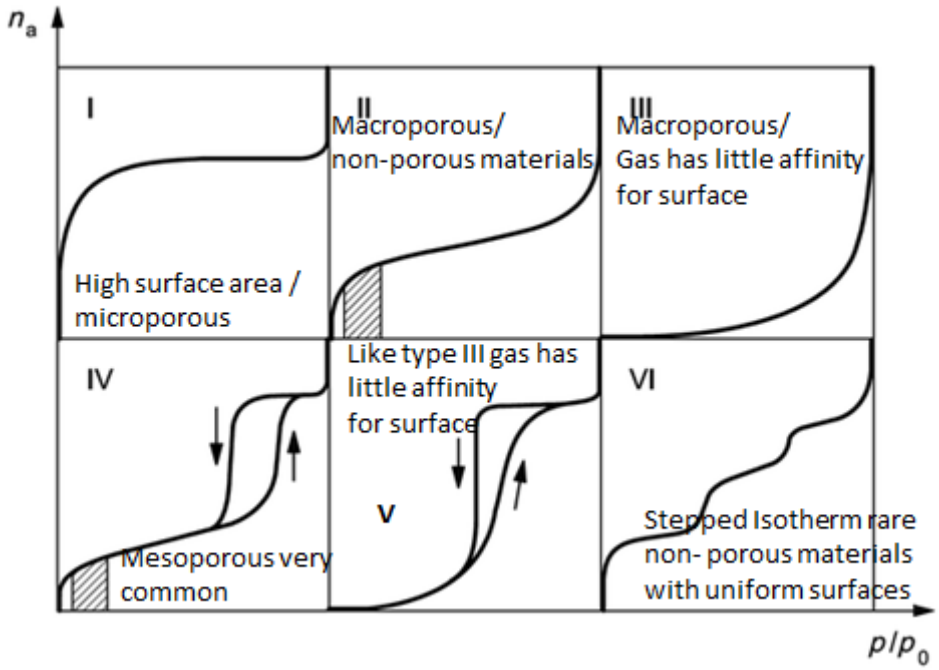

Figure 2.9 IUPAC recommended the six main classifications of adsorption isotherm. Taken and modified from.[50]

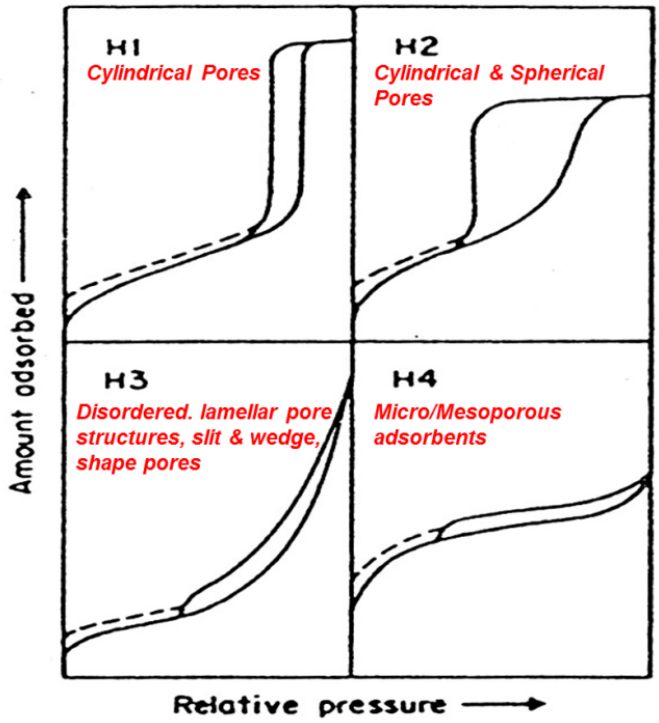

Figure 2.10 Subtypes of N_2 adsorption-desorption isotherms demonstrate pore shape/structure and distribution. H stands for hysteresis. [50]

A simple mechanistic histogram of adsorption and desorption is shown in Figure 2.11. This demonstrates the pore filling and emptying at different stages numbered from 1–8 for mono- and multilayer adsorption. At stage 3, the multilayer of adsorption begins. Hence, the pores are fully filled with gas, and the adsorption reaches maximum, represented by stage 5. At this stage, the desorption process starts. However, when desorption reaches stage 8, there are still some molecules stacked on the wall of the pore, and the multilayer desorption is reduced. This process is repeated several times to achieve a series of increasing and (usually) predetermined fixed pressure points until the relative pressure within the system reaches just below 1 (typically 0.995 for N_2/LN_2 systems). The resulting plot of adsorbed gas against relative pressure produces the adsorption branch of the isotherm. The pressure within the system is then gradually lowered,

again to achieve fixed pressure points, until the relative pressure drops to the desired level, commonly 0.1 for mesoporous materials.[49]

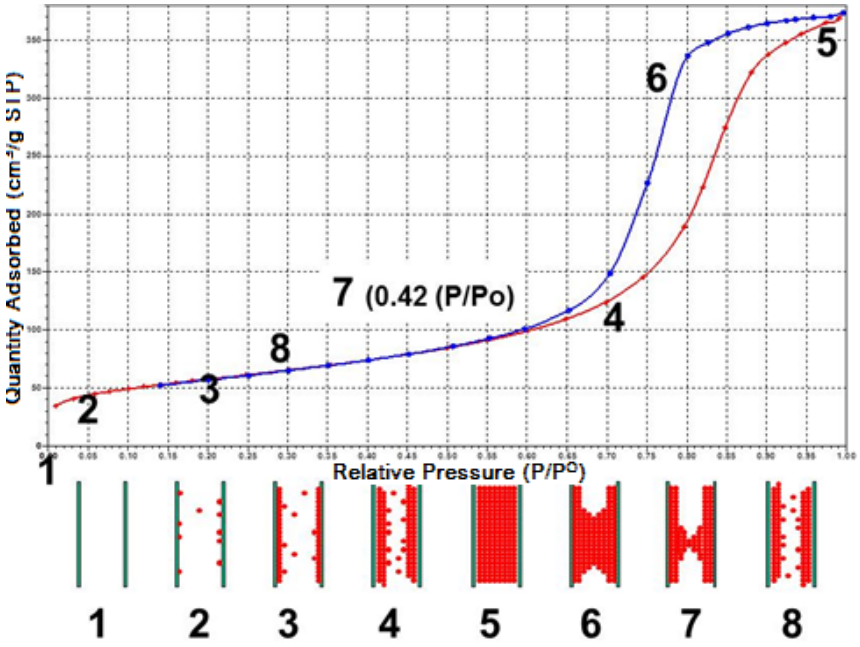

Figure 2.11 Schematic of the gas adsorption process showing pore filling and emptying at various stages of the isotherm. Provided by Micromeritics Analytical Services.

The BET surface analyses were run on a Micromeritics TriStar 3020 instrument. The sample was first degassed at 350°C under vacuum for six hours and then allowed to cool under a flow of dry, clean nitrogen. Subsequently, the sample is placed in the chamber to obtain the resulting data.

2.8 Solid-state Magic Angle Spinning Nuclear Magnetic Rasonance (MAS NMR)

The local environment (ordering) of crystalline solids can be investigated by solid-state magic angle spinning nuclear magnetic resonance (SS MAS NMR) spectroscopy. NMR spectroscopy is normally used to study chemical structure

using simple one-dimensional techniques. Two-dimensional techniques are also used to identify the structure of more complicated molecules. Zeolite frameworks consist of networks of different elements which possess nuclear spin (I) and therefore are NMR active; for example, ^{29}Si (I = 1/2), ^{27}Al (I = 3/2), and ^{23}Na (I = 5/2) are all NMR-active isotopes with natural abundance of 4.7%, 100% and 100%, respectively.[6,51] Solid-state NMR is able to probe many difficult questions of zeolite chemistry. Some of them are given below.[51]

In relation to the Si, Al, arrangement in the zeolite framework (corresponding to catalytic processes), MAS NMR can yield information on these important issues:

- Quantitative analysis of Si and Al environments
- Investigation of isomorphous replacement in a zeolite structure
- Exchangeable cation positions and movement
- Identification of catalytic (proton) acidity
- Framework geometry and dynamics

When an applied magnetic field on a molecule having nuclei are surrounded by electrons, different nuclear interactions can be observed as shown in Figure 2.12.

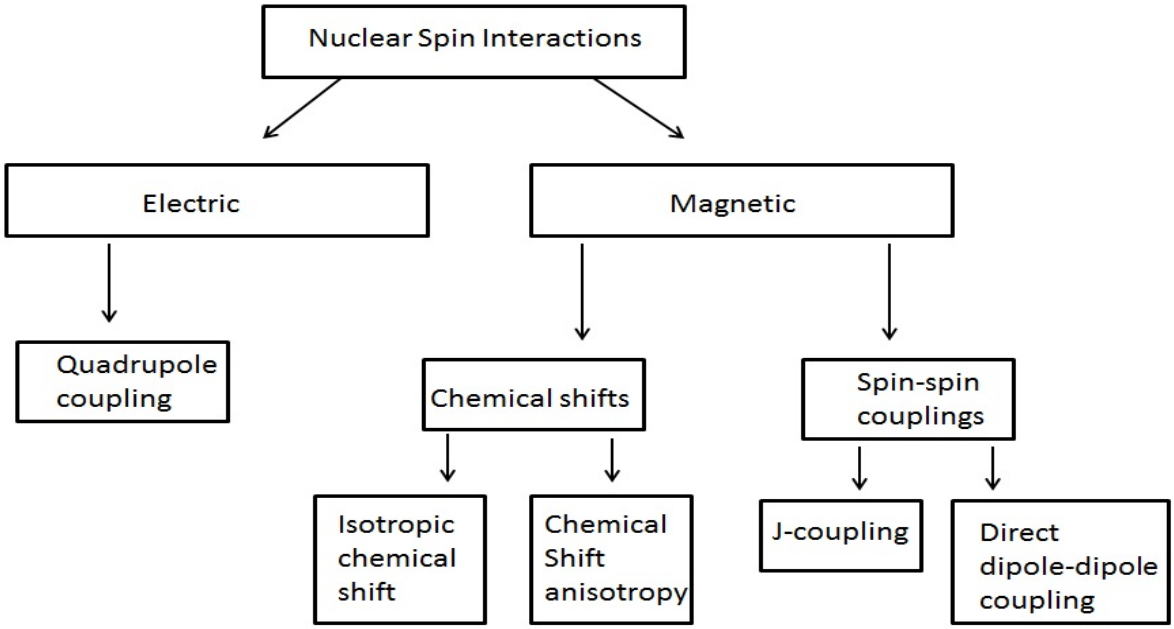

Figure 2.12 Different nuclear interactions occur in NMR analysis.

Nucleus spins interact with the electrons and also with the applied field; there is a direct interaction between each nuclear spin and the applied magnetic field. Such interaction is called a Zeeman interaction. The direct interactions between nuclei are called dipole-dipole interactions. The nuclear spin interacts with the electrons, and they interact with another nuclear spin; this is called J-coupling. The interaction of the nucleus and electrons and of electrons to the magnetic field is called chemical shift. Nuclear spin interacts with the electrons around the nucleus; this is called quadrupole interaction or quadrupole coupling. This is the only interaction which involves the interaction of the nucleus and the electric fields. The quadrupole interaction is called electric interaction, whilst all others are called magnetic interactions.

In the presence of an applied magnetic field, signals are generated in the form of chemical shift. Different magnetic fields collaborate differently from the supplied magnetic field. Chemical shift relates to the frequency of electromagnetic radiation absorbed by a nucleus in a calibrated magnetic field and

will also depend on the local geometry of the nucleus. An induced field is present because of the collision of available electrons surrounding the nucleus, and it resists the supplied magnetic field. Nuclei are shielded by having higher electron density, whilst the relatively low-electron-density nuclei are described as being deshielded. In those systems with separately high electron density, signal broadening occurs because of anisotropic interaction, thus decreasing the NMR spectral resolution. Because of the free movement of molecules in solutions, anisotropic interactions are averaged. However, in solids, the free movement of atoms or molecules is generally negligible, and so the anisotropic interactions must be averaged using a technique called magic angle spinning (MAS). In this process, the solid sample is spun at a magic angle, θ_m, at 54.74^o to the direction of the magnetic field. The anisotropic shielding effect and dipolar interactions equation contain the term ($3\cos^2 \theta - 1$), which will be zero when θ_m is approximately 54.74^o. The zeolite framework follows the Loewenstein rule.[52] It was proposed by Walter Loewenstein in 1954 and states that when two tetrahedra are connected by an oxygen bridge, only one of the tetrahedral centres may be engaged by an Al atom. It means that Al—O—Al connectivity is forbidden, as the Al ion is fourfold coordinated to oxygen and therefore bears a negative charge. This rule is given as an explanation as to why the substitution of Al cannot exceed 50% of the zeolite framework.[53] Silicon can coordinate with a maximum of four Si or Al tetrahedra in the zeolite framework. Because of this, five different local environments can be observed in the ^{29}Si NMR spectrum with 0, 1, 2, 3 and 4 Al linkages, described as Si(0Al), Si(1Al), Si(2Al), Si(3Al) and Si(4Al), respectively.[53,54] An example is given in Figure 2.13 of the solid-state NMR spectrum of a sample (zeolite A) utilising tetramethylammonium hydroxide as an

organic structural directing agent (OSDA), which displays each of the five Si local environments. The chemical shifts cover a range of -84 ppm to -114 ppm, with some overlap of the individual environments. This is illustrated in Table 2.1. If the Si tetrahedron contributes only three corner oxygen atoms, a silanol group OH is generated. Cross polarisation (CP) MAS NMR of ^{29}Si can be used to confirm the presence of silanol species.[54]

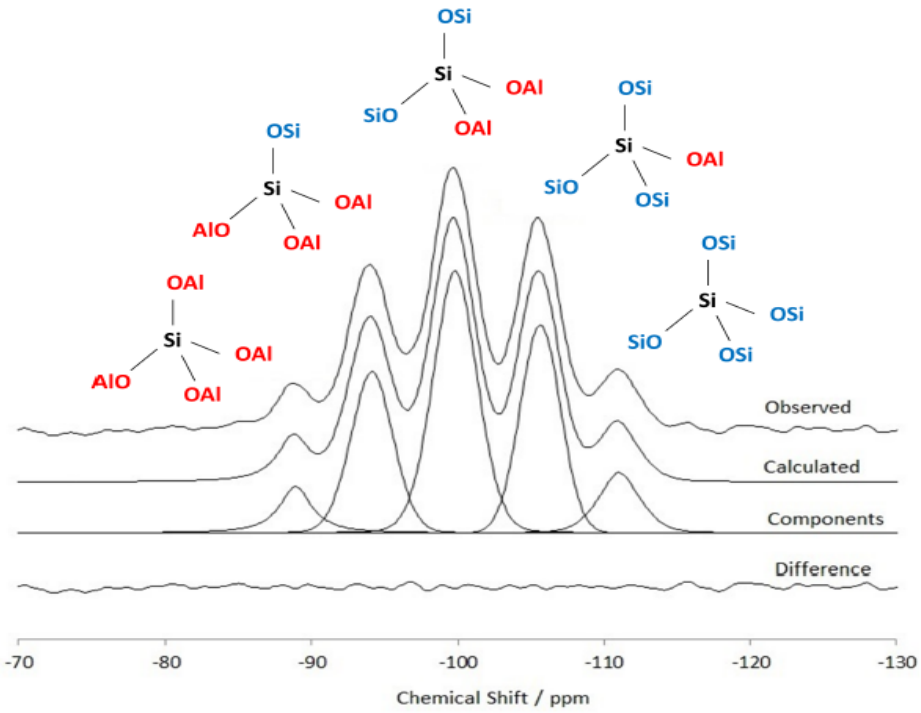

Figure 2.13 Solid-state MAS NMR spectrum of zeolite A. The five typical ^{29}Si chemical shifts: Si4(Al), Si(3Al), Si2(Al), Si(1Al) and Si(0Al). Taken from.[55]

Table 2.1 Ranges of ^{29}Si five different chemical shifts.

Notation	Si(4Al)	Si(3Al)	Si(2Al)	Si(1Al)	Si(0Al)
Coordination	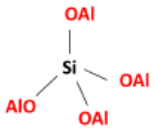				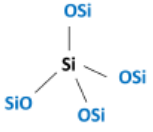
Chemical shift (ppm)	-80.0 to -90.5	-88 to -97	-93 to -102	-97.5 to -107.0	-102.0 to -116.5

^{29}Si and ^{27}Al MAS NMR spectra can also be used to calculate the Si/Al ratio of an as-synthesised zeolite sample with the help of equation (13).[52,53] Aluminium atoms in the zeolite frameworks are always surrounded by four silicon atoms. Hence, the overall contribution of aluminium atoms in the framework structure will be one-fourth the total number of Si—O—Al bonds. The intensity of each silicon signal is directly related to the number of mixed silicon atoms in the environment. Deconvolutions are required for the overlapped silicon signals in the spectrum of a zeolite sample to identify the intensity of a specific Si local environment. After that, the Si/Al ratio can be calculated,

$$\left(\frac{Si}{Al}\right)_{framework} = \frac{\left(\sum_{n=0}^{4} I_{Si(nAl)}\right)}{\left(\sum_{n=0}^{4} 0.25 n I_{Si(nAl)}\right)} \qquad (13)$$

where I represents the intensity of a particular ^{29}Si resonance, and n is the number of coordinated Al atoms for that structural unit.

As Al—O—Al linkage is forbidden in zeolite frameworks as described by the Loewenstein rule, if all Al are tetrahedra coordinated, then there is only one Al local environment observed in ^{27}Al SS MAS NMR. The chemical shift for [Al(OSi)$_4$] units occurs in a single vibration in the chemical shift range of 50–70 ppm. However, there are two extra Al environments that can also be observed, i.e., the penta- and octahedral-coordinated frameworks. The octahedral-

coordinated Al usually occupies the extra framework sites as a result of calcination, steaming or acid leaching and has a chemical shift of around 0–1 ppm, whilst the pentagonal framework has chemical shifts of around 29–30 ppm.[53,56]

All the NMR experiments in this work were performed by the EPSRC UK National Solid-State MAS NMR Service at Durham. Solid-state ^{29}Si and ^{27}Al spectra were recorded at 79.44 MHz using a Varian VNMRS spectrometer and a 6 mm (rotor o.d.) magic-angle spinning probe. They were obtained using direct excitation with a 5 μs 90° pulse and a 10.0 s recycle delay at ambient probe temperature (~25 °C) and at a sample spin rate of 6,000 Hz. Between 200 and 500 repetitions were accumulated. Spectral referencing was with respect to an external sample of neat tetramethylsilane (carried out by setting the high-frequency signal from tetrakis (trimethylsilyl) silane to -9.9 ppm).

2.9 Dynamic Light Scattering (DLS)

DLS is also known as photon correlation spectroscopy (PCS). This is one of the most famous techniques for the determination of the size distribution of nanoparticles in suspension. It is widely used in chemistry, biochemistry, physics and material sciences.[20,57] A beam of monochromatic light, e.g., from a laser, passes through the solution containing particles moving in Brownian motion causing a Doppler shift, where the wavelength of the incoming light is changed after the collision with the particle using an autocorrelator. The nature of the Doppler shift helps describe the particle size distribution of the sample in solution. It is also possible with the help of DLS to measure the diffusion coefficient and the autocorrelation function. Furthermore, this method has the potential to perform an accurate analysis of various other physical parameters, e.g.,

translational diffusion constant, molecular weight, radius of gyration etc. However, it is very difficult to analyse amorphous materials[57,58].

Generally, when a monochromatic light from a laser impinges on nanoparticles in the solution, it is then diffracted in all directions. So the particles give a second source of diffracted light. The intensity of the emitted light is measured on a photomultiplier detector. The photomultiplier is generally located at 90^{o} to the light source and to the diffracted light. Two important collimator lenses were set up to focus the light onto the cell with the sample and before the photomultiplier[59] as shown in Figure 2.14.

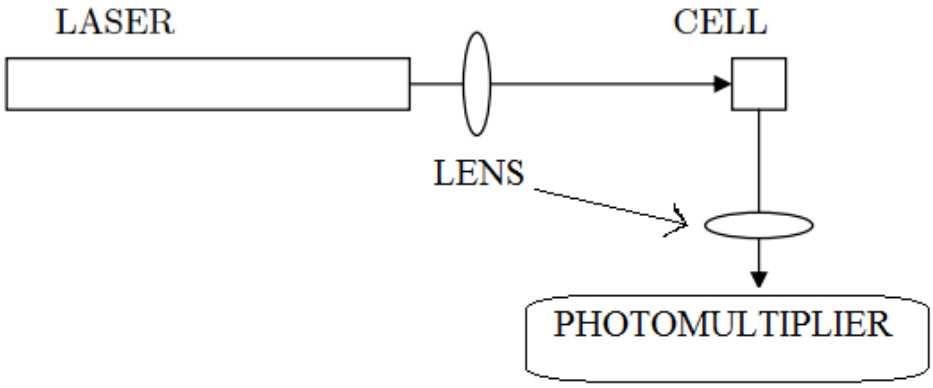

Figure 2.14 A simplified sketch of the dynamic light scattering instrument.

The oscillating intensity data consists of a huge spectrum of Doppler-shifted frequencies, which are directly recorded using a digital correlator. The correlator plays an important role in DLS for comparing the intensities of two signals in a short time τ (nano to microseconds), and the correlating function is used to calculate the similarities of the signals. The autocorrelation function in the form of an electric field is given by the established Siegart equation (14).[59]

$$G_1(t) = \lim_{t\to\infty} \frac{1}{T} \int_{-T}^{T} I(t)I(t+\tau)dt \qquad (14)$$

G_1 is the autocorrelation function at a specific wave at time *t,* and I is the intensity.

Meanwhile, the Siegart equation is used for second-order intensity correlation function and is defined by the following mathematical expression:

$$G_2(\tau) = 1 + \beta[G_1(\tau))]^2 \quad (15)$$

G_2 is the intensity autocorrelation function, and β is used as an experimental factor related to the angle of scattering in the DLS system. The most important function of the intensity autocorrelation function is the particle size observation.[59]

The Malvern Zetasizer Nano ZS instrument was used for measurements of particles from 0.6 nm to 6 microns. Accurate measurements of the zeta potential of the probe materials were made in diluted aqueous solution.

2.10 References

[1] A. Cichocki, *Microporous Mesoporous Mater.* **1999**, *29*, 369–382.

[2] H. Robson, K. P. Lillerud, in *Verif. Synth. Zeolitic Mater.*, Elsevier, **2001**, p. 265.

[3] Y. Yue, H. Liu, P. Yuan, C. Yu, X. Bao, *Sci. Rep.* **2015**, *5*, 9270.

[4] J. Cejka, H. V. Bekkum, A. Corma, F. Schueth, *Introduction to Zeolite Molecular Sieves*, Elsevier, **2007**.

[5] G. Kuhl, in *Verif. Synth. Zeolitic Mater.*, Elsevier Science B. V., **2001**, pp. 19–23.

[6] A. Dyer, *An Introduction to Zeolite Molecular Sieves*, John Wiley & Sons Australia, Limited, **1988**.

[7] C. N. R. Rao, K. Biswas, *Essentials of Inorganic Materials Synthesis*, Wiley, **2015**.

[8] R. M. Mohamed, H. M. Aly, M. F. El-Shahat, I. A. Ibrahim, *Microporous Mesoporous Mater.* **2005**, *79*, 7–12.

[9] R. M. Barrer, *Hydrothermal Chemistry of Zeolites*, Academic Press, London, **1982**.

[10] S. Mintova, V. Valtchev, *Microporous Mesoporous Mater.* **2002**, *55*, 171–179.

[11] C. S. Gittleman, A. T. Bell, C. J. Radke, *Catal. Letters* **1996**, *38*, 1–9.

[12] R. Szostak, Molecular Sieves - Principles of Synthesis and Rosemarie Szostak Springer, Thomson Science, **1989**.

[13] R. Gangele, P. Pawaiya, Y. Pandy, *Int. J. Sci. Res.* **2014**, 78–80.

[14] C. J. J. Den Ouden, R. W. Thompson, *Ind. Eng. Chem. Res.* **1992**, *31*, 369–373.

[15] J. D. Epping, B. F. Chmelka, *Curr. Opin. Colloid Interface Sci.* **2006**, *11*, 81–117.

[16] P.-P. E. A. De Moor, T. P. M. Beelen, R. A. Van Santen, *J. Appl. Crystallogr.* **1997**, *30*, 675–679.

[17] S. L. Burkett, M. E. Davis, *J. Phys. Chem.* **1994**, *98*, 4647–4653.

[18] C. S. Tsay, A. S. T. Chiang, *Microporous Mesoporous Mater.* **1998**, *26*, 89–99.

[19] H. Chen, C. Song, W. Yang, *Microporous Mesoporous Mater.* **2007**, *102*, 249–257.

[20] T. A. M. Twomey, M. Mackay, H. P. C. E. Kuipers, R. W. Thompson, *Zeolites* **1994**, *14*, 162–168.

[21] Z. Guo, A. G. Jones, N. Li, *Chem. Eng. Sci.* **2006**, *61*, 1617–1626.

[22] Y. Vafaeian, M. Haghighi, S. Aghamohammadi, *Energy Convers. Manag.* **2013**, *76*, 1093–1103.

[23] S. Askari, S. Miar Alipour, R. Halladj, M. H. Davood Abadi Farahani, *J. Porous Mater.* **2013**, *20*, 285–302.

[24] V. Krishnakumar, "Crystal Growth_Introduction," can be found under http://www.slideshare.net/krishslide/crystal-growth-39462667, **2014**.

[25] S. V. Verdaguer, "Synthesis in solution," can be found under http://www.icmm.csic.es/csc/?page_id=172, **n.d.**

[26] S. Bosnar, B. Subotic, *Croat. Chem. Acta* **2002**, *75*, 663–681.

[27] P. Cubillas, M. W. Anderson, in *Zeolites Catal. Synth. React. Appl. Vol 1* (Eds.: A. Corma, S. Zones), Wiley-VCH, **2010**, pp. 1–55.

[28] G. P. Thomson, *Proc. Phys. Soc.* **1948**, *61*, 403–416.

[29] L. V. Azaroff, *Introduction to Solids*, McGraw-Hill Book Company. Inc, NY, **1960**.

[30] S. Duckett, B. Gilbert, M. Cockett, *Foundations of Molecular Structure Determination*, Oxford University Press, **2015**.

[31] C. W. Eley, S. C. E. Tsang, The Rational Design of Photocatalytic Semiconductor Nanoparticles, University of Oxford, **2014**.

[32] T. Jia, Photocatalytic Hydrogen Production over Layered Materials, University of Oxford, **2014**.

[33] C. Suryanarayana, M. G. Norton, *X-Ray Diffraction: A Practical Approach*, Springer Science & Business Media, NY, **1998**.

[34] A. W. Chester, E. G. Derouane, *Zeolite Characterization and Catalysis*, Springer Science & Business Media, NY, **2009**.

[35] J. Grebenkemper, "Powder X-ray Diffraction - Chemwiki," can be found under http://chemwiki.ucdavis.edu/Analytical_Chemistry/Instrumental_Analysis/Diffraction/Powder_X-ray_Diffraction#Bragg's_Law, **n.d.**

[36] B. David, K. Wayne, D, *Microstructural Characterization of Materials*, John Wiley & Sons, **1999**.

[37] R. F. Egerton, *Physical Principles of Electron Microscopy*, Springer US, Boston, MA, **2005**.

[38] W. Sigle, *Annu. Rev. Mater. Res* **2005**, *35*, 239–314.

[39] Y. Liao, *Objective Aperture in TEM*, GlobalSino, **2006**.

[40] S. G. Lipson, H. Lipson, D. S. Tannhauser, *Optical Physics*, Cambridge University Press, Cambridge, UK, **1998**.

[41] I. M. Watt, The Principles and Practice of Electron Microscopy | Materials Science | Cambridge University Press, Cambridge University Press, **1997**.

[42] S. Amelinckx, V. D. Dyck, J. V. Landuyt, G. Van Tendeloo, *Electron Microscopy: Principles and Fundamentals*, VCH, Weinheim, **1997**.

[43] S. Swapp, "Scanning Electron Microscopy (SEM)," can be found under http://serc.carleton.edu/research_education/geochemsheets/techniques/SEM.html, **n.d.**

[44] M. V Martinez, "A Basic Understanding of Scanning Electron Microscopy (SEM) and Energy Dispersive X-ray Detection (EDX)," can be found under http://www.forensicevidence.net/iama/sem-edxtheory.html, **n.d.**

[45] S. Brunauer, P. H. Emmett, E. Teller, *J. Am. Chem. Soc.* **1938**, *60*, 309–319.

[46] K. S. W. Sing, *Adv. Colloid Interface Sci.* **1998**, *76–77*, 3–11.

[47] K. S. W. Sing, *Pure Appl. Chem.* **1985**, *57*, 603–619.

[48] Xamplified, "Adsorption Isotherm and its Types | Chemistry Learning," can be found under http://www.chemistrylearning.com/adsorption-isotherm/, **2009**.

[49] S. Naumov, Hysteresis Phenomena in Mesoporous Materials, Von der Fakultät für Physik und Geowissenschaften der Universität Leipzig genehmigte, **2009**.

[50] A. Connelly, "A brief guide to BET: Earth and Environment," can be found under http://www.see.leeds.ac.uk/business-and-consultation/facilities/techniques-available/bet/a-brief-guide-to-bet/, **2015**.

[51] S. Li, L. Zhou, A. Zheng, F. Deng, *Chinese J. Catal.* **2015**, *36*, 789–796.

[52] M. J. Duer, Introduction to Solid-State NMR Spectroscopy, Blackwell Science, **2004**.

[53] J. Klinowski, *Annu. Rev. Mater. Sci.* **1988**, *18*, 189–218.

[54] M. Hunger, J. Karger, H. Pfeifer, J. Caro, B. Zibrowius, M. Bulow, R. Mostowicz, *J. Chem. Soc., Faraday Trans. I* **1987**, *83*, 3459–3468.

[55] K. M. Leung, Zeolite Frameworks with Beta Cages, Department of Chemistry, University of Oxford, **2015**.

[56] W. Lutz, *Adv. Mater. Sci. Eng.* **2014**, *2014*, DOI 10.1155/2014/724248.

[57] M. Sartor, *Chem. - A Eur. J.* **2011**, *17*, 11230–11236.

[58] R. Pecora, *Dynamic Light Scattering*, Springer US, Boston, MA, **1985**.

[59] B. Nail, "Dynamic Light Scattering - Chemwiki," can be found under http://chemwiki.ucdavis.edu/Analytical_Chemistry/Instrumental_Analysis/Microscopy/Dynamic_Light_Scattering, **n.d.**

Chapter 3

3. Synthesis of MOR Zeolite and ZnS Nanoclusters

Highly siliceous crystalline mordenite zeolite was synthesised without an organic template (OSDA). Ludox HS30 was used as the silicon precursor, whilst sodium aluminate was utilised as the Al source. The ion-exchange method was performed in two steps to create zinc sulfide (ZnS) nanoclusters in the pore network of the MOR framework. Zinc nitrate $Zn(NO_3)_2 \cdot 6H_2O$ was used as a source of Zn^{2+} ions, and sodium sulfide was utilised as a source of S^{2-} ions in this ion exchange. The as-synthesised mordenite (NaMOR) zeolite and exchanged samples (first ZnMOR, and then ZnSMOR) were characterised using powder X-ray diffraction (XRD), solid-state nuclear magnetic resonance spectroscopy (SS MAS NMR), scanning electronic microscopy (SEM), transmission electron microscopy (TEM), N_2 adsorption and desorption BET surface analysis and energy-dispersive X-ray spectroscopy (EDXS). A decrease in the unit cell parameter was observed from NaMOR to ZnSMOR. BET N_2 adsorption and desorption analysis showed a significant drop in internal pore areas in the ZnSMOR sample. There is a remarkable change in the adsorption isotherm of the ZnSMOR sample as compared to that of ZnMOR. This change can be explained by the presence of zinc ions (Zn^{2+}) after ion exchange and hints at the presence of zinc sulfide nanoclusters. EDXS confirmed the presence of Zn and S in the final exchanged mordenite samples. TEM provided evidence of ZnS accumulated to the surface and adhered to the inner surface of the pore channels.

3.1 Experimental

3.1.1 Chemicals, Reagents Used and Synthesis Procedure

Sodium hydroxide (NaOH), analytical reagent grade (99.4% Fisher Scientific UK), was used as alkali to make a basic medium for the solution and to provide a metal cation. Sodium aluminate ($AlNaO_2$) (ca 8% H_2O 99.9% Al), ordered from ABCR GmbH and Co, was used as the aluminium source. Ludox HS-30 (30% colloidal silica with pH 9.8), ordered from Sigma Aldrich, was used as the silicon source. Doubly deionised water (made in the lab) was used as solvent. $Zn(NO_3)_2 \cdot 6H_2O$ (98% extra pure, ordered from Sigma-Aldrich) was used as the Zn source, and Na_2S (98% pure, ordered from Sigma-Aldrich) was the sulfide source for the ZnS formation.

3.1.2 Synthesis of Mordenite Zeolite

Initially, some test experiments were performed with two different silica sources to choose the best silica source for zeolite synthesis using the recipe given on the IZA website.[1] Fumed silica and Ludox HS30 with similar molar composition as shown in Table 3.1 were tested under different experimental conditions.

Table 3.1 Molar ratio of mordenite zeolite.

Mordenite	**Na_2O**	**Al_2O_3**	**SiO_2**	**H_2O**
Molar Ratio	6	1	20	780

The synthesis was carried out without the addition of any template/organic structure-directing agent (OSDA). All the synthesis conditions used are listed in Table 3.2. Sodium hydroxide (NaOH) was dissolved in distilled water (10 ml).

Sodium aluminate ($AlNaO_2$) was then added to the NaOH solution and stirred until a transparent solution was formed. Ludox HS-30/fumed silica was added to the solution which was kept stirred for 24 hours. Hence, a uniform gel was formed. The pH of the gel was tested with pH paper and kept >10 before transferring to an autoclave (bomb). The gel was transferred to a Teflon liner and sealed in a stainless-steel autoclave and hydrothermally treated. The product was then removed, thoroughly washed with deionised water and dried overnight at 110^{o}C. The same procedure was repeated for all *as-synthesised* mordenite samples. Calcination was not undertaken because all the experiments were performed without organic structure-directing agents (OSDA). For the synthesis of mordenite zeolite, 50 ml, 100 ml and 250 ml Parr reactors (autoclaves) were used.

Table 3.2 The *as-synthesised* mordenite zeolite and experimental conditions used.

Experiments with sample codes	Experimental conditions				Relative crystallinity (%)
	Aging with Stirring time (hrs)	Time (hrs)	Temperature °C	pH tested with pH paper	
MOR01	24	24	170	>10	Not calculated
MOR02	24	36	170	>10	Not calculated
MOR03	24	48	170	>10	Not calculated
MOR04	24	72	170	>10	Not calculated
MOR05	24	96	170	>10	7
MOR06	24	120	170	>10	48
MOR07	24	144	170	>10	63
MOR08	24	168	170	>10	130

3.1.3 Ion-Exchange Method

The semiconductor nanoclusters were synthesised in aqueous solution using the method previously published by Iacomi[2] with a few modifications. The purest and highly crystalline *as-synthesised* sample was used for the syntheses of ZnS semiconductor nanoclusters as a guest material in the pores. A fivefold excess of zinc nitrate ($Zn(NO_3)_2$) relative to the number of sodium ions was dissolved in 50 ml of water and stirred with a known mass of *as-synthesised* mordenite zeolite for 24 hours. The mixture was then filtered and washed with deionised water to remove the excess $Zn(NO_3)_2$.

The powder was then dried at 110°C. This process was repeated three times. The Zn^{2+} ion-exchanged mordenite (Zn-MOR) zeolite was then treated with Na_2S to synthesise the ZnS nanoclusters. The molar ratio of Na_2S to Na^+ in the *as-synthesised* mordenite zeolite was 5 to maximise cation exchange. A schematic two-step possible chemical exchange general reactions are given below:

$$\text{STEP 1} \quad NaMOR + Zn(NO_3)_2 \longrightarrow ZnMOR + Na^+$$

$$\text{STEP 2} \quad ZnMOR + Na_2S \longrightarrow ZnSMOR + 2Na^+$$

The mixture was stirred for 24 hours and repeated three times. The final product ZnS within the pores of *as-synthesised* mordenite zeolite was dried in the oven overnight and then characterised on the following analytical techniques.

3.2 Results and Discussion

3.2.1 Powder X-ray Diffraction Patterns of Mordenite Zeolite

The powder pattern of *as-synthesised* mordenite zeolite in a series of reaction times, e.g., 24, 48, 72, 96 and 120 hours, is shown in Figure 3.1. All these syntheses were carried out with the use of a fumed silica precursor. When the gel was treated hydrothermally for 24 hours, an amorphous phase was formed. It was observed that when the crystallisation period increased, the crystallinity also increased[3]. When the aluminosilicate gel was hydrothermally treated for 72 hours, a crystalline phase appeared in addition to the amorphous phase, with the peaks being consistent with the gismondine (GIS) zeolite structure compared with the reference pattern of GIS[1] as shown in Figure 3.1. When the crystallisation time reached 96 hours, a mixture of MOR, GIS and an amorphous phase was observed. The sample prepared from the gel mixture was treated for 120 hours; a

highly crystalline mordenite phase and a few impurity peaks were observed in the pattern near 36^{O}–38^{O}. The XRD powder patterns were designated by the corresponding zeolite codes MOR and GIS. A phase transition occurred among the amorphous and mixed phases of zeolite gismondine (GIS) and mordenite. It was observed that there was a sudden phase transition occurring from GIS to MOR after 96 hours for 120 hours.

The second series of experiments was performed by using Ludox HS30 (colloidal silicon source) at different crystallisation periods from 24 to 168 hours. A clean amorphous phase has been observed from the X-ray diffraction powder pattern of 24 hours, as shown in Figure 3.2. When treated at 36 hours or above (up to 168 hours), the MOR crystalline phase appeared and was identified from X-ray diffraction powder patterns using literature MOR powder patterns.[1,2,4–6] The crystallinity of all the samples was calculated using the equation (16) reported by Hurem et al.[3] The powder pattern of the 36-hour sample showed mixed amorphous and crystalline phases. Similarly, the powder patterns of 48, 72 and 96 hours showed a mixture of amorphous and mordenite zeolite phases, where crystalline phase is increasingly dominant in the amorphous phase as the crystallisation time increases. In the X-ray diffraction powder pattern of 168 hours sample, a pure-phase mordenite zeolite free of amorphous phases was observed.

Using equation (16), relative crystallinity was calculated by comparing the sum of the integral of high-intensity peaks of these samples with those of the reference sample of the pure single crystal of aluminium oxide showing a remarkable increase in relative crystallinity by increasing crystallisation time. The obtained crystallinity values of all the *as-synthesised* samples are illustrated in Figure 3.3.

$$\text{Relative Cry} = \frac{\sum \text{I}_{(\text{high crystalline peaks})}}{\sum \text{I}_{(\text{Reference})}} \times 100\% \qquad (16)$$

I is the integral intensity of the highest and the most prominent XRD peaks.

An extra peak indicated by (*) shown in Figure 3.2 was observed in all *as-synthesised* mordenite powder patterns. It could not in part be identified from the powder patterns found by the International Zeolite Association (IZA). It was concluded that the use of a colloidal silicon source has great influence on the syntheses of mordenite zeolite.[7] Sample (MOR08) in Table 3.2 synthesised at 170^{O}C for 168 hours' crystallisation time was reproduced and was utilised further for the cation-exchange process, i.e., the growth of ZnS in the pores of MOR frameworks. Figure 3.4 shows the powder patterns of two exchanged mordenite zeolite samples, ZnMOR and ZnSMOR, compared to the *as-synthesised* sample NaMOR.

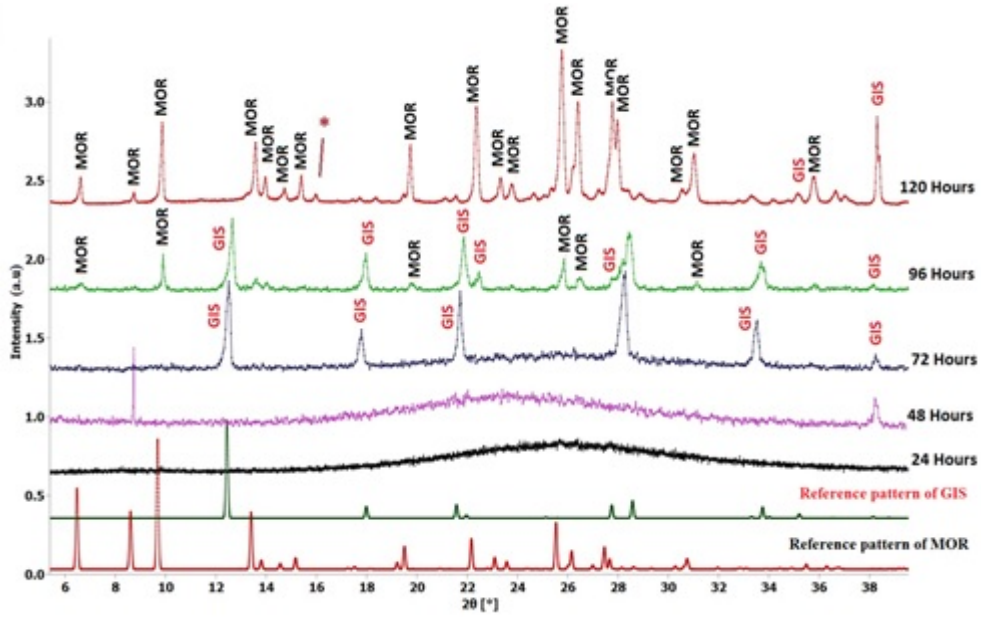

Figure 3.1 The X-ray diffraction patterns of the as-synthesised MOR using a fumed silica source as a function of increasing crystallisation time.

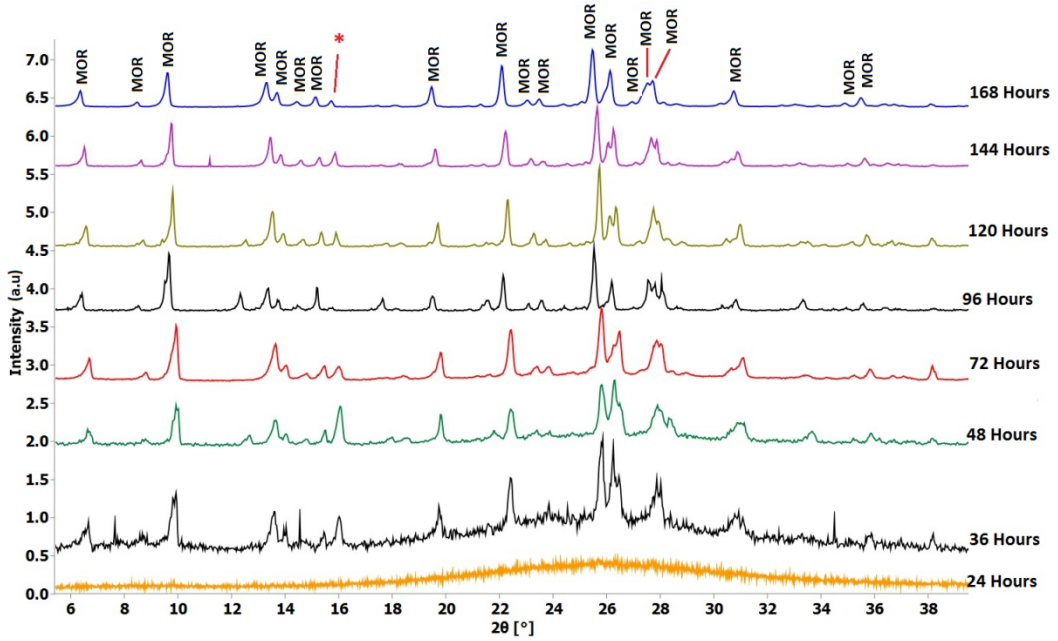

Figure 3.2 The X-ray diffraction patterns of the as-synthesised MOR using Ludox HS30 as the silica source as a function of increasing crystallisation time.

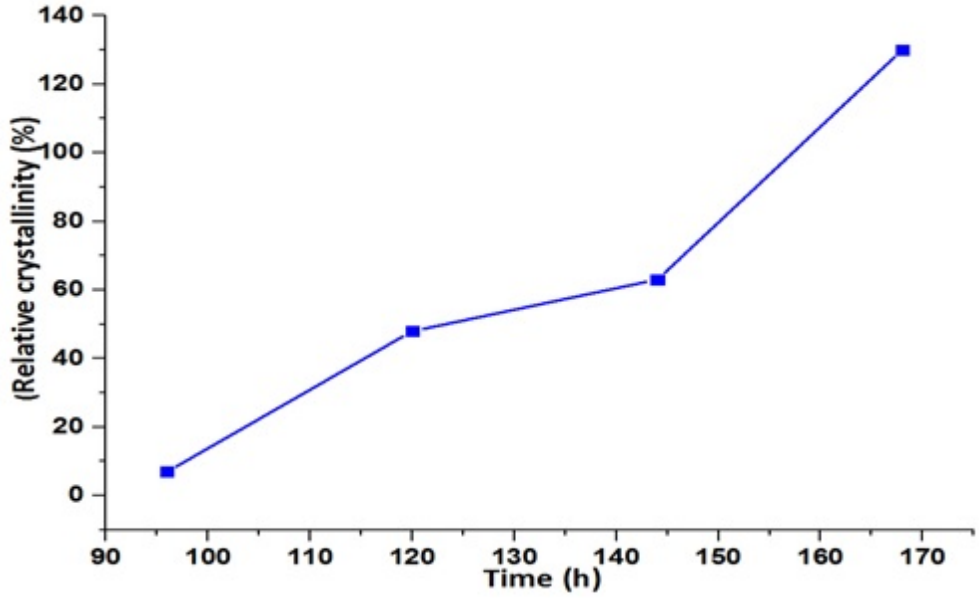

Figure 3.3 Crystallinity of MOR zeolite as a function of crystallisation time calculated from the peaks' integrals.

Figure 3.4 also includes the reference MOR pattern taken from the IZA website.[1] There were no extra peaks for Zn-MOR and ZnS-MOR, compared to Na-MOR. However, it is very difficult for X-ray diffraction to examine the semiconductor nanoclusters in the confined spaces of mordenite because of the

overlapping of signals in the patterns.[6,8] But still there were some signs with the help of which it may be identified; a small shift of individual peaks to higher 2theta (2θ) were observed from Na-MOR to ZnS-MOR. This small shift between individual patterns corresponds to the change in unit cell parameters.[2,6] The unit cell parameters were calculated for all samples (using a software named unit cell refinement programme) and are listed in Table 3.3. It was noticed that after each ion-exchange step, the unit cell volume decreased. This reveals the presence of ZnS nanoclusters inside the MOR framework. Additionally, the MOR framework crystallinity remained after the ZnS nanocluster formation.[2,6]

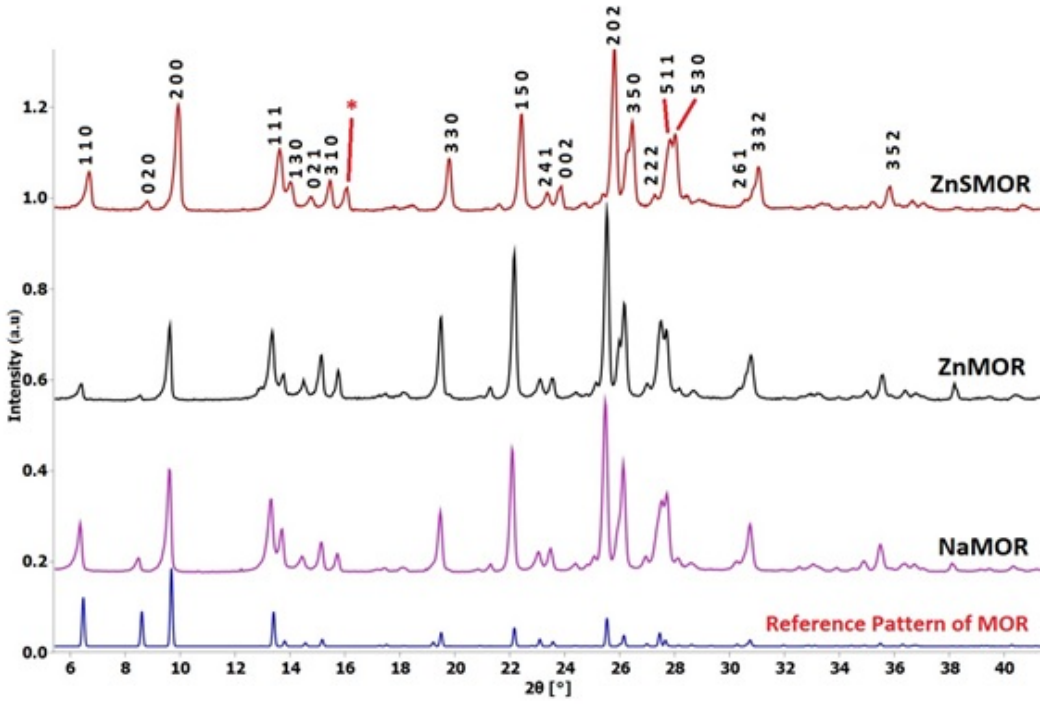

Figure 3.4 X-ray powder diffraction of the NaMOR and mordenite exchanged with Zn^{2+} and ZnS nanoclusters represented as ZnMOR and ZnSMOR, respectively. The bottom curve is the reference pattern of mordenite.

Table 3.3 Unit cell parameter and volume of as-synthesised MOR zeolite, ZnS and Na^+ ion-exchanged MOR.

Sample Code	a (Å)	b (Å)	c (Å)	v $(Å)^3$
Na- MOR	18.308±0.003	20.106±0.003	7.622±0.001	2805.85±0.51
Zn- MOR	18.241±0.003	19.953±0.003	7.596±0.001	2765.88±0.51
ZnS- MOR	17.872±0.003	19.780±0.003	7.531±0.001	2663.76±0.47

3.2.2 Scanning Electron Microscopy (SEM)

All the *as-synthesised* mordenite samples were characterised by SEM to identify morphology and particle size. Some of the MOR samples were reproduced by using 50 ml, 100 ml and 250 ml polytetrafluoroethylene (PTFE) liners in a Parr reactor for 168 hours of crystallisation time at autogenous pressure and were characterised using SEM. Elongated boat-shaped crystals of 50–60 μm and long, spherical crystals of 13–15 μm diameter were observed using 50 ml and 100 ml Teflon liner containers in the Parr reactor, respectively, as shown in Figure 3.5 (a) and (b). Using a 250 ml Teflon liner container in the Parr reactor with the same experimental conditions used for the 50 ml and 100 ml Teflon liner containers, a round structure made of aggregated rods of size 40–45 μm was observed as shown in Figure 3.5 (c). Table 3.4 illustrates the three different Teflon liner volumes used with the same experimental conditions producing different particle shapes corresponding to those in Figure 3.5. Different morphologies have been observed at different experimental conditions, thus showing that the morphology of the mordenite zeolites depends on the synthesis conditions.[9] Some of the morphologies of mordenite presented here also match with those already reported

in the literature.[9–11] It is also observed that at different synthesis stages, different morphologies and sizes were observed as can be seen in Figure 3.6.

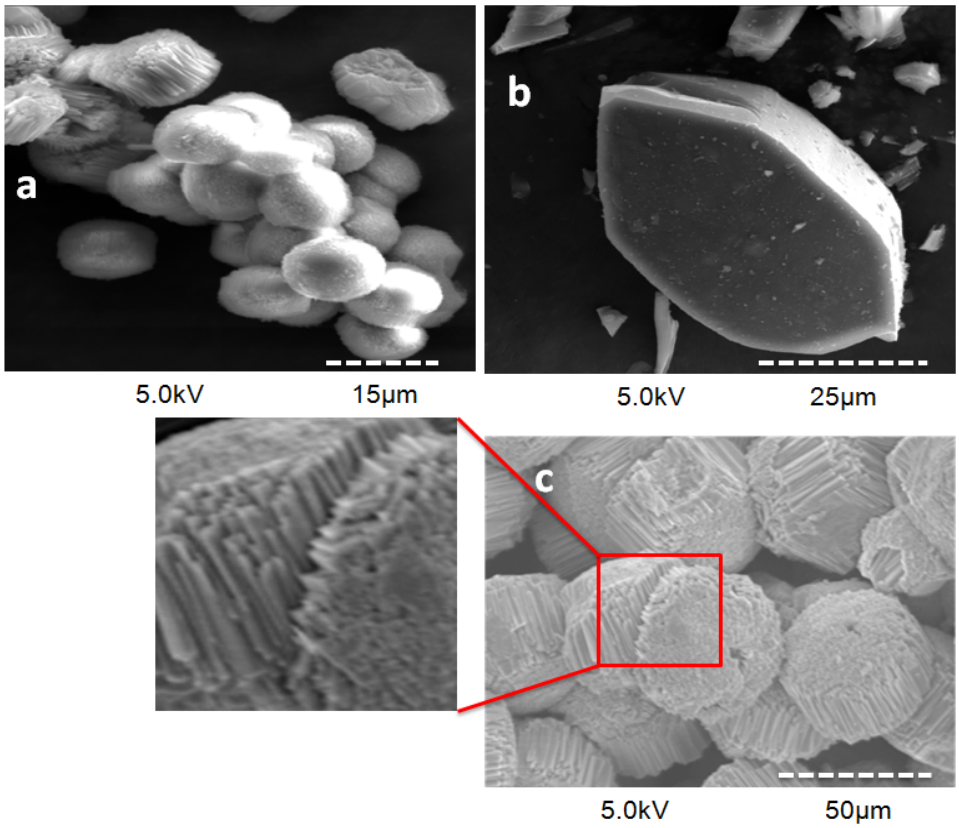

Figure 3.5 Different PTFE liners produce different morphologies of mordenite zeolite using otherwise the same experimental conditions. (a) 250 ml, (b) 100 ml and (c) 50 ml PTFE liners were used in the Parr reactor.

It does not appear that the morphology is affected by the exchange with Zn and S. Although there were some crushed particles observed as shown in Figure 3.7, most of them retained their original size and morphology.

Table 3.4 Different sizes produced by using different PTFE liner volumes in the Parr reactor (autoclave).

Samples	Experimental Conditions			PTFE liner vol (ml)	Particle size (µm)
	Temp °C	Time (Hrs)	Mixing time (Hrs)		
NaMOR (a)	170	168	24	50	50±10
NaMOR (b)	170	168	24	100	13±5
NaMOR (c)	170	168	24	250	40±5

Table 3.5 Observed relative crystallinity and crystal sizes of the as-synthesised mordenite zeolite powder.

Sample code	Crystallisation time (Hrs)	Crystal size (µm)	Relative degree of crystallinity (%)
MOR01	24	-	Not Calculated
MOR02	36	-	Not Calculated
MOR03	48	-	Not Calculated
MOR04	72	-	Not Calculated
MOR05	96	10±10	7
MOR06	120	20±10	48
MOR07	144	30±10	63
MOR08	168	40±10	130

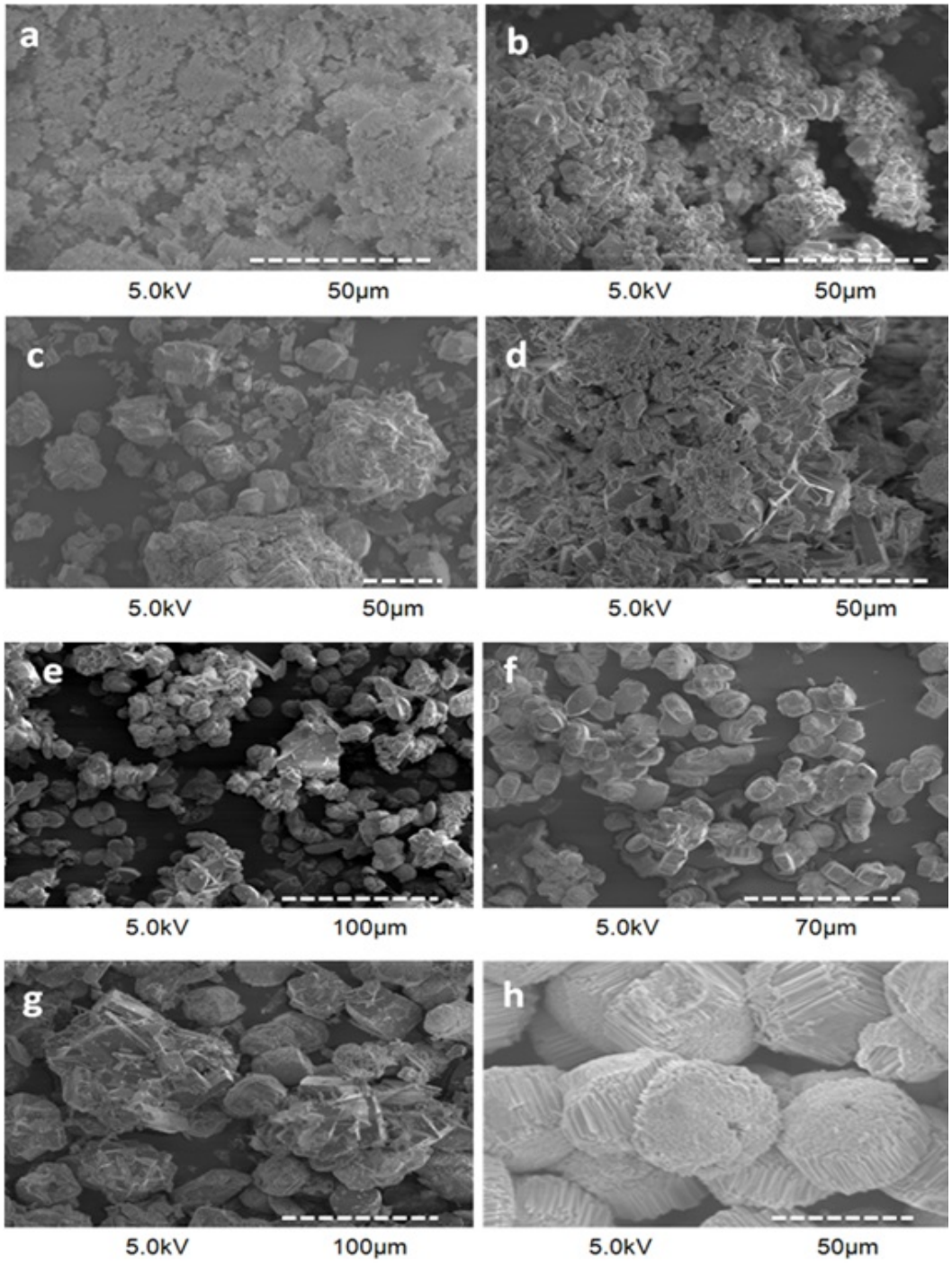

Figure 3.6 SEM micrographs of *as-synthesised* mordenite zeolite illustrated different morphologies and particle sizes in samples, using similar reaction conditions: (a–d) unidentified morphologies, (e–g) different morphologies and particle size in the range 10–40 µm and (h) uniform particle shapes having size 40–45 µm. Note: Size is lengthwise for all the samples relative to bar scales.

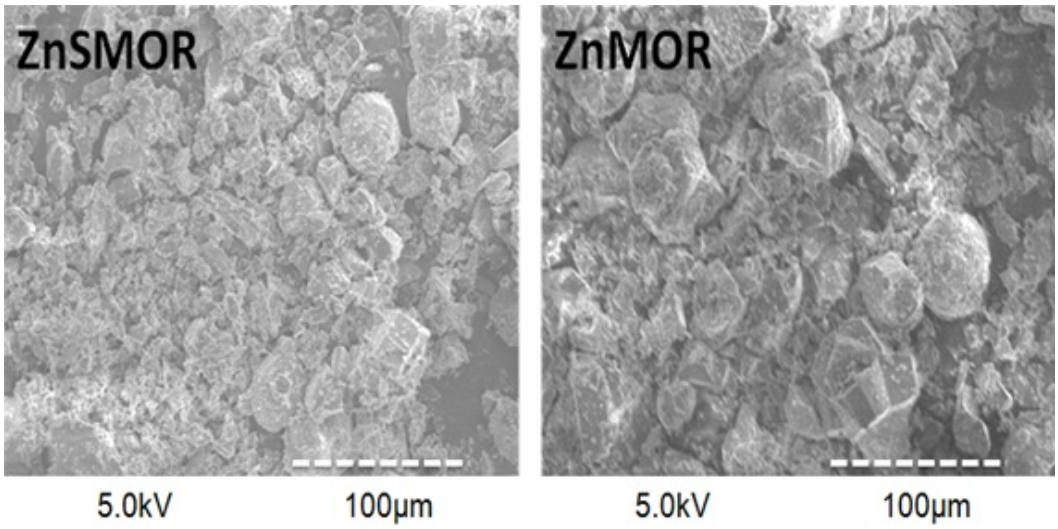

Figure 3.7 SEM micrograph of the ZnMOR and ZnSMOR after the Zn^{2+} ion exchange and ZnSMOR after the formation of ZnS in the as-synthesised mordenite pore network.

3.2.3 Transmission Electron Microscopy (TEM)

TEM is used to investigate the ZnS nanoclusters in the pore network of *as-synthesised* mordenite zeolite. The TEM micrographs observed large images of the NaMOR sample as shown in Figure 3.8. Some of the fragments of the *as-synthesised* MOR samples were too thick to be imaged in TEM.

Single crystals of NaMOR and ZnSMOR were examined to investigate the Na cation exchange and whether the ZnS nanocluster growth is inside the pore channels of MOR or decorating the surface of MOR. It was observed that both the crystals are beam sensitive, so the diffraction patterns weakened and disappeared within two seconds after exposure to the beam. As this is the original MOR sample (prior to Zn or S ion exchange), zinc (Zn) and sulfur (S) peaks were not observed in the EDX spectrum for either crystal as shown in Figure 3.8 (top right and bottom). The surface of this sample looks smooth, and no ZnS dots were visible.

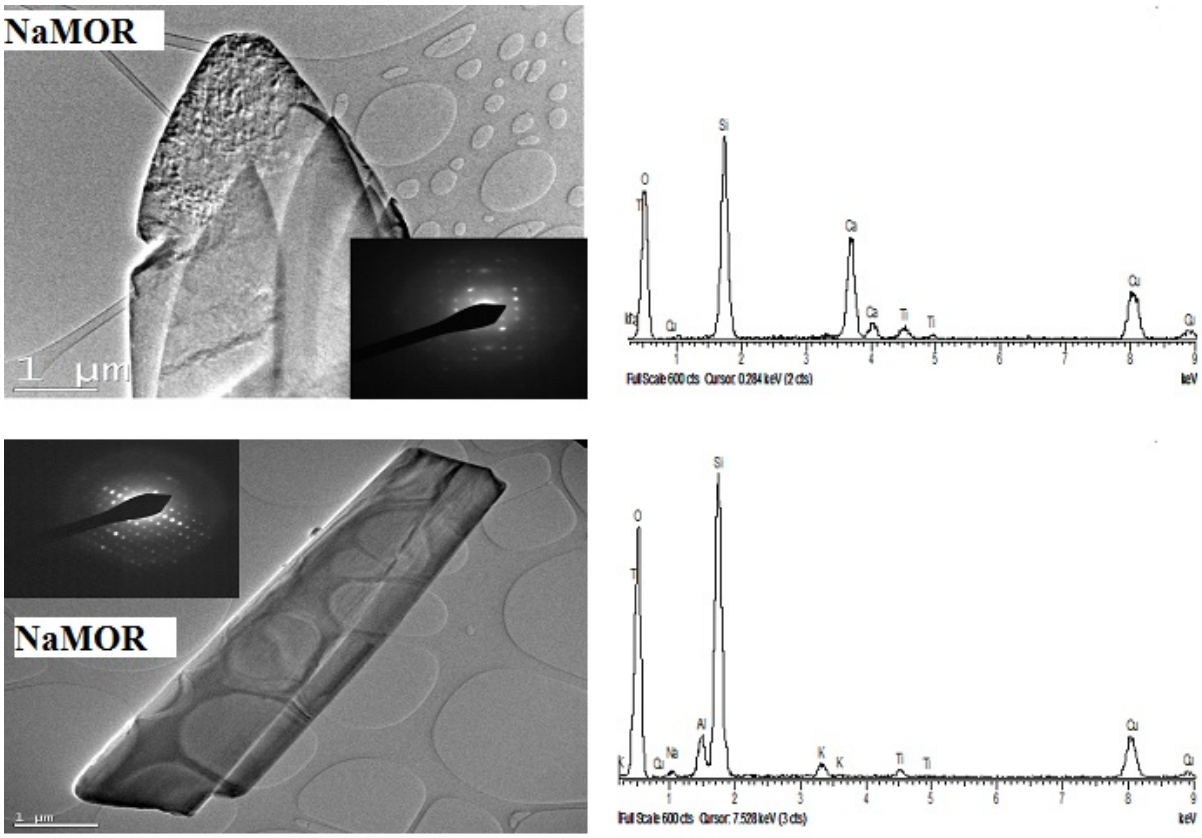

Figure 3.8 TEM images of two different crystals (left) and their respective elemental composition spectra (right) of the *as-synthesised* NaMOR.

In the ZnSMOR samples, two different single crystals were examined, and the high-resolution micrographs are shown in Figure 3.9. For this sample, it was very difficult to record the diffraction pattern of the micrograph because the weakening of the pattern occurred in less than one second. But in some parts of the high-resolution image recorded, very small ZnS crystals approximately 2–5 nm in diameter can be seen on the surface as shown in Figure 3.10. Using the electron diffraction multiple diffused ring, as seen in Figure 3.10, confirmed the presence of ZnS nanoclusters. This evidence was also supported by Saha et al.[12] where the diffused multiple rings appeared because of the ZnS nanocluster. The reported size of the normally synthesised ZnS nanoparticles in aqueous medium is

in the range of 4–13 nm[12] whereas the micropore size according to IUPAC is <2 nm in diameter.

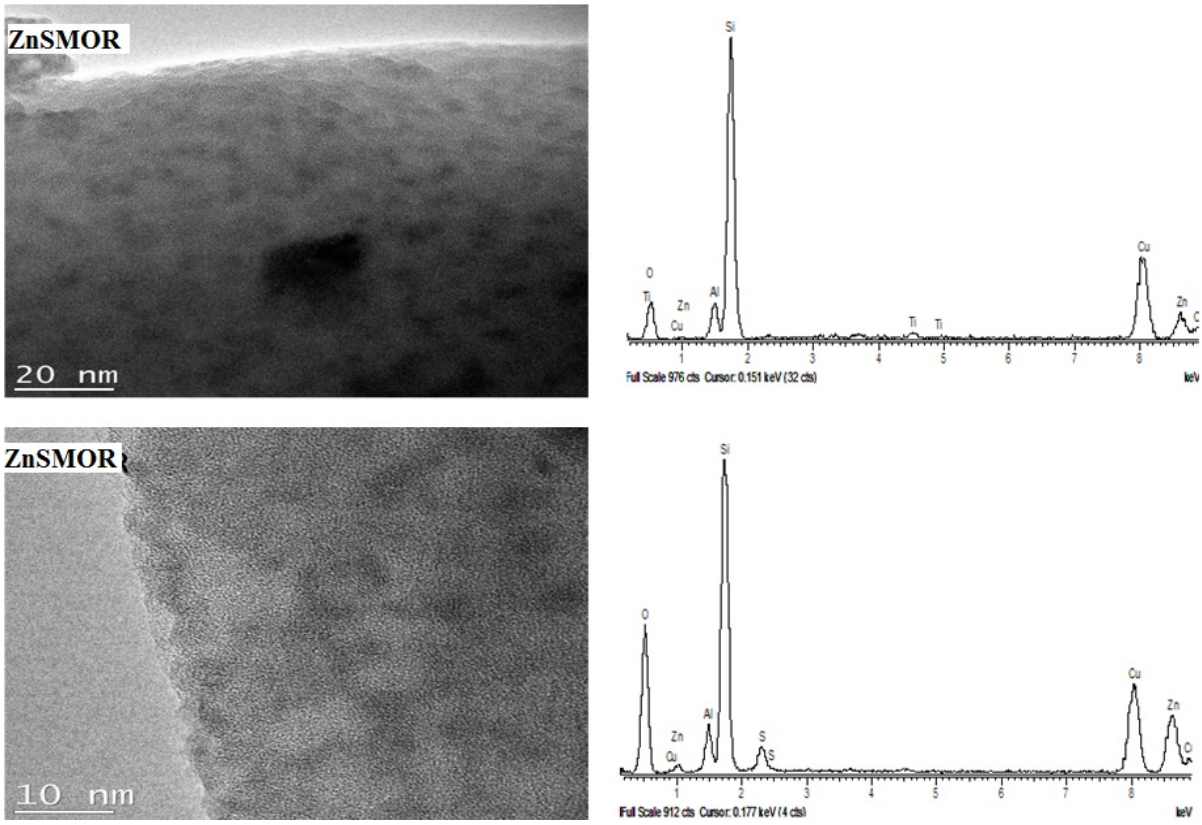

Figure 3.9 High-resolution TEM images of two different crystals (left) and their respective elemental composition spectra (right) of the *as-synthesised* ZnSMOR sample.

It is observed from the TEM images that the ZnSMOR sample has a different surface compared to the NaMOR sample. The recorded energy-dispersive X-ray pattern confirmed the presence of Zn and S atoms in this sample (ZnSMOR), as shown in Figure 3.9 (right top and bottom).

Therefore, upon close observation, we concluded that either the ZnS may successfully synthesise on the surface of the MOR or it may occur in the pore channels of *as-synthesised* NaMOR.

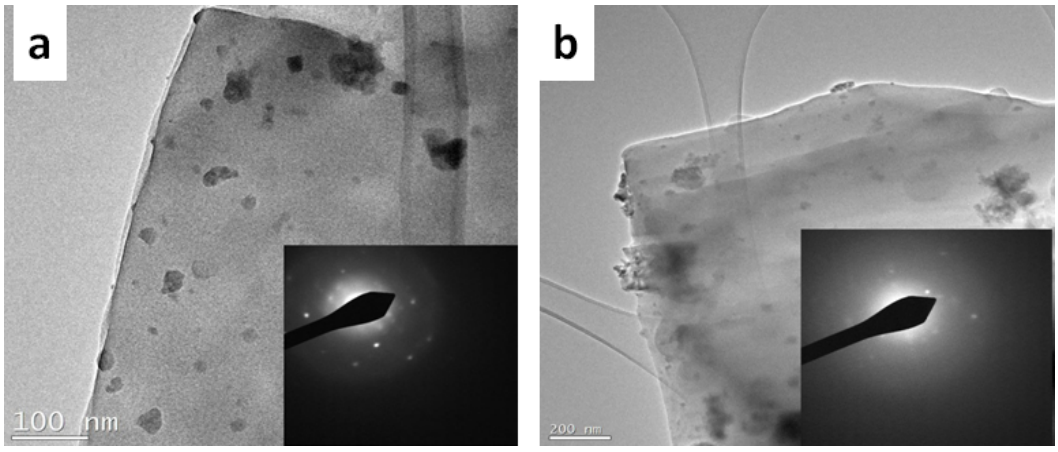

Figure 3.10 TEM images show the diffused rings of ZnS in the ZnSMOR sample.

3.2.4 Energy-Dispersive X-ray Spectroscopy

EDXS is used to investigate the quantitative and qualitative compositions of Zn and S in the samples (NaMOR, ZnMOR, ZnSMOR). Small areas of the samples were scanned for the consideration of elemental analysis. The presence of Zn and S in different stages of the ZnS formation can be identified by EDX.

EDS mapping is shown in Figure 3.11. The sample is examined for the distribution of chosen elements including Zn and S. Figure 3.11 (a) shows the mapped area, and Figure 3.11 (b) shows primarily the carbon support on which the sample is mounted. Figure 3.11 (c) represents the Si element whilst Figure 3.11 (d) shows the Al content of the sample. Figure 3.11 (e and f) represents oxygen and sodium, respectively. Figure 3.11 (g and h) are the S and Zn signals from the sample, respectively. From Figure 3.11 g and h, the Zn and S represent white dots that can be seen in exactly at the same position. So here we can say that Zn and S link to each as ZnS.

Figure 3.12 illustrates the EDS spectrum of the analysed area of the sample, composed of all the elements mentioned in Figure 3.11. Table 3.6 shows different elements in wt% in the NaMOR, ZnMOR and ZnSMOR samples. The

framework-building elements, i.e., Si, Al and O, are similar in all samples. The amount of Na in NaMOR dropped from 2.82 wt% to 1.02 wt%, and the presence of 3.31 wt% of Zn indicated that Zn ions were successfully incorporated into the MOR framework by the ion-exchange step. The amount of Zn in ZnS remained the same after the exchange with the Na_2S solution, and 1.22 wt% of S is also present in the same sample. The silicon-to-aluminium ratio (SAR) remains the same as the parent sample NaMOR after the exchange in samples ZnMOR and ZnSMOR. Meanwhile, a decrease in Na/Al ratio from NaMOR to ZnMOR indicated a successful exchange with Zn in the framework. The ratio of Zn/Al is approximately similar in the ZnMOR and ZnSMOR samples as shown in Table 3.7.

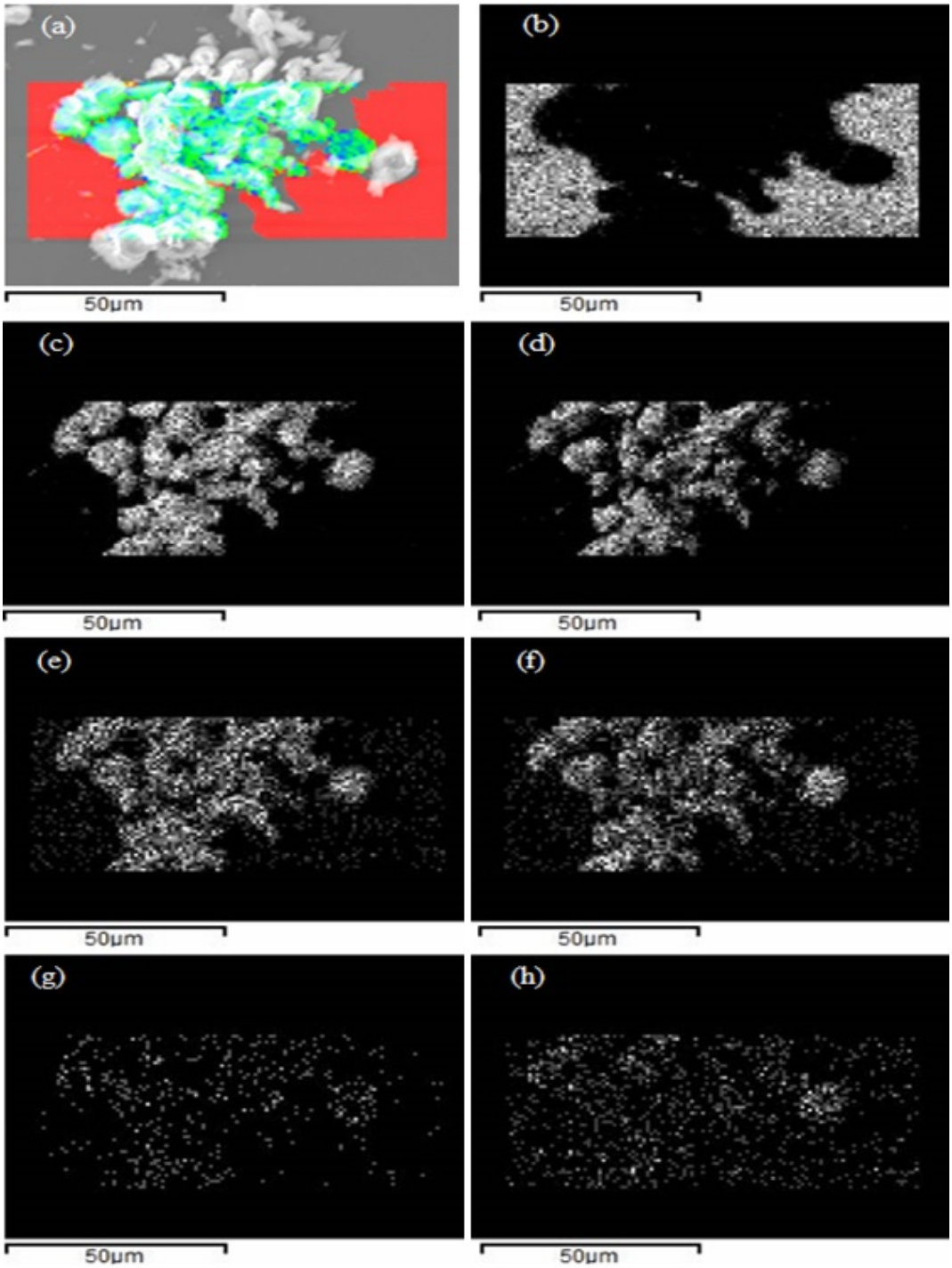

Figure 3.11 EDX micrographs of elemental distribution of (a) the ZnSMOR sample; (b) is the supported carbon for sample; (c) and (d) show the Si and Al atoms, respectively; (e) and (f) are oxygen and sodium atoms, respectively and (g) and (h) show the S and Zn atoms, respectively, where the low contrast of images (g) and (h) is due to their low concentration.

The Zn and S peaks can also be seen in the spectra as shown in Figure 3.12.

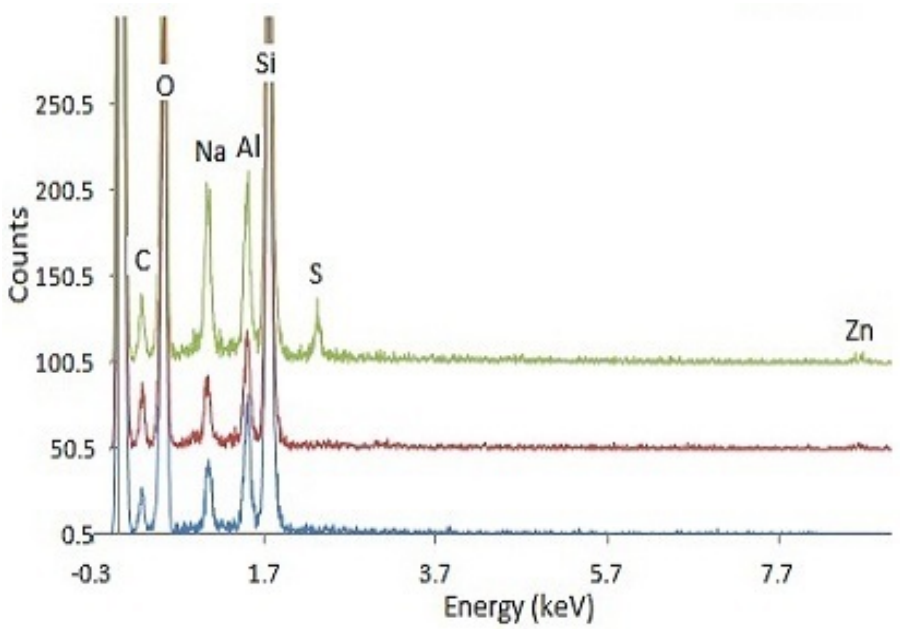

Figure 3.12 EDXS spectra NaMOR (no S and Zn detected), ZnMOR spectra (Zn detected), ZnSMOR (Zn and S detected), and Na, Zn peaks can be seen near 8 KeV.

The variation of the concentration of Na and the presence of Zn and S provide evidence that the ion exchange was successfully done. The detection of S in the sample ZnSMOR suggests the growth of ZnS nanoclusters as a guest molecule either in the pore channels of the MOR framework or on the surface of the mordenite, which is also observed in the TEM analysis.

Table 3.6 Weight percent (%) chemical composition obtained by EDX.

Sample Codes	Weight Percent (%)					
	Si	Al	O	Na	Zn	S
NaMOR	20.88±1.21	3.59±0.86	60.50±0.93	2.82±0.54	-	-
ZnMOR	27.24±4.82	2.92±0.93	61.08±3.17	1.02±0.61	3.31±0.91	-
ZnSMOR	17.96±8.87	3.20±1.35	60.02±4.97	2.50±0.68	3.73±0.83	1.22±0.23

Table 3.7 Ratios of Si, Na, Zn and S with respect to Al in NaMOR, ZnMOR and ZnSMOR.

Sample Codes	Si/Al	Na/Al	Zn/Al	Zn/S
NaMOR	8±1	0.75±0.02		
ZnMOR	8±1	0.42±0.03	1.31±0.01	
ZnSMOR	8±1	0.69±0.02	1.00±0.01	3.14±0.04

3.2.5 BET Surface Analysis

BET analysis determined the precise specific surface area of porous materials by nitrogen multilayer adsorption measured as a function of relative pressure using a fully automated analyser. The technique emphasises external area and pore area evaluations to determine the total specific surface area in m^2/g yielding important information in studying the effects of surface porosity and particle size in many applications.

BJH analysis can also be employed to determine pore area and specific

pore volume using adsorption and desorption techniques. This technique characterises pore size distribution independent of the external area because of the particle size of the sample. The BET equation[13] in section 2.7 is typically used to measure the surface area using the gas adsorption isotherm and can be considered to compare internal and external surface areas.[13,14] The t-plot is also an important method used to calculate the micro- and mesoporous volumes and the total surface area of a crystalline material by comparing them with a nonporous material having similar surface chemistry.[15] N_2 gas adsorption on the samples NaMOR, ZnMOR and ZnSMOR were undertaken and the resulting data presented in Table 3.8. The literature value for the BET surface area and micropore volume of mordenite-type materials is in the range of 30-323 m^2/g and 0.008–205 cm^3/g, respectively.[16]

The surface area of *as-synthesised* mordenite is lower than the reported values. As described in Table 3.8, ZnMOR sample has 8% smaller surface area than the NaMOR sample, which shows a small decrease in the area when sodium (Na^+) is replaced by zinc (Zn^{2+}) in the framework. Meanwhile, there is a large 69% change in the total surface area of mordenite after the synthesis of ZnS in the mordenite framework, and when the sodium ion (Na^+) was used to balance the framework anion, it did not affect the structure of the mordenite framework.[2,6]

Table 3.8 N_2 adsorption on mordenite zeolite before and after synthesis and ZnS nanocluster BET surface analysis and pore distribution.

Sample Codes	Total Surface Area (m^2/g)	Internal Surface Area (m^2/g)	External Surface Area (m^2/g)	Micropore Volume (cm^3/g)
NaMOR	29.4 ± 0.1	26.6	2.9	0.010
ZnMOR	27.1 ± 0.1	24.1	3.2	0.009
ZnSMOR	8.52 ± 0.1	4.1	4.4	0.002

The micropore volume of NaMOR is 0.010 cm^3/g whilst the micropore volume of ZnMOR and Zn-MOR are 0.009 and 0.002 cm^3/g, respectively, showing a decrease in micropore volume because of the nanoclusters in the pore channels. Garcia et al. in 1999 also reported the same effect of CdS nanoclusters in the MOR pore network.[17] The small decrease in the internal surface area after the exchange of Zn^{2+} is 2.5 m^2/g, and there is a massive decrease of 20.1 m^2/g after the formation of ZnS nanoclusters inside the mordenite pores. A significant decrease in the internal surface area after the synthesis of ZnS in the pore channels of MCM-41 zeolite was published by Pourahmad et al. in 2015[18] The result shows a very small increase in the external surface area, 0.2 m^2/g, after Zn^{2+} ion exchange and then a significant increase in the external surface area, 1.3 m^2/g, after the formation of ZnS nanoclusters. However, the total surface area decreased remarkably; hence, ZnS can still be outside the pores and block access to the internal pore volume of the zeolite structure. This assumption is also supported by the TEM analysis in section 3.2.3.

When the amount of nitrogen was adsorbed on all the samples at the same conditions, a type II isotherm was obtained in each case. The type II adsorption isotherm was discussed in section 2.4.5, describing how gas has low affinity for surface. In Figure 3.13, the presence of ZnS semiconductor nanoclusters in the mordenite leads to a dramatic change in the mesoporous desorption. A large delay was observed in the sample composed of ZnS nanoclusters in the pores whereas the pores are disordered and have lamellar structure and are wedge shaped as observed from the ZnSMOR isotherm. The desorption isotherm of the parent sample (NaMOR) and the Zn^{2+} exchanged sample ZnMOR as shown in Figure

3.14 and Figure 3.15, respectively, observed a very small change in the hysteresis loops of the isotherm. As whole, there is a delay in the N_2 desorption from NaMOR to ZnMOR but less than the ZnSMOR sample whereas the large hysteresis loops show the pores are cylindrical in structure, and spherical voids were observed from the isotherm.

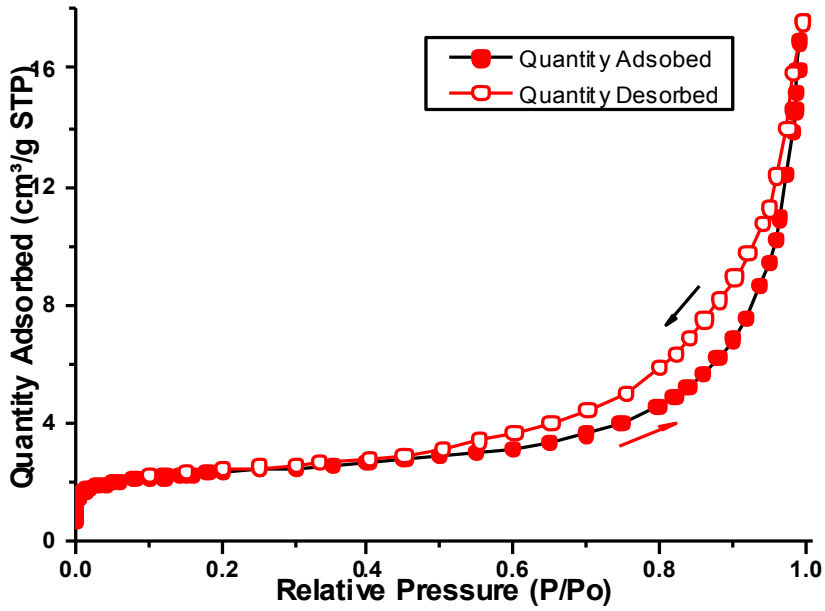

Figure 3.13 N_2 adsorption (red spheres) and desorption (white spheres) isotherms of ZnSMOR.

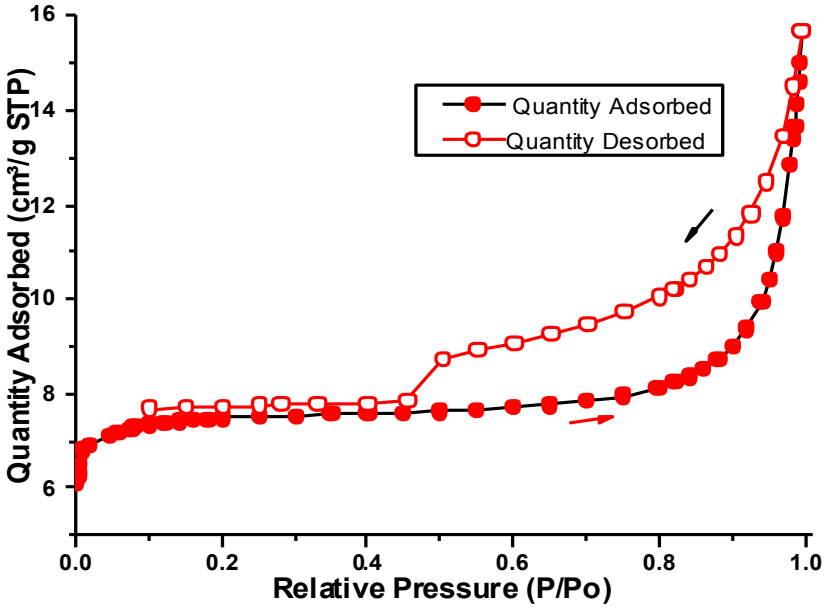

Figure 3.14 N_2 adsorption (white spheres) and desorption (red spheres) isotherms of NaMOR.

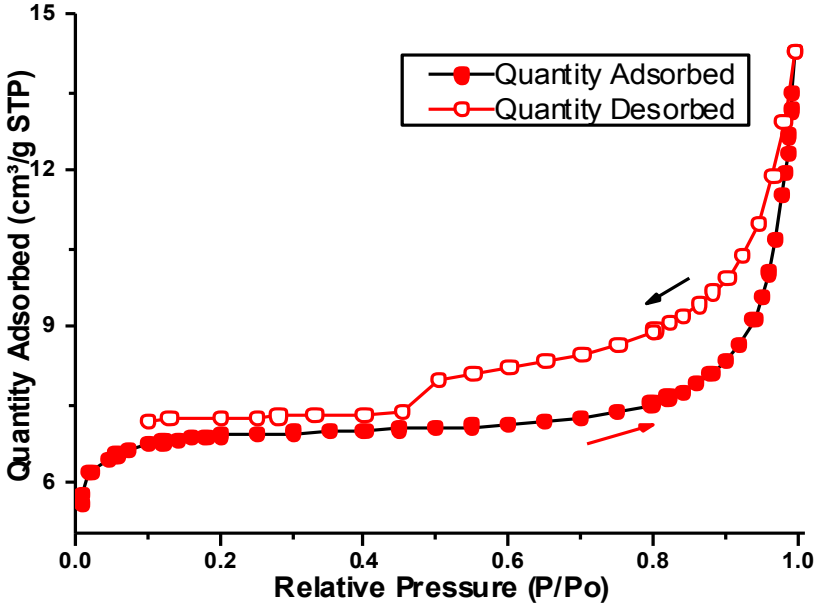

Figure 3.15 N_2 adsorption (white spheres) and desorption (red spheres) isotherms of ZnMOR.

According to the IUPAC, the pore diameters are categorised in three ranges, i.e., <2 nm are microspores, >2–50 nm are mesopores and >50 nm are macropores.[19] A smooth pore distribution was observed in the NaMOR and ZnMOR samples whereas after the formation of the ZnS on the surface or inside the pores, disorder behaviour observed in the pore distribution in the curves shown in Figure 3.16. In Figure 3.13, the average pore diameter on the nitrogen adsorption shows variations in the pore volume observed from NaMOR to ZnSMOR, whilst there was a significant decrease in the average pore diameter. A remarkable decrease in the micropore volume of ZnSMOR sample shown in Table 3.8 suggests that some of the pore may be blocked by the ZnS, or it may directly depend on the size of the exchanging cation or ZnS nanocluster or particle aggregation; if the size of the synthesised ZnS nanocluster is larger, it more effectively decreases the pore volume.[17,20]

There is also a high possibility of the pore blocking being caused by the ZnS nanocluster in the present scenario.[21]

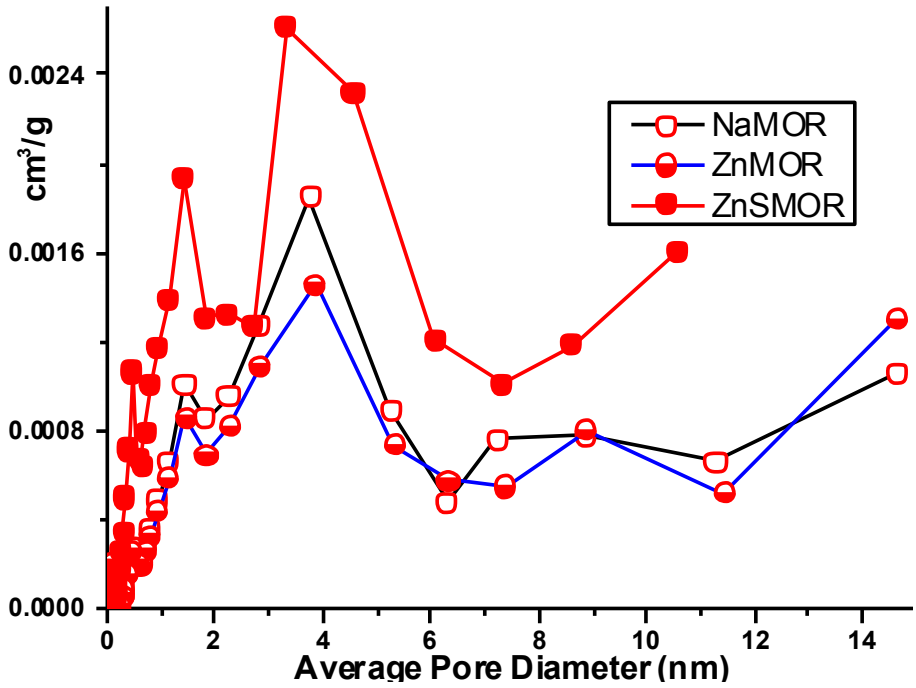

Figure 3.16 BJH pore size distribution from the nitrogen desorption curve for NaMOR (white circles), ZnMOR (half-red circles) and ZnSMOR (red circles). Note: the data is normalised.

3.2.6 Solid-state Magic Angle Spinning Nuclear Magnetic Resonance (MAS NMR)

Silicon is tetrahedrally coordinated in the zeolite framework; therefore, it has five different potential environments including Si(nAl) where n (n≤4) is the number of Al atoms connected to silicon via oxygen bridges.

Generally, ^{27}Al MAS NMR spectra show that the central transition for all aluminium-containing materials have only a single resonance at 54±1 ppm assigned to the framework tetrahedrally coordinated Al atom (Al(4)).[9,22] ^{27}Al

chemical shift of octahedral coordination or extra framework (Al(6)) of Al-containing materials occurs in the range of -13.2 ppm to +1.4 ppm.[23]

The chemical shift of ^{27}Al for NaMOR is 54.767 ppm; for ZnMOR, 54.278 ppm and for ZnSMOR, 54.522 ppm. The resonance of ^{27}Al in ZnMOR is slightly shifted to a higher field from 54.767 ppm to 54.278 ppm as shown in **Figure 3.17.** The chemical shift of ZnMOR is asymmetrical compared with that of NaMOR and ZnSMOR. This might be due to the two different environments of Al given the presence of Zn and Na in the framework. When ZnMOR was treated with Na_2S, part of the extra framework Zn^{2+} ions reacted with S^{2-} to form ZnS. Some of the Zn^{2+} ions were replaced by Na^{+} ions (from Na_2S). It is assumed that the Zn and Na are coordinated with Al. The chemical shift of the ^{27}Al MAS NMR of the sample ZnSMOR signal is nearly the same as that of NaMOR. After the formation of ZnS, the Al adopts the same environment as for the unexchanged sample (NaMOR), and hence, the ZnSMOR chemical shift moves towards its original position.

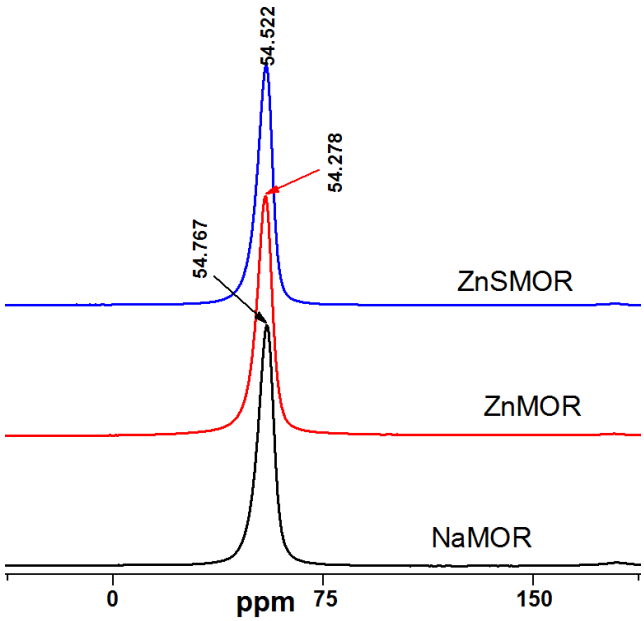

Figure 3.17 ^{27}Al solid-state MAS NMR spectra of NaMOR (black), ZnMOR (red), and ZnSMOR (blue) samples.

The ^{29}Si MAS NMR spectrum of the mordenite NaMOR sample shows two different Si environments. The parent NaMOR sample and the exchanged samples, i.e., ZnMOR and ZnSMOR, have two resonance signals at -112 ± 1 ppm, and -105 ± 1 ppm as shown in Figure 3.18 corresponding to the Si(0Al), Si(1Al) of local environments, respectively, whilst there is a shoulder at a lower chemical shift ascribed to Si(2Al)[5,22]. There was no obvious change in the NaMOR Si environment after the ion exchange and the growth of ZnS in the mordenite frameworks. The ^{29}Si MAS NMR spectra of all the three samples were fitted by using deconvolution of the observed signals into Gaussian components, which are presented in Figure 3.19. However, there is no obvious change observed in ^{29}Si MAS NMR for all the three investigated samples. All the solid-state MAS NMR results are illustrated in Table 3.9.

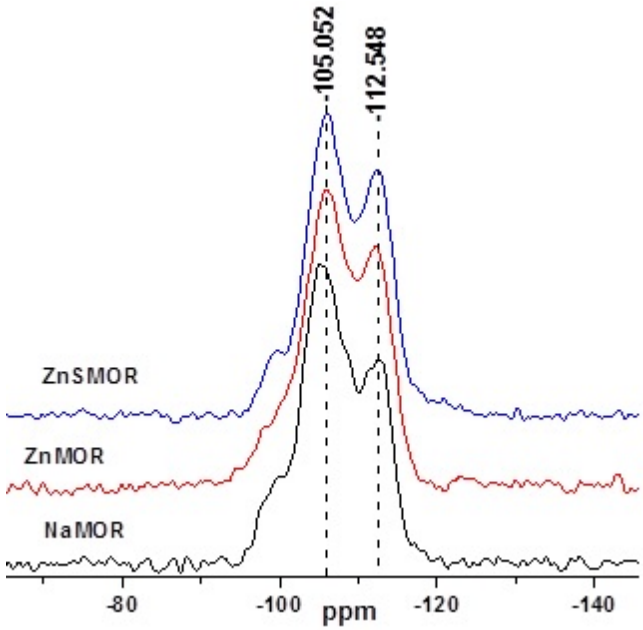

Figure 3.18 ^{29}Si solid-state MAS NMR spectra of the as-synthesised sample NaMOR (black), ZnMOR (red) and ZnSMOR (blue) after the ion exchange.

The ^{23}Na nuclei can be examined by solid-state MAS NMR because it has 100% natural abundance and a magnetogyric ratio. It may disclose some important information about the effects of ZnS nanoclusters in the MOR frameworks. ^{23}Na MAS NMR spectrum of the NaMOR sample, as shown in Figure 3.20, gives a signal at -11.84 ppm.[24] But after exchange of sodium (Na) with zinc (Zn), the ^{23}Na chemical shift of the ZnMOR samples gives two distinct signals at 7.39 ppm and -20.98 ppm. After the exchange with Zn^{2+}, the framework of ZnMOR contained both Zn^{2+} and Na^{+} as charge-balancing cations. Therefore, two sodium environments, a Na^{+} with either a Na^{+} ion or Zn^{2+} ion as a neighbour, were observed. A broadening of the ^{23}Na solid-state NMR was also observed in the ZnMOR sample after the Zn exchange. After the second step of the exchange process, in which ZnS is grown in the pore channels of MOR using the Na_2S solution, the framework Zn^{2+} reacted with S^{2-} to form a ZnS nanocluster. ^{23}Na MAS spectra of the ZnSMOR sample observed only one sodium environment at -

16.17 ppm. This feature may prove the growth of ZnS in the MOR pore network. It may be assumed that after ZnS growth in the pores, the charge is balanced by the Na^+ ion.

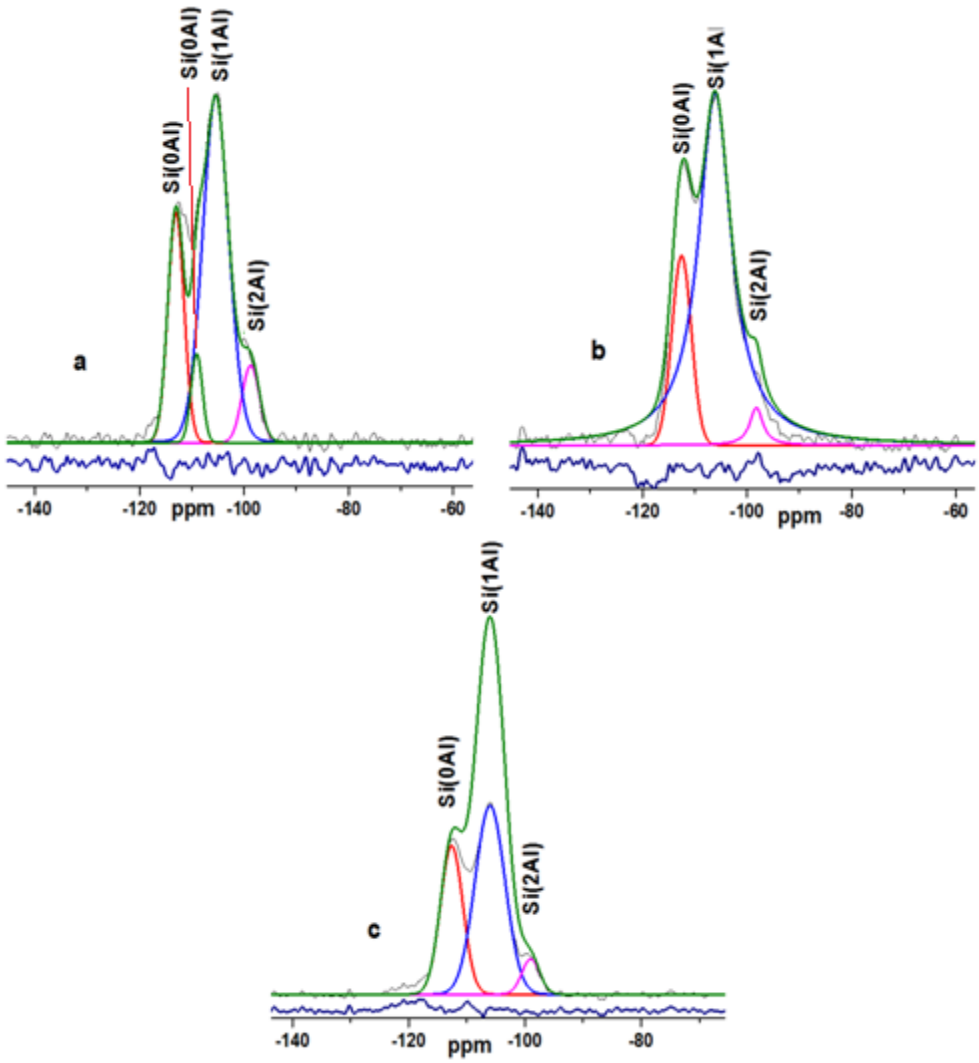

Figure 3.19 Deconvoluted spectra of ^{29}Si NMR of (a) NaMOR, (b) ZnMOR and (c) ZnSMOR. NaMOR and ZnMOR show three similar Si coordination environments, whilst in ZnSMOR, four environments can be discerned.

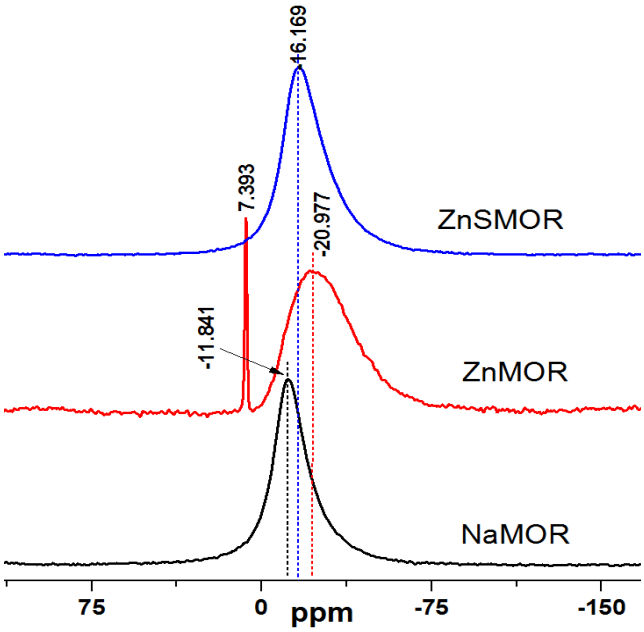

Figure 3.20 ^{23}Na solid-state MAS NMR spectra of the parent sample NaMOR (black), ZnMOR (red) and ZnSMOR (blue) before and after ZnS nanocluster growth.

^{23}Na MAS NMR spectra are similar before and after the Zn^{2+} ion exchange and ZnS growth in the mordenite pore channels. Similarly, ^{27}Al MAS spectra are also similar before and after the Zn^{2+} ion exchange and ZnS growth in the mordenite pore channels. Equation (17) (discussed in section 2.4.6) was used to calculate the silicon-to-aluminium ratio of the as-synthesised sample of NaMOR, which is 8, consistent with that of a highly siliceous zeolite,

$$\left(\frac{Si}{Al}\right)_{framework} = \frac{\left(\sum_{n=0}^{4} I_{Si(nAl)}\right)}{\left(\sum_{n=0}^{4} 0.25 n I_{Si(nAl)}\right)} \qquad (17)$$

where $I_{Si(nAl)}$ is the relative intensity of the $Si(OAl)_n(OSi)_{4-n}$ component.

The overall conclusion of the above results and discussion can be summarised by the proposed two-step cation-exchange mechanism shown in Figure 3.21. The synthesis of ZnS nanoclusters is shown in Figure 3.21, which illustrates the ion-exchange process in the mordenite framework. This suggests that during the exchange with Zn^{2+}, Na^{+} cations are moved from their initial position, which results in a change in their chemical shifts. However, once the

sulfidation process was performed by adding S^{2-} ions, Na^{+} ions from the sodium sulfide (Na_2S) returned to their original positions, and hence, the chemical shift from -20.98 ppm moved to a lower field of -16.7 ppm. A similar process happens with the ^{27}Al chemical shift as well.

Table 3.9 ^{27}Al, ^{29}Si, ^{23}Na solid-state MAS NMR data taken from the samples NaMOR, ZnMOR and ZnSMOR.

Sample	Si/Al Ratio	^{27}Al Sites	δ (ppm)	^{29}Si Sites	δ (ppm)	^{23}Na Sites	δ (ppm)
NaMOR	8±1	1	54.767	2	-112.5	1	-11.841
					-105.052		
ZnMOR	8±2	1	54.278	2	-112.231	2	-20.977
					-105.973		7.393
ZnSMOR	8±1	1	54.522	2	-112.363	1	-16.169
					-105.981		

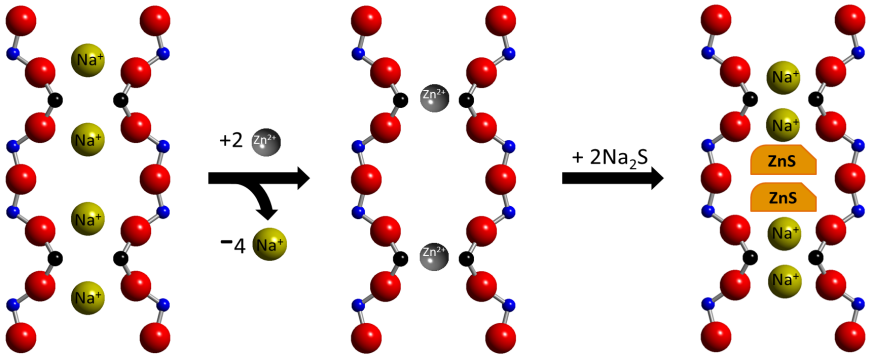

Figure 3.21 A proposed two-step schematic mechanism of the formation of ZnS nanoclusters in the MOR framework.

3.3 Discussion

A new route has been introduced for synthesis of ZnS nanoclusters in the pore channels of mordenite zeolite. The synthesis was carried out on solution-based ion-exchange reactions. Zeolites are composed of void matrices and can be used for synthesis of semiconductors such as ZnS, CdS, PbS, TiO_2 etc.[4,25,26] Therefore, there are many applications where zeolite acts as host of semiconductor nanoclusters, e.g., optoelectronic devices, photo catalysts, sensors, LED, displays etc. Generally, semiconductor nanoclusters exhibit quantum confinement effects when their size becomes equal to the Bohr radius of the bulk exciton in such a way that their natures have character between the bulk and molecular properties of matter. This effect leads to a significant change in electronic structure as well as in physical and chemical properties.[27] It is also very important to note that zeolites can act as photocatalytic reactions; they provide specific physical properties such as control of charge transfer and the electron transfer process. Liu et al.[28] in 1992 reported the encapsulation of TiO_2 in zeolite Y via ion exchange of zeolite in an aqueous solution of ammonium titanyl oxalate monohydrate ($(NH_4)_2TiO(C_2O_4)_2H_2O$). Characterisation gave the evidence that Ti species successfully exchanged with the cation in the zeolite in the form of small-cluster particles.[28] In 1999, Chen et al.[29] reported the synthesis of TiO_2 nanoclusters in the pore network of Y-zeolite. They reported that the photochemical activity of TiO_2 in the TiO_2 zeolite system was more than five times than what was in the bulk system by decomposition of ethanol. Raymond et al. successfully synthesised semiconductor nanoclusters of ZnS and members of the ternary Cd_xZn_yS system on the synthetic Na-mordenite as host material. The initial reaction was based on the ion-exchange method in aqueous

solution followed by treatment with hydrogen sulfide gas. They used various absorption techniques for the identification of ZnS and the ternary Cd_xZn_yS system.[30]

The synthetic approach described in the experimental section is straightforward and leads to materials containing ZnS as expected; however, the control of Zn/S stoichiometry shows significant challenges. In the chemistry involved in the synthesis of the ZnS nanocluster shown in Figure 3.21, it is clear that the reaction is readily reversible, i.e., whilst ZnS is formed, the Na of the Na_2S reagent becomes the zeolite charge balance forcing the ZnS nanoclusters to reside within the pore network of mordenite zeolite. The powder XRD patterns showed that there is no loss of framework structure after Zn and S ion exchanges. A small shift to higher 2θ is observed in both Zn-MOR and ZnS-MOR samples as an indication of a decrease in unit cell parameters. ^{29}Si NMR gives three local Si environments, and all ^{27}Al NMR spectra are tetrahedral-coordinated and showed that the mordenite framework is not affected after the growth of ZnS within the pore channels. The presence of Zn and S ions in ZnMOR and ZnSMOR samples is evident in EDX elemental analysis. The increase in BET surface area analysis confirms the formation of ZnS that may be placed on the pore mouth of the mordenite zeolite framework.

3.4 Conclusion

Mordenite zeolite was synthesised without using any organic structure-directing agents. The powder patterns show that there is no loss of framework structure after Zn and S ion exchanges. A small shift to higher 2θ is observed in both Zn-MOR and ZnSMOR samples as an indication of a decrease in unit cell parameters. ^{29}Si NMR gives three local Si environments, and all ^{27}Al are tetrahedral coordinated. ^{23}Na NMR gives two signals which indicate the successful incorporation of Zn^{2+} ions into the MOR framework. The presence of Zn and S ions in ZnMOR and ZnSMOR samples is evident in EDX. BET surface area analysis confirms the formation of ZnS, but it is difficult to determine whether such formation is on the surface of the mordenite zeolite crystals or within the framework channels.

3.5 References

[1] "IZA Commssion on Natural Zeolites structure data base," can be found under http://www.iza-structure.org/databases/, **2005**.

[2] F. Iacomi, *Surf. Sci.* **2003**, *532–535*, 816–821.

[3] Z. Hurem, D. Vucelic, V. Markovic, *Zeolites* **1993**, *13*, 145–148.

[4] O. Raymond, H. Villavicencio, V. Petranovskii, J. M. Siqueiros, *Mater. Sci. Eng. A* **2003**, *360*, 202–206.

[5] A. Lv, H. Xu, H. Wu, Y. Liu, P. Wu, *Microporous Mesoporous Mater.* **2011**, *145*, 80–86.

[6] M. M. Garcia, H. Villavicencio, M. Hernandez-Velez, O. Senchez, J. M. Martinez-Duart, *Mater. Sci. Eng. C* **2001**, *15*, 101–104.

[7] L. V. D. S. Júnior, A. O. S. Silva, B. J. B. Silva, S. L. Alencar, *Mod. Res. Catal.* **2014**, *1*, 49–56.

[8] O. Raymond, H. Villavicencio, E. Flores, V. Petranovskii, J. M. Siqueiros, *J. Phys. Chem. C* **2007**, *111*, 10260–10266.

[9] T. Sano, S. Wakabayashi, Y. Oumi, T. Uozumi, *Microporous Mesoporous Mater.* **2001**, *46*, 67–74.

[10] J. Warzywoda, A. G. Dixon, R. W. Thompson, A. Sacco, *J. Mater. Chem.* **1995**, *5*, 1019.

[11] S. Ueda, H. Murata, M. Koizumi, *Minsocam.Org* **1973**, *65*, 1012–1019.

[12] S. Saha, K. Bera, P. C. Jana, *Int. J. Soft Comput. Eng.* **2011**, *1*, 23–26.

[13] S. Brunauer, P. H. Emmett, E. Teller, *J. Am. Chem. Soc.* **1938**, *60*, 309–319.

[14] M. E. Hodson, *Mineral. Mag.* **1998**, *62*, 634–635.

[15] A. Galarneau, F. Villemot, J. Rodriguez, F. Fajula, B. Coasne, *Langmuir* **2014**, *30*, 13266–13274.

[16] P. Sharma, P. Rajaram, R. Tomar, *J. Colloid Interface Sci.* **2008**, *325*, 547–557.

[17] H. V. Garcia, M. H. Velez, O. S. Garrido, J. M. M. Duart, J. Jimenez, *Solid. State. Electron.* **1999**, *43*, 1171–1175.

[18] A. Pourahmad, *Int. J. Nano Dimens.* **2015**, *6*, 83–88.

[19] K.-J. Kim, H.-G. Ahn, *Microporous Mesoporous Mater.* **2011**, *152*, 78–83.

[20] B. Tyburce, C. Kappenstein, P. Cartraud, E. Garnier, *J. Chem. Soc. Faraday Trans.* **1991**, *87*, 2849.

[21] Z. Fang, B. Bueken, D. E. De Vos, R. a. Fischer, *Angew. Chem Int. Ed.* **2015**, *54*, 7234–7254.

[22] J. Klinowski, *Annu. Rev. Mater. Sci.* **1988**, *18*, 189–218.

[23] P. J. P. Dirken, J. B. H. Jansen, R. D. Schuiling, *Am. Mineral.* **1992**, *77*, 718–724.

[24] P. Duxson, J. L. Provis, G. C. Lukey, F. Separovic, J. S. J. Van Deventer, *Langmuir* **2005**, *21*, 3028–3036.

[25] Y. Wang, N. Herron, *J. Phys. Chem.* **1987**, *91*, 257–260.

[26] J. E. Mac Dougall, H. Eckert, G. D. Stucky, N. Herron, Y. Wang, K. Moller, T. Bein, D. Cox, *J. Am. Chem. Soc.* **1989**, *111*, 8006–8007.

[27] H. Tang, G. Xu, L. Weng, L. Pan, L. Wang, *Acta Mater.* **2004**, *52*, 1489–1494.

[28] X. Liu, K. K. Iu, J. Kerry Thomas, *Chem. Phys. Lett.* **1992**, *195*, 163–168.

[29] H. Chen, A. Matsumoto, N. Nishimiya, K. Tsutsumi, *Colloids Surfaces A Physicochem. Eng. Asp.* **1999**, *157*, 295–305.

[30] E. J.-A. Oscar, H. Villavicencio, J. A. Diaz-Hernandez, V. Petranovskii, M. Herrera, O. Raymond-Herrera, *Chem. Mater.* **2014**, *26*, 6152–6159.

Chapter 4
Pretreatment Synthesis of NanoZSM-5

4. Synthesis of NanoZSM-5 with and without Ultrasound Pretreatment

In this work, we aimed to develop a novel method for the synthesis of nanoZSM-5 on the basis of pretreatment/aging before the subsequent hydrothermal process. The ultrasound-assisted synthesis processes have been developed, and the synthesised zeolites were investigated by a number of analytical techniques. Two different pretreatment methods have been compared for synthesis to identify the most favourable method for synthesising nanosized ZSM-5 zeolite. The nanoZSM-5 zeolite was synthesised from alkaline aluminosilicate gel using two different aging (pretreatment) methods, i.e., static (without stirring and ultrasound) and ultrasonication (using ultrasound bath) before the hydrothermal synthesis process. The comparative study of both methods has similar experimental conditions such as pretreatment time, crystallisation period and temperature at autogenous pressure. Micro- and nanoZSM-5 were characterised by X-ray powder diffraction (XRD), scanning electron microscopy (SEM), dynamic light scattering (DLS), transmission electron microscopy (TEM), N2 adsorption/desorption, BET surface analysis and solid-state magic angle spinning nuclear magnetic resonance spectroscopy (SS MAS NMR).

4.1 Experimental

4.1.1 Chemicals, Reagents Used and Syntheses

Tetrapropylammonium hydroxide (TPAOH) (Sigma Aldrich, 1.0M in H_2O) and sodium hydroxide (NaOH) (99.4% Fisher Scientific UK) were used as to make a basic medium and to provide a metal cation. Sodium aluminate ($NaAlO_2$) (ca 8% H_2O 99.9% Al), ordered from ABCR GmbH and Co, was used as aluminium source, and Ludox HS-40 with pH 9.8, Sigma Aldrich 40% colloidal silica, was used as the silicon source. Doubly deionised water (made in the lab) was used as a solvent. Ammonium nitrate (NH_4NO_3) (Sigma Aldrich, ACS reagent ≥98 %, with pH 4.5–6), was used for the ion exchange to build an acidic site on the outer and the inner surface of the probe materials.

4.2 Synthesis of ZSM-5 Zeolite

ZSM-5 (MFI) zeolite crystals were synthesised using the method given in the International Zeolite Association (IZA) website[1] with a few modifications, i.e., different Si/Al, synthesis temperature and crystallisation time. TPAOH as an organic structure-directing agent (OSDA) and sodium hydroxide (NaOH) were used as a basic media, and an extra framework cation of a known amount was dissolved in distilled water. Sodium aluminate ($NaAlO_2$) was used as the Al source; a known mass was then added to the NaOH solution and was kept stirred until a transparent solution was formed. Ludox HS-40 with pH 9.8, used as Si precursor, was then added to the solution dropwise. To reduce the aggregation, ethanol was also used as a solvent added dropwise whilst stirring for 15 minutes. Pretreatment was applied at different duration times to enhance crystallinity and

crystal growth; the mixture was then transferred into a PTFE liner. A simplified flow sheet of synthesis mechanism is shown in Figure 4.1. All the gel mixtures were made of the following molar composition in Table 4.1.

Table 4.1 Molar composition of reacting materials.

Materials	Na_2O	Al_2O_3	SiO_2	H_2O
Ratio	16.7	0.5	60	116

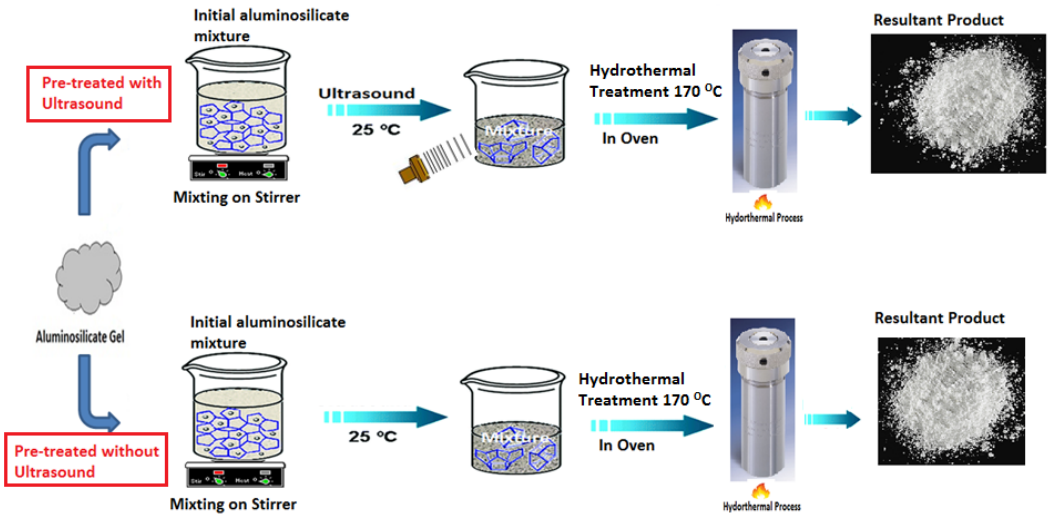

Figure 4.1 Simplified synthesis mechanism of ZSM-5 zeolite with and without ultrasound pretreatment.

The PTFE liner was fitted into a stainless-steel autoclave and hydrothermally treated at 150–170°C for 24–72 hours. The product was then removed, thoroughly washed with deionised water, and dried at 110°C overnight.

4.2.1 Nucleation and Crystal Growth Mechanism

The aging/pretreatment process is very important in producing a uniform and highly crystalline material. The aging process helps continue the crystallisation process; it has a great influence on the crystal growth rate. In any particular reaction, there are two basic proposed mechanisms of zeolite syntheses: (i) solution-mediated transport mechanism and (ii) solid hydrogel transformation mechanism.[2] Peter-Paul et al.[3] described the crystal growth mechanism by optimising the pretreatment method of aging prior to a hydrothermal synthesis method; this influenced crystal growth without any effect on the amorphous colloidal aggregates. Tosheva et al.[2] reported that the formation of nuclei under an ambient condition delayed the crystallisation process. However, it may be expected that the kinetics of that crystallisation process is slow. This process is schematically presented in Figure 4.2, synthesis of FAU-type zeolite. (i) The system consists of nuclei during the chemical evolution. (ii) Crystallisation was initiated when crystal growth resulted in propagation from the gel. (iii) Consequently, a secondary crystallisation step appears where spontaneous aggregation of the particles occurs around the crystallisation centre leading to Ostwald ripening. Watson et al.[4] proposed a mechanism of the colloidal particles formed in the initially clear solution aged for six months under an ambient condition, which produced the typical MFI framework geometrical features. The authors described the synthesis mechanism; during the mixing of the materials, the primary nuclei grouped together and produced the primary crystallite, wherein the primary crystallites fused and converted into larger crystals. It was also

claimed that aging under an ambient condition has a significant effect on the crystallisation process.

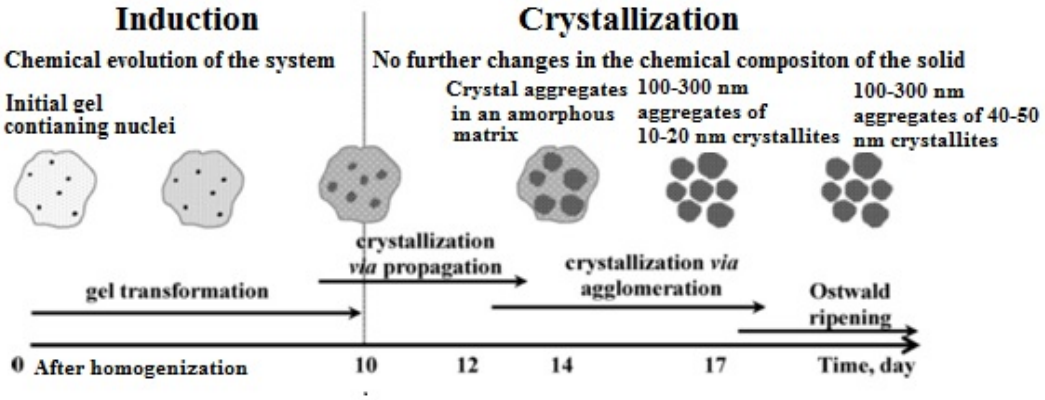

Figure 4.2 Schematic representation of the crystallisation mechanism of FAU-type zeolite synthesised under an ambient condition, taken from.[2]

Čižmek et al.[5] studied the influence of aging time and temperature of the synthesis of MFI-type zeolites. The authors reported that nucleation might take place during the aging initiated in the gel in the crystallisation process. The species in the aged gel is responsible for the crystal size distribution for the synthesis of MFI-type zeolite. The authors observed that there is a very small effect on the crystal morphology whilst it exerted a considerable effect on the size and crystallisation product.

Two different methods of pretreatment/aging are briefly discussed in this chapter. The aluminosilicate gel mixtures were pretreated for different time periods using the following processes:

a) Static aging/pretreatment (without ultrasound)

b) Pretreatment with ultrasound

4.2.1.1 Static Aging (Pretreatment) without Ultrasound

In this method, the aluminosilicate gel was left for a specific time in the beaker without any kind of disturbance at room temperature. It was then poured into the Teflon liner, which was then transferred to the Parr reactor. The Parr reactor was then kept in the oven for the hydrothermal process for various crystallisation times.

There are various factors, including static aging, which are reported to have a great impact on the syntheses of nanocrystals.[3] Such kinds of pretreatment/aging were published in the literature by using clear solution for synthesis of nanocrystalline ZSM-5, by using a clear solution.[2,3]

4.2.1.2 Pretreatment with Ultrasound

In this method, the gel mixtures were treated with ultra-sonication for a specific time at room temperature. They were then processed for crystallisation (hydrothermal treatment). During the ultrasound treatment, the temperature of the solution also increases; in 30 minutes, temperature increases in the range of 50°C to 60°C. This increase in temperature helps in solvent evaporation whilst obviously also increasing the concentration of the solution. In addition, some experiments used chilled water/ice to control the temperature of the water bath.

The ultrasound significantly affects aging as well as the crystallisation period, which is directly related to nucleation.[6,7] The application of ultrasound also helps in reducing the degree of aggregation. Two aspects can explain this phenomenon: (a) During ultra-sonication, the temperature of the water in the bath increases up to 70°C, which ultimately increases the gel temperature to 60–70°C.

This increase in temperature helps increase the nucleation rate by evaporating the solvent, thus increasing the concentration of the gel and creating more nuclei.[6,8,9] (b) The collapse of the bubbles during sonication is responsible for creating high-energy microjets, which may create more space for newborn nuclei in the solution, which ultimately increases nucleation rate during ultrasound pretreatment.[6–9]

4.2.2 Calcination and Activation of the Catalysts (NanoZSM-5)

The as-synthesised product (powder) received after the hydrothermal treatment was dried overnight at 110°C, and then it was further treated at 550°C for five hours in the presence of N_2 flow. All the samples were then characterised with different physicochemical techniques to examine the effect of pretreatments on particle/crystallite size distribution after the syntheses.

4.3 Results and Discussion

4.3.1 Powder X-ray Diffraction (XRD) of ZSM-5 Zeolite

Powder X-ray diffraction is a standard technique for the identification of crystal structure and crystallinity. This technique gives information about the lattice-plane spacing and the relative amount of the crystalline phases.

The test experiments of the syntheses of ZSM-5 were carried out at different time periods of the hydrothermal process, to obtain pure ZSM-5 standard synthesis conditions for the subsequent syntheses for nanoZSM-5. The test experiments have been performed without using ultrasound. By optimising synthesis conditions, characteristic ZSM-5 peaks appeared as soon as the

crystallisation time was increased from 36 to 48 hours. According to the results shown in Figure 4.3, when the gel was treated for 72 hours at 150°C, the ZSM-5 powder pattern was observed, and it confirmed what was already reported in the literature.[1,10–12]

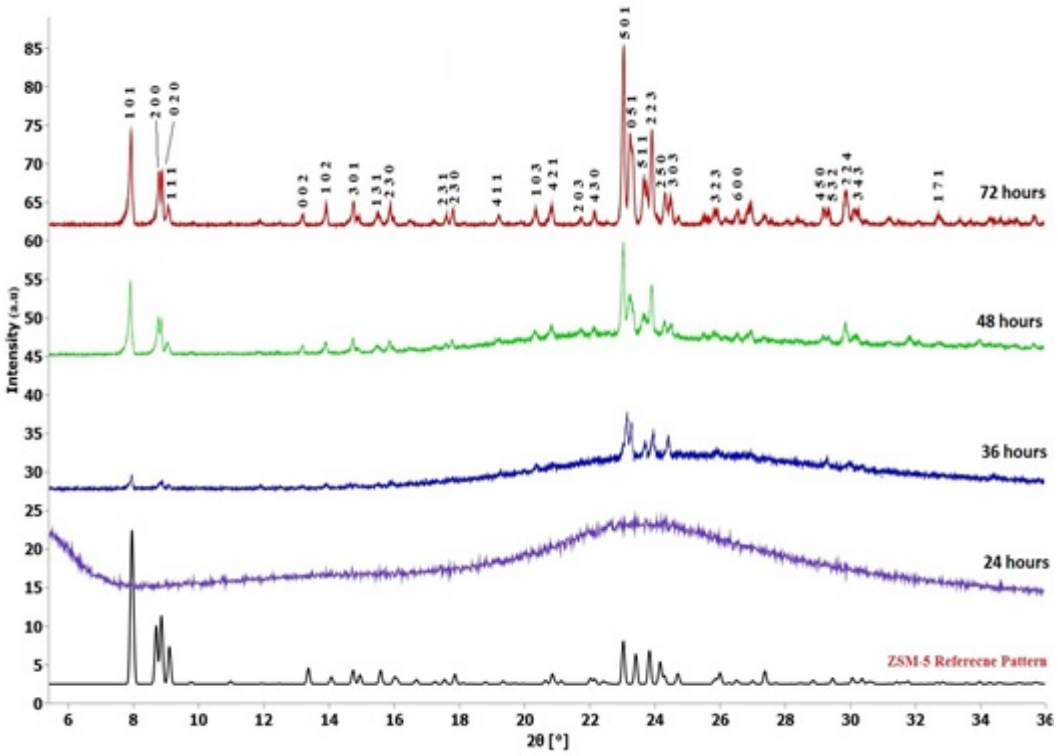

Figure 4.3 XRD pattern of test experiments of *as-synthesised* ZSM-5 at different crystallisation times and at the same temperature.

A conversion in symmetry from orthorhombic to monoclinic was observed after calcination as shown in Figure 4.4. Different factors published includes calcination at 550°C in which transformation of symmetry (orthorhombic to monoclinic) was observed, i.e., sodium and aluminium contents and temperature.[10,13] ZSM-5 was prepared using TPAOH and calcined at 550°C for five hours. ZSM-5 was characterised by XRD measurement before and after calcination in N_2 flow. XRD measurement was carried out for the sample before calcination in the range of $5° < 2\theta < 50°$ at room temperature compared to those

measured from the monoclinic model in space group $P2_1/n$ whilst in the calcined samples at 550°C, the peak position of the pattern was compared to the orthorhombic symmetry of space group $Pn2_1a$ or *Pnma*.[10,13,14] The *hkl* 2 0 0 and 0 2 0 peaks at 2θ = 8– 9° are significantly separated in the orthorhombic pattern as compared to the monoclinic pattern. Similarly, the *hkl* 5 0 1 and 0 5 1 peaks at 2θ = 23–23.5° and the hkl 5 1 1 and 2 2 3 peaks at 23.5–24° are more obvious in the orthorhombic pattern than in the monoclinic pattern. The unit cell parameters of both orthorhombic and monoclinic patterns were calculated with the help of the UnitCell programme. All the calculated parameters are listed in Table 4.2.

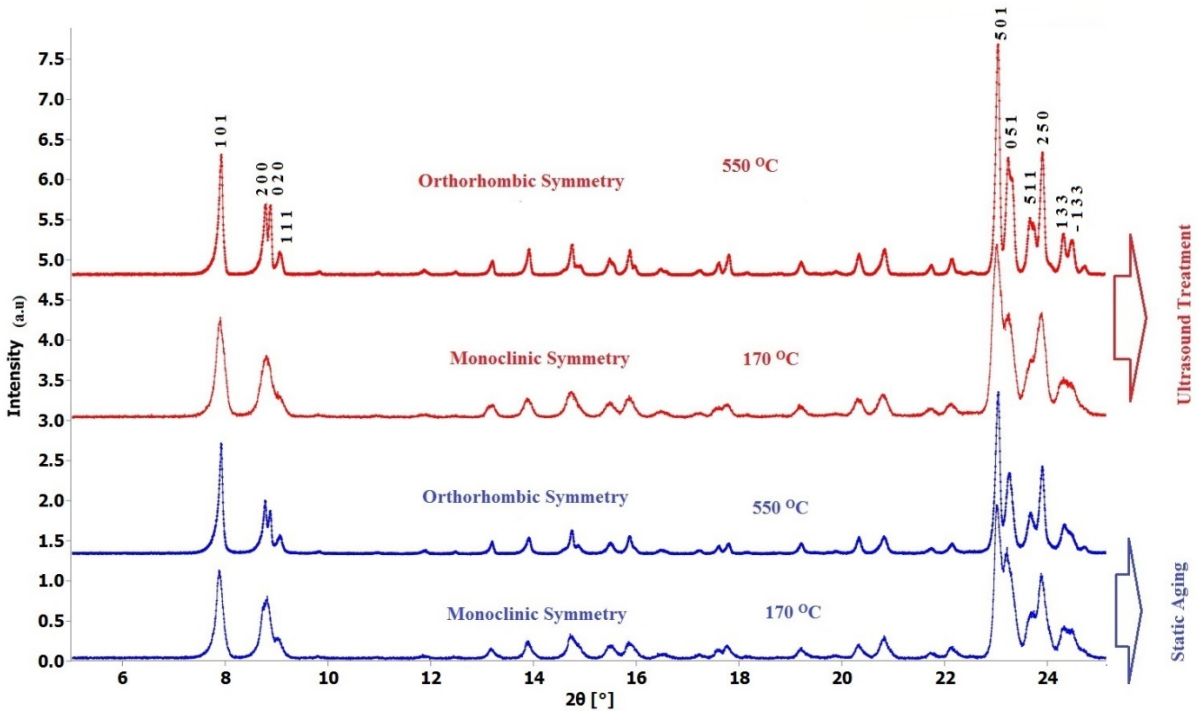

Figure 4.4 XRD pattern of as-synthesised ZSM-5 zeolite transition from orthorhombic to monoclinic after calcination at 550°C.

Table 4.2 As-synthesised nanoZSM-5 with and without ultrasound, unit cell parameters calculated with help of the UnitCell programme.

Mode of Treatment	Symmetry (↓)	a (Å)	b (Å)	c (Å)	α (°)	β (°)	γ (°)
With Ultrasound	Monoclinic	20.01±0.01	20.06±0.01	13.54±0.03	90	85	90
	Orthorhombic	20.44±0.01	19.97±0.01	13.83±0.01	90	90	90
Without Ultrasound	Monoclinic	20.22±0.02	20.019±0.01	13.60±0.02	90	87	90
	Orthorhombic	20.15±0.03	19.95±0.03	13.80±0.04	90	90	90

Figure 4.5 shows the X-ray diffraction pattern of the *as-synthesised* ZSM-5 with increasing time duration of static aging at room temperature before the hydrothermal process. A small broadening was observed in the diffraction pattern from sample (a) to (e) treated for 15, 30, 60, 90 and 120 minutes' aging.

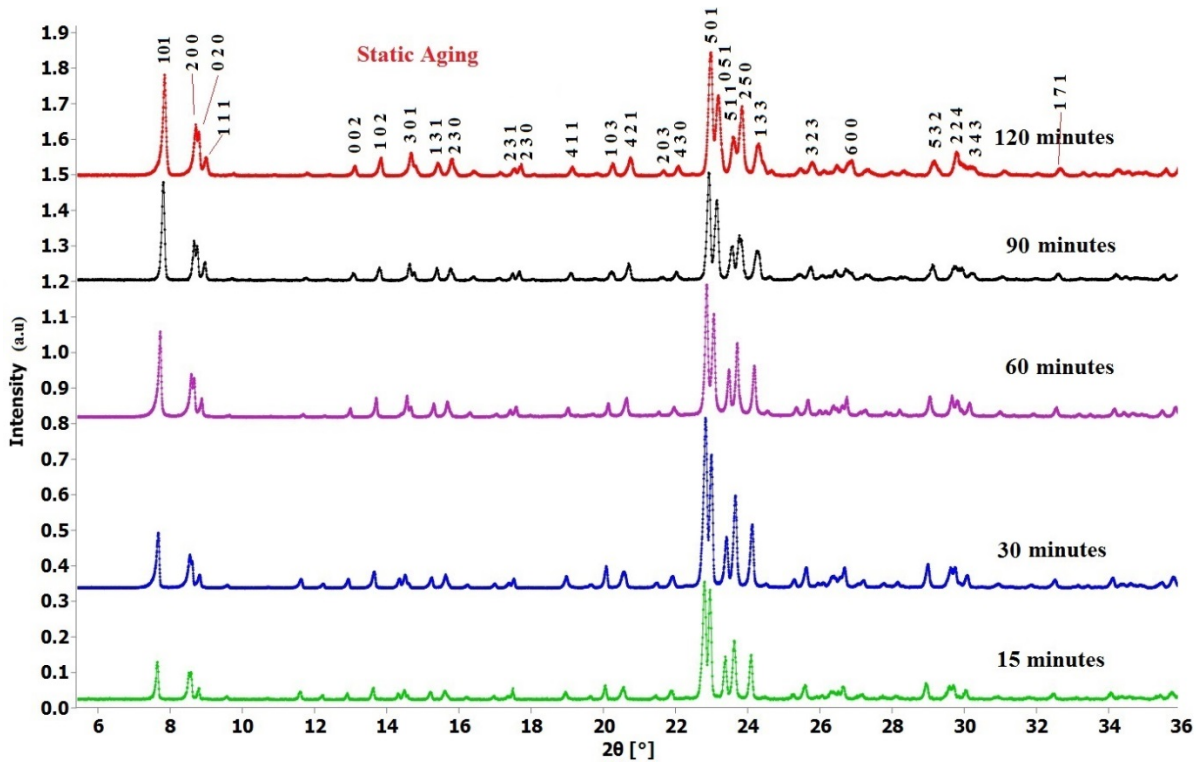

Figure 4.5 X-ray diffraction of *as-synthesised* samples of ZSM-5 zeolite using static aging: (a) 15 min, (b) 30 min, (c) 60 min, (d) 90 min, and (e) 120 min at 170°C.

Table 4.3 shows the average values of three full width half maximum (FWHM) of the high intensity and single peaks from 20 (2θ) to 26 (2θ) of each sample derived from the X'pert HighScore software and their relative crystallinity calculated with the help of the equation in section 3.2.1.

Table 4.3 Representing the observed average FWHM values corresponding to static-aging time and relative crystallinity of *as-synthesised* ZSM-5 zeolite.

Samples	Aging Time (minutes)	FWHM (2θ)[^{o}]	Crystal Size (nm)	Relative Crystallinity (%)
a	15	Not Calculated	Not Calculated	15
b	30	Not Calculated	Not Calculated	32
c	60	Not Calculated	Not Calculated	48
d	90	0.08±0.01	165	59
e	120	0.09±0.03	150	65

As shown in Figure 4.6, it was observed that the temperature of ultrasound bath increases with time. However, the temperature of water in the bath was controlled to around 15–20°C using chilled water. Upon ultrasound pretreatment, no effect was observed on the powder diffraction patterns or the framework of *as-synthesised* nanoZSM-5 zeolite. But a very small increase in the average FWHM of the peaks from 2θ = 20 to 26° was observed, as presented in Table 4.4. The crystallite size was calculated with the help of the Scherrer equation for Gaussian peaks; details are in section 2.4.1. The detailed crystallite sizes are presented in

Table 4.4. A significant reduction in crystallite size was observed by using ultrasound pretreatment.

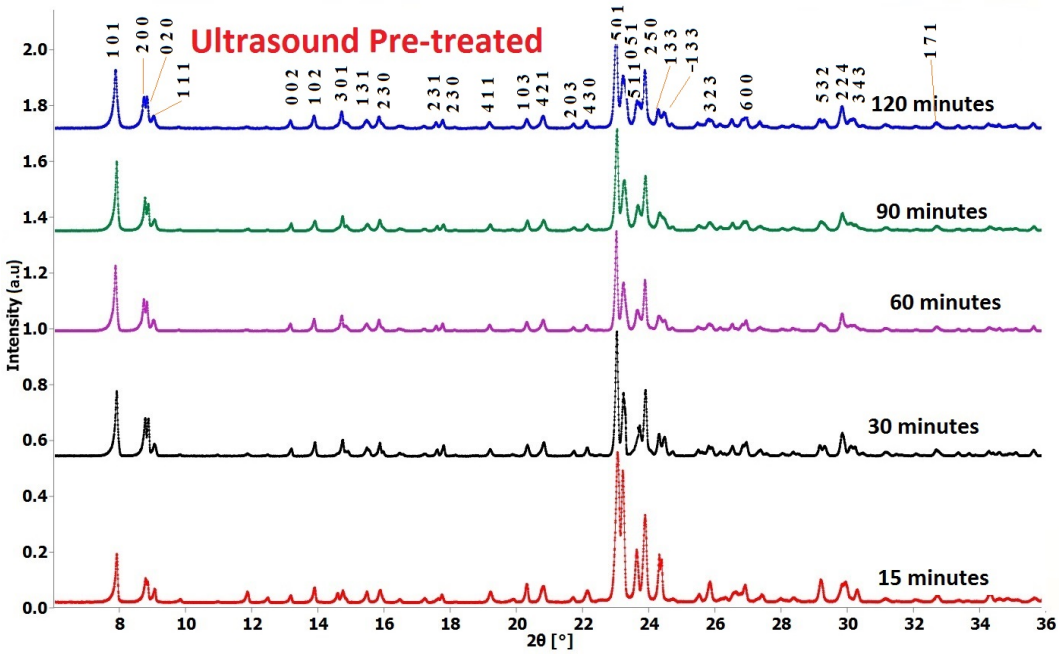

Figure 4.6 X-ray diffraction of as-synthesised samples of ZSM-5 zeolite using ultrasound pretreatment: (a) 15 min, (b) 30 min, (c) 60 min, (d) 90 min, and (e) 120 min.

Table 4.4 Representing the observed average FWHM values corresponding to ultrasound pretreatment time and relative crystallinity of *as-synthesised* ZSM-5 zeolite.

Samples	Ultrasound Assisted Time (minutes)	FWHM (2θ)[^{O}]	Crystallite Size (nm)	Relative Crystallinity (%)
A	15	Not Calculated	Not Calculated	42
B	30	Not Calculated	Not Calculated	48
c	60	0.13±0.01	78	55
d	90	0.15±0.03	66	67
e	120	0.23±0.02	47	82

In both cases (with ultrasound pretreatment and without ultrasound pretreatment), the X-ray diffraction patterns obtained have sharp reflections, indicating high-crystallinity products. Figure 4.7 shows that relative crystallinity consistently increases with time for the ultrasonic method whereas the crystallinity of the static-aging samples appears to level off at around 65%. The ultrasound has a significant influence on crystallinity and can therefore help shorten the crystallisation time.[7,15,16]

The change in crystallinity occurs because of the ultrasound applied before the hydrothermal treatment, which enhances the nucleation rate (produces more nuclei in the mixture) and hence the crystallite size.[7] Therefore, we have demonstrated that the ultrasound pretreatment can be an effective method to control particle size distribution and to minimise the crystallisation time, to meet the required time period for the synthesis of nanoZSM-5 catalysts.

Figure 4.5 and Figure 4.6 showed a significant difference in peak broadening. The peaks of the diffraction patterns of ultrasound-treated samples are broader than those of the obtained diffraction patterns obtained from static-aging samples. The peak broadening is related to crystallite size. Thus, it is clear that the ultrasound pretreatment plays a vital role in controlling crystallite size and crystallisation.[17]

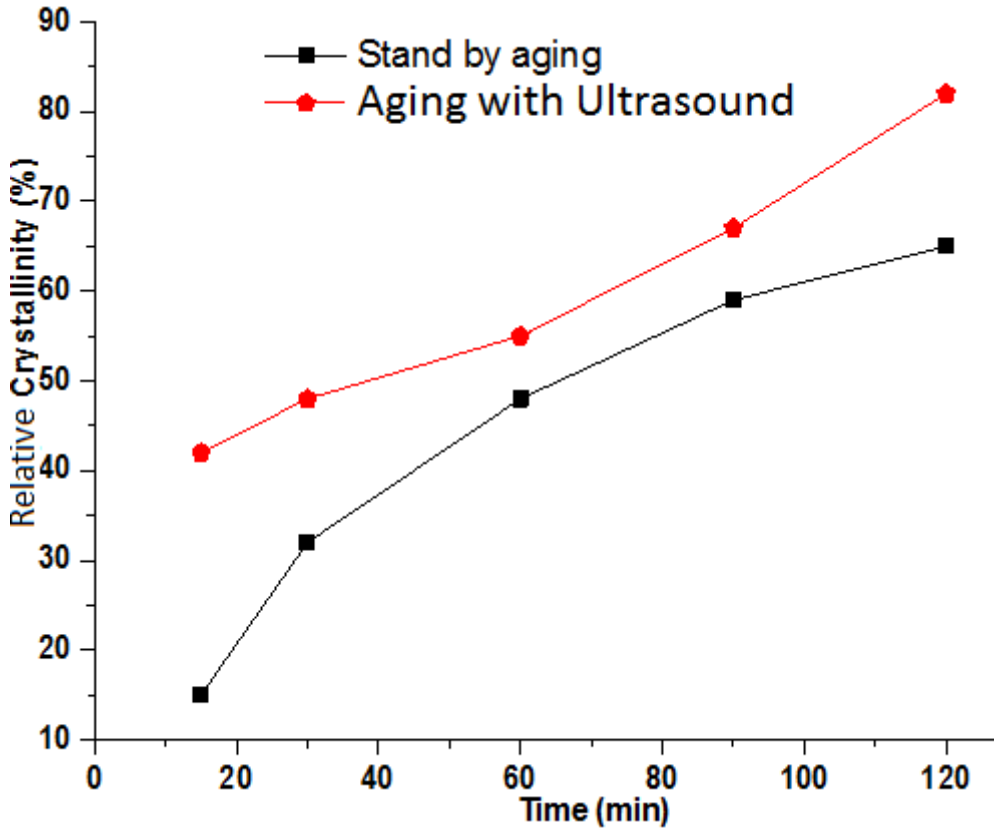

Figure 4.7 *As-synthesised* nanoZSM-5 zeolite using ultrasound pretreatment (red) and static/standby aging (black) showing relative crystallinity increases with time.

4.3.2 Transmission Electron Microscopy (TEM)

The Gatan Digital Micrograph software was used for the quantitative analysis of the average particle size in nanometre scale. Figure 4.8 illustrated the TEM images of sample (a), (b), (c) and (d) of the particle size distribution of *as-synthesised* micro- and nanoZSM-5 pretreated by static aging before hydrothermal treatment. The particle size of the sample treated in 15-minute static aging was too large for TEM imaging; therefore, we were unable to produce the image of the sample. The particle size of a single crystal of the *as-synthesised* sample (a) was observed to be approximately >5 µm (5,000 nm) and has rectangular morphology, whilst the 1–2 µm (1,000–2,000 nm) diameter particles in sample (b) have square morphology as shown in Figure 4.8. Samples (a) and (b) were treated for 30

minutes and 60 minutes, respectively. Aggregates of smaller particle sizes of approximately 700–1,000 nm diameter were observed for sample (c), treated in 90-minute static aging, as seen in Figure 4.8 (c). The recorded image of sample (d) shows a particle size in the range of 500–800 nm. The nanoparticles of zeolite catalysts reported in the literature used the static-aging method for long periods (several days).[6,15,18] The results also presented here are consistent with the reported results in the literature. But we performed a short period of static aging before conventional hydrothermal treatment for the syntheses of nanoZSM-5 catalysts using different experimental conditions.

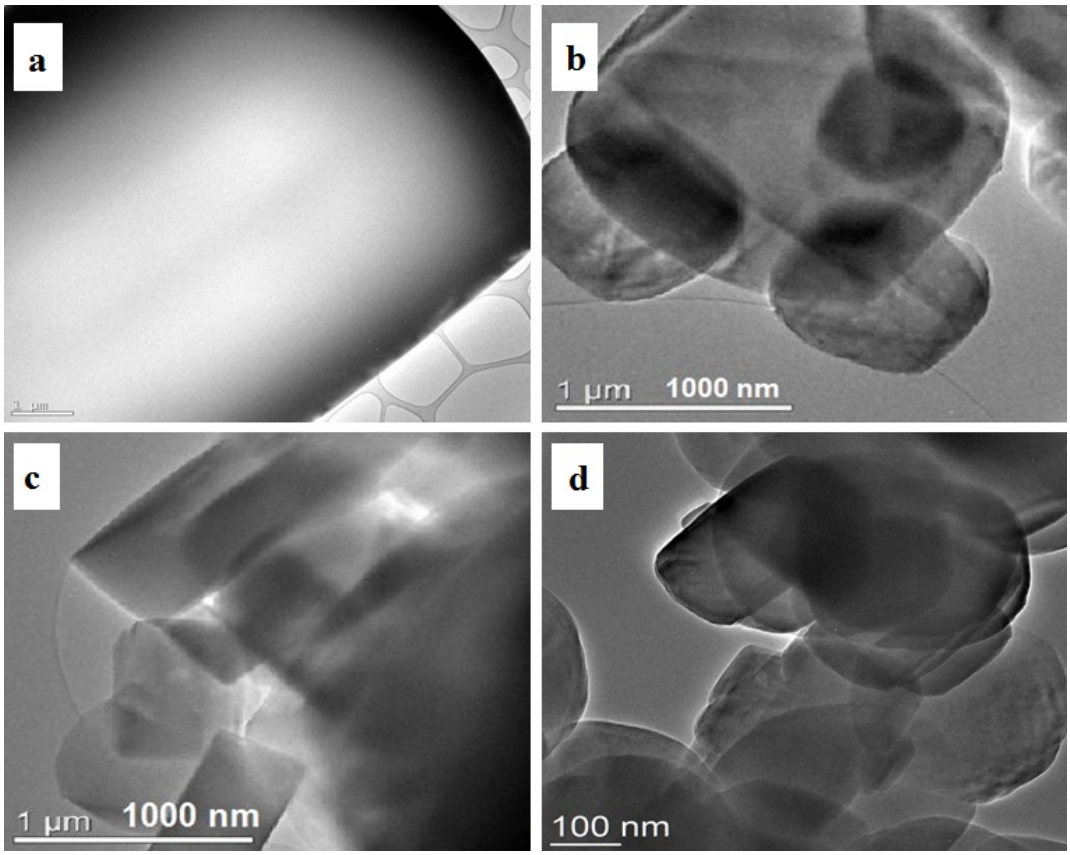

Figure 4.8 TEM images of the as-synthesised micro- and nanoZSM-5 using the static-aging method. Samples were pretreated for (a) 30 minutes, (b) 60 minutes, (c) 90 minutes and (d) 120 minutes at 170°C synthesis temperature.

Figure 4.9 demonstrated TEM images of samples (a), (b), (c) and (d) of the *as-synthesised* nanoZSM-5 catalyst pretreated with ultrasound. The particle size

of the sample treated with ultrasound for 15-minute aging was large enough and out of the range of TEM. Figure 4.9 (a) represents the samples treated with ultrasound for 30 minutes showing that cubic crystals were prepared. Each single crystal is approximately 500–1,000 nm in diameter. Some small particles are also observed to have attached to the surface of the large particles. This suggested that the particle sizes were not uniformly distributed. However, in Figure 4.9 (b), more uniform particles were obtained, which are in the range of 400–500 nm diameter. Similarly, sample (c) shows similar morphology to that of sample (b). These small aggregated particles have 400 nm diameter. Figure 4.9 (d) illustrates the sample pretreated with ultrasound before hydrothermal treatment and shows a nonuniform morphology. These nanoZSM-5 particles have 50–100 nm diameters. It was observed that the nanoparticles are very beam sensitive and lose crystallinity within 10–30 seconds of exposure to the electron beam. Some of the calculated nanocrystallite sizes from the X-ray diffractions using the Scherrer equation also corresponded to the TEM crystallite sizes as described in Table 4.4. The average particle sizes illustrated in Table 4.5 are observed on TEM. The difference between the calculated crystallite size from XRD diffraction and the one observed on the TEM are nearly coincide. This might be because FWHM is affected by the structure strain.

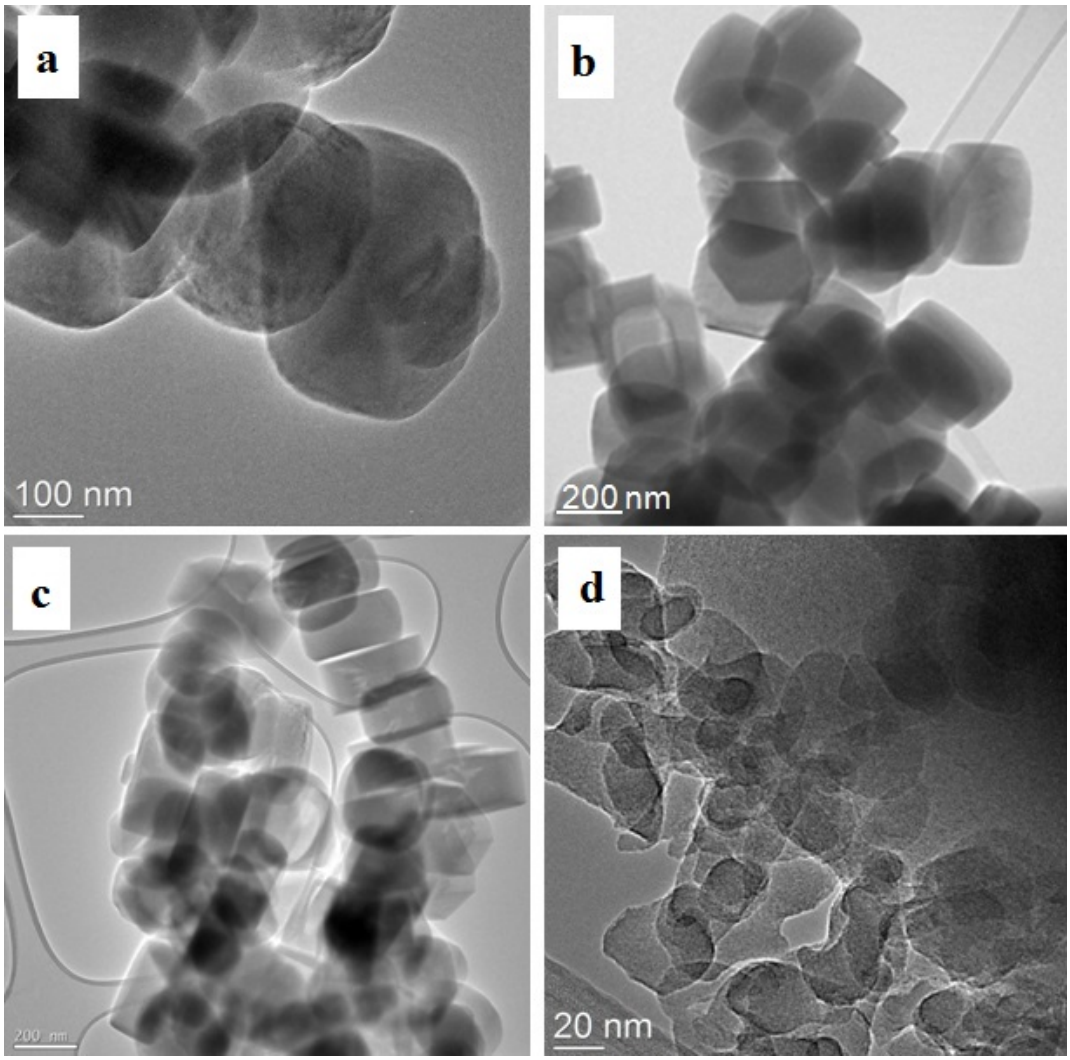

Figure 4.9 TEM images of the as-synthesised nanoZSM-5 using ultrasound pretreatment for (a) 30 minutes, (b) 60 minutes, (c) 90 minutes and (d) 120 minutes at 170°C synthesis temperature.

Table 4.5 Average particle size of *as-synthesised* ZSM-5 observed on TEM micrographs using static and ultrasound pretreatments.

Sample	Pretreatment		Particle size, nm
	Duration, minute	Aging method	
A	30	Static	5000±10
		Ultrasound	900±15
B	60	Static	2000±10
		Ultrasound	500±10
C	90	Static	800±10
		Ultrasound	400±5
D	120	Static	600±10
		Ultrasound	80±10

4.3.3 Scanning Electron Microscopy (SEM)

SEM micrographs demonstrated the two different pretreatment methods of the *as-synthesised* nanoZSM-5 morphology and particle size distribution. Figure 4.10 (a), (b), (c) and (d) show the images of the *as-synthesised* nanoZSM-5 particles using static aging before the hydrothermal treatment. A very high aggregation of particles was observed when *as-synthesised* samples were pretreated with static aging. Figure 4.10 (a) illustrates a single particle size is >10 μm (10,000 nm), with small particles aggregated together. The aggregations are clearly visible and observed an average size of 1,000–5,000 nm for each component of the large particle. Increasing the static-aging time period reduces the aggregation. The best result observed was of sample (e) at approximately 500 nm, pretreated for 120 minutes of static aging whilst samples (b) and (c) have spherical morphology having particle sizes ranging from 8 to 10 μm (8,000–10,000 nm) and 4 to 8 μm (4,000–8,000 nm) diameter. Sample (d) has square morphology with particle size ranging from 1,000 to 1,500 nm. In the *as-synthesised* powder samples using static-aging treatment, disorder morphology was observed as well as a decrease in

particle size. Treated with ultrasound, the *as-synthesised* nanoZSM-5 particles ranged from 7 μm (7,000 nm) to 300 nm in diameter as shown in Figure 4.11 (a), (b), (c) (d) and (e). The particles have square-shaped morphology. It is assumed that these aggregations are an intergrowth of the nanoparticles (primary particles) which build the large particles. It was also observed that using the ultrasound treatment, the aggregation decreases. Samples (a), (b) and (c) show similar morphology and an observed average particle dimension of 7 μm (7,000 nm), 3 μm (3,000 nm) and 800 nm, respectively, whilst sample (d) shows a square morphology made of small square units of 300–500 nm. In the *as-synthesised* sample (e), the observed particle size was 200–300 nm using ultrasound pretreated for 120 minutes.

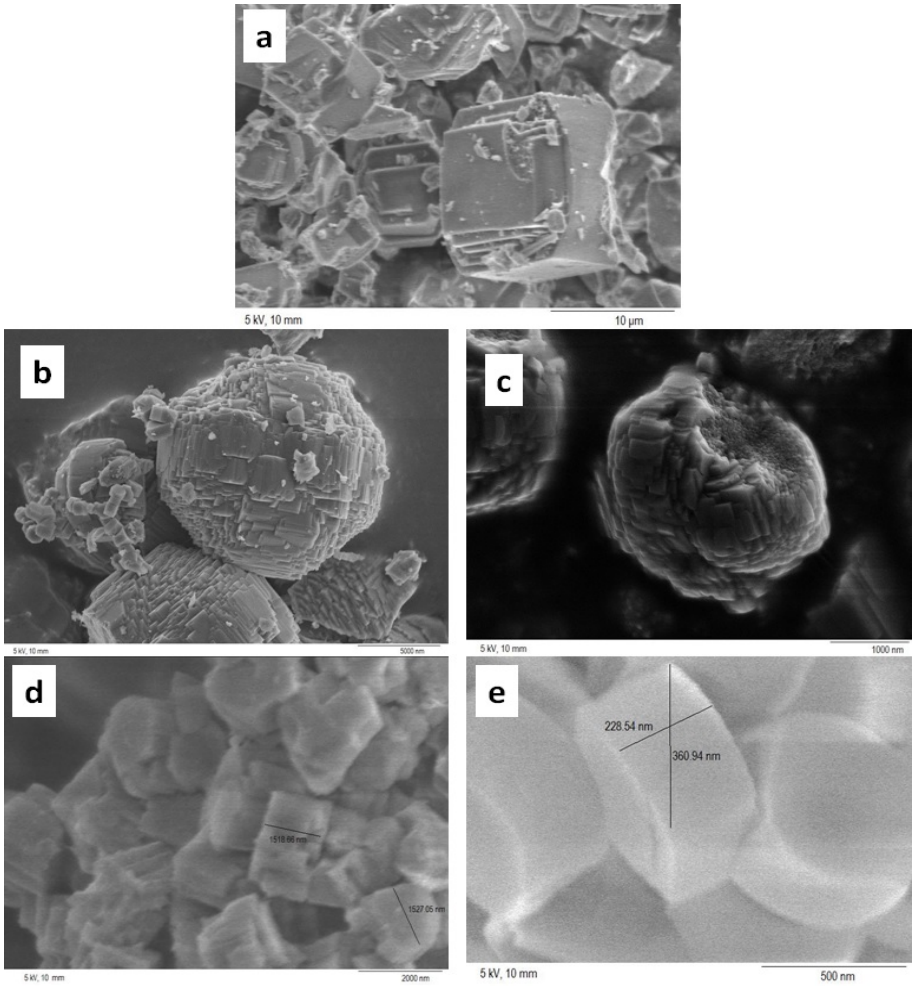

Figure 4.10 SEM images of the *as-synthesised* micro- and nanoZSM-5 pretreatment static aging, for (a) 15 minutes, (b) 30 minutes, (c) 60 minutes, (d) 90 minutes and (e) 120 minutes at 170°C synthesis temperature.

The observed average particle sizes using SEM analysis are illustrated in Table 4.6. The morphology of some of the samples observed on the SEM of both pretreatment methods was similar to those morphologies observed in TEM micrographs.

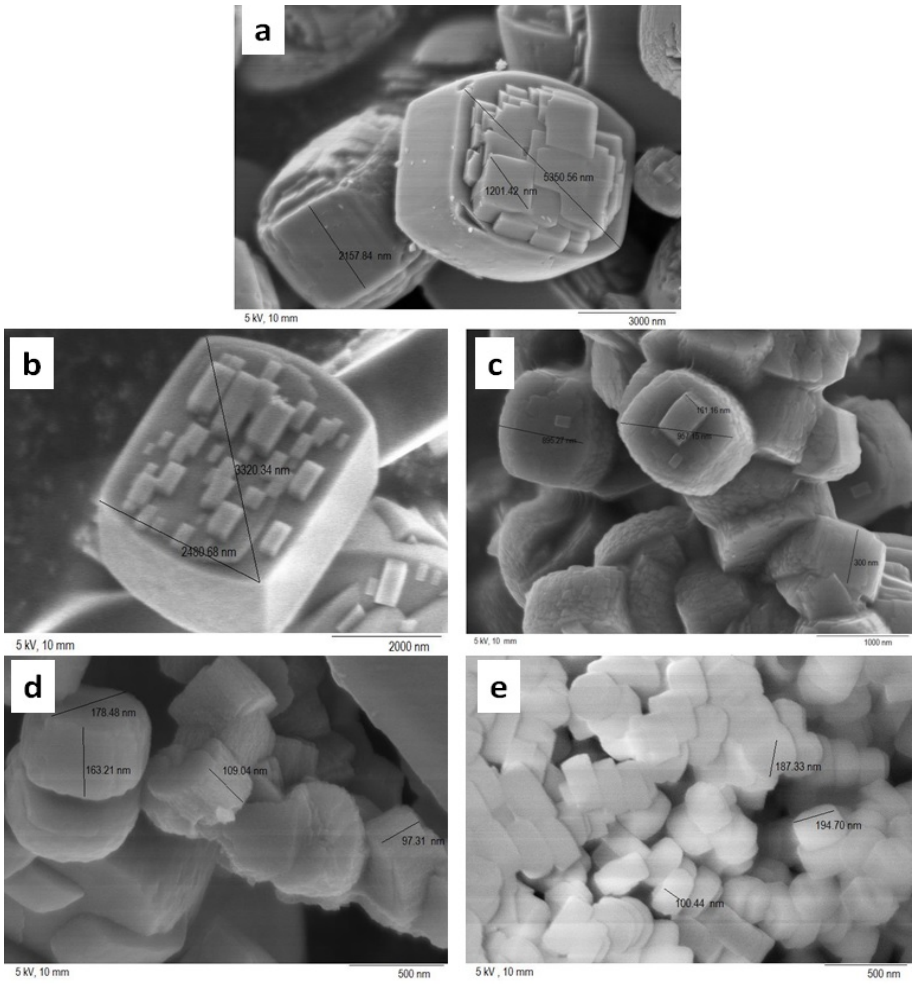

Figure 4.11 SEM images of the as-synthesised micro- and nanoZSM-5 using ultrasound pretreatment for (a) 15 minutes, (b) 30 minutes, (c) 60 minutes, (d) 90 minutes and (e) 120 minutes at 170°C synthesis temperature.

Table 4.6 Average particle size of *as-synthesised* ZSM-5 obtained on SEM micrographs using static and ultrasound pretreatments.

Methods of Pretreatment	Average Representative Particle Size (nm)				
	a	**b**	**c**	**d**	**e**
Pretreatment Time (minutes)	15	30	60	90	20
Ultrasound	7000±10	3000±20	800±10	400±10	200±15
Static	10000±10	10,000±20	6000±15	1000±10	500±10

4.3.4 Dynamic Light Scattering (DLS)

Particle size distribution was investigated by dynamic light scattering of the as-synthesised samples shown in (a), (b), (c) and (d) without the application of ultrasound pretreatment. In dynamic light scattering, the scanning scale ranges from 0 nm to 10,000 nm. The system was unable to analyse the sample treated for 15-minute static aging because the particle size was out of the range of the setup scale in the DLS system measurement. This shows that the average particle size was greater than 10 μm (10,000 nm). DLS measurement of sample (a) showed an aggregated particle size of 5–6 μm (5,000 nm to 6,000 nm). As the static-aging duration was increased, the particle size was reduced. In Figure 4.12, spectra (b), (c) and (d) illustrate the average particle sizes 3,000 nm, 1,300 nm and 600 nm of the samples treated at 60 minutes, 90 minutes and 120 minutes, respectively; the particle size subsequently decreased.

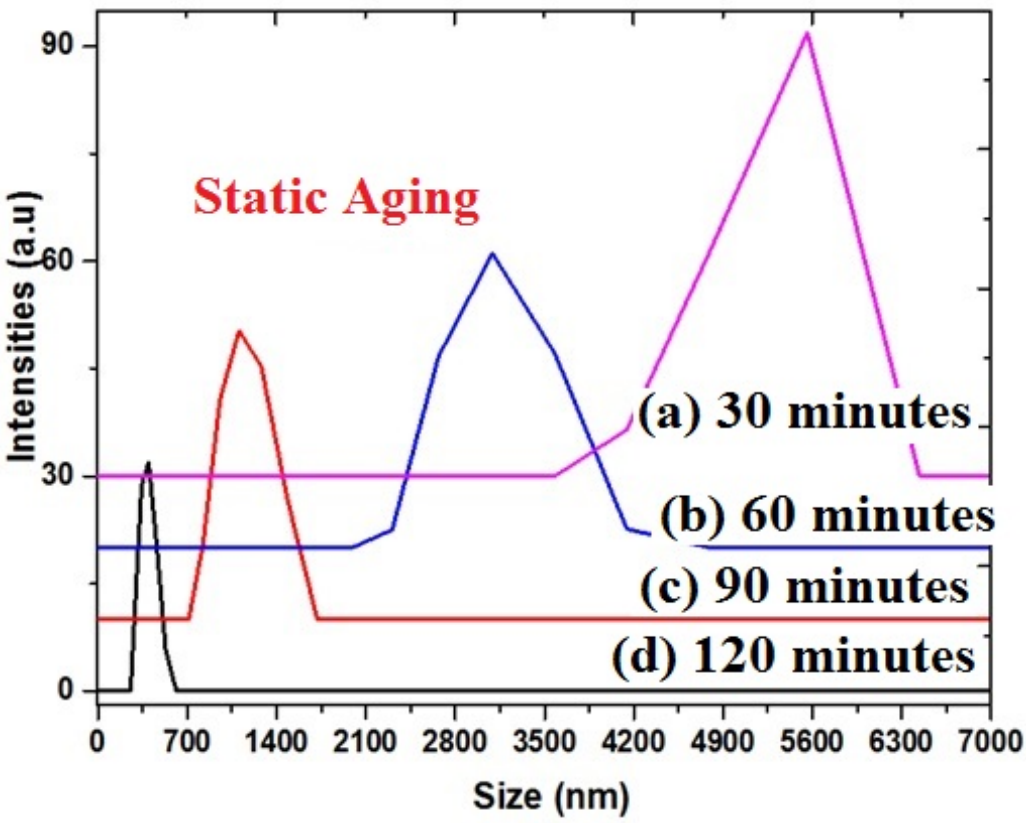

Figure 4.12 DLS data of the *as-synthesised* ZSM-5 samples using static aging at 30 minutes, 60 minutes, 90 minutes and 120 minutes at 170°C crystallisation.

The analysis of the particle size distribution of the samples *as-synthesised* with ultrasound pretreatment was confirmed by DLS as shown in Figure 4.13 (a), (b), (c), (d) and (e). The average particle size was obtained in the colloidal solution of the crystalline suspension of *as-synthesised* nanoZSM-5. Samples (a) to (e) were treated with ultrasound for different time intervals, i.e., 15 minutes, 30 minutes, 60 minutes, 90 minutes and 120 minutes, respectively. The observed average particle size of the samples treated for 15 and 30 minutes was 6,000 nm and 2,500 nm, respectively. A significant reduction of the average particle sizes of samples (c), (d) and (e) (800 nm, 500 nm and 50–100 nm, respectively) was observed. It was also observed that particle size decreases as the ultrasound treatment time increases. The particle size summary of both pretreatment methods are listed in Table 4.7

The results shown in Figure 4.13 of samples treated with ultrasound differ strongly from the results obtained in Figure 4.12 for those treated with static aging with respect to morphology as well as particle size distribution. It was observed that the DLS measurement has good agreement with the data obtained from SEM analysis.[19,20]

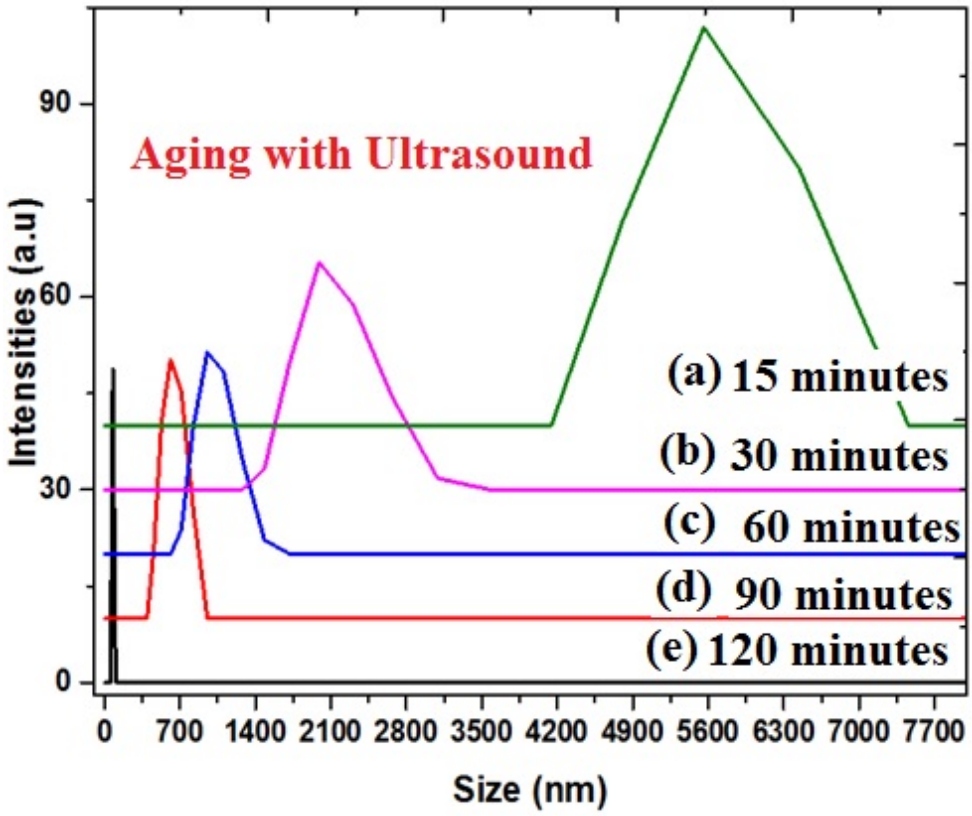

Figure 4.13 DLS data of the as-synthesised ZSM-5 samples using ultrasound aging at 30 min, 60 min, 90 min and 120 min at 170^{O}C crystallisation.

It can be concluded that by using ultrasound pretreatment, a relatively monodispersed sample of the nanoZSM-5 particles was produced with an average diameter of 50–100 nm. Sonication also helps in the reduction of particle aggregations.

Table 4.7 Particle size of *as-synthesised* ZSM-5 obtained on DLS using static and ultrasound pretreatment.

Methods of Pretreatment	Particle Size (nm)				
	a	**b**	**c**	**d**	**e**
Pretreatment Time (minutes)	15	30	60	90	120
Ultrasound pretreatment	8000±10	4000±20	900±15	600±20	200±10
Static pretreatment	11000±10	5000±20	2000±15	1200±10	600±15

4.3.5 Energy-Dispersive Spectroscopy (EDS)

The chemical composition of all the *a- synthesised* samples was analysed by EDS. EDS measurement is one of the best techniques to confirm each component of the as-synthesised nanoZSM-5. EDS was used during TEM measurements to obtain the average weight percent elemental composition of *as-synthesised* ZSM-5 samples (a), (b), (c), (d) and (e).

Table 4.8 and Table 4.9 illustrate the percent composition of Si, Al and O, which are the main components of the *as-synthesised* nanoZSM-5 framework structure. The calculated SAR is in the range of 50–65 in the pretreatment samples. The observed difference in SAR may be due to the handling of the mixture during syntheses.

Table 4.8 Weight percent (%) chemical composition of as-synthesised ZSM-5 zeolite using static aging obtained by EDS.

Sample	Weight (%) Elemental Composition			Si/Al
	Si	Al	O	
a	30	0.49	58	63±2
b	30	0.51	55	60±3
c	29	0.45	57	65±5
d	30	0.48	59	63±4
e	28	0.52	58	55±3

Table 4.9 Weight percent (%) chemical composition of as-synthesised ZSM-5 using ultrasound pretreatment obtained by EDS.

Sample	Weight (%) Elemental Composition			Si/Al
	Si	Al	O	
a	23	0.41	58	57±3
b	22	0.48	57	47±5
c	24	0.44	58	60±2
d	24	0.36	58	65±5
e	23	0.42	58	58±3

Table 4.10 and Table 4.11 show the particle sizes observed using different analytical techniques of *as-synthesised* samples using static and ultrasound pretreatments with respect to the same SAR from 50 to 65. These results correspond to the already reported results of nanocrystalline ZSM-5 synthesised with respect to SAR from 50–60.[12,21] However, their synthesis mechanism and pretreatment methods are different from our proposed methods of pretreatment.

Table 4.10 Particle size distribution of as-synthesised ZSM-5 zeolite observed on different spectroscopic techniques with respect to SAR using static-aging pretreatment.

Samples	Average Representative Particle Size (nm)				Si/Al (SAR)	Relative Cryst (%)
	XRD	TEM	SEM	DLS		
a	Not Calculated	Not Calculated	10000±10	11000±10	63±2	15
b	Not Calculated	2000±10	9000±20	5000±20	60±3	32
c	Not Calculated	1000±10	60000±15	2000±15	65±5	48
d	165±3	800±10	1000±10	1200±10	63±4	59
e	150±2	500±15	500±10	600±15	55±3	65

Table 4.11 Particle size distribution of *as-synthesised* ZSM-5 zeolite observed on different spectroscopic techniques with respect to SAR using ultrasound pretreatment.

Samples	Average Representative Particle Size (nm)				Si/Al (SAR)	Relative Crystallinity (%)
	XRD	TEM	SEM	DLS		
a	Not Calculated	Not Calculated	7000±10	8000±10	63±2	42
b	Not Calculated	900±15	3000±20	4000±20	60±3	48
c	78±4	500±10	800±10	900±15	65±5	55
d	66±2	400±5	400±10	600±20	63±4	67
e	47±5	80±10	200±15	200±10	55±3	82

4.3.6 N_2 Adsorption/Desorption

Surface areas were determined by using the BET equation discussed in section 2.4.5. It was observed that most of the samples have a broad pore diameter range, from 50 and 150 Å. The textural properties of each sample including the pore volume, BET surface area and external surface area all increased with an increase in pretreatment static method as shown in Figure 4.14 and Table 4.12. Generally, the internal surface area decreased with little respect to the particle size distribution. A significant increase of 38% in the external surface area from sample (a) to (b) was observed. The overall increase in external surface area from sample (a) to (e) is about 62% treated with static aging at 15 minutes and 120 minutes, respectively.

Type IV Langmuir adsorption/desorption isotherms were observed for *as-synthesised* micro- and nanoZSM-5 as shown in Figure 4.14. This is the most common type of isotherm observed in mesoporous materials as discussed in detail in section 2.4.5. The observed isotherms of sample (a), (b), (d) and (e) correspond to subtypes H3 and H4. However, samples (c) and (d) demonstrated the subtype H2 isotherm. The pores of samples (a), (b), (c) are disordered, have lamellar structure, slit and wedge shaped, whilst according to subtype H2, cylindrical and spherical pores are expected for samples (c) and (d). The filling of the pore volume also decreased as long as the pretreatment time increased as observed in Figure 4.14.

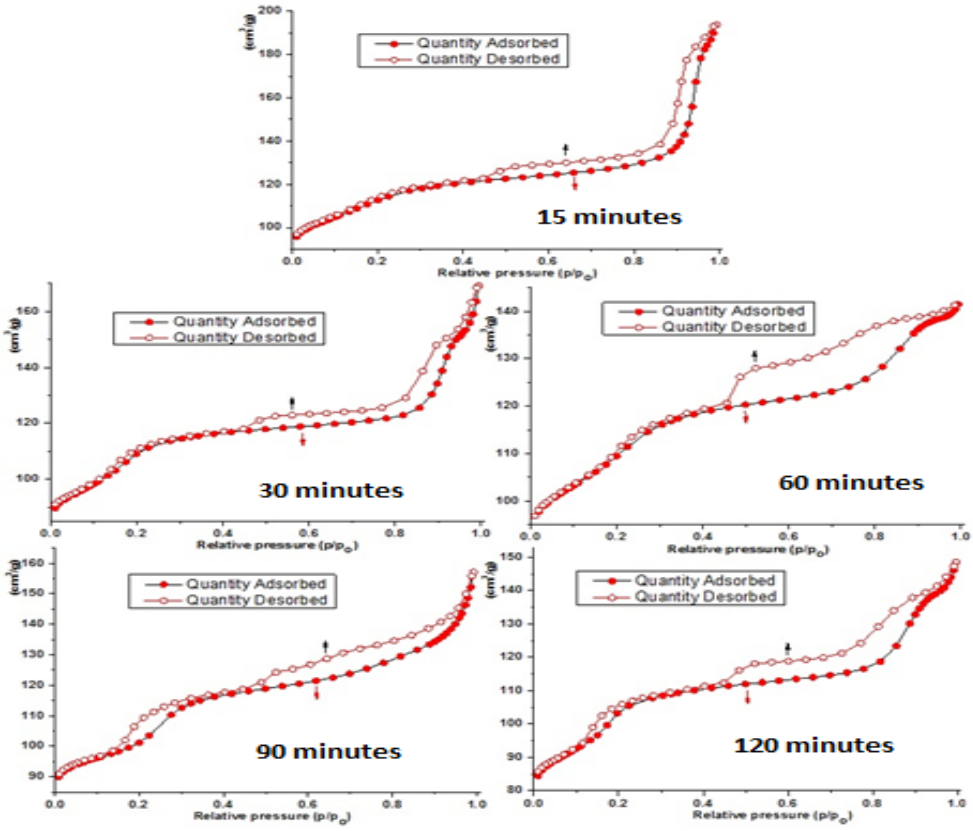

Figure 4.14 N_2 adsorption/desorption isotherms of micro- and nanoZSM-5 using static aging for (a) 15 min, (b) 30 min, (c) 60 min, (d) 90 min and (e) 120 min at 170°C crystallisation.

Table 4.12 BET surface area, external surface area and pore volume observed of as-synthesised samples treated with static method of aging.

Samples	Pretreatment Time (min)	SAR (Si/Al)	S_{BET} (m^2/g)	$S.A_{Ext}$ (m^2/g)	Pore Vol(cm^3/g)	Relative Crystallinity (%)
a	15	63±1	143±2	65.63	0.04±0.01	15
b	30	60±3	272±2	106.72	0.07±0.01	32
c	60	65±2	316±7	140.86	0.08±0.01	48
d	90	63±4	354±1	172.47	0.08±0.01	59
e	120	55±4	388±2	185.75	0.09±0.01	65

The nitrogen adsorption and desorption isotherms of the samples pretreated using ultrasound are quite similar to the type IV Langmuir isotherm as shown in Figure 4.15 (a), (b), (c), (d) and (e). Samples (a), (b) and (c) correspond to the subtype H4 Langmuir adsorption and desorption isotherm. According to the subtype H4 isotherm, the *as-synthesised* nanoZSM-5 samples (a), (b) and (c) are composed of micro- and mesopores. It is suggested that samples (d) and (e) are similar to subtype H1, which described mesopores as having a cylindrical shape of the as-synthesised nanoZSM-5. Also, samples (d) and (e) give a steep capillary condensation step observed at 0.5–0.9 (p/p_o), which is the property of an order of mesoporous solids with large uniform pore sizes.[22,23] Table 4.13 illustrates a remarkable increase in external surface area and BET surface area from sample (a) to (e), when pretreated with ultrasound from 15 to 120 minutes, respectively. There is a 23% increase in external surface area from sample (a) to (b), whilst there is an 11% increase in external surface area from sample (d) to (e) pretreated with ultrasound for 90 and 120 minutes, respectively. There is a significant 51%

increase in external surface area in samples (a) and (e) pretreated with ultrasound for 15 minutes and 120 minutes, respectively.

Table 4.13 BET surface area, external surface area and pore volume observed of as-synthesised samples treated with static method of aging.

Samples	Pretreatment Time (min)	SAR (Si/Al)	$S.A_{Total}$ (m^2/g)	$S.A_{External}$ (m^2/g)	Pore Volume (cm^3/g)	Relative Crystallinity (%)
a	15	57±4	294±2	117±3	0.08±0.01	42
b	30	47±5	373±2	151±3	0.09±0.01	48
c	60	60±3	389±3	171±2	0.11±0.01	55
d	90	65±5	407±1	214±1	0.12±0.01	67
e	120	58±3	410±1	239±4	0.13±0.01	82

The pore size distribution analysis was examined by the BJH (Barrett-Joyner-Halenda) method of adsorption for all *as-synthesised* samples obtained both with and without ultrasound treatments. Figure 4.16 (a), (b), (c), (d) and (e) show that the initial micropore filling occurs from 1.5–2 nm, which is considered a micropore by the IUPAC system (<2 nm), whilst the adsorption occurs in the range of 2–50 nm considering the mesoporous materials.[24] So all the *as-synthesised* samples pretreated with the static method of aging is considered microporous and mesoporous ZSM-5. It was also observed that the pore distribution is not uniform in samples (a) and (b). On the other hand, the uniform pore distribution observed in samples (c), (d) and (e) are shown in Figure 4.16.

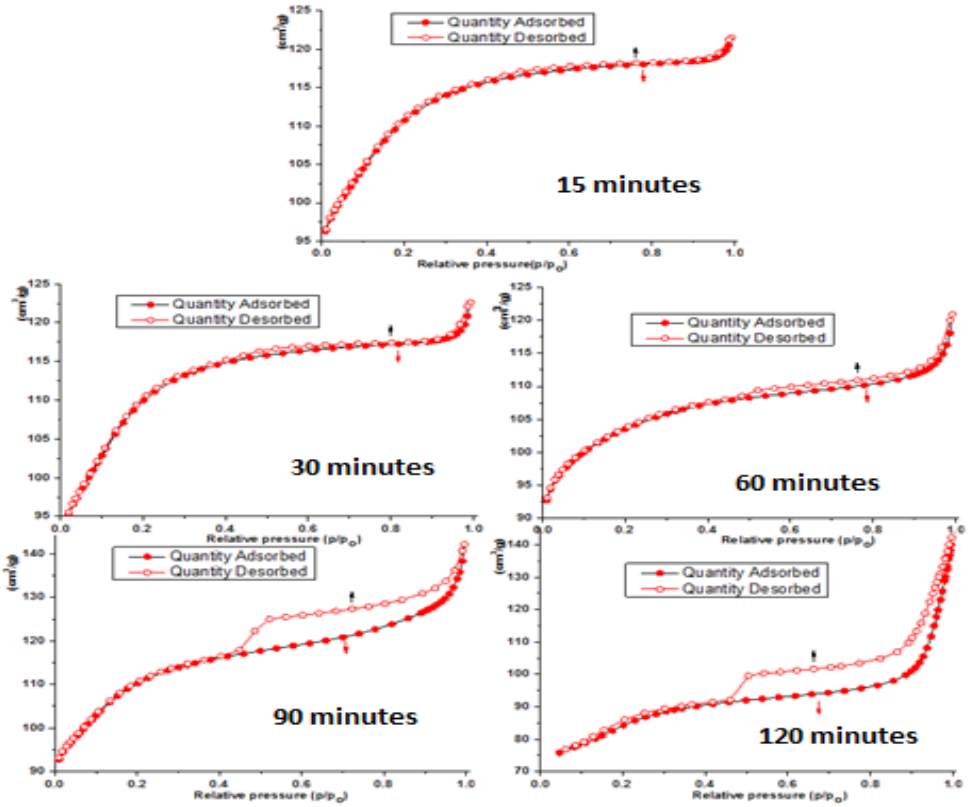

Figure 4.15 N_2 adsorption/desorption isotherms of micro- and nanoZSM-5 using ultrasound pretreatment for (a) 15 min, (b) 30 min, (c) 60 min, (d) 90 min and (e) 120 min at 170°C crystallisation.

Figure 4.17 (a), (b), (c), (d) and (e) fall within the mesoporous range from 2–50 nm according to the IUPAC system. Sample (a) showed a disordered pore size distribution, and the filling of the pore was observed to start only above 2 nm, so sample (a) is composed of mesopores only. On the other hand, in samples (b) to (e), the adsorption initiated below 2 nm, indicating they are composed of micropores as well as mesopores. The samples pretreated using ultrasound for a long duration observed a uniform micropore and mesopore distribution. It was observed that as long as the pretreatment time increases, the uniform pore distribution occurs along with higher crystallinity.[25,26]

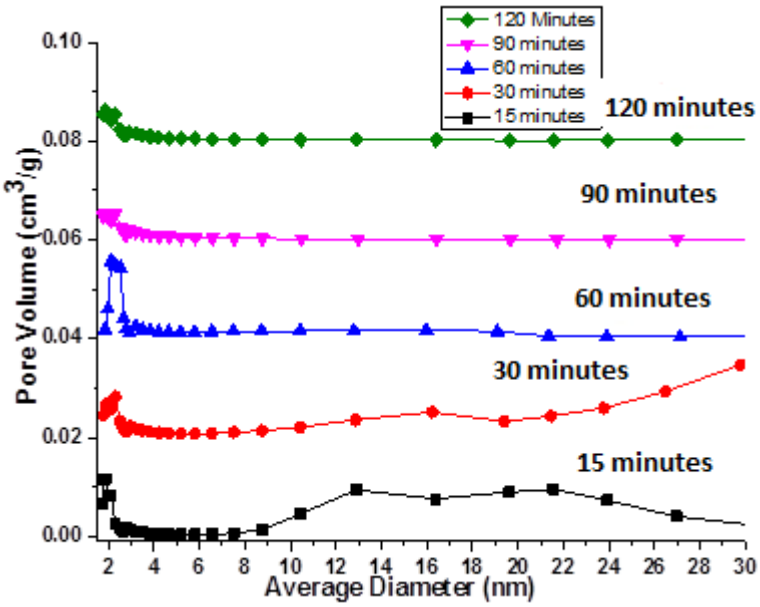

Figure 4.16 BJH pore size distribution of the samples treated with static aging at (a) 15 min, (b) 30 min, (c) 60 min, (d) 90 min and (e) 120 min.

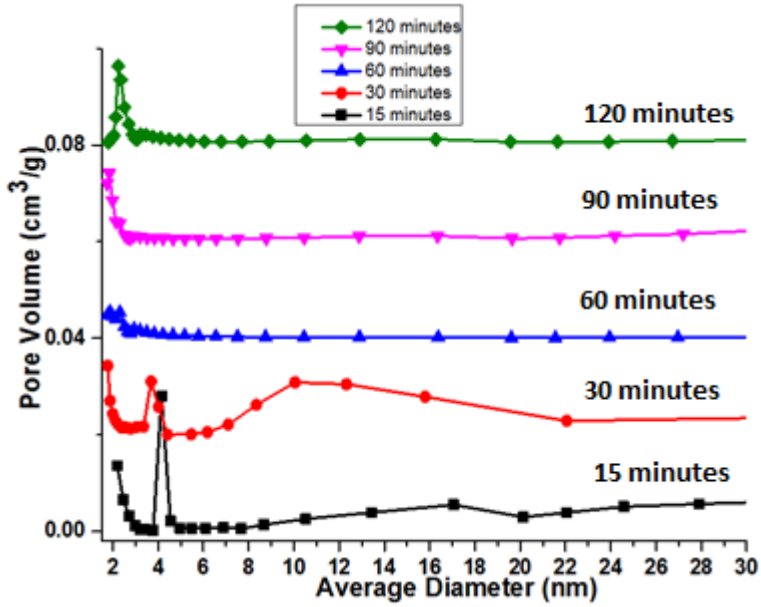

Figure 4.17 BJH pore size distribution of the samples treated using ultrasound treatment at (a) 15 min, (b) 30 min, (c) 60 min, (d) 90 min and (e) 120 min.

It is concluded that ultrasound is extremely effective in obtaining nanoparticles that have higher specific surface area and external surface area. Comparing the pore volumes, there is a huge difference between two different methods of pretreatment. Not only is there a significant effect of ultrasound on

crystallinity and particle size distribution, but ultrasound also enhances the physicochemical characteristics of the nanoZSM-5 catalyst. [17]

4.3.7 Solid-state Magic Angle Spinning Nuclear Magnetic Resonance (MAS NMR)

Tetramethylsilane (TMS) is the standard reference compound used in NMR analysis. In the zeolite system, silicon is tetrahedrally coordinated in the framework. Therefore, it has five different potential environments including Si(nAl) where n ($n \leq 4$) is the number of Al atoms connected to silicon via oxygen bridges.

The ^{27}Al MAS NMR spectra can reveal detailed information about the zeolite framework compared to other spectroscopic techniques. Generally, ^{27}Al MAS NMR spectra of the central transition aluminium-containing materials give a single resonance at 54 ppm assigned to the framework tetrahedrally coordinated Al atom (4Al).[27,28] ^{27}Al chemical shift of octahedral coordination or extra framework (Al(6)) of Al-containing materials occurs in the range of -13.2 ppm to +1.4 ppm.[29]

The chemical shift of ^{27}Al for *as-synthesised* calcined micro- and nanoZSM-5, 54.58 and 0 ppm respectively, described the tetrahedrally coordinated Al framework and octahedrally coordinated non-Al framework as shown in Figure 4.18 (a), (b), (c), (d) and (e). It was observed that by changing the pretreatment period using the static method, there was has no effect on the tetrahedrally coordinated Al framework; all the peaks have the same symmetry. However, there is an increased in aluminium nonframework (octahedrally coordinated) resonance at 0 ppm. Zhang et al.[30] reported that particle size

decreases with an increasing amount of non-Al framework. In the result presented in Figure 4.18, extra frame aluminium increases from sample (a) to (e) and observes a very small peak broadening. ^{27}Al MAS NMR spectra confirm the tetrahedrally coordinated Al(4) framework of ZSM-5 samples as well as the resonance at 0 ppm assigned to Al(6) nonframework (octahedrally coordinated).[26–28,30]

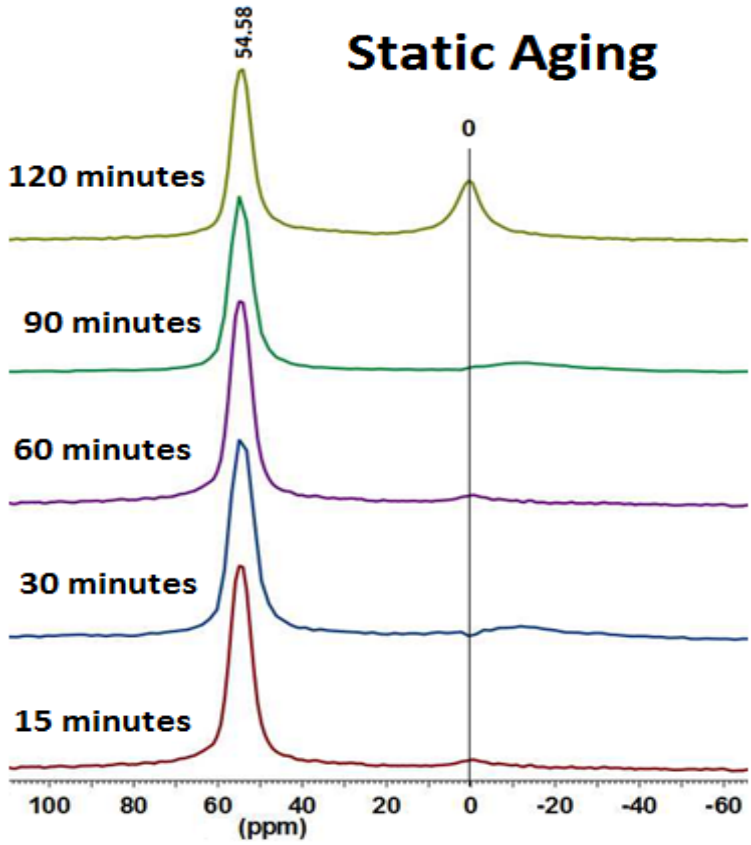

Figure 4.18 ^{27}Al MAS NMR of as-synthesised samples using static method of aging at 15 min, 30 min, 60 min, 90 min and 120 min.

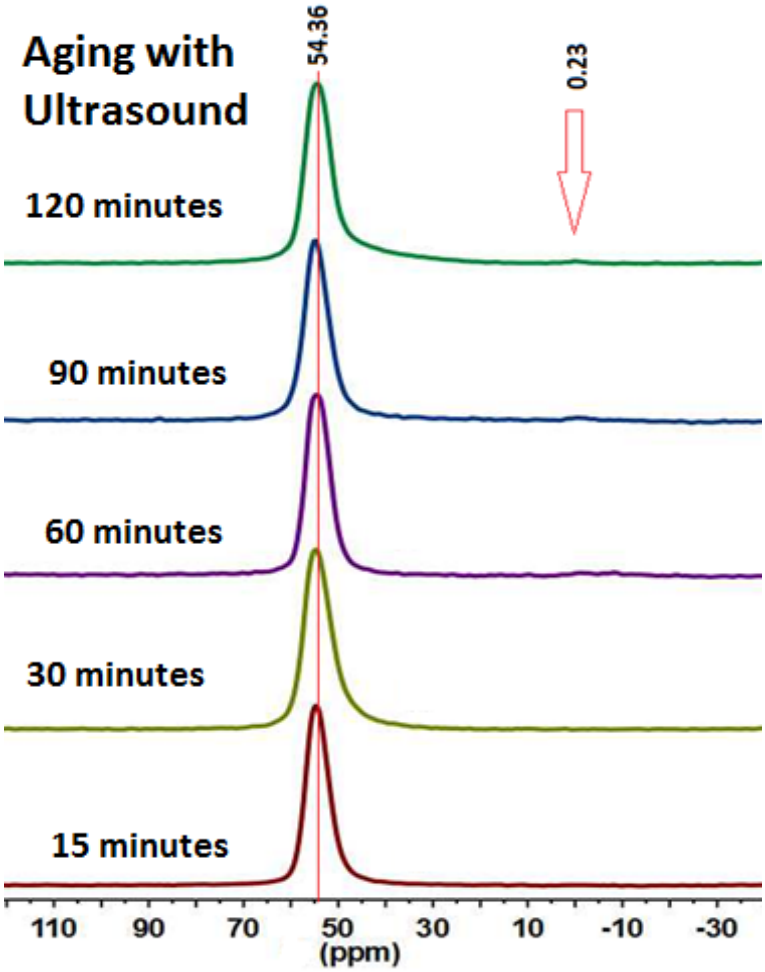

Figure 4.19 ^{27}Al MAS NMR of as-synthesised samples using ultrasonic method of aging at 15 min, 30 min, 60 min, 90 min and 120 min.

On the other hand, the *synthesised* samples using ultrasound pretreatment as shown in Figure 4.19 (a), (b), (c), (d) and (e) produced the same chemical shift of ^{27}Al MAS NMR at 54.36 whilst in a very small quantity of octahedrally coordinated Al(6), the extra framework aluminium at 0 ppm was observed only in samples (d) and (e). No peak broadening was observed as the particle size decreased from (a) to (e). The amount of Al(4) and Al(6) can be calculated using the ^{27}Al MAS NMR spectra. However, to calculate the Si/Al ratio (SAR), only the Al(4) chemical shift was considered.

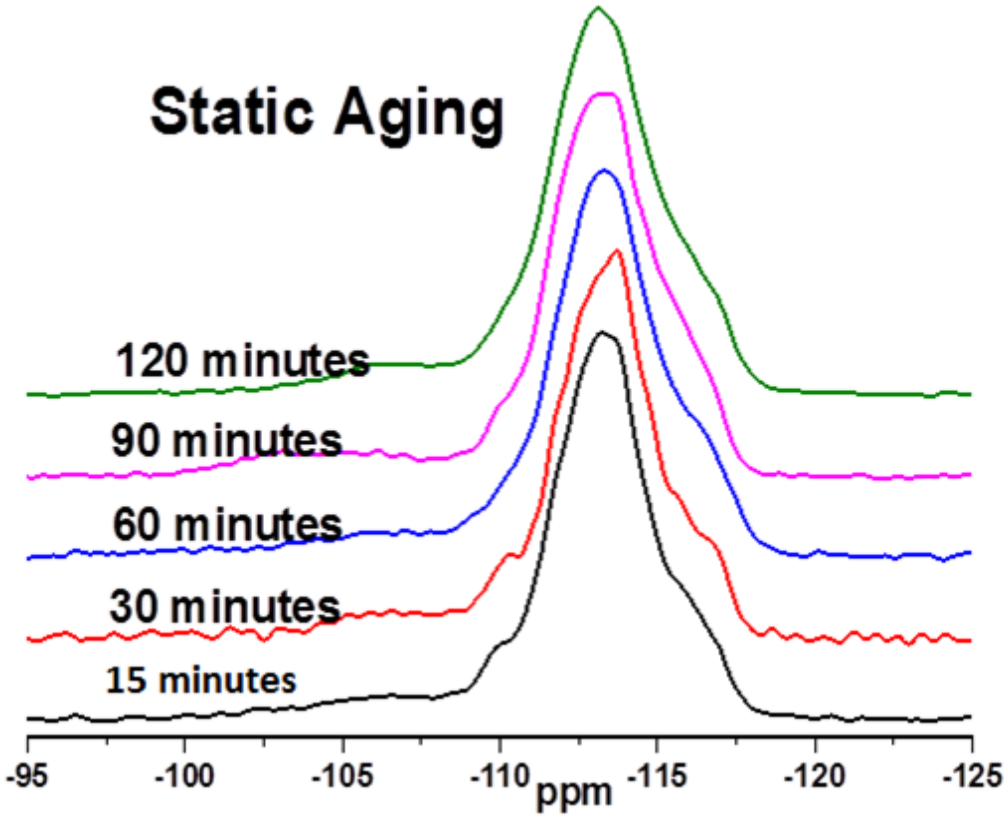

Figure 4.20 ^{29}Si MAS NMR of as-synthesised ZSM-5 zeolite using the static method of aging at 15 min, 30 min, 60 min, 90 min and 120 min.

The *as-synthesised* samples pretreated with the static method of aging were analysed using ^{29}Si MAS NMR. The structural features and the Al coordination of zeolites are based on the ^{29}Si chemical shift. Different chemical shift ranges have been found from -105 ppm to -120 ppm for structural units Si(0Al) and Si(1Al).[28,31] In Figure 4.20 (a), (b), (c), (d) and (e), the ^{29}Si MAS NMR spectra were composed of a single major chemical shift of -113 ppm with shoulders at the right and left of all the analysed samples.

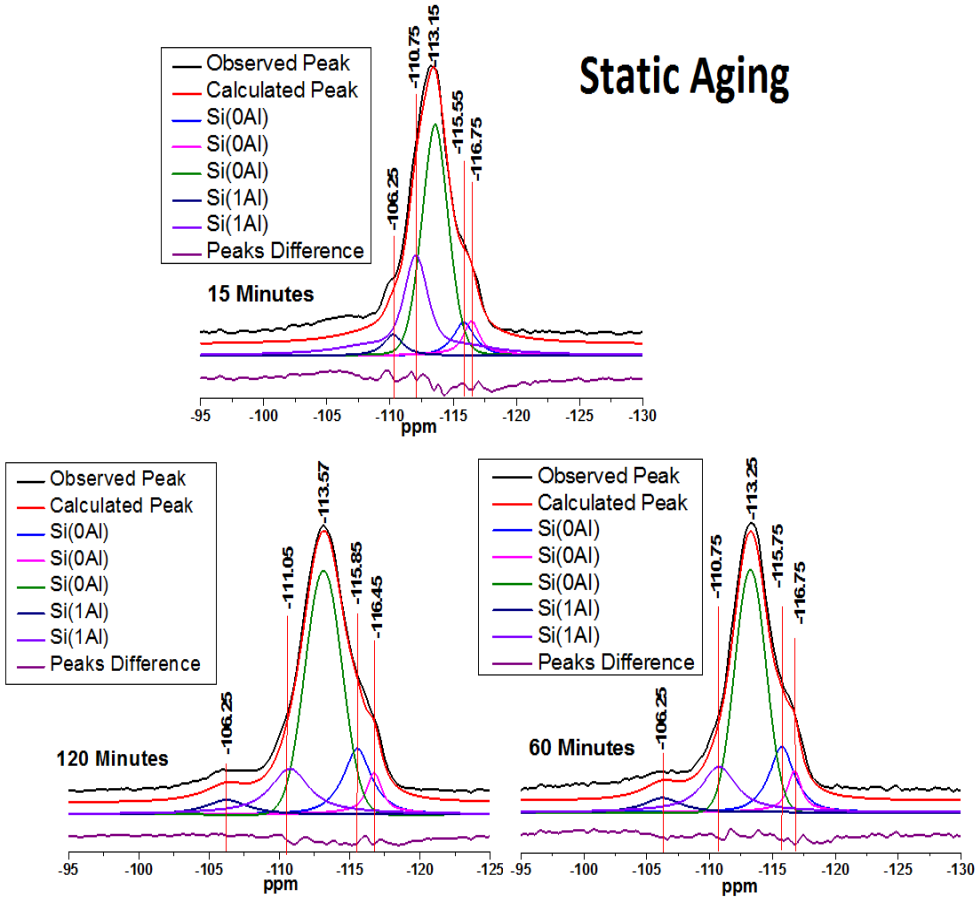

Figure 4.21 ^{29}Si MAS NMR deconvoluted spectra of *as-synthesised* ZSM-5 zeolite using the static method of aging at 15 min, 60 min and 120 min.

^{29}Si MAS NMR spectra were deconvoluted for samples (a), (c) and (e) as shown in Figure 4.21. There were some low-intensity peaks observed after deconvolution of the spectra of samples (a), (c) and (e). It was difficult to resolve those peaks or to assign individual NMR signals to specific crystallographic sites. The disorder of peak difference in Figure 4.21 shows that there are still minor peaks which need to be resolved. There is no literature available for such kind of resonance of a framework structure which gives matched structure accuracy.[28] All the ^{29}Si MAS NMR spectra were composed of chemical shift of -116 ppm which is related to the quaternary silicon with aluminium (0Al) in samples (a), (c) and (e). There is a broad shoulder at -106 ppm chemical shift observed because of silanol groups at the surface of the ZSM-5 catalyst. Peak broadening was

observed in each deconvoluted spectrum for each peak, increasing as long as the particle size decreased from (a) to (e), and this is also supported by the literature.[32,33]

Figure 4.22 (a), (b), (c), (d) and (e) show the ^{29}Si MAS NMR spectra of the samples of *as-synthesised* nanoZSM-5 which were subjected to ultrasound pretreatment. All the spectra have similar features as discussed earlier and also previously reported in the literature.[30,33–36] The ultrasound pretreated samples for 15, 30, 60, 90 and 120 minutes. A chemical shift of -113 ppm was observed as a major peak along with a narrow shoulder, which was observed to the right of the main peak, whilst a broad and low-intensity chemical shift to the left was also observed. Four different peaks were observed after deconvolution of the ^{29}Si MAS NMR spectra of samples (a), (c) and (e) as shown in Figure 4.23. A chemical shift of -116 ppm corresponds to the quaternary Si with (0Al) whilst at 106 ppm there was a broad and low-intensity peak. This is due to the presence of silanol OHSi*$(OSi)_3$ group at the surface of the nanocrystalline ZSM-5. It was previously reported that the broadening may occur in the chemical shift range of -100 to -110 ppm.[26,33,36] This assumption was also supported after the analysis of Si cross polarisation was carried out, and a chemical shift of -103 ppm was observed because of the polarisation transfer from ^{1}H to ^{29}Si. This will be discussed in more detail in Chapter 5.

It was concluded that similarities have been found in both data. However, the appearance of very low intensities unresolved chemical shifts in the *as-synthesised* samples treated with static aging yet to be identified, which was absent in the *as-synthesised* samples using pretreatment ultrasound. Peak

broadening was observed in both cases as long as the particle size decreases from sample (a) to (e).

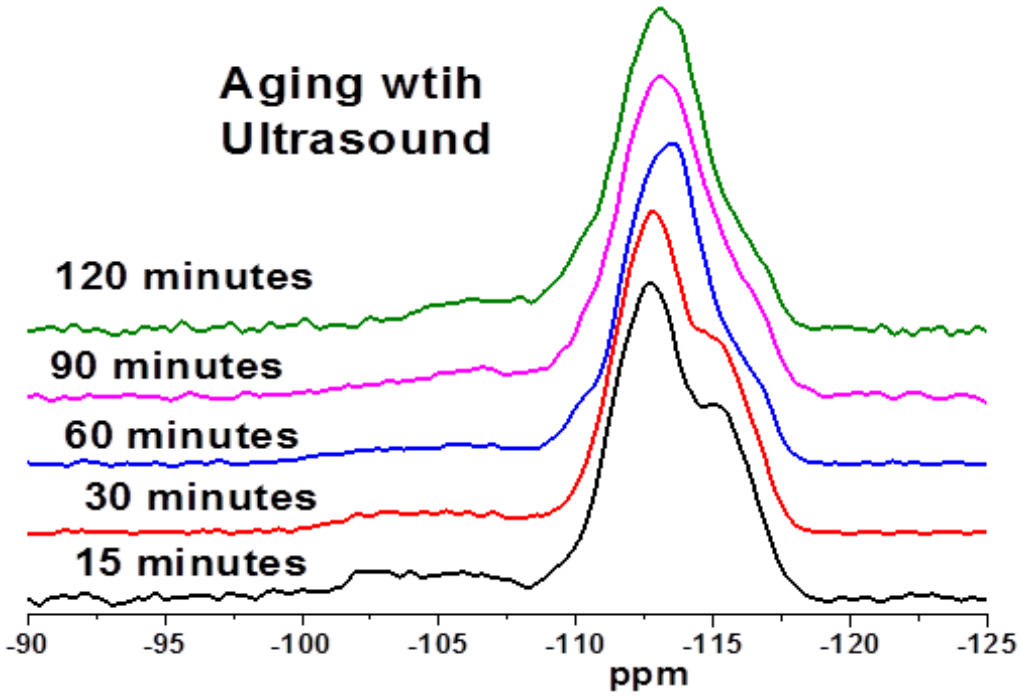

Figure 4.22 ^{29}Si MAS NMR spectra of *as-synthesised* ZSM-5 zeolite using ultrasound pretreatment method at 15 min, 30 min, 60 min, 90 min and 120 min.

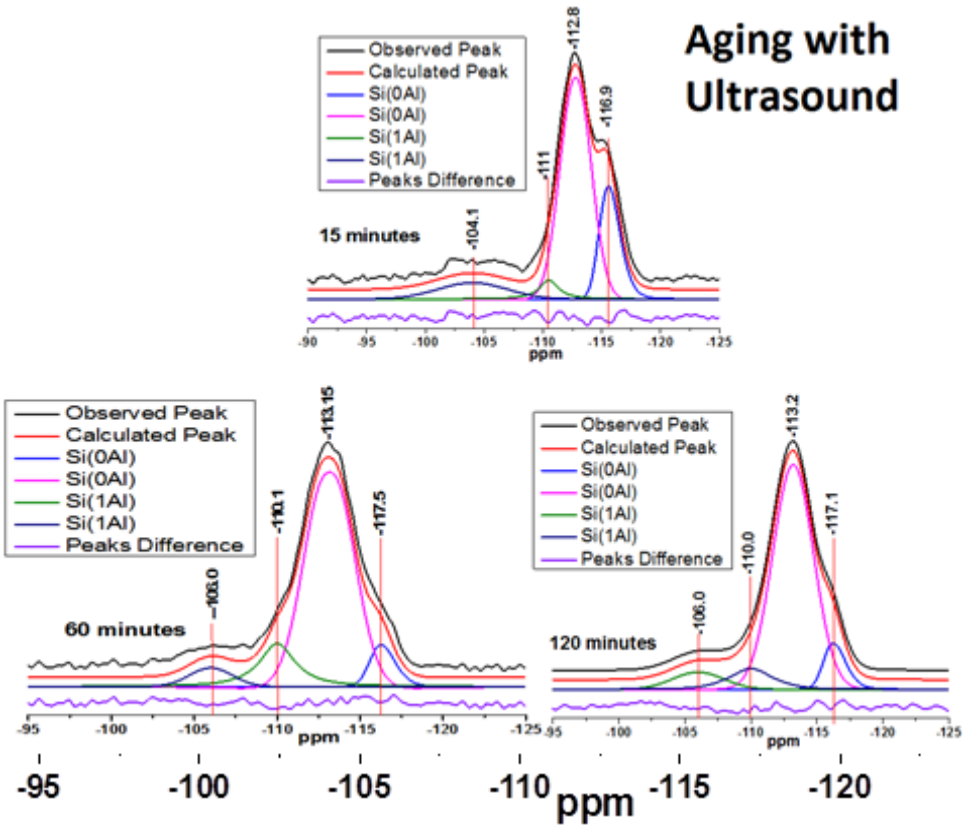

Figure 4.23 ^{29}Si MAS NMR deconvoluted spectra of *as-synthesised* ZSM-5 zeolite using ultrasound pretreatment method at 15 min, 60 min and 120 min.

4.4 Discussion

The efficiency and selectivity of porous catalyst systems are the main topic of the researcher in recent decades. The efficiency and selectivity of the catalyst depends on the number of active sites on the external surface area in relation to the number of accessible sites through pore channels and the characteristic path length. So far a number of publications have reported on the synthesis of nano zeolite crystals being efficient in catalysis using different synthesis methods. Ultrasound has not had any obvious effect on the zeolite framework, but it enhanced the crystallinity as well as the crystallite size of the zeolite. Ultrasound plays a vital role in chemical reactivity, which is called sonochemistry. Ultrasound enhances the rate of a chemical reaction and the properties of the product and also increases the

yields of the product.[7,18] Ultrasound also helps enhance the dissolution process.[18] The bubbles formed because the ultrasonic waves produced acoustic cavitation that preferentially collapsed near the solid surface and generated a localised hot spot. The implosive collapse is similar to an adiabatic process in its final stage and is responsible for this whole extreme-conditions characteristic of sonochemistry. This extreme condition in the acoustic cavitation permits the formation of unique materials. The reaction takes place because of the cavitation derived from the ultrasound, a process that defines the growth and explosive collapse of microscopic bubbles.[37,38] It is important to control the greater degree of preparation and properties because of the hydrothermal synthesis of zeolite with respect to nucleation and crystal growth rates, and the resulting particle size distribution is important to tailor.

In this chapter, we studied two different initial steps (ultrasound treatment and standby aging) before the hydrothermal treatment for the synthesis of nanoZSM-5 zeolite although the reaction conditions were the same for all the experiments in all steps of synthesis.

Ultrasound-assisted nanoZSM-5 was successfully synthesised. X-ray diffraction and high-resolution TEM analysis confirmed the particle dimension was in the range of 50–100 nm synthesised using ultrasound treatment for 120 minutes before the crystallisation process; the reaction was carried out at 170^{O}C. XRD patterns confirmed the ZSM-5 structure as reported in the literature.[6,31,39] The phase change from monoclinic to orthorhombic symmetry was also observed after calcination at 550^{O}C of the nanoZSM-5 powder. The single peaks at $2\theta = 8–9^{O}$ was split into two peaks having *hkl* values 2 0 0 and 0 2 0. Ardit et al. in 2015[40] reported the phase transition from monoclinic to orthorhombic

symmetry initiating at about 67^{O}C; as the temperature increases, the peak splitting also increases. The reversible phase transition in ZSM-5 zeolite was first reported by Wu et al. in 1979.[10] They reported that the phase transition occurs because of (010) pentasil layers along the c-axis having a small change in the Si—O—Si bond angle and Si—O bond distance. However, the twin-domain orthorhombic phase changes into monoclinic after absorption of the aromatics or small sorbate molecules.[10,14,40]

The product was characterised by using various characterisation techniques. SEM results confirmed uniform morphology having a particle dimension in the range of 100–300 nm of the sample synthesised at 170^{O}C for 120 minutes of ultrasound pretreatment. On the other hand, the static-aging pretreatment method resulted in a nonuniform morphology having a particle dimension of about 500–800 nm synthesised at 170^{O}C aging time for 120 minutes. Enhanced textural properties were observed for sample (e) treated at the highest time period using ultrasound, including a high external surface area of 239.8 cm^3/g. EDX elemental analysis confirmed the consistency in the Si/Al ratios of all the samples. DLS data is also consistent with SEM data. ^{27}Al and ^{29}Si coordination using solid-state MAS NMR confirmed the framework structure. Those results also correspond to reported results in literature.

Overall, a comparison of the results of both the ultrasound-assisted pretreatment and static aging showed that using ultrasound pretreatment can produce high-crystalline nanoparticles in a much shorter period of time than static aging.

4.5 Conclusion

First-time ultrasound-assisted nanoZSM-5 was successfully synthesised in a short period of time. X-ray diffraction and high-resolution TEM analysis confirmed the average particle size was in the range of 50–100 nm synthesised at 120 minutes of hydrothermal treatment at 170°C. XRD also observed that the ultrasound enhanced the crystallinity of the nanoZSM-5 catalyst powder. SEM results confirmed uniform morphology with an average particle size ranging from 100 to 300 nm at 120 minutes of ultrasound pretreatment. On the other hand, the static-aging pretreatment method resulted in disordered morphology with an average particle size of about 500–800 nm at the same treatment time of 120 minutes. Enhanced textural properties were observed for sample (e) treated at the highest time period using ultrasound, including a high external surface area of 239.89 cm^3/g. ^{27}Al and ^{29}Si coordination using solid-state MAS NMR confirmed the framework structure.

Overall, a comparison of the results of both the ultrasound-assisted pretreatment and static aging showed that using ultrasound pretreatment can produce high-crystalline nanoparticles in a much shorter period of time than static aging.

4.6 References

[1] "IZA Commission on Natural Zeolites structure data base," can be found under http://www.iza-structure.org/databases/, **2005**.

[2] L. Tosheva, V. P. Valtchev, *Chem. Mater.* **2005**, *17*, 2494–2513.

[3] P.-P. E. A. De Moor, T. P. M. Beelen, R. A. Van Santen, *J. Appl. Crystallogr.* **1997**, *30*, 675–679.

[4] J. N. Watson, A. S. Brown, L. E. Iton, J. W. White, *J. Chem. Soc. Faraday Trans.* **1998**, *94*, 2181–2186.

[5] A. Čižmek, B. Subotica, D. Kralj, V. Babić-Ivančić, A. Tonejc, *Microporous Mater.* **1997**, *12*, 267–280.

[6] J. Kong, X. Sheng, Y. Zhou, Y. Zhang, S. Zhou, Z. Zhang, *J. Porous Mater.* **2014**, *21*, 241–249.

[7] S. Askari, S. Miar Alipour, R. Halladj, M. H. Davood Abadi Farahani, *J. Porous Mater.* **2013**, *20*, 285–302.

[8] H. Li, J. Wang, Y. Bao, Z. Guo, M. Zhang, *J. Cryst. Growth* **2003**, *247*, 192–198.

[9] J. H. Bang, K. S. Suslick, *Adv. Mater.* **2010**, *22*, 1039–1059.

[10] E. L. Wu, S. L. Lawton, D. H. Olson, A. C. Rohrman, G. T. Kokotailo, *J. Phys. Chem.* **1979**, *83*, 2777–2781.

[11] T. F. Degnan, G. K. Chitnis, P. H. Schipper, *Microporous Mesoporous Mater.* **2000**, *35-36*, 245–252.

[12] M. M. M. Mostafa, K. N. Rao, H. S. Harun, S. N. Basahel, I. H. A. El-Maksod, *Ceram. Int.* **2013**, *39*, 683–689.

[13] D. G. Hay, H. Jaeger, G. W. West, *J. Phys. Chem.* **1985**, *89*, 1070–1072.

[14] D. G. Hay, H. Jaeger, *J. Chem. Soc, Chem. Commun* **1984**, 1433.

[15] S. Abbasian, M. Taghizadeh, *Int. J. Chem. React. Eng.* **2014**, *12*, 1–8.

[16] O. Andac, M. Tatlıer, A. Sirkecioglu, I. Ece, A. Erdem-Senatalar, *Microporous Mesoporous Mater.* **2005**, *79*, 225–233.

[17] Y. Vafaeian, M. Haghighi, S. Aghamohammadi, *Energy Convers. Manag.* **2013**, *76*, 1093–1103.

[18] M. Abrishamkar, S. N. Azizi, H. Kazemian, *J. Inorg. Gen. Chem.* **2010**, *636*, 2686–2690.

[19] G. Majano, A. Darwiche, S. Mintova, V. Valtchev, *Ind. Eng. Chem. Res.* **2009**, *48*, 7084–7091.

[20] S. Mintova, V. Valtchev, *Microporous Mesoporous Mater.* **2002**, *55*, 171–179.

[21] R. M. Mohamed, H. M. Aly, M. F. El-Shahat, I. A. Ibrahim, *Microporous Mesoporous Mater.* **2005**, *79*, 7–12.

[22] H. X. Vu, R. Eckelt, U. Armbruster, A. Martin, *Nanomaterials* **2014**, *4*, 712–725.

[23] M. Bjørgen, F. Joensen, M. Spangsberg Holm, U. Olsbye, K.-P. Lillerud, S. Svelle, *Appl. Catal. A Gen.* **2008**, *345*, 43–50.

[24] C. Lastoskie, K. E. Gubbins, N. Quirke, *J. Phys. Chem.* **1993**, *97*, 4786–4796.

[25] R. V. Grieken, J. M. Sotelo, J. A. Melero, *Microporous Mesoporous Mater.* **2000**, *39*, 135–147.

[26] A. Petushkov, S. Yoon, S. C. Larsen, *Microporous Mesoporous Mater.* **2011**, *137*, 92–100.

[27] O. Raymond, H. Villavicencio, E. Flores, V. Petranovskii, J. M. Siqueiros, *J. Phys. Chem. C* **2007**, *111*, 10260–10266.

[28] J. Klinowski, *Annu. Rev. Mater. Sci.* **1988**, *18*, 189–218.

[29] P. J. P. Dirken, J. B. H. Jansen, R. D. Schuiling, *Am. Mineral.* **1992**, *77*, 718–724.

[30] W. Zhang, X. Han, X. Liu, X. Bao, *Microporous Mesoporous Mater.* **2001**, *50*, 13–23.

[31] F. J. Van Der Gaag, ZSM-5 Type Zeolites :Synthesis and Use in Gasphase Reactions with Ammonia, Delft University Press, **1987**.

[32] A. Petushkov, Synthesis and Characterization of Nanocrystalline and Mesoporous Zeolites, **2011**.

[33] C. J. H. Jacobsen, C. Madsen, T. V. W. Janssens, H. J. Jakobsen, J. Skibsted, *Microporous Mesoporous Mater.* **2000**, *39*, 393–401.

[34] K. F. M. G. J. Scholle, W. S. Veeman, P. Frenken, G. P. M. Van der Velden, *Appl. Catal.* **1985**, *17*, 233–259.

[35] R. Faulkner, J. DiVerdi, Y. Yang, T. Kobayashi, G. Maciel, *Materials (Basel)*. **2012**, *6*, 18–46.

[36] S. L. Burkett, M. E. Davis, *J. Phys. Chem.* **1994**, *98*, 4647–4653.

[37] O. Andac, M. Tatlıer, A. Sirkecioglu, I. Ece, A. Erdem-senatalar, *Microporous Mesoporous Mater.* **2005**, *79*, 225–233.

[38] H. Xu, B. W. Zeiger, K. S. Suslick, *Chem. Soc. Rev.* **2013**, *42*, 2555–2567.

[39] G. Reding, T. Maurer, B. Kraushaar-Czarnetzki, *Microporous Mesoporous Mater.* **2003**, *57*, 83–92.

[40] M. Ardit, A. Martucci, G. Cruciani, *J. Phys. Chem.* **2015**, *119*, 7351–7359.

Chapter 5
Interrupted Synthesis of NanoZSM-5 with and without Ultrasound

5. Synthesis of NanoZSM-5

5.1. Chemicals, Reagents Used and Synthesis Procedure

Tetrapropylammonium hydroxide (TPAOH), ordered from Sigma Aldrich, 1.0 M in H_2O, and sodium hydroxide (NaOH), analytical reagent grade (99.4%) from Fisher Scientific UK, were used to make a basic medium and act as a metal cation. Sodium aluminate ($NaAlO_2$) (ca 8% H_2O 99.9% Al), ordered from ABCR GmbH and Co, was used as the aluminium source. Ludox HS-40 with pH 9.8, ordered from Sigma Aldrich (40% colloidal silica), was used as the silicon source. Doubly deionised water was used as the solvent. Ammonium nitrate (NH_4NO_3), which was ordered from Sigma Aldrich (ACS reagent ≥98 %, with pH 4.5–6), was used for the ion exchange to build an acidic site on the outer and inner surface of the synthesised materials.

5.2. Synthesis of ZSM-5 Zeolite

ZSM-5 (MFI) zeolite crystals were synthesised from the recipe on the International Zeolite Association (IZA) website[1] with few modifications, using TPAOH as an organic structure-directing agent (OSDA). A known amount of sodium hydroxide (NaOH), used as an extra framework cation, was dissolved in

distilled water. Sodium aluminate ($AlNaO_2$) was then added to the NaOH solution and kept stirred until a transparent solution was formed. Ludox HS-40 with pH 9.8 was then added to the solution dropwise. To reduce aggregation, ethanol was added dropwise whilst stirring for 15 minutes. Then the mixture was transferred into a PTFE liner, which was placed in a preheated oven at 170°C for 24 hours. All the gel mixtures used the molar composition shown in Table 5.1. Ultrasound interruption was applied for 15 minutes after every two hours during the crystallisation period. The solution was then cooled for five minutes after taking it out from the oven to enhance crystallinity and crystal growth and to reduce crystallite size.

Table 5.1 Molar composition of reacting materials.

Materials	Na_2O	Al_2O_3	SiO_2	H_2O
Ratio	16.7	0.5	60	116

The PTFE liner was fitted into a stainless-steel autoclave and hydrothermally treated at $170^{O}C$ for 24 hours. The product was then removed, thoroughly washed with deionised water, and dried at $110^{O}C$ overnight.

5.2.1. Zeolite Synthesis Mechanism

The zeolite synthesis mechanism consists of complex nucleation and crystal growth. To enhance the nucleation step of the crystallisation mechanism, we studied different aging techniques before hydrothermal treatment because nucleation occurs during the aging. The inorganic precursor gel produced uniform and highly crystalline material using optimised reaction conditions. A number of different routes for zeolite synthesis mechanism have been proposed. The most prominent issue arising in the discussion of this mechanism was particle aggregation. Therefore, particle aggregation is one of the main focuses of

synthetic research in zeolite chemistry. To understand zeolite synthesis and crystal growth mechanism, numerous studies have been reported. Sharma et al.[2] proposed a successful mechanism starting from primary nanoparticles of gel, which then nucleate and end up with cubic crystal aggregates as shown in Figure 5.1. The primary nanoparticles of the gel can lead to any of the three proposed mechanisms depending on the reaction condition. Path I describes the conversion of the primary nanoparticles into crystals after passing through dissolution and monomeric growth. Path II explains the seeding mechanism for the conversion of the primary nanoparticles to crystals. Path III describes the formation of aggregates of the nanoparticles, which then convert into a large crystal. Abrishamkar et al.[3] reported a zeolite crystallisation mechanism using various techniques for enhancing the nucleation period prior to hydrothermal treatment.

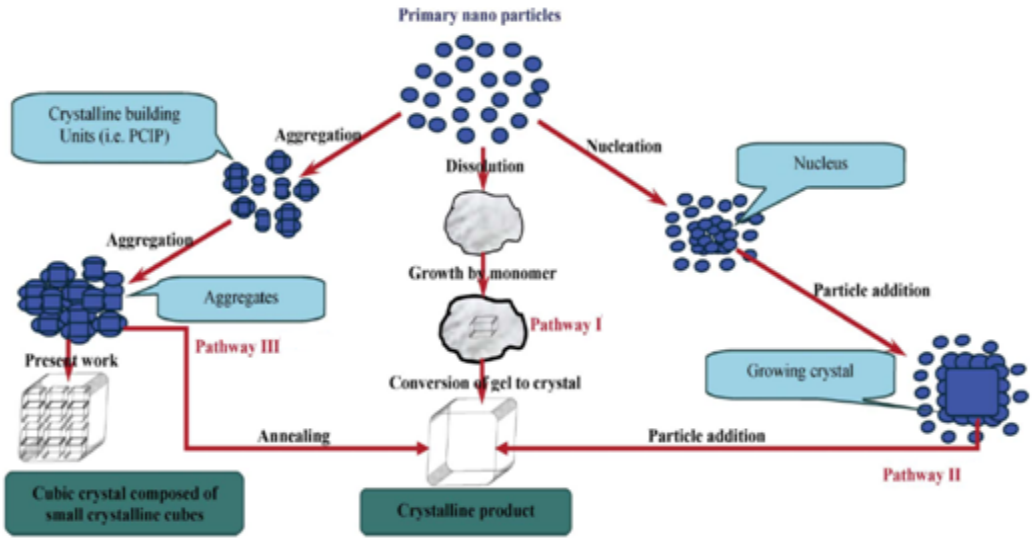

Figure 5.1 Three different mechanisms representing zeolite crystal growth. In Path I, the considered monomer precursor and the amorphous gel particles maintained average size. Path II follows with the addition of primary particles and growth of the crystals. In Path III, large particles were grown from the aggregation of the small particles.[2]

5.2.2. Interrupted-Ultrasound Treatment

The mixtures were pretreated with ultrasound, and then, after every two hours during hydrothermal treatment, the mixtures were repeatedly treated with ultrasound for 15 minutes after five minutes of cooling the mixture. The temperature for each experiment was kept at 170°C during the hydrothermal treatment.

All experiments were performed with the same methods of synthesis, but the crystallisation temperature in some of the experiments was increased during the hydrothermal treatment. In this method, the temperature was increased after every two-hour interruption with ultrasound treatment and the static method of aging for 15 minutes. Starting from 25°C for the first two hours, the sample was then treated with/without ultrasound for 15 minutes. Following this, the temperature was raised to 40°C for the next two hours and so on. When the temperature reached 160°C, the temperature was increased to 170°C. After this last increase in temperature, the crystallisation temperature was kept constant at 170°C for the remaining eight hours of the 24-hour experiment.

The total interrupted time in this method was 180 minutes plus 60 minutes of cooling (five minutes of cooling for each interruption) in the 24-hour experiments.

5.2.3. Calcination and Activation of the Catalysts (NanoZSM-5)

The product (powder) was dehydrated overnight at 110°C, and then it was calcined at 550°C for five hours in the presence of N_2 flow. All the samples were

then characterised to examine the effect of the interrupted treatment on particle/crystallite size distribution after the syntheses.

5.3. Results and Discussion

5.3.1. Powder X-ray Diffraction (XRD)

Powder X-ray diffraction was used to identify the structural framework of crystalline materials. Crystallite size and crystallinity were also calculated from the *as-synthesised* ZSM-5 powder X-ray diffraction patterns.

Different experiments were performed to optimise the parameters and reactant materials for the synthesis of nanoZSM-5. These experiments were carried out for different hydrothermal treatment times at different temperatures to determine standard synthesis conditions with the interrupted-synthesis method. The crystallisation temperature was increased by 10°C in each single experiment performed from 100°C to 170°C for 24 hours. No diffraction peaks were observed for the samples heated to 100–140°C for the 24-hour experiments. Different factors have been published which were reported to enhance crystallisation rate, such as seeding, crystallisation time, crystallisation temperature and the use of structure-directing agent (SDA)/templates.[4–7] The characteristic ZSM-5 peaks appeared as soon as the crystallisation temperature increased to 150°C for the 24-hour hydrothermal treatment period. The crystallisation temperature was increased by 10°C in each single experiment performed from 100°C to 170°C for 24 hours. According to the results shown in Figure 5.2, when the gel was treated for 24 hours at 150°C, a mixed phase of ZSM-5 and amorphous powder pattern was observed in sample (a). When the temperature increased to 160°C, the

crystallinity increased as can be observed by the reduced amorphous signals in the powder pattern obtained from sample (b). A pure phase was observed when the gel was treated at 170°C for 24 hours, which confirmed what was reported in the literature.[8–10] An extra experiment was also performed to examine the further effect of longer time (48 hours) at 170°C as shown in Figure 5.2, which obtained a similar diffraction pattern as the one treated for 24 hours.

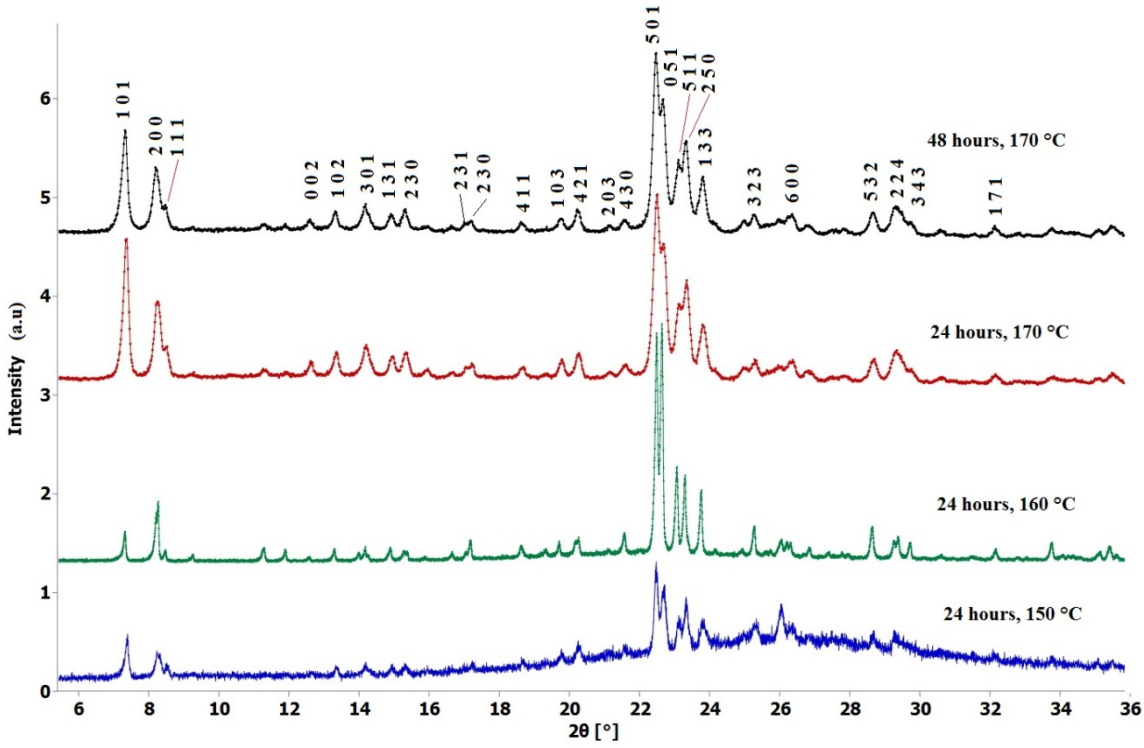

Figure 5.2 X-ray diffraction of test experiments of *as-synthesised* ZSM-5 zeolite at different crystallisation temperatures.

There was no obvious change observed in structural framework in the interrupted method during hydrothermal treatment. Only the phase transition was observed from monoclinic symmetry to orthorhombic as discussed in section 4.3.1.

After the use of ultrasound in pretreatment in the hydrothermal process, the ultrasound was used for the first time in interrupted synthesis in the hydrothermal process of nanoZSM-5 zeolite synthesis. Venkatathri[11] reported the

interrupted synthesis of ZSM-5 but did not explain the procedure or the mode of interruption during synthesis. Numerous experiments were performed with and without ultrasound-interrupted syntheses and at a constant temperature of 170°C and also with increasing temperature from 25°C to 170°C during the course of crystallisation as shown in Figure 5.3. The crystallinity of all the samples was calculated with help of equation (1). The crystallite sizes of all the obtained X-ray diffraction patterns were also calculated using Scherrer's equation discussed in section 2.4.1,

$$\boldsymbol{RC} = \frac{\sum \boldsymbol{I}_{(high\ crystalline\ peaks)}}{\sum \boldsymbol{I}_{(Reference)}} \times \mathbf{100}\% \qquad (1)$$

where RC is the relative crystallinity and *I* is the peaks integrated area.

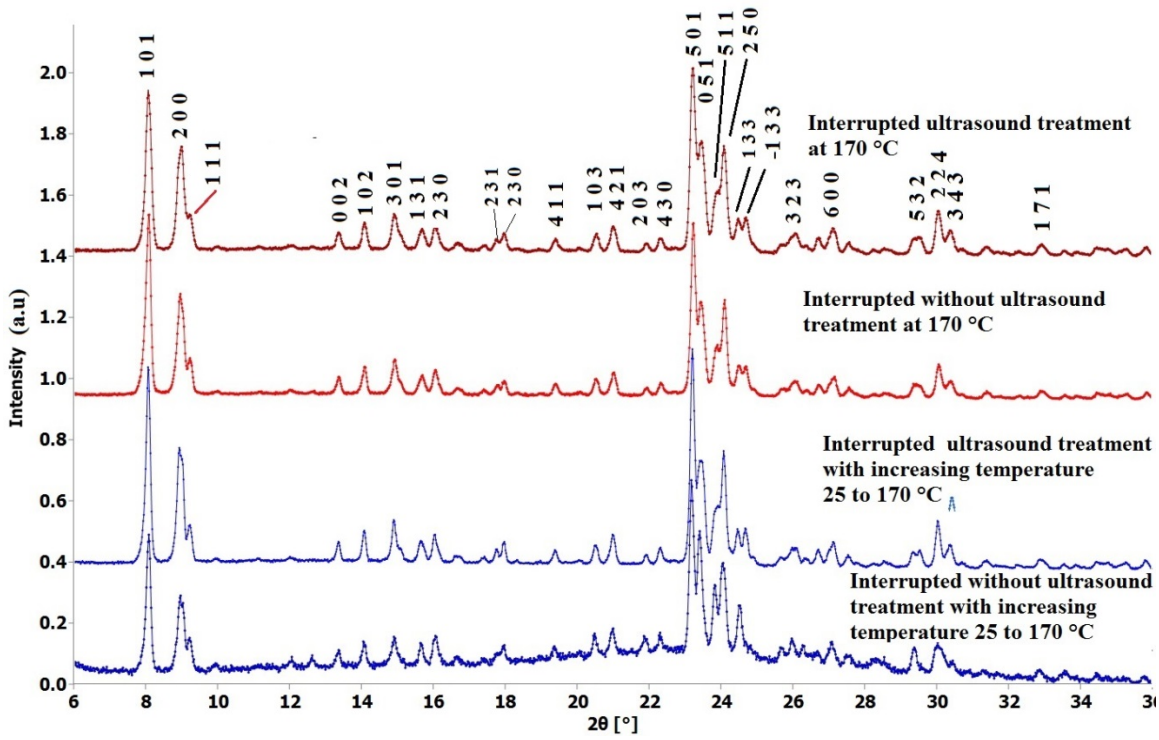

Figure 5.3 X-ray diffraction of the *as-synthesised* nanoZSM-5 by different methods of interruption with and without ultrasound.

The calculated data are illustrated in Table 5.2. The X-ray powder diffractions of samples (d) and (c) are of the as-synthesised nanoZSM-5 with and

without ultrasound-interrupting crystallisation process, respectively. From the diffraction patterns, broadening was observed in the Bragg peaks of sample (d), which was synthesised using interrupted ultrasound as compared to sample (c), which was synthesised without using ultrasound. The calculated crystallite size of both samples was 27 nm and 85 nm, respectively. A significant reduction in crystallite size was observed by using the ultrasound-interrupting crystallisation process. Variation in the average FWHM of the peaks ranging from 20–30° 2θ is listed in Table 5.2. Similarly, the X-ray diffraction pattern of samples (a) and (b) are shown in Figure 5.3. Sample (a) treated without ultrasound shows the presence of both crystalline and amorphous phases. Hence, the pattern was composed of an amorphous phase, so neither crystallinity nor crystallite size was calculated. The X-ray diffraction of sample (b) showed a single-phase ZSM-5 powder pattern. The calculated relative crystallinity and crystallite size of all the experiments are illustrated in Table 5.2. Table 5.3 illustrates the unit cell parameters of the samples synthesised with interrupted ultrasound at 170ºC, and interrupted ultrasound has no significant effect on the crystal lattice.

Table 5.2 The as-synthesised nanoZSM-5 samples interrupted synthesis with and without ultrasound, crystallite size and the calculated relative crystallanity (%).

Samples	Time of Interrupted Modes (min)		Crystallisation Temperature °C	FWHM (2θ)[°]	Crystallite Size (nm)	R. Cry (%)
	With Ultrasound	Without Ultrasound				
a	-	180	Increased 25 to 170	N.C	N.C	N.C
b	180	-	Increased 25 to 170	0.12±0.01	87±10	40±5
c	-	180	Constant at 170	0.13±0.06	85±5	80±4
d	180	-	Constant at 170	0.35±0.03	27±5	120±6

Table 5.3 Unit cell parameters, calculated with help of the UnitCell programme, of the samples synthesised with interrupted ultrasound at constant temperature (170ºC) and with interrupted ultrasound at increasing temperature (25ºC to 170ºC).

Symmetry (↓)	a (Å)	b (Å)	c (Å)	α (°)	β (°)	γ (°)
Interrupted with ultrasound and constant temperature	20.10±0.01	19.85±0.01	13.81±0.03	90	90	90
Interrupted with ultrasound and increasing temperature	20.04±0.02	19.87±0.02	13.83±0.01	90	90	90

5.3.2. Transmission Electron Microscopy (TEM)

The crystallite size distribution of the *as-synthesised* nanoZSM-5 was studied using high-resolution TEM. Figure 5.4 shows TEM images of sample (a), (b), (c) and (d) of nanoZSM-5 synthesised for 24 hours with and without ultrasound-interrupted treatment. Samples (a) and (b) show different particle sizes and have different morphologies. X-ray powder diffraction of sample (a) showed the presence of an amorphous phase, whilst sample (b) was a single ZSM-5 powder diffraction pattern. Sample (a) was not treated with ultrasound for 24 hours with increasing temperature from 25°C to 170°C. During the last eight hours of hydrothermal treatment, the temperature was uniform at 170°C. Some large cookie-like morphology crystals were observed at 2 μm (2,000 nm) diameter. Some smooth surfaces of the particle showing the amorphous material in the same sample are shown in Figure 5.4. Sample (b) was synthesised with interrupted ultrasound, with a temperature profile identical to that of sample (a). A rectangular or brick-like aggregated morphology was observed, which is completely different from that of sample (a). The aggregated particles are ~500 nm in size.

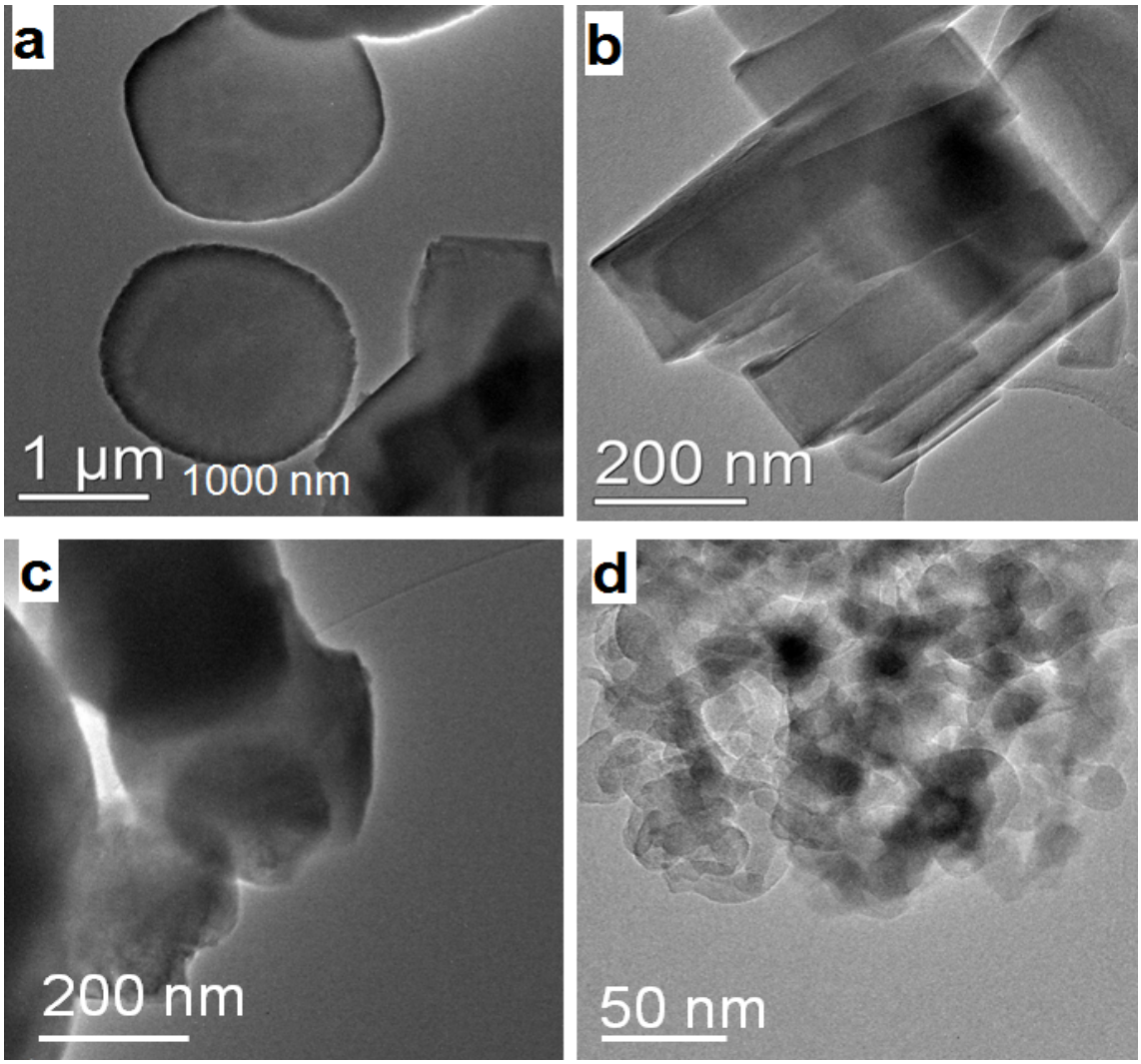

Figure 5.4 TEM micrographs of the *as-synthesised* samples: (a) interrupted synthesis without ultrasound with increasing temperature from 25°C to 170°C, (b) interrupted synthesis with ultrasound with increasing temperature from 25°C to 170°C, (c) interrupted synthesis without ultrasound at a constant temperature of 170°C, (d) interrupted synthesis with ultrasound at a constant temperature of 170°C.

TEM images of the *as-synthesised* nanoZSM-5 particles without and with interrupted ultrasound at 170°C for 24 hours are shown in Figure 5.4 (c) and (d). respectively. Sample (c) was synthesised without the use of ultrasound but with a static aging interruption for 15 minutes after every two hours of hydrothermal treatment. The particles observed have similar morphology as that of sample (a), but the recorded particle dimension was ≤400 nm. Sample (d), which was

synthesised with interrupted ultrasound, shows an undefined morphology with very small particle sizes ranging from 10 nm to 30 nm.

It is concluded that ultrasound treatment has a remarkable influence on the product phase, including particle size reduction and an enhancement of crystallinity. By comparing the TEM micrograph of this data with the data reported in the previous chapter, close agreement is seen for the effect of ultrasound to produce nanoZSM-5 using different experimental conditions.

5.3.3. Scanning Electron Microscopy (SEM)

The particle size and morphology of samples (a), (b), (c) and (d) synthesised without and with interrupted ultrasound were also studied by SEM. Figure 5.5 (a) and (b) show the SEM images of the samples synthesised without and with ultrasound for 24 hours with increasing temperature as explained previously. The SEM image of the sample (a) powder does not show any particular morphology. Figure 5.5 (a) shows the particle size ranges from micro- to nanosize. Physically more than half of *as-synthesised* product powder was composed of hard solid large chunks, which were crushed using mortar and pestle. The SEM image of the *as-synthesised* sample (b) using interrupted ultrasound with increasing temperature is shown in Figure 5.5. Elongated hexagonal aggregated slab morphology was observed having 300–500 nm particle dimensions, whilst the thickness of the particle is about 100 nm. Such kind of morphology was also reported by Moreno-Piraja et al.[12] although the particles have very large dimensions at >5 μm produced under normal conventional hydrothermal synthesis at 150°C for 24 hours.

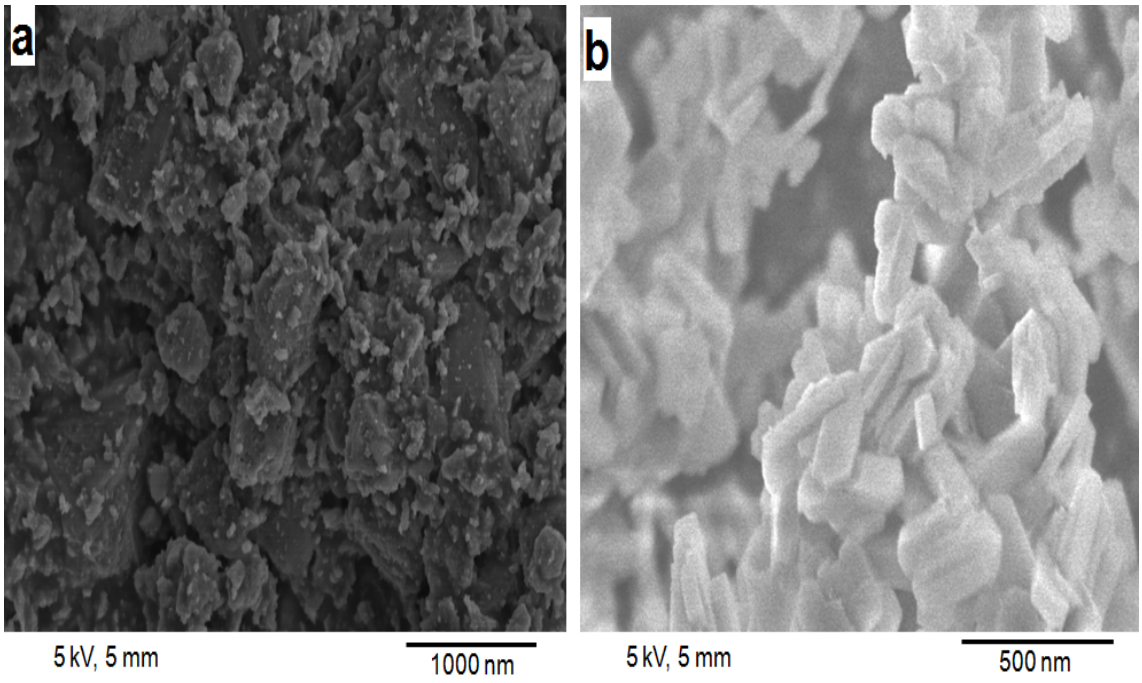

Figure 5.5 SEM images of the *as-synthesised* samples: (a) interrupted synthesis without ultrasound with increasing temperature from 20°C to 170°C, (b) interrupted synthesis with ultrasound with increasing temperature from 20°C to 170°C.

Figure 5.6 (c) and (d) show SEM micrographs of the *as-synthesised* samples with and without interrupted ultrasound at 170°C for 24 hours, respectively. Both samples have similar morphology with rounded corners and edged squares. Sample (c) has uniform morphology but has nonuniform particle dimensions ranging from 100 nm to 500 nm, whilst in Figure 5.6 (d), which shows the SEM of the sample synthesised with interrupted ultrasound, the particles have uniform morphology. Some small particles were observed which have dimensions of <100 nm, but the average particles have a size range of 100–200 nm. Venkatathri[11] reported particle dimensions of 500 nm for the interrupted synthesis of ZSM-5 without the use of ultrasound after six days' crystallisation time. Hunger et al.[13] reported a large particle size, >20 μm, but having similar morphology to that of sample (c). Cizmek et al.[14] reported the same morphology

of sample (d) although large particle sizes were produced using the influence of time and temperature synthesis conditions.

The particles that have been synthesised without the use of ultrasound have not only irregular morphology but also nonuniform particle sizes.

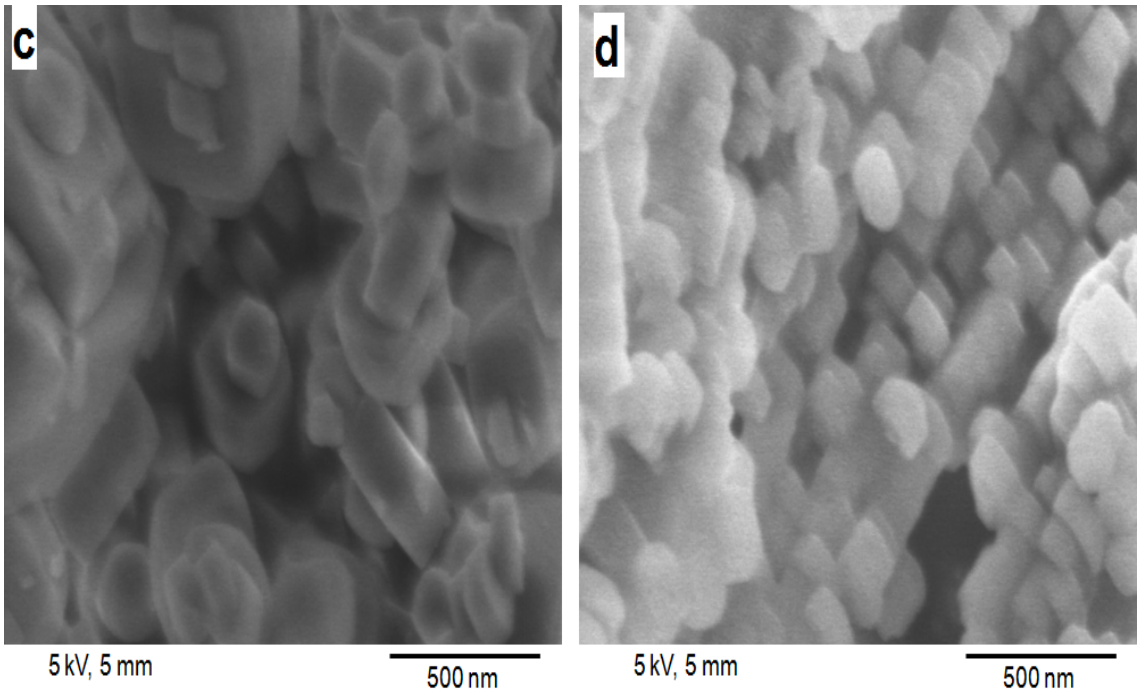

Figure 5.6 SEM images of the as-synthesised samples: (c) interrupted synthesis without ultrasound at a fixed temperature of 170°C, (d) interrupted synthesis with ultrasound at a fixed temperature of 170°C.

5.3.4. Dynamic Light Scattering (DLS)

DLS was used to investigate the particle size distribution of all the *as-synthesised* naoZSM-5 using different preparation methods. Figure 5.7 (a) and (b) show the samples prepared without and with ultrasound-interrupted synthesis with increasing temperature from 25°C to 170°C for 24 hours, respectively. Sample (a) was composed of crystalline and amorphous large aggregations of the particles as observed in the X-ray diffraction, TEM and SEM analysis. The average dimension of the particle size observed using DLS was around 1,000 nm.

Similarly, the observed particle size was 400–500 nm for sample (b). DLS also observed particle aggregation in sample (b).

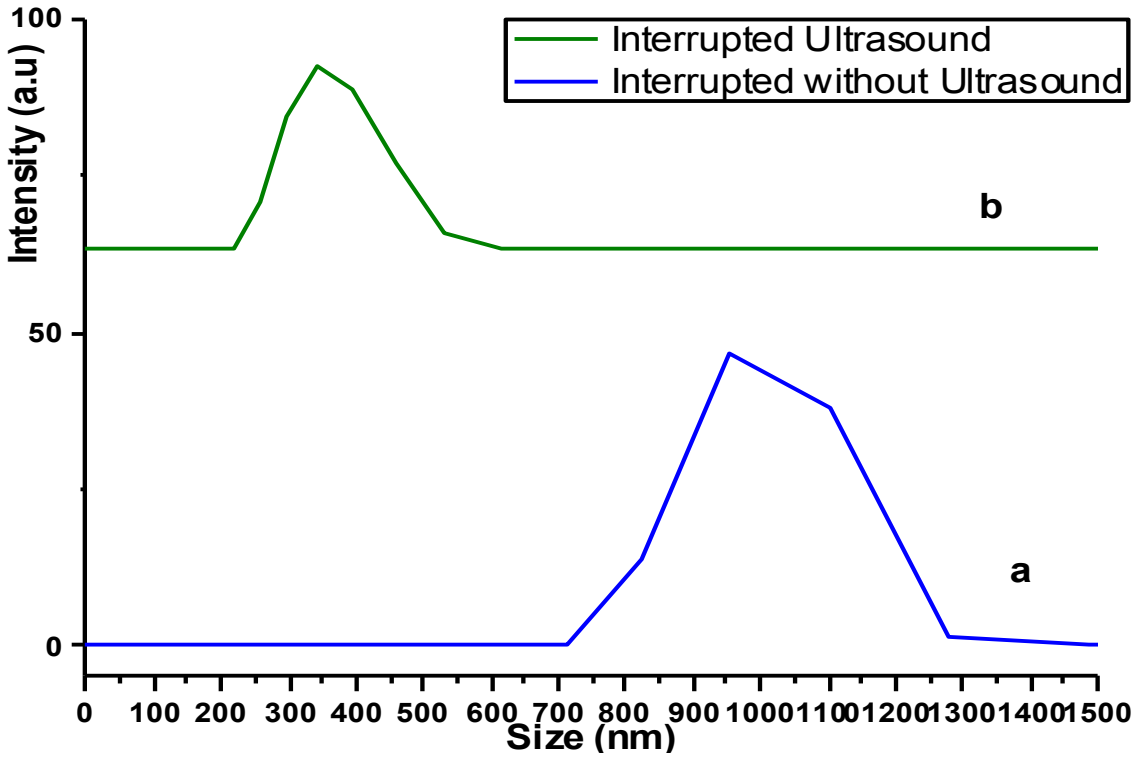

Figure 5.7 DLS data of the *as-synthesised* micro- and nanoZSM-5 samples: (a) interrupted synthesis without ultrasound with increasing temperature from 20°C to 170°C, (b) interrupted synthesis with ultrasound with increasing temperature from 20°C to 170°C.

DLS measurement of the samples synthesised with uniform heating at 170°C without and with interrupted-ultrasound treatment is shown in Figure 5.8 (c) and (d), respectively. The observed average particle size was 400–500 nm for sample (c) whilst the average particle size observed in sample (d) was 10–50 nm as shown in Figure 5.8 (d). This DLS analysis on sample (d) shows a significant effect of the ultrasound and the interruption of the hydrothermal conventional treatment on the particle size distribution in the product zeolite.

In terms of heating, the samples synthesised with increasing temperature without ultrasound show larger particles than an equivalent sample synthesised

with ultrasound shown in Figure 5.7. The samples shown in Figure 5.8 synthesised at constant heat for 24 hours produce smaller particles. It was previously explained that the crystallisation rate is slower at lower temperature, whilst the crystallisation process takes place faster at high temperature. The X-ray diffraction and TEM data produced on the samples agree very closely with that of the data obtained on DLS.[15–18] All the obtained data of the *as-synthesised* data are compared in Table 5.4 .

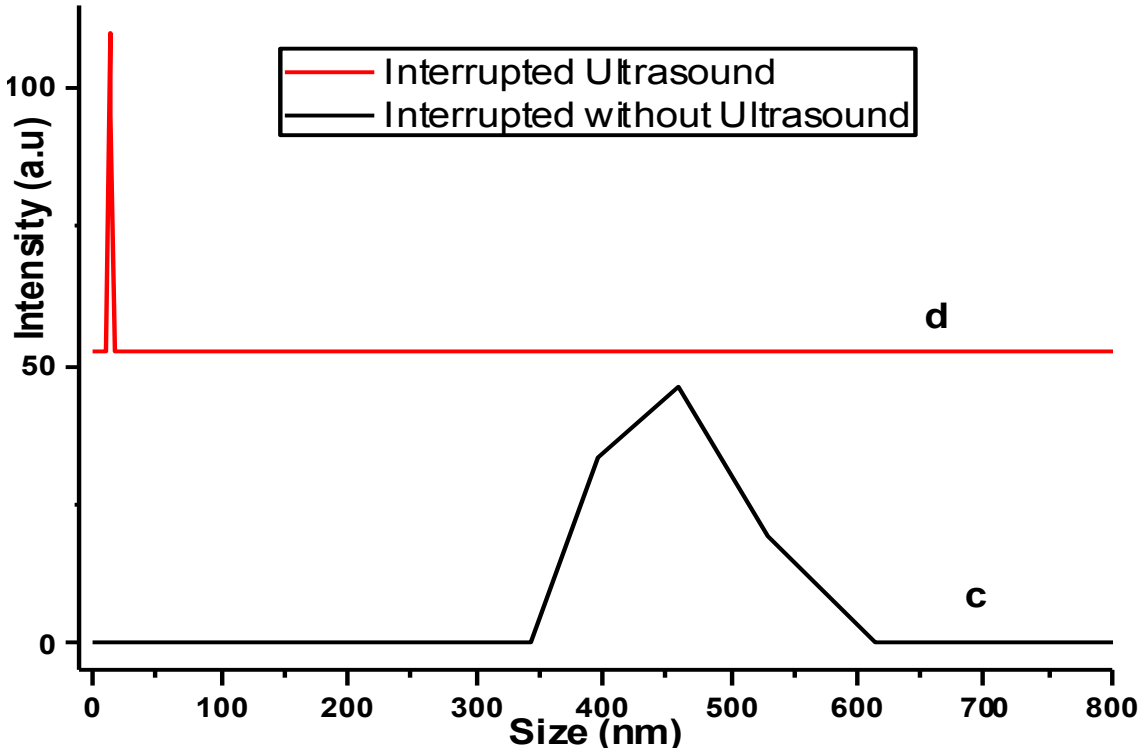

Figure 5.8 DLS data of the as-synthesised micro- and nanoZSM-5 samples: (c) interrupted synthesis without ultrasound at 170°C, (d) interrupted synthesis with ultrasound at 170°C.

Table 5.4 Comparing the particle size distribution obtained from XRD, TEM, SEM and DLS analysis of the synthesised samples with and without interrupted-ultrasound treatment.

Samples	Time of Interrupted Modes (min)		Particle Size (nm)				R. Cry (%)
	With Ultrasound	Without Ultrasound	XRD	TEM	SEM	DLS	
a	-	180	N.C	200±20	3000±10	3000±20	48
b	180	-	87±10	500±20	800±15	800±10	55
c	-	180	85±5	400±15	300±20	600±10	67
d	180	-	27±5	30±10	150±20	20±15	82

5.3.5. Energy-Dispersive Spectroscopy (EDS)

EDS analysis was used to confirm each component of the as-synthesised nanoZSM-5. EDS was used on TEM to obtain the average weight percent elemental composition of each *as-synthesised* ZSM-5 sample. From the EDS histograms in Figure 5.9, it can be seen that all the samples are composed of silicon and aluminium oxides, which are the constituent elements (Si, Al and O) of the zeolite framework (ZSM-5). The average weight percent (wt%) of all the basic elements of the framework is illustrated in Table 5.5. Table 5.6 illustrates the particle sizes observed for the different spectroscopic techniques of *as-synthesised* samples with ultrasound pretreatments along with the SAR (Si/Al) from 30 to 40.

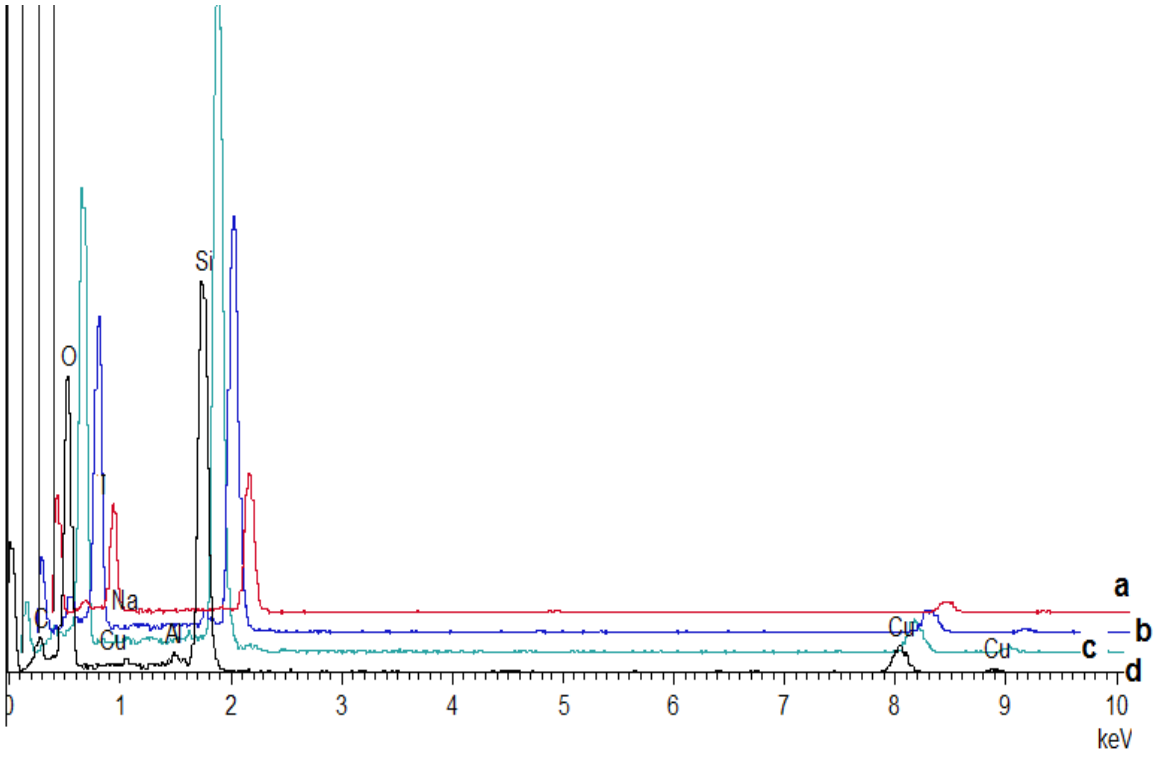

Figure 5.9 EDS histogram illustrating the elemental composition of the as-synthesised samples (a), (b), (c) and (d).

These SAR results are similar to the already reported results of the as-synthesised ZSM-5 zeolite.[10,12,19] However, the synthesis mechanism and the pretreatment methods in this study are different from what the literature reported.

Table 5.5 Average weight percent (%) chemical composition obtained on EDS static with and without interrupted-ultrasound synthesis.

Sample	Average wt (%) Elemental Composition			Si/Al
	Si	Al	O	
a	21±2	0.53±0.12	29	40±5
b	22±1	0.63±0.32	41	35±4
c	22±1	0.68±0.22	35	32±7
d	22±1	0.59±0.13	37	38±3

Table 5.6 Particle size distribution investigated on different spectroscopic and microscopic techniques with respect to SAR using ultrasound pretreatment.

Samples	Average Particle Size (nm)				Si/Al (SAR)	Relative Crystallinity (%)
	XRD	TEM	SEM	DLS		
a	N.C	200±20	3000±10	3000±20	40±5	Not calculated
b	87±10	500±20	800±15	800±10	35±4	40
c	85±5	400±15	300±20	600±10	32±7	80
d	27±5	30±10	150±20	20±15	38±3	120

5.3.6. N_2 Adsorption/Desorption

Textural properties of *as-synthesised* nanoZSM-5 samples (a), (b), (c) and (d) were determined by N_2 adsorption/desorption measurements. The physisorption isotherm was used to identify the isotherm type and the nature of the N_2 adsorption and desorption processes, i.e., monolayer-multilayer, capillary condensation or micropore filling and emptying. BET analysis was used to calculate the actual surface area using the isotherm obtained. Generally, the BET analysis provided that the estimated value of C was neither too low nor too high, and the BET plot is leaner in the region of the isotherm containing point B.[20,21] The BJH model was used to calculate the pore size distribution of the as-synthesised samples of ZSM-5. Figure 5.10 (a) and (b) show the type IV (IUPAC classification) N_2 adsorption and desorption isotherms of the synthesised samples without and with interrupted ultrasound, respectively. Sample (a) shows monolayer adsorption and low affinity for the adsorption molecules, whilst in sample (b), a small hysteresis step can be seen at 0.4–0.9 (p/p_o) showing

mesopores with multilayer adsorption.[22,23] However, these isotherms were also closely related to subtype H4, which describes the structure of microporous and mesoporous materials.[24]

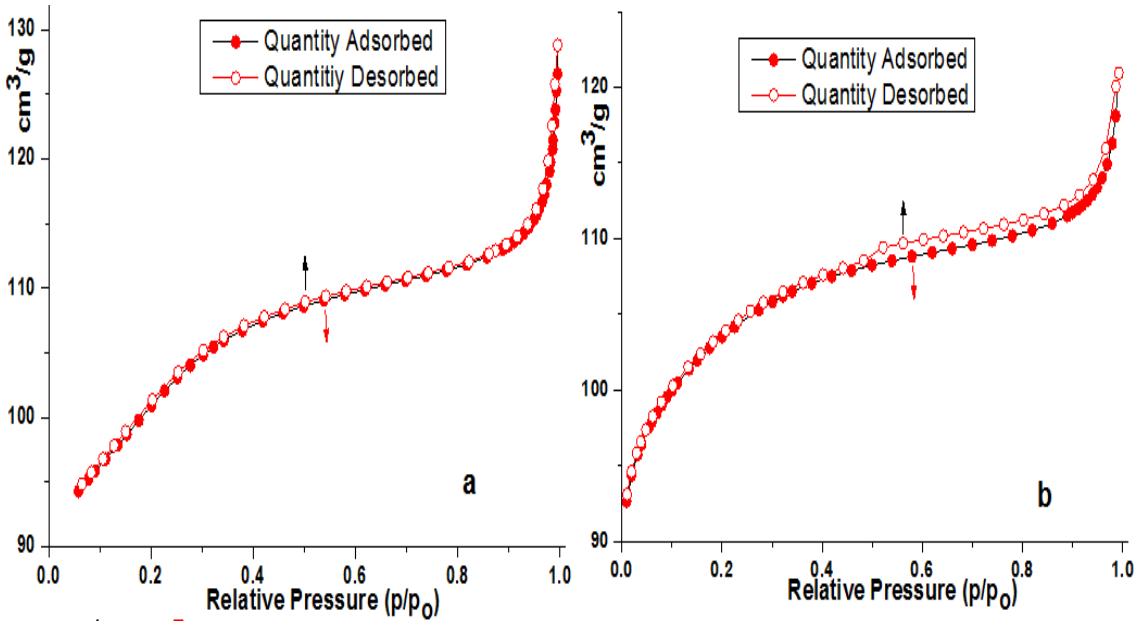

Figure 5.10 N_2 adsorption/desorption isotherms of micro- and nanoZSM-5 of the samples: (a) interrupted synthesis without ultrasound with an increasing temperature of 25–170°C, (b) interrupted synthesis with ultrasound with an increasing temperature of 25–170 °C.

The samples in Figure 5.11 (c) and (d) were synthesised according to the same procedure but at a constant temperature of 170°C, as with samples (a) and (b). The N_2 adsorption and desorption shows a slightly different behaviour. A small hysteresis in sample (c) shows that the material has a uniform surface but low capability for adsorption (gas molecules). On the other hand, sample (d) has a huge hysteresis step ranging from 0.4 to 0.9 (p/p_o) consistent with multilayer mesoporous adsorption and desorption. The isotherm obtained from samples (c) and (d) correspond to type IV and subtype H4, which are characteristics of microporous and mesoporous materials.[24,25]

Table 5.7 shows that there was a significant increase in the external surface area as well as the total surface area (S_{BET}) using ultrasound and with reduction in particle size distribution. By using the BJH method for pore size distribution, variation was observed in the pore volume with particle size decrease.

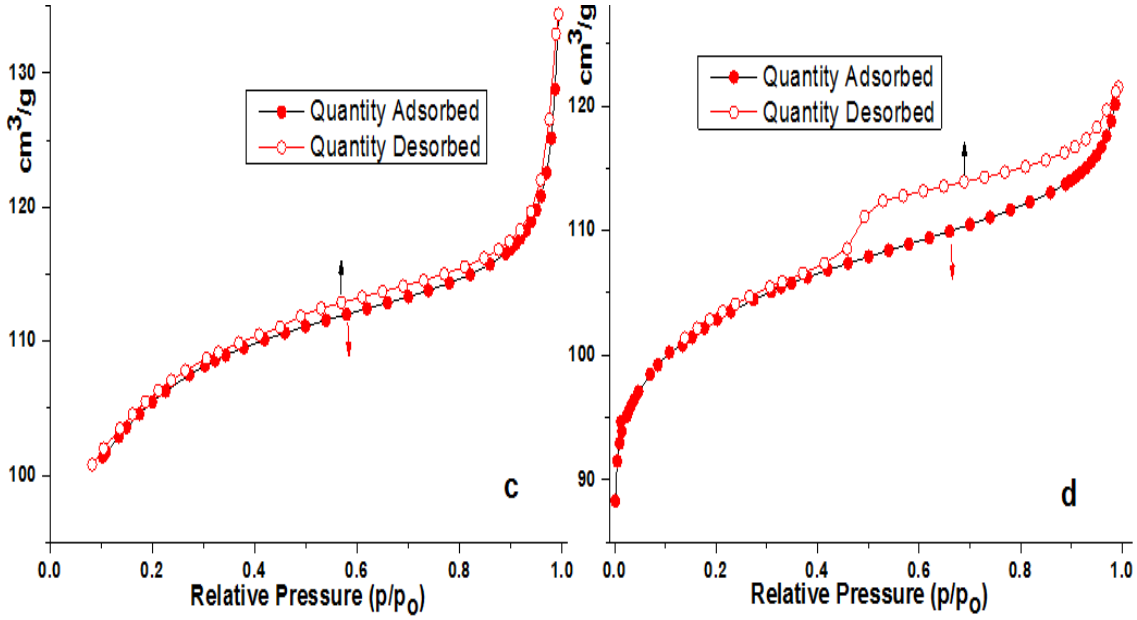

Figure 5.11 N_2 adsorption/desorption isotherms of micro- and nanoZSM-5 of the samples: (c) interrupted synthesis without ultrasound at 170°C, (d) interrupted synthesis with ultrasound at 170°C.

Table 5.7 BET surface area, external surface area and pore volume of the nanoZSM-5 prepared with and without ultrasound-interrupted synthesis.

Samples	Time of Interrupted Modes (min)		SAR (Si/Al)	S_{BET} (m^2/g)	$S.A_{Ext}$ (m^2/g)	Pore Vol. (cm^3/g)	R. Cry (%)
	With Ultrasound	Without Ultrasound					
a	-	180	40	318±6	61	0.13	48
b	180	-	35	348±4	100	0.05	55
c	-	180	32	388±2	185	0.13	67
d	180	-	38	439±5	186	0.14	82

The mesopore distribution and the pore volume were calculated with the help of the BJH method of N_2 adsorption. Figure 5.12 (a) and (b) show the data for the *as-synthesised* samples treated with interrupted static aging and ultrasound, respectively, during conventional hydrothermal synthesis. From BJH, N_2 adsorption, shown in Figure 5.12, started just before 2 nm of the pore diameter, whilst the pore distribution centre occurs in between 3 nm and 4 nm. The observed zigzagging curve of sample (a) is a characteristic of the disorder of the pore distribution as compared to sample (b). This characteristic was also reported by Liu et al.[26]

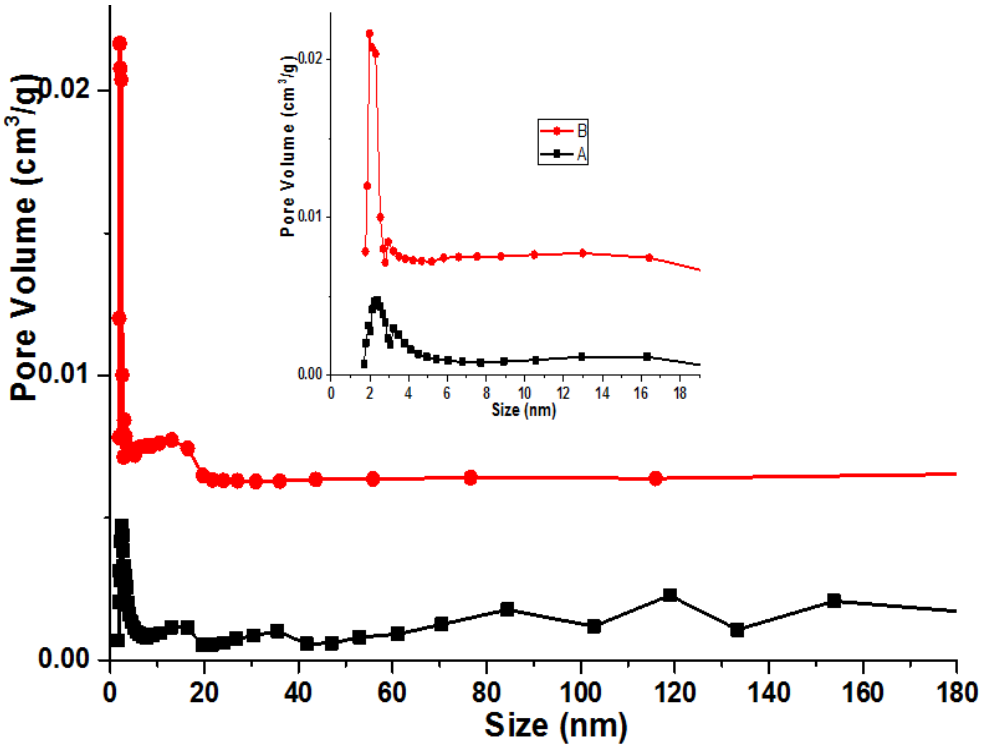

Figure 5.12 N_2 adsorption/desorption of micro- and nanoZSM-5: (a) interrupted synthesis without ultrasound with an increasing temperature of 25–170°C, (b) interrupted synthesis with ultrasound with an increasing temperature of 25–170°C.

Similarly, Figure 5.13 (c) and (d) report BJH results for samples synthesised with the same procedure but at a constant heat during the crystallisation period. A disordered mesopore distribution was observed with the

help of BJH N_2 adsorption in sample (c), whilst uniform pore distribution was observed in sample (d). The narrow distribution centre was found to be just over 3 nm in both cases.

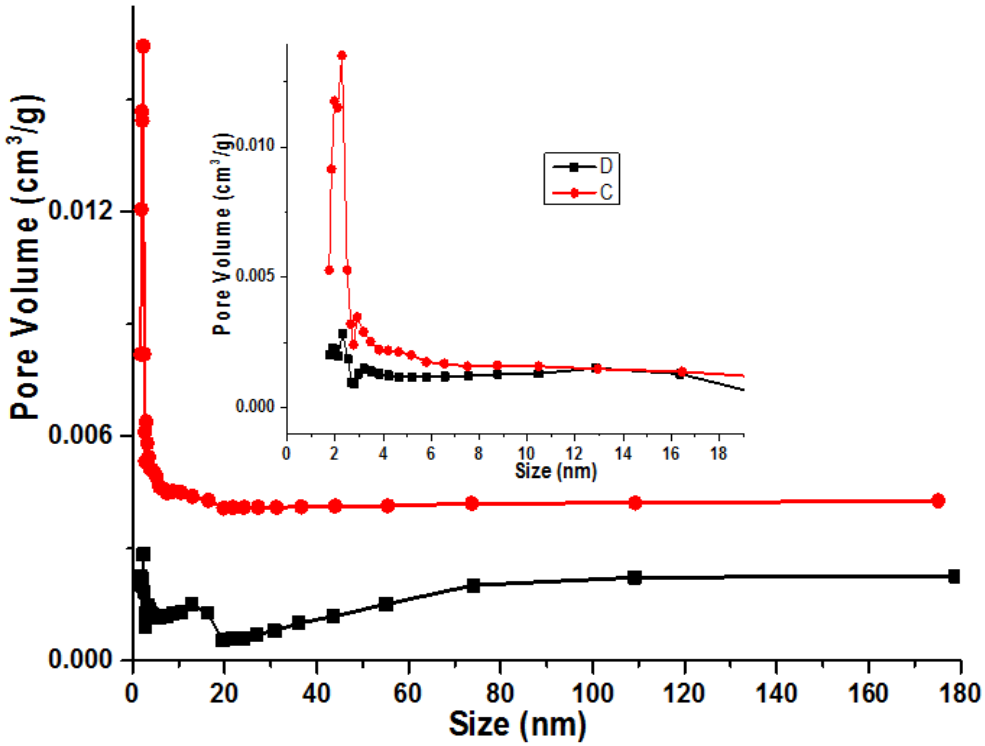

Figure 5.13 N_2 adsorption/desorption of micro- and nanoZSM-5: (c) interrupted synthesis without ultrasound at 170°C, (d) interrupted synthesis with ultrasound at 170°C.

5.3.7. Solid-state Magic Angle Spinning Nuclear Magnetic Resonance (MAS NMR)

Silicon is tetrahedrally coordinated in the framework; therefore, it has five different potential environments including Si(nAl) where n (n≤4) is the number of Al atoms connected to silicon via oxygen bridges.

The ^{27}Al MAS NMR spectra are used for the quantitative analysis of aluminium and its location and coordination in aluminosilicate materials. Generally, ^{27}Al MAS NMR spectra described for all aluminium-containing materials have only a single resonance at 54 ppm and another at 0 ppm assigned to the framework tetrahedrally coordinated Al atom (Al(4)) and a nonframework aluminium atom octahedrally coordinated Al(6), respectively.[27–29] The ^{27}Al MAS NMR spectra all of the as-synthesised samples are shown in Figure 5.14 (a), (b), (c) and (d). Samples (a) and (b) were synthesised with the interrupting crystallisation process with increasing temperature from 25°C to 170°C, as explained in previous sections. A distinct broadening of the line width was observed as the particle size decreased from (a) to (d).[30] The resonance at 0 ppm was not observed for sample (c), whilst a very small chemical shift was observed at 0 ppm from samples (a), (b) and (d) dependent on the Al concentration in the solution/gel.[28] This is consistent with the data observed in EDS elemental analysis in section (5.3.5). Quadrupolar effects are responsible for the ^{27}Al MAS NMR line broadening.[31] However, the small particles exhibit high surface energy, which has more influence in the lattice and may cause broad peaks to appear in the ^{27}Al MAS NMR spectra.

The ^{29}Si MAS NMR spectra of the sample in Figure 5.15 (a), (b), (c) and (d) are quite similar to those previously reported.[30,32] ^{29}Si MAS NMR spectra of each include a major chemical shift of -113 ppm with an overlapping signal at -115 ppm. Those are assigned to the Si(0Al) coordination in the ZSM-5 framework. There is also a broad resonance from -103 to -106 ppm which is assigned to Si(1Al) for each the samples of the ZSM-5 framework.[21,29,32] The chemical shift of -103 ppm and -106 ppm gives evidence of the presence of the silanol group on the surface.[11,21,30] The ^{29}Si MAS NMR spectra was also supported by the $^{1}H \rightarrow {}^{29}Si$ cross polarisation (CP) MAS NMR spectra as shown in Figure 5.16 (a), (b), (c) and (d). There are two main chemical shift values observed at 103 ppm and 112 ppm. These values confirm that the terminal hydroxyl group is directly connected to the Si atom in the SiO_4 tetrahedron (Si(1OH)). The concentration of the silanol group increased with decreasing particle size from sample (a) to (d) from 1,000 nm to <50 nm, respectively, as shown in Figure 5.16 and Figure 5.17.

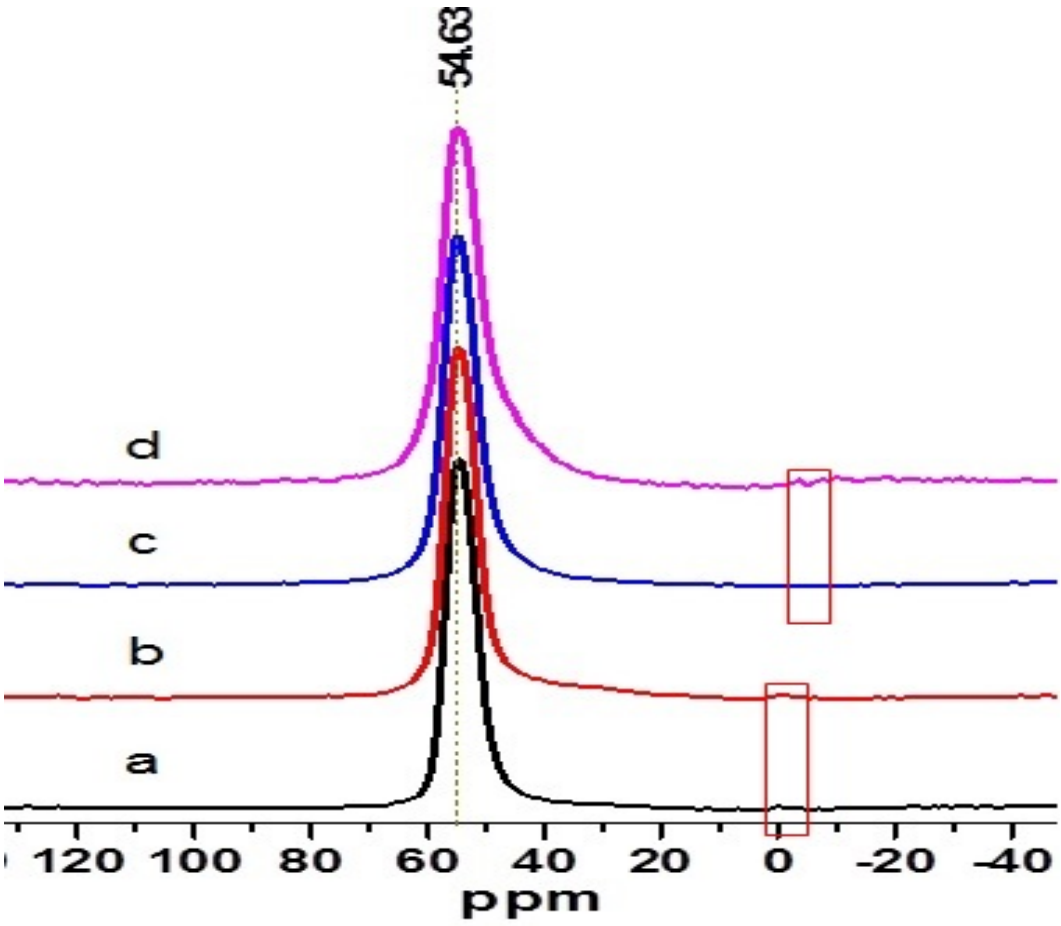

Figure 5.14 ^{27}Al spectra of the samples obtained by different synthesis methods: (a) interrupted synthesis without ultrasound with increasing temperature from 25^{o}C to 170^{o}C, (b) interrupted synthesis with ultrasound with increasing temperature from 25^{o}C to 170^{o}C, (c) interrupted synthesis without ultrasound at a constant temperature of 170^{o}C, (d) interrupted synthesis with ultrasound at 170^{o}C.

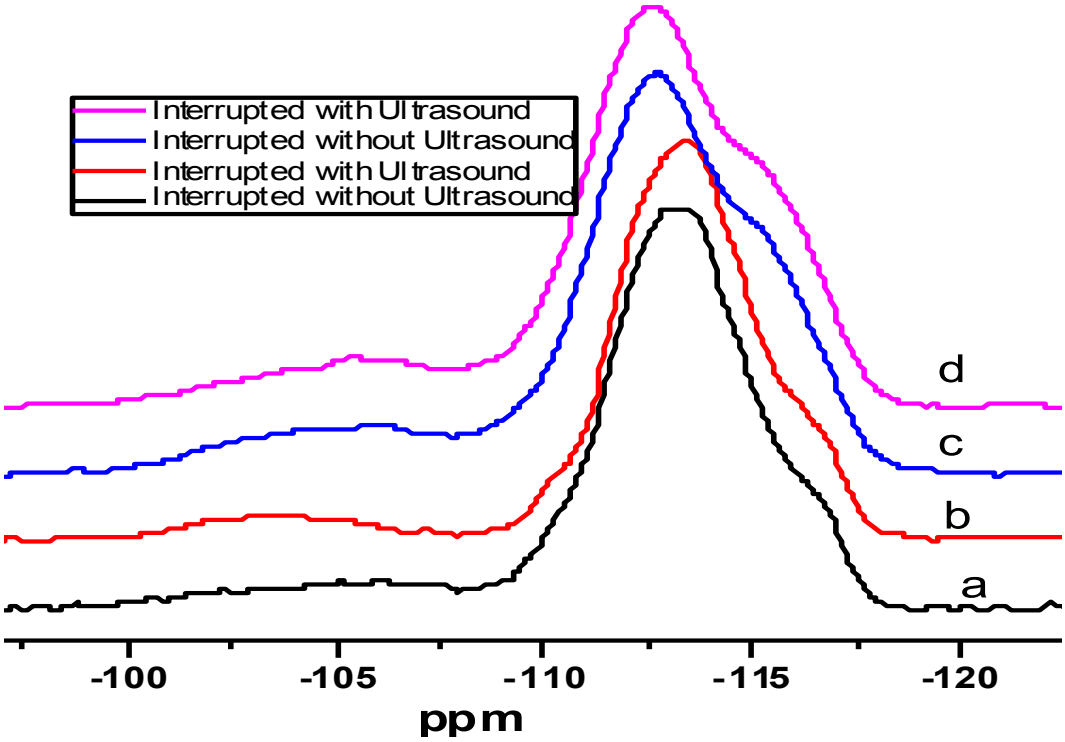

Figure 5.15 ^{29}Si spectra of the samples obtained by different synthesis methods: (a) interrupted synthesis without ultrasound with increasing temperature from 25°C to 170°C, (b) interrupted synthesis with ultrasound with increasing temperature from 25°C to 170°C, (c) interrupted synthesis without ultrasound at a constant temperature of 170°C, (d) interrupted synthesis with ultrasound at 170°C.

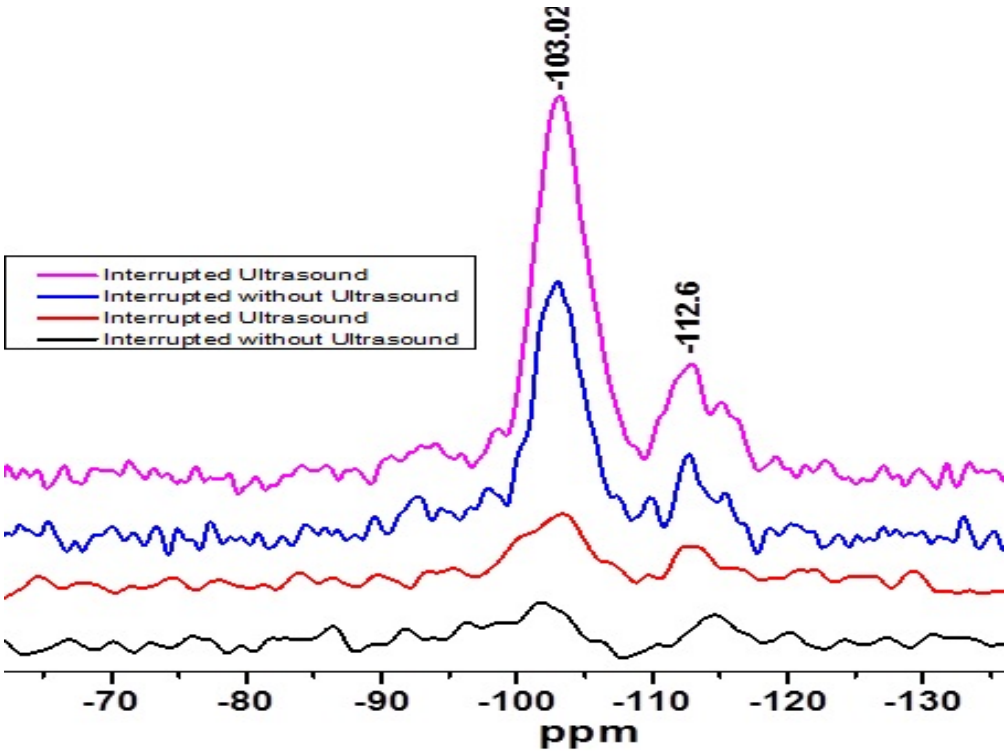

Figure 5.16 $^{1}H \rightarrow ^{29}Si$ cross polarization (CP) spectra of the samples obtained by different synthesis methods: (a) interrupted synthesis without ultrasound with increasing temperature from 25°C to 170°C, (b) interrupted synthesis with ultrasound with increasing temperature from 25°C to 170°C, (c) interrupted synthesis without ultrasound at a constant temperature of 170°C, (d) interrupted synthesis with ultrasound at a constant temperature of 170°C.

^{29}Si MAS NMR was used to determine the local coordination environment of silicon and aluminium. Deconvolution of all the ^{29}Si MAS NMR spectra are shown in Figure 5.17 (a), (b), (c) and (d). Sample (a), as explained in the X-ray diffraction section (5.3.1), is composed of crystalline and amorphous phases. The ^{29}Si spectra illustrate that there are ≥10 chemical shift peaks observed. Most of the resonance occurs in the range of -110 ppm to -117 ppm. Such kinds of ^{29}Si spectra

have been reported in the literature but without assignment of all the chemical shifts of the spectra.[29] The spectra of sample (a) were automatically deconvoluted using the *VnmrJ NMR* software, whilst the spectra of samples (b), (c) and (d) were deconvoluted manually using a Microsoft spreadsheet. Sample (b) has some small roughness in the peak difference line, indicating that there are still some small chemical shifts, which are unaccounted for in the deconvolution. Four peaks recorded in sample (b) from -116.3 ppm to -111 ppm are assigned to Si(0Al) crystallographically; these are inequivalent sites, whilst the peak at 103.5 ppm is related to Si(1Al) coordination. This peak is normally associated with the silanol group ($(SiO)_3SiOH$). On the other hand, samples (c) and (d) as shown in Figure 5.17 were highly crystalline nanoZSM-5 as explained in section 5.3.1 and showed a smooth line in the peak difference plot. There are four peaks recorded in samples (c) and (d). The peaks from -116 ppm to -112 ppm are assigned to the Si(0Al) coordination whilst the peaks at -110 ppm to -105 ppm are related to Si(1Al) sites. The peak at 105 ppm with low intensity is normally related to the silanol group. Also, it was noticed that the calculated peak overlap on the observed peaks of all the samples shown in Figure 5.17 (b), (c) and (d) results in a very fine and precise deconvolution. The increase in the aluminium site in samples (c) and (d) may also confirm the increase of the acidic site on the surface, as the terminal silanol group increased as the particle size decreased to $\leq$30 nm. Obviously, broadening was also observed, and the number of peaks reduced from sample (a) to (d) confirmed the particle size reduction from sample (a) to (d).

^{27}Al and ^{29}Si MAS NMR spectra confirmed the nanoZSM-5 framework structure. Line width broadening of both the spectra showed that the crystallite size decreased. The acidic site increased as the particle size decreased.

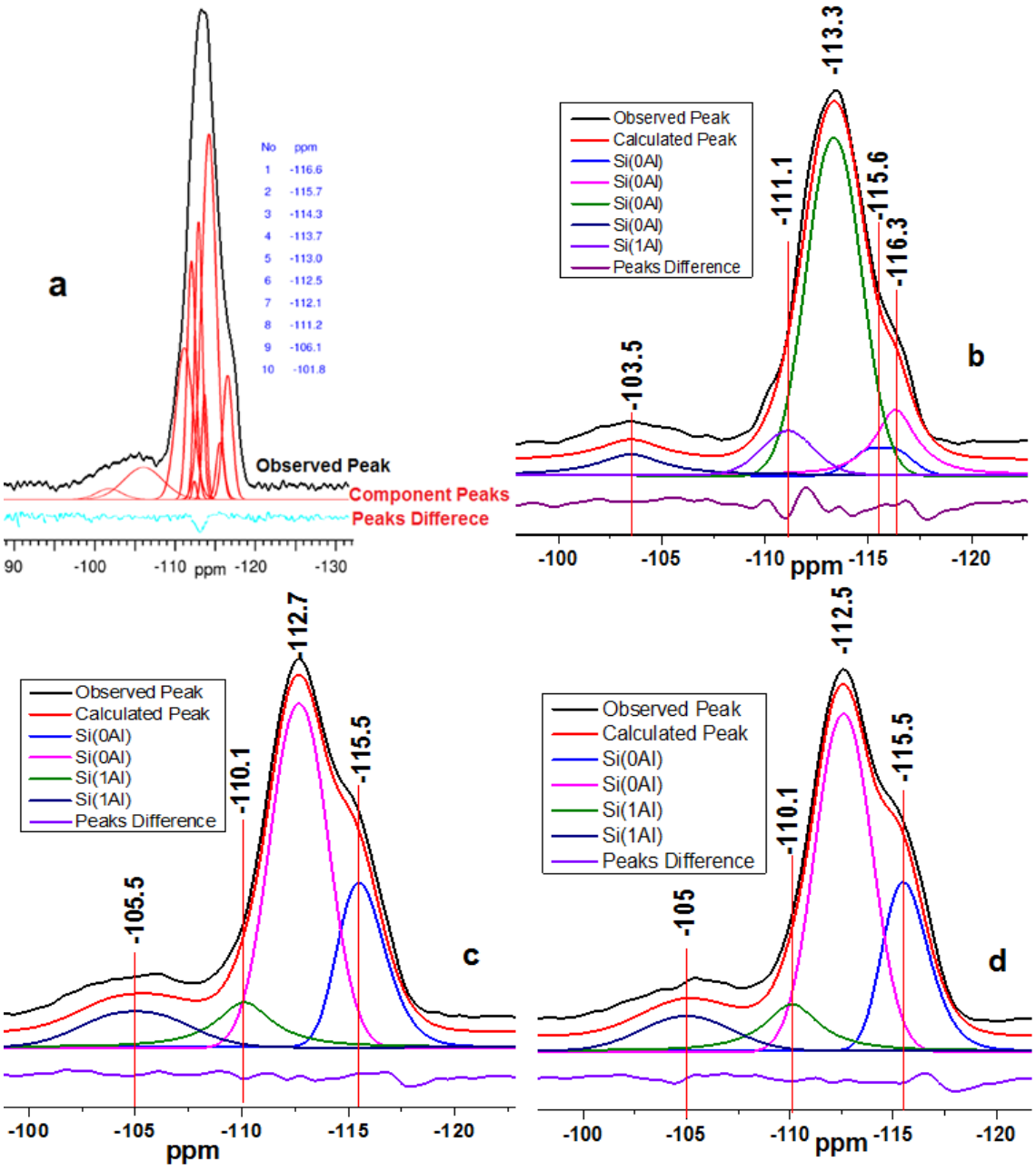

Figure 5.17 Deconvoluted ^{29}Si spectra of all the samples obtained by different synthesis methods: (a) interrupted synthesis without ultrasound with increasing temperature from 25^{o}C to 170 ^{o}C, (b) interrupted synthesis with ultrasound with increasing temperature from 25^{o}C to 170^{o}C, (c) interrupted synthesis without ultrasound at a constant temperature of 170^{o}C, (d) interrupted synthesis with ultrasound at a constant temperature of 170^{o}C.

5.4. Discussion

In this research, I have established a new route for the synthesis of nanoZSM-5 zeolite using ultrasound-interrupted aging. We proposed that aging has great influence on the nucleation process, which is directly related to the particle size distribution. As outlined, zeolites therefore involve a complex process; nucleation plays a key role in process crystallisation, crystal structure and size distribution.

For any solution-based crystallisation process, the nature of the resulting crystal will depend on the relative rates of two separate processes: nucleation and growth.

Nucleation is defined as the process by which discrete particles of a new phase are used in a previously single-phase system – in our case, a homogenous solution or gel. It has been established that these two processes are indeed separable.

The proposed nuclei are invariably very small, and furthermore, they only have transitory existence on most crystallisation processes although that situation may be different in the crystallisation of zeolites. It is generally answered that particles formed early in the nucleation process begin to grow immediately. Nuclei which form later attain smaller and smaller sizes corresponding to shorter and shorter growing times. This concept is thus at the heart of our strategy to synthesise nanoscale zeolites via interrupted growth.

No completely satisfactory theory has been worked out concerning the precise mechanism of the formation of nuclei in zeolite synthesis.

Conventional fluctuation theory postulates the formation of supersaturated solutions, some of which coalesce into a ‘nucleus’ only when the statistical fluctuation of their concentration brings a sufficiently large number of them

together to form a particle of a size that is thermodynamically stable as compared to the dissolution of the particle. This results in a critical particle size that can survive in solution without being redissolved. The free energy diagram for nucleation of a 'critical nucleus' is given below.

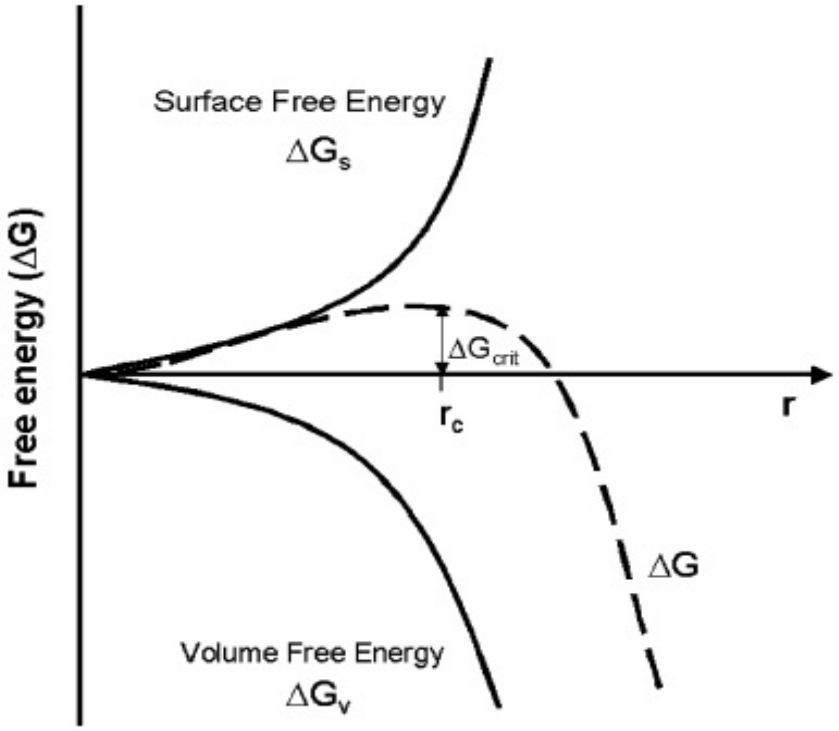

Figure 5.18 Free energy diagram for nucleation. Taken from[33]

The shortcomings of this 'classical' theory are evident in the crystallisation of zeolites, and nucleation of zeolitic solids from solution does not proceed via aclaric pathway but follows much more complex routes. Although there is abundant literature on zeolite nucleation, it is recognised that 'molecular' details are generally lacking, leaving many fundamental questions unanswered.

Defining the features of zeolite synthesis is the formation of so-called 'precursors'. Crystallisation of zeolites is therefore a complex process which is completed in different steps. Erdemir et al.[33] reported on crystallisation and nucleation mechanisms; they reported that the precursors properly mixed to form

a supersaturated solution lead to dissolved molecules and the start of aggregation. These aggregates then lead to the formation of nuclei, which is a metastable phase called nucleation. This is a first-order phase transition. The nucleation leads to the diffusion of particles known as growth units/primary units. This process occurs on the surface of existing nuclei, as discussed in section 2.2.3, because of crystal growth.

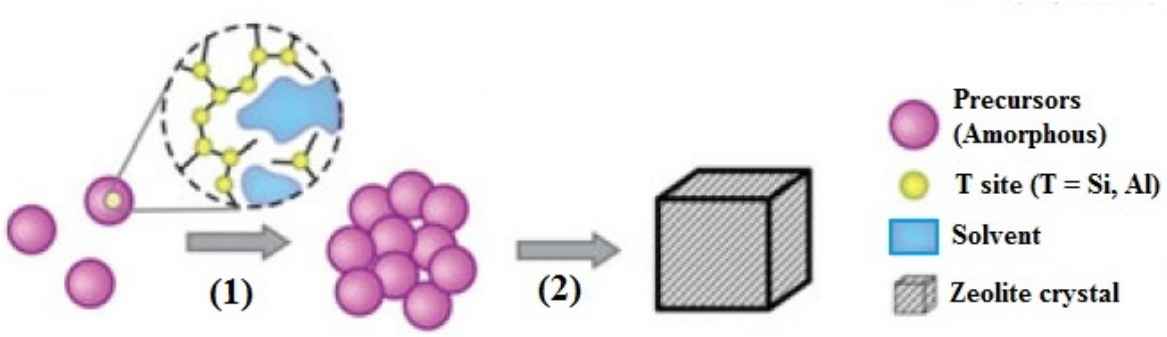

Figure 5.19 (1) One pathway of zeolite nucleation involves the aggregation of primary particles followed by their structural rearrangement. The primary particles are composed of aluminosilicate polymers with entrained solvent. (2) Conversion into the crystalline product. During this process, the amorphous aggregate involves structural rearrangement. The crystals may contain voids or defects (e.g., misaligned domains). Taken from[34]

It is very difficult to understand the mechanism of nucleation and crystallisation processes; although considered from previous research, nucleation occurs in the aging step of crystallisation. Therefore, we used ultrasound-interrupted treatment during the hydrothermal process to control particle size distribution and crystallisation. The key features of zeolite synthesis mechanism include the formation of nuclei from the precursors composed of primary particles (1–6 nm), bulk aggregates (0.1–1 μm) and gels.[34] The presence of precursors in the synthesis solutions of zeolite advances a two-step mechanism of nucleation, whilst the group of precursors provides a substrate for heterogeneous nucleation

or increases the high solute (Si and Al) concentration, which decreases the energetic barrier for nucleation.[34] According to the classical nucleation theory (CNT), zeolite nucleation is not composed of monomers/oligomers, which convert into clusters of size. An ultrasound-interrupted treatment for 15 minutes gives more time for the nuclei to transition to the metastable stage. The hydrothermal treatment increases the process of crystallisation. During the hydrothermal process, less nuclei may diffuse to form growth units. The hydrothermal process interrupted by means of ultrasound reduced the particle aggregation in the gel, therefore, and reduced the particle size during the next hydrothermal treatment for two hours at 170°C. The whole process of aging with ultrasound and then two hours of hydrothermal treatment sped up the crystallisation process. So after 24 hours, we prepared a highly crystalline nanoZSM-5 zeolite having a particle size of <100 nm. On the other hand, the synthesis route followed the same procedure under the same experimental conditions comparatively without ultrasound treatment giving less crystalline nanoZSM-5 zeolite having a large particle size of >200 nm as shown in Figure 5.20. The nanoZSM-5 crystallinity was confirmed by X-ray diffraction. TEM and SEM determined the crystallite size and morphology. The textural properties were investigated by N_2 adsorption and desorption BET surface analysis. ^{27}Al and ^{29}Si MAS NMR confirmed the framework composition and presence of the silanol group at the surface of the nanoZSM-5.

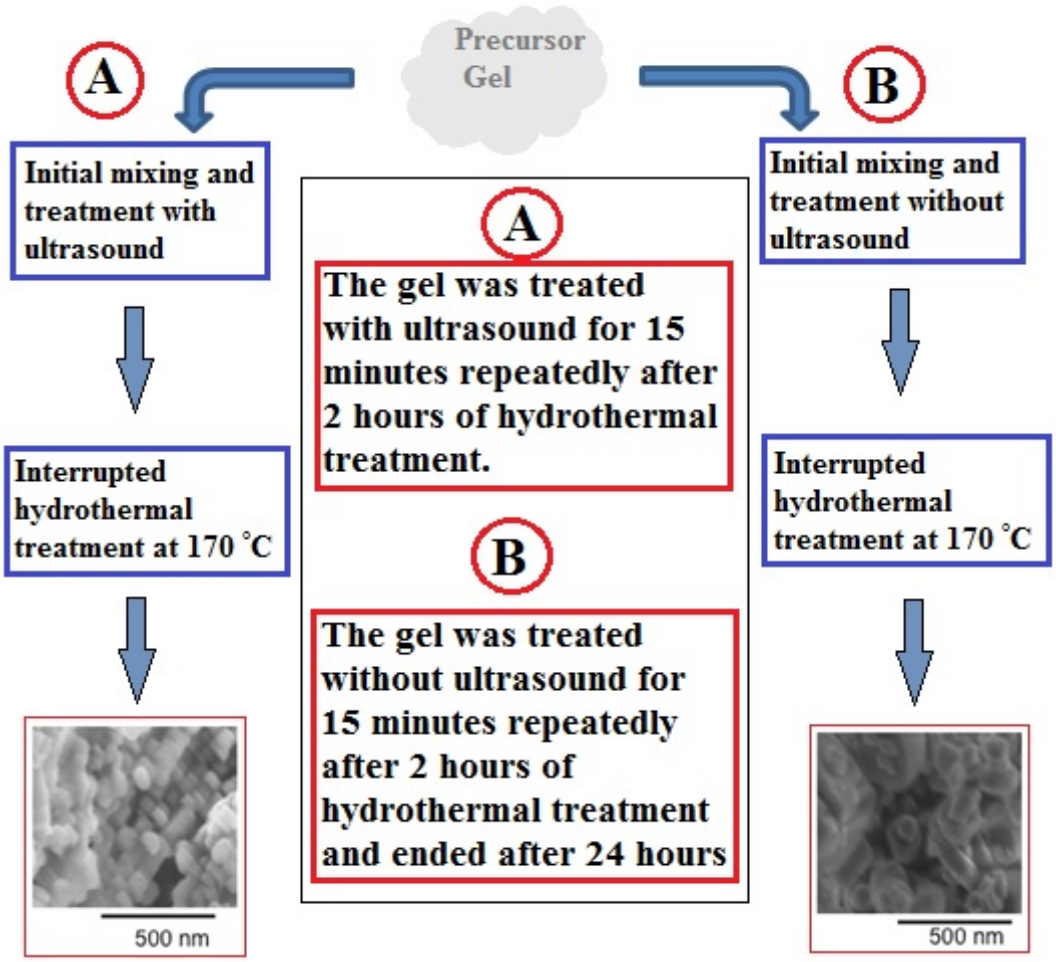

Figure 5.20 Flow sheet of synthesis mechanism of nanoZSM-5 using ultrasound and without ultrasound-interrupted hydrothermal treatment at 170°C.

5.5. Conclusion

The hydrothermal process interrupted by means of ultrasound reduced particle aggregation in the gel, thus the particle size in the next hydrothermal treatment for two hours at 170°C. The whole process of aging with ultrasound and then two hours of hydrothermal treatment sped up the crystallisation process and hence reduced particle size distribution. After 24 hours, we received a highly crystalline nanoZSM-5 zeolite having a particle size of <100 nm. On the other hand, the synthesis route followed the same procedure under the same experimental conditions comparatively without ultrasound treatment giving a less crystalline nanoZSM-5 zeolite having a large particle size of >200 nm. All the synthesised samples were then characterised by XRD for the framework confirmation and calculation of particle size distribution. HRTEM and SEM were used for particle size distribution and for determination of crystallite morphology. DLS was used for particle size distribution. EDX was used to calculate the Si/Al ratio and elemental analysis. N_2 adsorption and desorption was used for surface analysis and pore size distribution. Solid-state MAS NMR was used for structure and framework confirmation and for the calculation of Si/Al ratio.

5.6. References

[1] "IZA Commission on Natural Zeolites structure data base," can be found under http://www.iza-structure.org/databases/, **2005**.

[2] P. Sharma, J. Yeo, M. H. Han, C. H. Cho, *RSC Adv.* **2012**, *2*, 7809.

[3] M. Abrishamkar, S. N. Azizi, H. Kazemian, *J. Inorg. Gen. Chem.* **2010**, *636*, 2686–2690.

[4] R. Karimi, B. Bayati, N. Charchi Aghdam, M. Ejtemaee, A. A. Babaluo, *Powder Technol.* **2012**, *229*, 229–236.

[5] Z. Qin, L. Lakiss, L. Tosheva, J.-P. Gilson, A. Vicente, C. Fernandez, V. Valtchev, *Adv. Funct. Mater.* **2014**, *24*, 257–264.

[6] S. Mintova, V. Valtchev, E. Vulcheva, S. Veleva, *Mater. Res. Bull.* **1992**, *27*, 515–522.

[7] J. Aguado, D. P. Serrano, J. M. Escola, J. M. Rodriguez, *Microporous Mesoporous Mater.* **2004**, *75*, 41–49.

[8] W. Song, R. E. Justice, C. A. Jones, V. H. Grassian, S. C. Larsen, *Langmuir* **2004**, *20*, 8301–8306.

[9] F. Pan, X. Lu, Q. Zhu, Z. Zhang, Y. Yan, T. Wang, S. Chen, *J. Mater. Chem. A* **2014**, *2*, 20667–20675.

[10] X. Wenyang, L. Jianquan, L. Wenyuan, Z. Huiming, L. Bingchang, *Zeolites* **1989**, *9*, 468–473.

[11] N. Venkatathri, *React. Kinet. Catal.Lett.* **2007**, *91*, 283–289.

[12] J. C. Moreno-Piraján, V. S. Garcia-Cuello, L. Giraldo, *J. Thermodyn. Catal.* **2010**, *1*, 1–8.

[13] M. Hunger, J. Karger, H. Pfeifer, J. Caro, B. Zibrowius, M. Bulow, R. Mostowicz, *J. Chem. Soc., Faraday Trans. I* **1987**, *83*, 3459–3468.

[14] A. Čižmek, B. Subotica, D. Kralj, V. Babić-Ivančić, A. Tonejc, *Microporous Mater.* **1997**, *12*, 267–280.

[15] H. Awala, J.-P. Gilson, R. Retoux, P. Boullay, J.-M. Goupil, V. Valtchev, S. Mintova, *Nat. Mater.* **2015**, *14*, 447–451.

[16] I. Schmidt, C. Madsen, C. J. H. Jacobsen, *Inorg. Chem.* **2000**, *39*, 2279–2283.

[17] G. Majano, A. Darwiche, S. Mintova, V. Valtchev, *Ind. Eng. Chem. Res.* **2009**, *48*, 7084–7091.

[18] S. Mintova, V. Valtchev, *Microporous Mesoporous Mater.* **2002**, *55*, 171–179.

[19] S. Sklenak, J. Dědeček, C. Li, B. Wichterlová, V. Gábová, M. Sierka, J. Sauer, *Phys. Chem. Chem. Phys.* **2009**, *11*, 1237–1247.

[20] K. S. W. Sing, *Pure Appl. Chem.* **1985**, *57*, 603–619.

[21] R. V. Grieken, J. L. Sotelo, J. M. Menéndez, J. A. Melero, *Microporous Mesoporous Mater.* **2000**, *39*, 135–147.

[22] S. Li, L. Zhou, A. Zheng, F. Deng, *Chinese J. Catal.* **2015**, *36*, 789–796.

[23] L. Ma, I. Jia, X. Guo, L. Xiang, *Chinese J. Catal.* **2014**, *35*, 108–119.

[24] K. Gao, S. Li, L. Wang, W. Wang, *RSC Adv.* **2015**, *5*, 45098–45105.

[25] T. F. S. Grecco, E. A. Urquieta-Gonzalez, P. Reyes, M. Oportus, M. do C. Rangel, *J. Braz. Chem. Soc.* **2014**, *25*, 2444–2454.

[26] Y. Liu, X. Zhou, X. Pang, Y. Jin, X. Meng, X. Zheng, X. Gao, F.-S. Xiao, *Chem Cat Chem* **2013**, *5*, 1517–1523.

[27] P. Duxson, J. L. Provis, G. C. Lukey, F. Separovic, J. S. J. Van Deventer, *Langmuir* **2005**, *21*, 3028–3036.

[28] C. F. Cheng, H. H. Cheng, L. L. Wu, B. W. Cheng, in *Stud. Surf. Sci.*

Catal., **2005**, pp. 113–118.

[29] J. Klinowski, *Annu. Rev. Mater. Sci.* **1988**, *18*, 189–218.

[30] W. Zhang, X. Bao, X. Guo, X. Wang, **1999**, *60*, 89–94.

[31] W. Basler, H. Lechert, K. Paulsen, D. Rehder, *J. Magn. Reson.* **1981**, *45*, 170–172.

[32] C. J. H. Jacobsen, C. Madsen, T. V. W. Janssens, H. J. Jakobsen, J. Skibsted, *Microporous Mesoporous Mater.* **2000**, *39*, 393–401.

[33] D. Erdemir, A. Y. Lee, A. S. Myerson, *Acc. Chem. Res.* **2009**, *42*, 621–629.

[34] J. D. Rimer, M. Tsapatsis, *MRS Bull.* **2016**, *41*, 393–298.

Conclusion and Future Work

Conclusion

This thesis consists of two major parts. The first part is the synthesis and characterisation of mordenite zeolite and ZnS nanoclusters in the pore channels of mordenite zeolite. Mordenite zeolite synthesis was controlled by temperature and crystallisation time, whilst the synthesis of ZnS was carried out in a solution-based ion-exchange process. Na_2S was used as a sulfur source instead of H_2S gas, which is usually employed in the literature. The study of mordenite zeolite synthesis has shown that the degree of crystallinity depends on crystallisation time and temperature. The XRD powder pattern showed that there is no loss of framework structure after Zn and S ion exchange. The decrease in the calculated unit cell parameter of the crystal lattice shown in the samples was found to be in the following order: NaMOR > ZnMOR > ZnSMOR. The presence of Zn and S ions in ZnMOR and ZnSMOR samples is evident in EDX elemental analysis. The increase in the BET surface area analysis confirms the formation of ZnS that may be placed on the pore mouth of the mordenite zeolite framework. ^{29}Si NMR gives three local Si environments, and all ^{27}Al NMR spectra revealed a tetrahedral coordination of Al atoms and showed that the mordenite framework is not affected after the growth of ZnS within the pore channels.

The second part of the thesis describes the study of nanoZSM-5 zeolite (MFI framework) using an ultrasound pretreatment and interrupted crystallisation. All the experiments were performed under similar experimental conditions during crystallisation in both methods. The study revealed that the decrease in crystallite

size depends on the ultrasound pretreatment as well as the interrupted treatment of crystallisation. Decreasing the crystallite size by using ultrasound treatment also leads to a greater degree of crystallinity of nanoZSM-5 by using ultrasound treatments.

The synthesis of nanoZSM-5 zeolite has a wide application in catalytic processes in the petroleum industry for catalysis. The zeolite activity plays a vital role in the petroleum industry as a catalyst, so the nanocrystalline ZSM-5 would further impact the efficiency of catalytic processes because of its size. Ultrasound has a great impact on the crystallisation process as well as on the particle size of the zeolites. The zeolite manufacturers may take advantage of the ultrasound treatment synthesis to improve the quantity and crystallinity of the nanoZSM-5 zeolites.

Future work

Future study is in progress on the first part of the thesis for further characterisation, tests and the application for the fabrication of semiconductor nanoclusters.

The two different ultrasound treatment methods can be further optimised by treating the gel before or after the crystallisation process. These methods may also be modified by using different modes of ultrasound treatment for further studies. A combination of microwave and ultrasound may be used to enhance the particle size of the synthesised zeolite. The method can also be modified by using ultrasound instead of the hydrothermal process to enhance further crystallinity and the crystallite size of the ZSM-5 zeolite.

List of Abbreviations

Al……. Aluminium

B…….…….. Boron

Be…….…… Beryllium

BET……..…… Brunauer-Emmett-Teller

BJH……..…… Barrett-Joyner-Halenda

BSE……..…Back Scattering Electrons

Ca…….……...…… Calcium

Cd…….…….……..… Cadmium

Cl…….……..... Chlorine

CNTs…….…….……. Carbon Nano Tubes

DLS…….…… Dynamic Light Scattering

DME……...……. Dimethyl Ether

DMN…….. …….Dimethylnaphthalene

EDXS……..… Energy-dispersive X-ray Spectroscopy

EELS……..…. Electron Energy Loss Spectroscopy

EXAFS…… Extended X-ray Absorption Fine Structure

F……...…… Fluorine

FAU…….…… Faujasite

FT-IR…… Fourier Transform Infra-Red

FWHM……. Full Width Half Maximum

Ga……..…….. Gallium

GIS…….……. Gismondine

H……. Hydrogen

ICP-AES……. Inductively Coupled Plasma atomic Emission Spectroscopy

IUPAC…… International Union of Pure and Applied Chemistry

IZA……..International Zeolite Association

K…….. Potassium

LTA…….……. Linda Type A

LTL…….…….. Linda Type L

MCM-41……..……. Mobil Catalytic Material 41

MFI…… Mobil-five

MOR…….. Mordenite

N…….……... Nitrogen

Na……..…… Sodium

O..…….. Oxygen

P…….…… Phosphorus

PBU…..……..Primary Building Units

PCS…… Photon Correlation Spectroscopy

PL…..…… Photoluminescence

PTFE.……. Polytetrafluoroethylene

S……. Sulphur

SAED……. Selected Area Electron Diffraction

SAR…… Silicon to Aluminium Ration

SBU…… Secondary Building Units

SDA……. Structure Directing Agent

SEM……. Scanning Electron Microscopy

Si……..…… Silicon

SSMASNMR… Solid State Magic Angle Spinning Nuclear Magnetic Resonance

T…… Tetrahedra

TEAOH…. Tetraethylamonium Hydroxide

TEM…… Transmission Electron Microscope

TEOS…….. Tetraethyl Orthosilicate

TMOS……. Tetramethyl Orthosilicate

TMS……Tramethylsilane

TPABr……. ……Tetrapropylammonium Bromide

TPAOH…… …..Tetrapropylammonium hydroxide

TPD…… Temperature-Programme Desorption

USP…….Ultrasonic spray pyrolysis

UV-vis……. Ultra Violet-visible

Wt…….. .Weight

XRD…… X-ray Diffraction

Zn……. ..Zinc

ZSM-5……..…….. Zeolite Socony Mobil-5

XRD Peak Fittings

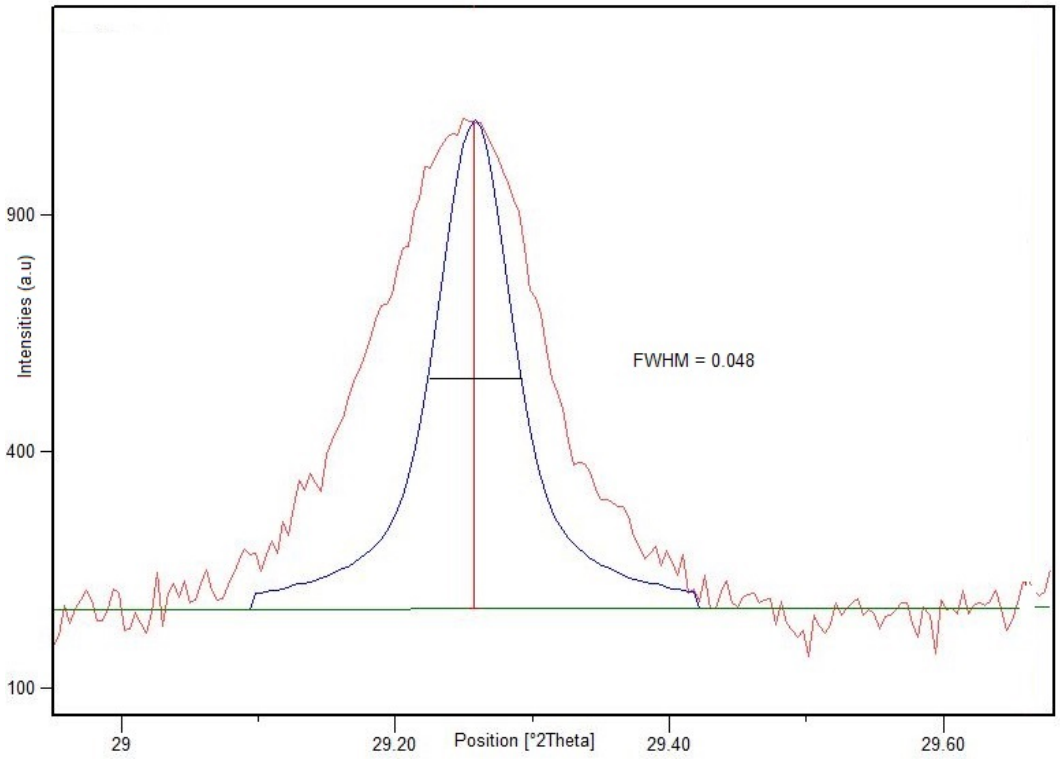

Before peak fittings the FWHM value was 0.0480 using X'Pert HighScore.

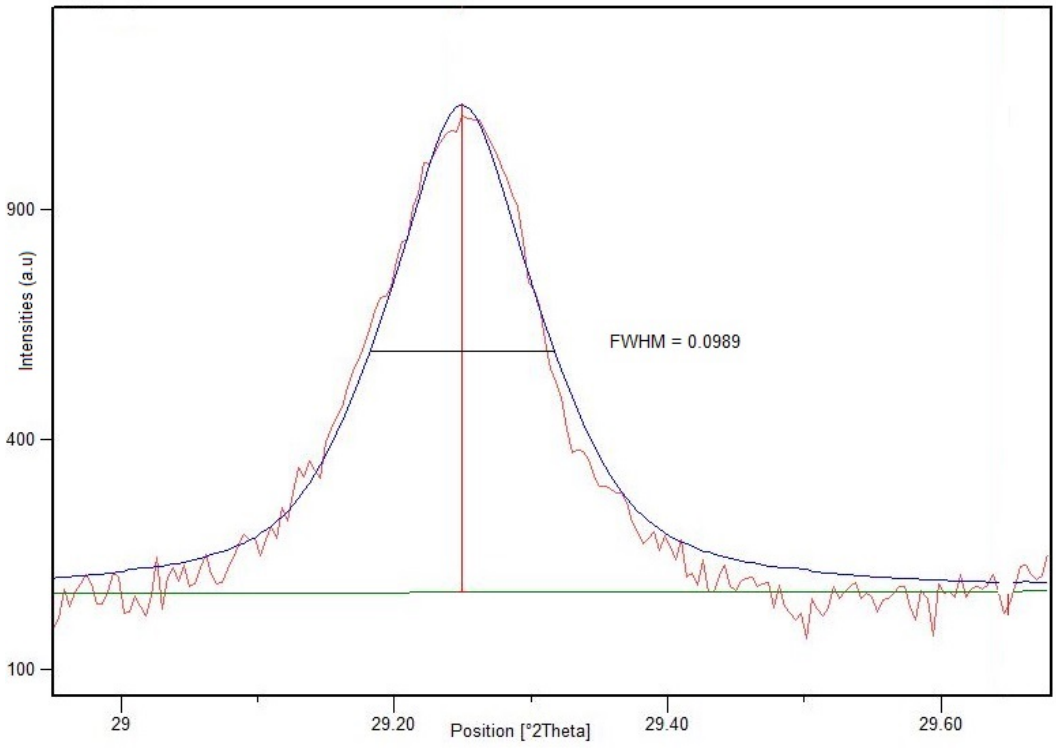

After peak fittings the FWHM value increased to 0.0986 using X'Pert HighScore software.

So, the error was estimated as:

After peak fitting – Before peak fittings = 0.0986 – 0.048 = 0.0506